2017-07-01

A Comprehensive Coal Conversion Model Extended to Oxy-Coal Conditions

Troy Michael Holland
Brigham Young University

A Comprehensive Coal Conversion Model Extended to Oxy-Coal Conditions

Troy Michael Holland

A dissertation submitted to the faculty of
Brigham Young University
in partial fulfillment of the requirements for the degree of

Doctor of Philosophy

Thomas H. Fletcher, Chair
David O. Lignell
Sean Smith
Morris Argyle
Bradley C. Bundy

Department of Chemical Engineering

Brigham Young University

ABSTRACT

A Comprehensive Coal Conversion Model Extended to Oxy-Coal Conditions

Troy Michael Holland
Department of Chemical Engineering, BYU
Doctor of Philosophy

Oxy-fired coal combustion is a promising potential carbon capture technology. Predictive CFD simulations are valuable tools in evaluating and deploying oxy-fuel and other carbon capture technologies either as retrofit technologies or for new construction. However, accurate predictive simulations require physically realistic submodels with low computational requirements. In particular, comprehensive char oxidation and gasification models have been developed that describe multiple reaction and diffusion processes. This work extends a comprehensive char conversion code (the Carbon Conversion Kinetics or CCK model), which treats surface oxidation and gasification reactions as well as processes such as film diffusion, pore diffusion, ash encapsulation, and annealing. In this work, the CCK model was thoroughly investigated with a global sensitivity analysis. The sensitivity analysis highlighted several submodels in the CCK code, which were updated with more realistic physics or otherwise extended to function in oxy-coal conditions. Improved submodels include a greatly extended annealing model, the swelling model, the mode of burning parameter, and the kinetic model, as well as the addition of the Chemical Percolation Devolatilization (CPD) model. The resultant Carbon Conversion Kinetics for oxy-coal combustion (CCK/oxy) model predictions were compared to oxy-coal data, and further compared to parallel data sets obtained at near conventional conditions.

Keywords: comprehensive coal conversion, oxy-coal, annealing, sensitivity analysis, uncertainty quantification

ACKNOWLEDGEMENTS

This dissertation exists because of the generous counsel, support, and inspiration of far more people than I can list here; however, I would like to take a few lines to express gratitude for my most influential friends and family. First, I would like to thank my parents for the many opportunities and conveniences they sacrificed for themselves to promote the well-being of their children. Their consistent, daily choices made my pathway to an advanced degree apparent, but, more importantly, it taught me that my path forward was paved by and for people, not academic achievement.

Next, I must acknowledge my wife, who at this moment is attempting to raise three children with a husband who is absent far more hours than she wants him to be. We chose long hours and postponed more stable career choices to better secure our children's future, and she shared the burden willingly. While I'm on the subject of children, I have to thank them for their consistent, enthusiastic, and, above all, *shrill* daily welcome home. Without their needs to think of, we may well have made more convenient employment choices.

From a professional viewpoint, my graduate school career would never have made it off the ground without an advisor, and it could have turned into long, painful years without a great advisor. I chose to continue my advanced education at Brigham Young University in large measure because of my great confidence in the faculty, but even among such a skilled and compassionate group, I feel privileged to have studied under Dr. Thomas Fletcher. He had the experience to know what I should be doing, and the wisdom (and patience) to know when I should figure it out for myself. He came to BYU as a matter of faith and sacrifice for the good of

students he hadn't even met, and I personally know of no one who has benefitted more from his choice to let kindness dictate his priorities.

I was fortunate to complete the bulk of my research as a graduate research assistant at Los Alamos National Laboratories. Here I had several skilled and patient mentors, but I would particularly like to acknowledge Dr. Sham Bhat for the long hours of what must have been frustratingly low-level discussions of statistical modeling and uncertainty quantification. I would also like to thank Dr. Joel Kress. While Dr. Kress is certainly a gifted scientist, those of us who have benefitted from his leadership have done so in large part because he is one of relatively few managers who leads more than he manages. I consider the difference between management and leadership to be the difference between bean counting and people building, and Joel excels at pushing people one step farther towards their potential, and then waiting for their professional problems to solve themselves.

I would also like to acknowledge other mentors, including the members of my committee (Drs. David Lignell, Sean Smith, Morris Argyle, and Brad Bundy) both for their work on my committee and from their counsel and teaching throughout my undergraduate and graduate work. I also learned from the mentorship of Drs. James Gattiker and Peter Marcy at Los Alamos, and Drs. Christopher Shaddix and Ethan Hecht at Sandia National Laboratories, as well as numerous members and industrial advisors of the Carbon Capture and Simulation Initiative and the Carbon-Capture Multidisciplinary Simulation Center.

Finally, and most importantly, I found that graduate school was an Edisonian experience, where I made a long list of mistakes, both technical and otherwise, followed by brief breakthroughs. This has broadly been my experience with life in general and it gives me an opportunity to reflect on and appreciate the grand plan that my Heavenly Father has for his

children. It is by design that I can make mistakes and learn from them, and by divine intervention that mistakes need not be permanent and can even turn to triumphs.

Funding Acknowledgements:

This material is based upon work supported by the Department of Energy, National Nuclear Security Administration, under Award Number DE-NA0002375.

Funding for this work was also provided by the Department of Energy through the Carbon Capture Simulation Initiative. This report was prepared as an account of work sponsored by an agency of the United States Government. Neither the United States Government nor any agency thereof, nor any of their employees, makes any warranty, express or implied, or assumes any legal liability or responsibility for the accuracy, completeness, or usefulness of any information, apparatus, product, or process disclosed, or represents that its use would not infringe privately owned rights. Reference herein to any specific commercial product, process, or service by trade name, trademark, manufacturer, or otherwise does not necessarily constitute or imply its endorsement, recommendation, or favoring by the United States Government or any agency thereof. The views and opinions of authors expressed herein do not necessarily state or reflect those of the United States Government or any agency thereof.

TABLE OF CONTENTS

LIST OF TABLES

LIST OF FIGURES

NOMENCLATURE

Parameter(s)	Description
a	A parameter for determining the mean of the annealing activation energy distribution
$A_{d,0}$	The initial value of A_d (s^{-1})
A_d	The preexponential factor of the annealing reaction (s^{-1})_
A_p	Particle area (m^2)
$A_{R,1}$-$A_{R,8}$	The preexponential factor for 8 reactions and 2 reverse reactions. These come largely from correlations, and can be adjusted for specific data.
B_f	A factor used to split the log normal distribution of the annealing activation energy into a bimodal, irregular distribution
B_r	A factor used to split the log normal distribution of the annealing activation energy into a bimodal, irregular distribution
b	A parameter for determining the mean of the annealing activation energy distribution
c	A parameter for determining the mean of the annealing activation energy distribution
c_0	The number of stable bridges
c_{HR}	An NMR structure based swelling parameter
c_j	The j^{th} coefficient of the NMR correlations
C_p	The per mass heat capacity of the char particle J/kg/K
D_j	The j^{th} principal component or basis function in the emulator for the model discrepancy (δ)
$d_{p,0}$	The initial particle diameter, in microns
E_A	The activation energy in the annealing reaction
E_d	The activation energy in the annealing reaction
E_c	The activation energy for computing the CO/CO_2 ratio in cal/mol
$E_{R,1}$-$E_{R,8}$	The activation energy for 8 reactions and 2 reverse reactions. These come largely from correlations, and can be adjusted for specific data.
f_i	The fraction of active sites in bin “i" in the thermal annealing model
f	The conversion of char in annealing reactivity TGA experiments
HHR	Higher Heating Rate
HR	The initial heating rate of the raw coal particle (K/s)
IP	Internal parameters for GPMSA
K_j	The j^{th} principle component or basis function in the emulator for the model (η)
k_i	The rate constant of reaction “i” in the particle
MC_R	Measured coal reactivity (post annealing)
m_p	The mass of the char particle (kg)
M_δ	The average molecular weight of the side chains in a coal “monomer”
M_{cl}	The average molecular weight of an aromatic cluster in a coal “monomer”
N	The intrinsic order of R2 (formation of CO_2 by combustion). This defaults to unity, but can be adjusted to explore other kinetic regimes.
PC_R	Model-predicted coal reactivity (post annealing)
p_0	An NMR parameter for the fraction of intact bridges in the coal pseudo monomer.

P_i	The partial pressure of reactive gas “i" at the surface of the particle
$r_{p,i}$	The rate of reaction “i” in the particle
s_{min}	A proximate analysis based swelling parameter
s_{var}	An NMR structure based swelling parameter
T_g	The gas temperature (K)
T_p	The particle temperature or the peak particle temperature (K)
T_s	The temperature of the surroundings for radiative heat transfer (K)
v_j	The weighting factor in the form of a GP multiplied by the j^{th} PC for δ
w_j	The weighting factor in the form of a GP multiplied by the j^{th} PC for η
$\mathbf{x}$	The vector of model inputs in GPMSA
X_c	The percentage carbon from the ultimate analysis
y	The prediction (with uncertainty) of the model+discrepancy+observational error
α	The mode of burning parameter
β	A length-scale parameter in GPMSA
δ	The discrepancy between a model and reality, typically due to incomplete system knowledge or the ubiquitous, imperfect assumptions used to develop a model
$\Delta H_{rxn,i}$	The enthalpy of reaction “i" in the particle
ε	The observational error (noise) in experimental observations
ε_p	Particle emissivity
η	The effectiveness factor (used with the Thiele modulus)
η	Any model accepting inputs $\mathbf{x}$ and parameters $\boldsymbol{\theta}$ (or an emulator thereof)
λ	A weighting factor to modify the variance in GPMSA
λ_{w_Os}	A nugget to modify the variance in GPMSA
μ_{Ed}	The mean of the annealing activation energy distribution (kcal/mol)
Φ_i	The Thiele modulus
ψ	A random pore model parameter. This value has some uncertainty, and defaults to 4.6.
ρ	A length-scale parameter in GPMSA
Σ	A matrix of covariances in the GPMSA formulation
σ	Stefan-Boltzman constant or a parameter in the log normal distribution
σ_0	The initial standard deviation of the annealing activation energy distribution (kcal/mol)
σ_{Ed}	The standard deviation of the annealing activation energy distribution (kcal/mol) (σ_0 divided by p_0)
σ+1	The coordination number (i.e., the number of attachments per cluster in the coal, determined by NMR spectroscopy)
$\boldsymbol{\theta}$	The vector of model parameters in GPMSA
τ/f	A random pore model parameter. This value has some uncertainty, and defaults to 12.
Ω	The swelling coefficient ($d_p/d_{p,0}$)

1 INTRODUCTION

The U.S. needs affordable, clean, secure energy for the future. Coal has played an integral role in providing the energy necessary for first-world conditions for many decades, and currently provides 37% of U.S. electricity production (with slight variation year to year) (DoE, 2013). Moreover, if coal consumption trends continue, U.S. reserves will hold out for decades. This vital fuel has also maintained a stable, narrow price range for the past six decades (relative to the highly volatile natural gas and oil prices) (EIA, 2012), so the U.S. can expect future financial viability. Coal is not "clean," but current and emerging solutions can clean up post-combustion products, and since the U.S. controls enormous coal deposits, it can provide financially secure, long-term energy via internal resources through well established and improving technologies.

While coal-based power contributes heavily to modern quality of life, it also has a well-deserved reputation for emissions. Recently proposed Environmental Protection Agency (EPA) regulations aim to reduce these emissions. In light of these regulations and in support of the continuing effort to provide clean, low-cost energy, oxy-coal (coal combustion in a stream of oxygen and recycled flue gas) has been proposed as a potential low-cost technology solution for both carbon capture and simultaneous reduction of NO_x and SO_x emissions (Smith, 2012).

Oxycoal combustion has been reviewed thoroughly elsewhere (Wall et al., 2009; Scheffknecht et al., 2011), but in essence it consists of injecting high purity O_2 with the

pulverized coal rather than the conventional air-fired method. To reduce the boiler temperatures to manageable levels, the flue gas is typically recycled, producing a combustion environment with high concentrations of CO_2, O_2, and (potentially) H_2O. The flue gas then contains very high concentrations of CO_2, and the CO_2 is thus relatively easy to capture.

While an oxycoal system simplifies carbon capture, it also radically changes the environment the coal particles experience. The new environment changes the O_2 diffusion rate, may cool the char particle via endothermic gasification, and may alter the overall char consumption rate due to gasification reactions (Hecht et al., 2012). These effects and others such as reduced flame temperature, delayed ignition, decreased acid gases, and increased gas emissivity can largely be ascribed to differences between CO_2 and N_2 (the respective diluents in oxycoal and air-fired pulverized coal systems) (Wall et al., 2009). The change in diluent gas induces several interrelated effects that alter the burnout time and radiative behavior of the system, so accurate CFD predictions of oxycoal combustion require models that describe these phenomena. This dissertation extends a single-particle, comprehensive char conversion model to account for the extreme conditions and phenomena of char conversion in the oxy-coal environment. Specifically, a historically successful comprehensive code is evaluated for model success and submodel sensitivity in the oxy-coal environment, the sensitive submodels are updated to include relevant physics, and the extended model is validated against oxy-coal laboratory-scale data.

2 LITERATURE REVIEW

The following literature review discusses the fundamentals of coal, the transformation of raw coal to char and the subsequent conversion of char, and past modeling techniques (both simple and highly detailed). The review concludes with an extensive review of the literature that describes the highly influential char annealing process.

2.1 Coal

Coal is fossilized organic matter, and, like the organic matter that precedes the mineral, coal has a highly variable composition. Coal falls broadly into 4 ranks: lignite, subbituminous, bituminous, and anthracite (Hendrickson, 1975), and within each category, the coal varies greatly in molecular and atomic composition (indicated by proximate and ultimate analysis, respectively). Because of the wide range of constituents, a given parent coal has highly variable properties and spawns chars with similarly variable reactivities (Smoot and Smith, 1985).

2.1.1 Char Conversion Process

Coal char results from devolatilizing raw coal, and char conversion reacts away the non-mineral components of the char. The oxy-coal system replaces N_2 with CO_2 as the diluent, which gives rise to new complications during conversion. Senneca and Cortese (2014) found that char reactivity in a CO_2/O_2 mix is not the sum of CO_2/char and O_2/char reactivities, and suggest that the char, O_2, and CO_2 undergo unexplored interactions. Recent, related work has conflicting

results; some researchers report that CO_2 as a diluent decreases coal combustion rate, while others noted an increase in rate, and still others report both effects depending on temperature and O_2 concentration (Senneca and Cortese, 2012, 2014). Thermal deactivation, ash encapsulation, and time-dependent char composition also complicate the pertinent surface chemistry.

2.1.2 Char Ignition

When coal particles ignite, either the pyrolyzed gases or (in rare conditions) the surface of the char particle may ignite first (Chen et al., 2012). In oxy-coal combustion, the ignition process depends on heating rate, oxidizer concentration, gas medium flow rate, and gas medium composition (Essenhigh et al., 1989; Ponzio et al., 2008; Khatami et al., 2012).

In general, increasing heating rate or oxidizer composition decreases ignition delay, but the other factors of interest have more complicated relations. For example, many studies attribute ignition delay in CO_2 diluent to the higher heat capacity (C_p) of CO_2 over N_2, but Qiao et al. (2010) found that, in heterogeneous-only ignition, thermal conductivity (k) of the gas played a significant role, while C_p made only a slight difference. Khatami et al. (2012) also found that ignition delay changes little in quiescent media (i.e., media that have no gas flow) of CO_2 vs. N_2, but in laminar gas flow ignition delay with a CO_2 background gas is quite different than ignition delay in N_2. Liu et al. (2011) found that the influence of N_2 vs. CO_2 is actually small in a laminar entrained flow gasifier. In short, ignition delay and temperature changes involve many conflicting factors, and pose a significant modeling challenge.

2.1.3 Char Conversion Chemistry

Investigators have applied both global power law kinetic models and semi-global mechanisms to the CO_2/O_2/char system; both kinetic schemes proved inadequate to predict experimental results, and accurate prediction would likely require a detailed mechanism of complicated surface chemistry (Senneca and Cortese, 2012). Five gasification and three oxidation elementary steps (described in section 3.4) adequately capture the detailed char conversion (Liu and Niksa, 2004; Shurtz, 2011), but the relative importance of these reactions in oxy-coal systems may be radically different from the traditional combustion or gasification system.

2.1.4 Pore Evolution

Accurate models of char conversion require accurate models of pore evolution. The impact of the pore model depends on the reaction regime of the char combustion or gasification, with lower temperatures favoring reaction in micro and mesopores, while higher temperatures favor reaction in macropores; this is due to the respective importance of gasification versus oxidation and their associated temperature regimes (Laurendeau, 1978; Waters et al., 1988; Hampartsoumian et al., 1989). Because the oxy-coal system has a high CO_2 partial pressure (greater than 0.7 atm as opposed to ~0.15 atm in air fired systems), the pore model needs to take both oxidation and gasification effects into account. Surface diffusion limits combustion rates, so macropores (with readily available surface area) play a significant role for combustion, but gasification may occur in micropores as well. The char may gasify in the diffusion limited or in the reaction limited regime (or anywhere in between), and rates of gasification depend heavily on inorganic catalysis in the range of 1073-1163 K (Hurt et al., 1986; Waters et al., 1988; Hurt et al., 1991), but in high-temperature ranges the effects of catalysis on gasification are unknown.

The exact reacting surface area for a given coal is also unknown, so comprehensive particle combustion models that include pore diffusion must include a pore model to estimate the time-dependent amount of surface area. Random pore models have long been used to capture reactions in porous particles, but coal char adds an additional dimension of complexity with particles that change their porosity as the reaction proceeds. Gavalas (1980) attacked this problem with a classic model that used cylindrical pores and a derived probability density function (with parameters B_0 and B_1) to produce Equation 2-1, which predicts conversion as a function of time in a kinetically-controlled regime.

$$X_c = 1 - \exp\left(-2\pi\left[B_0 v^2 t^2 + 2B_1 vt\right]\right) \qquad 2\text{-}1$$

The pores are not likely to be cylindrical, but Gavalas (1980) believed that the parameters could compensate for this discrepancy; however, he did find that the model did not match experimental data above a conversion of about 0.7. Bhatia and Perlmutter (1980) created a similar model that could predict pore structure at any given conversion based on the initial pore volume, surface area, and length. Their work produced Equation 2-2, where τ is dimensionless time, σ is a particle size parameter, and ψ is a pore structure parameter.

$$X_c = 1 - \left(1 - \frac{\tau}{\sigma}\right)^3 exp\left[-\tau\left(1 + \frac{\psi\tau}{4}\right)\right] \qquad 2\text{-}2$$

They also found that the model differed from previous work at a conversion of about 0.75, but attributed this to differences in the modeling assumptions. It should be noted that the pore models given here are judged to be successful (or not) based on their ability to fit conversion data in a kinetically-controlled regime where surface area is directly proportional to reaction rate; this is problematic where different surface areas have different reactivities, and where reactivity changes with time (due to annealing).

More recently, Fei et al. (2011b) found that (at least in oxy-coal systems) previous random pore models were inadequate to capture pore structure at conversions above 0.7. They modeled the oxy-coal char conversion with the fractal random pore model (FRPM) for the 1200-1573 K range, and found that 1) the FRMP and the two-stage random pore model fit the data better than the random pore model and 2) the pore structural parameter has two distinct conversion regimes as shown in Equations 2-3 and 2-4 (Fei et al., 2011a).

$$\psi'_1 = \psi_0 \; when \; X_c < 0.7 \qquad 2\text{-}3$$

$$\psi'_1 = \psi_0 exp\big(\lambda(X - 0.7)\big) \; when \; X_c \geq .7 \qquad 2\text{-}4$$

2.1.5 Catalytic Activity

In general, catalytic minerals have little effect in diffusion limited regimes and tend to deactivate/vitrify at high temperature, so they would likely not play significant role in oxidation reactions in combustion temperature ranges. Gasification reactions, however, which become far more important in oxy-coal combustion, progress slowly, and may not reach a diffusion-limited regime. While the potential catalytic impact of inorganic ash on gasification reactions begs an interesting question, the high temperature of the system implies that the catalyzed and uncatalyzed reactions will have similar rates, and effects of catalysis will not be considered here.

2.2 Carbon Burnout Kinetics Model

The predictive modeling of coal char conversion hit a major milestone in 1998 with the development of the Carbon Burnout Kinetics (CBK) model. The original CBK code included four main components: a model for variation in particle reactivity, a single-film char oxidation model, a thermal deactivation model, and a physical property model (accounting for swelling and

ash inhibition) (Hurt et al., 1998). Later research has built on the CBK model, and provides the basis for the char burnout modeling in this work (Niksa et al., 2003; Liu and Niksa, 2004; Shurtz, 2011).[1]

2.2.1 Particle Reactivity Variability

Individual coal particles vary widely in their compositions for sufficiently large mean particle diameters. Hurt et al. (1998) constructed a statistical model to account for particle composition variation, and found significant deviation in the burnout time in a one-dimensional simulation comparing uniform particles to a statistical distribution (with diameters ~100 μm). The two distributions burned comparably up to 60-80% carbon conversion, and then diverged; the heterogeneous particle distribution burned out five times more slowly than the uniform distribution (Hurt et al., 1996); however, this submodel is computationally intensive and often neglected in CBK based codes (Shurtz, 2011).

2.2.2 Film Diffusion Model

Hurt et al. (1998) also employed a single-film to describe transport to and from the surface of the char particle, and more recently Hecht et al. (2013) compared the accuracy of three different film models in oxy-coal conditions. They used the Surface Kinetics in Porous Particles code (SKIPPY) as a high-cost, high-accuracy continuous-film model, and compared both a single-film and a double-film model to SKIPPY. This comparison showed that the low-cost, single-film model made significantly superior predictions of carbon combustion rate and particle

[1] See annealing literature review (section2.5) for a discussion of the CBK annealing model.

temperature over the double-film model (Hecht et al., 2013). The single-film model includes several assumptions: steady state, the ability to decouple the species continuity of the gases by employing an effective diffusivity, no homogenous reactions in the boundary layer, and the assumptions of Fick's law. With these assumptions and following Hecht et al. (2013), the species and energy continuity in the boundary layer are as shown in Equations 2-5 through 2-10.

$$\dot{N}_i = x_i \dot{N}_i - 4\pi r^2 c_t D_{i,eff} \frac{dx_i}{dr} \tag{2-5}$$

$$\dot{Q} = \sum \dot{N}_i h_i - 4\pi r^2 \lambda \frac{dT}{dr} \tag{2-6}$$

By integrating Equation 2-5, Equation 2-7 (which describes mass fraction as a function of position in the boundary layer) is produced, where κ_m is given by Equation 2-8. Similarly, integrating Equation 2-6 and balancing it with convective and radiative heat loss results in the energy balance in Equation 2-9 where κ is described by Equation 2-10. The variables κ_m and κ are mass and heat transfer versions of the Peclet number. The boundary layer is now described for the single-film model with relatively simple equations that introduce little error.

$$x_i = \frac{\dot{N}''_{i,p}}{\dot{N}''_{t,p}} + \left(x_{i,\infty} - \frac{\dot{N}''_{i,p}}{\dot{N}''_{t,p}} \right) e^{-\kappa_{m,i}} \tag{2-7}$$

$$\kappa_{m,i} = \frac{r_p \dot{N}''_{i,p}}{c_t D_{i,eff}} \tag{2-8}$$

$$\dot{N}''_{i,p} h_{c,p} - \epsilon\sigma\left(T_p^4 - T_w^4\right) = \sum \dot{N}''_i h_{i,p} + \frac{\bar{\lambda}}{r_p}\left[\frac{\kappa}{e^{\kappa} - 1}\right]\left(T_p - T_\infty\right) \tag{2-9}$$

$$\kappa = \frac{r_p}{\bar{\lambda}}\left[\sum \dot{N}''_i \bar{c}_{p,i}\right] \tag{2-10}$$

The double-film model is described by equations so similar to those above that it is not really meaningful to show them. The key differences are in the assumptions behind the two models. In the double-film case, there is an infinitely thin flame sheet where all heterogeneous chemistry instantly occurs, in contrast to the unreacting boundary layer of the single-film case. The equations above are therefore employed twice, once for the unreacting region between the particle surface and the flame sheet, and once from the flame sheet to the bulk gas. At the flame sheet, heat is released to both the surrounding gas and the particle surface. The choice of radial location for the flame sheet dictates how much energy is redirected to the particle, which can introduce substantial errors (Hecht et al., 2013).

The above models include Stefan flow, which gives them greater accuracy at greater computation expense. Mass transport in the boundary layer of combusting particles has often neglected the effects of Stefan flow and assumed equimolar counterdiffusion because the error introduced can be under 10%, but recent work has quantified the significant error arising from these assumptions in the oxy-coal system. Yu et al. (2013) compared burnout percentages and times in char particles reacting according to Equations 2-11 through 2-13, global mechanisms for the oxidation and dominant gasification reactions in an oxy-coal furnace.

$$2C + O_2 \rightarrow 2CO \qquad 2\text{-}11$$

$$C + CO_2 \rightarrow 2CO \qquad 2\text{-}12$$

$$C + H_2O \rightarrow CO + H_2 \qquad 2\text{-}13$$

They included all three equations as significant in oxy-combustion, and compared a single-film model (both with and without Stefan flow) to a continuous film model and data. This comparison showed that the O_2 mass transfer coefficient (k_{O2}) has very low net change in

considering Stefan flow, while k_{CO2} and k_{H2O} changed by up to 48.7 and 17%, respectively. Fortunately, models can address these inaccuracies by a correction factor, rather than including full Stefan flow computations (Yu et al., 2013). Similarly, Lewtak and Milewsak (2013) used a correction factor on equimolar counterdiffusion equations to bring the mass transfer values more in-line with real systems; this correction is easy to implement, and progressively more important in combustion at high oxygen concentrations.

The above studies show that particle combustion systems have several well-established film models to model boundary layers, and that in oxy-coal systems the Stefan flow is essential to the computation. For the best accuracy in low computation models, the single-film model with a correction factor for Stefan flow is both easy to compute and reasonably accurate. For highly accurate, comprehensive, predictive codes, a well-resolved continuous film model should be incorporated.

2.2.3 Ash Encapsulation

Hurt et al. (1998) created a widely accepted submodel for ash encapsulation (Cloke et al., 2003). They based this model on experimental evidence of an inverse correlation between ash fraction and carbon burnout (Vleeskens, 1986), and identified two important effects of mineral matter: 1) encapsulation, or the formation of a porous ash layer between reactants, and 2) dilution of the coal, which decreases the mass of carbon and reactive surface area available on a per volume basis (Hurt et al., 1998). The model captures these effects by assuming uniform dispersal of mineral matter in small grains; these grains agglomerate as the carbon-rich core oxidizes, and eventually stack into a porous shell.

The ash inhibition model of the original CBK code remains unchanged in the most current codes (Niksa et al., 2003; Shurtz and Fletcher, 2013). The original CBK code could accommodate high temperature combustion, where transport rate limits char combustion, and Hurt et al. (1998) postulated that this transport rate is hindered by 1) an inorganic-rich layer that hinders the combustion gases transporting to the char surface, and 2) incorporated mineral matter that reduces carbon mass and the reactive surface area per volume ratio. The model ultimately addresses these two inhibition mechanism using two parameters: δ_m (the minimum film thickness) and θ_{taf} (the critical film porosity). The code uses the characteristic size of mineral grains as δ_m, and θ_{taf} comes from coal data (or an estimation in the absence of data). CBK test calculations revealed that the near-extinction and reaction rates (at high conversions) depend heavily on δ_m and θ_{taf} respectively, so Hurt et al. (1998) chose values such that the model followed near-extinction and reaction rates from the data of several coals. Though Hurt et al. (1998) successfully used the above parameters and methodology, Cloke et al. (2003) found "The inclusion of ash inhibition in this model overestimated the resistance attributed by ash film. The pile-up of ash film surrounding char particle and its blowing off should be considered in a proper way to avoid the overestimation at the late stage of char combustion."

2.2.4 Coal Swelling Model

Shurtz (2011) used data from Sandia National Laboratories (Hurt et al., 1998) as well as existing swelling models (Mitchell et al., 1992) as a springboard to create a general char swelling model for particle heating rates greater than ~10^4 K/s. Using Equation 2-14,

$$\left(\frac{d}{d_0}\right)_{HHR} = s_{var}\left(\frac{T_{base}}{T}\right)^{C_{HR}} f(P) + s_{var} \qquad 2\text{-}14$$

Shurtz defined or fit the necessary parameters according to conditions, and indexed coals according to proximate and ultimate analysis (via NMR parameter correlations), creating a swelling model that fit several sets of data very well with minimal user inputs (Shurtz and Fletcher, 2013). However, the improved swelling model has not yet been implemented into modern CBK derivatives.

2.3 Other Char Conversion Models

2.3.1 Gasification

Many researchers have studied coal gasification, and obtained results important to the oxy-coal system. Niksa et al. (2003) and Liu and Niksa (2004) created the CBK/E and CBK/G char conversion models, and Shurtz (2011) combined and extended their results into the Char Conversion Kinetics (CCK) models. Niksa et al. (2003) extended the CBK model to include more accurate oxidation kinetics; these kinetics (a three step semi-global mechanism) retain the simplicity desired for computational models, and simultaneously describe global order, activation energy, and CO/CO_2 ratio over a wide range of combustion conditions (Hurt and Calo, 2001b). CBK/E incorporates three Arrhenius type kinetic expressions, where each expression has an activation energy and pre-exponential factor, but the pre-exponential factors are all correlated to the limiting step, and values chosen for the pre-exponential values (and their ratios to each other) allow the model to 1) follow data and 2) bring other steps to prominence in the appropriate temperature ranges. The activation energies for each step are generally fixed, with the limiting step kinetic parameters as the only adjustable parameters. The values of the pre-exponential factors and activation energies can be adjusted manually, fit to data, or found via a simple correlation to coal carbon content (Liu and Niksa, 2004).

Continuing from the CBK/E model, Liu and Niksa (2004) also created the CBK gasification (CBK/G) model by adding gasification rate laws, associated effectiveness factors, and a pore evolution description. The gasification reactions may become important in oxy-coal combustion because of the high CO_2 concentration surrounding the particles; this would necessitate appropriately (but simply) calculated effectiveness factors for the gasification reactions as they occur in the combustion system. Pores evolve in gasification due to both annealing and reaction, but only the annealing submodel will substantially affect char pore evolution at combustion temperature ranges (Liu and Niksa, 2004).

Shurtz (2011) synthesized the Char Conversion Kinetics (CCK) from the CBK/E source code and the ideas of the CBK/G model. This code pertains especially well to the oxy-coal system because it includes the kinetics, effectiveness factors, and transport equations for the eight-step mechanism for both gasification and combustion.

2.3.2 Global Char Oxidation Models

Because comprehensive codes like the CCK model require substantial computational power on the order of 15-75 seconds (on a single core) per particle, modeling a coal boiler with ~10 trillion coal particles per second would incur an absurd and unacceptable computational cost. Such situations are circumvented with global models of char combustion, and with numerous simplifying assumptions. Several CFD studies have explored the typical coal combustion modeling assumptions as they apply to oxy-coal systems. The intrinsic kinetics in O_2/CO_2 do not differ significantly from kinetics in air. However, other important assumptions such as multi-species diffusivity and the importance of various reactions in different temperature regimes differ significantly in O_2/CO_2 systems. The CFD portions of these studies use close

variations of Equations 2-11, 12, and 13 (shown in section 2.3.2) to model char conversion (Chui et al., 2003; Chen et al., 2010; Chen et al., 2012).

One CFD study compared char conversion in air to conversion in an oxy-fuel atmosphere using the method presented by Smith (1982) to model the relevant characteristics of the particles, and found that they could neglect the reaction in Equation 2-12 in the air fired case without loss of accuracy, but their predictions were significantly improved by accounting for CO_2 in the oxy-coal case (Smith, 1982; Kuhr et al., 2010). Several other studies included char conversion equations for H_2O, O_2, and CO_2 (assuming they all occurred in parallel), and found that all three types of conversion were important for the overall CFD results in some conditions and applications; however, they did not find that steam gasification was important for oxy-coal boilers (Nozaki et al., 1997; Toporov et al., 2008; Chen et al., 2010; Nikolopoulos et al., 2011). The impact of steam gasification will depend on the specific recycle and boiler configuration, which can drastically impact the amount of H_2O in the boiler.

2.4 Extended Thermal Annealing Literature Review

The impact of thermally-activated reactivity loss on carbon oxidation was observed decades ago (Nagle and Strickland-Constable, 1962). Since then, numerous researchers have documented char reactivity loss (Jenkins et al., 1973; McCarthy, 1982; Radovic et al., 1983b, a; Sahu et al., 1988; Suuberg et al., 1989; Beeley et al., 1996; Senneca et al., 1997), and developed several models to incorporate variable char reactivity in combustion modeling. The available annealing literature spans an eclectic mix of carbon based materials, preparation conditions, and char structural changes (both chemical and physical). The following literature review motivates and informs the updated annealing model developed in Chapter 6.

2.4.1 Thermally Induced Char Annealing: Processes and Key Observations

Numerous published studies have explored the loss of reactivity in carbonaceous precursors during heat treatment. These studies span decades of research, a plethora of investigative methods, a broad array of precursors, and a diverse set of char preparation conditions both relevant and irrelevant to practical char combustion. The cumulative results have shed much light on the process of thermal annealing, and though many details are still unknown or too complex (and variable between precursors) to feasibly model, several consistent points have emerged. These are detailed below in no particular order.

2.4.1.1 Time-scale of Annealing

Senneca et al. (1997) observed that at temperatures from 1173 to 1673 K, char oxidation and annealing appeared to occur on similar time scales, while Feng et al. (Feng et al., 2003b) noted significant reactivity decrease up to about 500 ms at heat treatment temperatures between 1173-1473 K (Senneca and Salatino, 2011). Two other studies (Tremel et al., 2012; Tremel and Spliethoff, 2013) also found that thermal annealing was essentially complete after no more than 500 ms of heat treatment between 1673 and 1873 K, but none of these studies had sufficient detail to closely examine what happens within that first 500 ms. The experiments referenced above were largely carried out at temperatures below practical coal-fired combustion conditions (~2000-2300 K). Davis et al. (1995) examined char deactivation at 1800 K with heat treatment times of 47 to 351 ms using several techniques, including x-ray diffraction (XRD) and high resolution transmission electron microscope (HRTEM) fringe imaging to examine char structure and crystallinity. They found that devolatilization was essentially complete by 47 ms and that crystallinity (with the implied loss of edges and imperfections that comprise active sites) was maximized by 117 ms. These conditions resulted in a 74% carbon loss by the time crystallinity-

based annealing was complete, indicating the potential for significant interference from oxidation, but 1800 K is still below practical combustion temperatures. Finally, in an attempt to discover the impact of these overlapping reactions, Senneca and Salatino (2006) mapped relative reaction rates of pyrolysis, combustion, and post-pyrolysis combustion for a wide range of temperatures. Their work confirmed that pyrolysis is essentially complete by about 1200 K, well before post-pyrolysis annealing or combustion are of significant concern. They also agreed with the other studies referenced that annealing and combustion occur at similar time scales at around 1800 K. Finally, they showed that post-pyrolysis thermal annealing rates are rapid compared to combustion above about 1800 K, which implies that annealing is essentially complete before combustion has a meaningful impact (for practical combustion conditions).

2.4.1.2 Impact of Reactive Gases on Thermal Annealing

From the previous section, it is unlikely that a model of practical combustion conditions would suffer from significant confounding between annealing and oxidation. However, in the interest of spanning a wide range of temperatures, it is worth noting the impact of such interference. Char heat treatment experiments are typically performed in an inert environment, specifically to avoid interference from reactive gases. Senneca et al. (Senneca et al., 2004, 2005; Senneca et al., 2007) found that, when the char was heated and occasional puffs of O_2 were added to the system, annealing (as measured by crystallinity observed via HRTEM) was significantly inhibited if the heat treatment temperature was less than approximately 1473 K. The HRTEM further revealed that activated oxygen complexes would form on the carbon layers of the char, but would become more and more sparse at higher temperatures. The authors theorized that the oxygen complexes hinder the alignment of graphite sheets, which reduces crystallinity

and slows the loss of active edge sites. They did not find a similar effect using CO_2 puffs instead of O_2.

On a side note, Feng and Bhatia (2002) also explored the formation and buildup of both CO_2 and O_2 complexes in an investigation of the validity of TGA data in carbon gasification kinetics. They also found that O_2 complex buildup could be significant in certain scenarios while CO_2 complexes were negligible. The O_2 complexes distort the rate of weight loss in TGA experiments, and cast considerable doubt on the validity of early burn off rates determined via TGA.

2.4.1.3 Carbon Annealing Regimes

Thermal annealing comprises innumerable reaction pathways, both chemical and physical, that reduce the number of active sites available for surface reactions. The specifics of these reaction pathways are generally unknown and nearly indeterminate (difficult or impossible to ascertain experimentally); however, several general trends can be observed or inferred. These trends include changes in ash structure, char morphology, and carbon crystallinity. Carbon in particular has been observed to have multiple regimes in structural changes. Zolin (2001) observed two "phases" of carbon below 1100 K. Char is not pure carbon and is somewhat amorphous, so the term "phase" is used loosely, but these two phases had distinct rates of reaction and it was theorized that the two phases arise due to certain annealing reactions that cannot be completed within a reasonable experimental time frame. Feng et al. (2003b) also observed a similar phenomenon at approximately 1400 K in the pursuit of a "true" annealing activation energy distribution; this was largely attributed to loss of heteroatoms and other changes rooted in pyrolysis as the first annealing regime, followed by higher activation energy

process in a distinctly different regime. The two distinct sets of annealing reactions imply that there could be multiple char annealing regimes where different causes of activity loss are dominant. In the two cases above, the bulk of activity change (about 87%) (Zolin et al., 2001) may be due to pyrolysis, while a broad array of more active processes become important at higher temperatures . In a more detailed analysis, Senneca and Salatino (2002) mapped deactivation regimes between 773 K and 2273 K, and found that pyrolysis and cross-linking of the carbon matrix occurred first, followed by higher activation energy changes in the carbon molecular structure. This evolving turbostratic structure proceeded in both series and parallel, with pyrolysis being most dominant up to ~1000 K, loss of defects between carbon layers dominating between ~1000 and ~1800 K, decreased in-plane defects between ~1800 and ~2300 K, and crystallite growth above ~2300 K. Naturally, each of these regimes contain numerous activated processes, resulting in a degree of overlap between regimes.

2.4.1.4 Annealing Rate Variation with Precursor Type

Different coals may have widely varying chemical properties and reactivities. Some of this variation is passed on to heat-treated chars, and must be taken into account. The body of coal research has shown unique results for such standard tests as a proximate and ultimate analysis of a given coal, as well as significant variation in coal analysis results within the same seam. More detailed analysis based on Nuclear Magnetic Resonance (NMR) spectroscopy data found that even when the ultimate analysis is similar, coal molecular structure (and thus coal properties) may differ widely (Genetti, 1999; Genetti et al., 1999). Though the influence of coal structure has not been widely investigated in the specific case of annealing, there are at least three distinct trends correlated with precursor structure.

The first trend is simply that deactivation experiments yield somewhat different results for any two precursors, even when all other preparation conditions are held constant, i.e., no two coals anneal along exactly the same path. This is unsurprising, but conversely, many studies show that heat-treated chars do converge towards the same reactivity (i.e., that of graphite). Hurt and Gibbins (1995) found that eight precursors all tended to converge in reactivity at high treatment temperatures, but the convergence was most marked in the residuals of actual boiler ash. The authors suggested (very plausibly in light of the general literature trends) that this greater convergence and annealing of char was due to the intense boiler conditions. The boiler was expected to have a peak temperature of 1800-2400 K and a residence time of ~1 s as opposed to the laboratory system with a peak temperature of 1700-2000 K and a residence time of ~70 ms. Zolin et al. (2000) similarly observed that high temperature heat treatments led to a single phase of carbon from a reactivity standpoint, and that all precursors tended towards graphitic reactivity.

Finally, several studies made the apparently paradoxical observation that inertinite rich coals were relatively reactive after extreme annealing treatments as compared to vitrinite rich coals (Beeley et al., 1996; Senneca et al., 1997; Russell et al., 2000; Zolin et al., 2002). Inertinite is a coal maceral that is relatively resistant to oxidation and thought to derive from prehistoric partially-combusted materials, while vitrinite is the most common coal maceral, derived from cellulose and lignin. At relatively mild conditions, annealed inertinite is less reactive than vitrinite macerals (as expected), but at high temperature treatments, the inertinite proves to be more deactivation resistant, and the vitrinite rich precursor may actually become relatively *less* reactive.

2.4.1.5 Impact of Heating Rate

The impact of heating rate on annealing is somewhat underexplored, as virtually all reactivity comparisons use chars prepared in a single apparatus, and that apparatus very often has a characteristic heating rate or a narrow range of heating rates. Thus, few studies have explored thermal deactivation in a given set of precursors over the vast range of heating rates from less than 1 K/s in TGA systems to as high as 10^5 K/s (or higher) in practical combustion conditions. Senneca and Salatino (2006) confirmed that pyrolysis rate and volatiles yield are significantly dependent on heating rate. Given that heteroatoms and crosslinking influence char reactivity, it is reasonable to expect that heating rate could also be an important factor in annealing. Cai et al. (1996) studied the impact of heating rate on various precursors, holding other preparation conditions fixed, and found that precursors with high tar yield were quite sensitive to heating rates between very low heating rates (ca. 1 K/s) up to intermediate heating rates of ~1000 K/s, with a plateau above about 1000 K/s. These chars showed a substantial *increase* in reactivity, and the authors theorized that this was due to the enhanced porosity that softening, high volatile coals experience with rapid devolatilization, and that there is an upper limit to this enhancement. It is unclear that enhanced porosity should properly fall under the heading of annealing, but loss of porosity due to micropores annealing shut or plugging with molten ash indicate that this is perhaps an appropriate addition to the "annealing" umbrella.

2.4.1.6 Impact of Peak Temperature

Peak temperature impact is somewhat more thoroughly investigated than that of heating rate, and affects such activated pathways as ash fusion, loss of surface area, catalyzed carbon reordering, hindered pyrolysis, and loss of catalysis. Some effects of T_{peak} are obvious in any Arrhenius form model simply because the high temperature exponentially accelerates the

activated processes, but other effects are more subtle, and impact not only how rapidly annealing proceeds, but also which pathways may be considered in the entire thermal deactivation process. The first set of processes, which in principle proceed at any temperature (albeit very slowly at low temperatures), are well covered in the preceding points of this summary. The most influential examples of the second class of annealing processes are briefly outlined below.

- As alluded to by the activation energy profile of the first annealing regime, (Feng et al., 2003b) pyrolysis is a process that has a widely distributed activation energy of its own. Though the extent of pyrolysis is partially a matter of treatment time, there is also a significant impact from peak treatment temperature (and heating rate). If either the heating rate or treatment temperature of the preparation conditions are significantly removed from that of industrial boilers, the char formed will have different chemistry, and thus follow a different activation energy distribution for subsequent annealing processes.
- Oxygen complexes form at a different rate and to a different degree depending on peak treatment temperature (Senneca et al., 2005). The presence of surface oxygen complexes hinders carbon sheet rearrangements, which impacts the types of annealing available at a given temperature.
- Russel et al. (2000) found that residual chars from industrial boilers (exposed to peak temperatures up to 2400 K) had similar surface area, chemical composition, and petrographic composition as laboratory chars formed at high heating rate, but the level of graphite crystallinity differed (likely because the laboratory chars were heated to only 2073 K). Petrographic similarity does not, however, necessarily translate to a similar annealing pathway. Senneca et al. (1997) found that the minerals kaolinite, calcite, and dolomite were no longer present at treatment temperatures above 1173 K, and that quartz is not detectable

above 1673 K, while another mineral (sillimanite) appears. As minerals fuse, they can flow and plug pores, leading to a loss of surface area. In chars prepared below the mineral fusion point, this source of activity loss is not possible. Also, the reactivity measurements of annealed char are typically performed via TGA in zone 1. Because the oxidation is kinetically limited in TGA measurements, the loss of catalytic activity due to fused minerals has a significant impact on the reactivity of those chars prepared at some $T_{peak} > T_{fusion}$ (Hecker et al., 1992).

- On a related, but less explored, note, inorganic minerals can influence the char formation process itself, not just the char reactivity. In some cases (between 873 and 1273 K) (Shibaoka et al., 1995; Senneca et al., 1998), mineral matter can aid in crosslinking and repolymerization of volatile matter. After pyrolysis, inorganic iron may catalyze carbon rearrangement towards a graphitic structure. Feng et al. (2002) detected graphite crystals (via XRD) growing around iron catalysts in heat-treated Yarrabee coal, and Wang et al. (1995) detected a similar phenomenon in coke from a blast furnace. Naturally, these catalytic effects are also negatively impacted when catalysts lose surface area due to fusion, or deactivate entirely due to vitrification.

Shim and Hurt (2000) observed that degree of char deactivation was almost entirely dependent on the peak temperature experienced by a char particle for a given precursor and heating rate. This is certainly due in part to the exponential temperature dependence of the annealing rate, but the effects listed above fundamentally alter the distribution of available annealing processes, which could also be included in a T_{peak} effect. For practical purposes, many of the effects based on peak temperature are irrelevant or complete at high heating rates and temperatures above about 1500 K. Because much of the relevant data is taken in the high heating

rate/high temperature region, and because ash content is diverse between coals, the data may be insufficient to fully capture alterations to the annealing activation energy distribution based on T_{peak}.

2.4.1.7 Annealing Impacts the Preexponential Factor Only

The oxidation reaction on a coal surface is thought to take place via active sites (edges, flaws in crystal structure, or reactive compounds) on the char surface, but the precise chain of reaction events is certainly complex, and not well described. This physical interpretation of events implies that thermal annealing may simply reduce the number of active sites available, resulting in a direct, linear reduction in activity with loss of active sites.

If annealing is interpreted as a reduction in the total number of active sites, simply reducing the preexponential factor of the oxidation reaction by an appropriate factor is an adequate method to capture annealing effects. However, more complex oxidation reaction schemes included multiple reaction steps involving surface intermediaries. For example, Liu and Niksa (2003; 2004) used five reaction steps for gasification, and three steps for O_2 char oxidation. These two sets of reactions were combined by Shurtz and Fletcher (2013) in the Carbon Conversion Kinetics (CCK) model, and also employed in the Carbon Conversion Kinetics for oxy-coal combustion code (CCK/oxy) (Holland and Fletcher, 2017). Liu and Niksa (2004) found that their model could not match their extensive compilation of coal combustion rate data without three distinct activated complex "pools" (one each for gasification via O_2, CO_2, and H_2O), while Senneca et al. (2007) observed that annealing appeared to decrease both the adsorption and desorption preexponential factors for char combustion. Taken together this implies that annealing may impact multiple steps of the complicated char conversion process,

and that comprehensive char models require kinetic expressions to model several of the potentially impacted reaction steps. Senneca et al. (2007) theorized that annealing expressions with the capacity to alter multiple preexponential factors could yield a more accurate model, but that much more investigation and data would be needed to appropriately capture annealing effects on multiple char conversion reaction steps. Despite the ambiguity around *which* preexponential factors should be reduced as a result of annealing, the body of literature and a specific study by Salatino et al. (1997) indicate that, under a broad range of preparation conditions, the activation energy of the gasification reaction remains essentially constant, and the preexponential factor alone is altered by the time-temperature profile.

2.4.1.8 Similarities and Differences in O_2 and CO_2 Thermal Deactivation

In the comprehensive char conversion models referenced above, the relevant annealing submodel embedded in the larger char conversion model treats reactivity loss as uniform for all reactive gases. The preexponential factor is simply multiplied by the fraction of remaining active sites during each time step to give a new rate constant appropriate for the time step. No comprehensive char conversion model has ever employed distinct annealing mechanisms and submodels for conversion due to O_2 vs CO_2, or even determined whether or not such a distinction is necessary. Because the oxy-coal system includes very high CO_2 concentrations, CO_2 gasification is not necessarily a negligible reactant, and the highly sensitive annealing model must be able to accommodate any differences implied by thermal deactivation data. It is reasonable to speculate that O_2 and CO_2 annealing may proceed along different pathways; Liu and Niksa (2004) observed that distinct reactive intermediaries were necessary for CO_2 and O_2, and Senneca et al. (2004) found very different propensities for surface intermediary formation. Senneca and Salatino found that O_2 reactivity loss appeared to have at least two distinct sets of

annealing parameters for different heat treatment intensities (above and below ~1500 K). As previously mentioned, the two regimes are consistent with distinct changes in turbostratic structure in the carbon matrix and inorganic mineral fusion which occurs roughly in the 1500 K temperature range. However, Senneca and Salatino (2002) *also* compared loss of CO_2 reactivity in the same experiment, and found evidence for only one regime throughout the temperature range tested (up to 2273 K). They speculated that turbostratic and mineral based reactivities that impact the O_2 reaction pathways may have a different or negligible impact on CO_2 activity loss (and vice versa). However, it must be noted that Senneca and Salatino only conducted a small study of only three precursors, and there is considerable uncertainty within the data.

Feng et al. (2003a) determined via XRD and HRTEM that, on the microstructural level at least, coal chars gasify in the same manner for conversion in both air and CO_2. Specifically, up to about 60% conversion, gasification is largely due to reactions at the edges of semi-ordered carbon crystals, while above 60% conversion, gasification attacks entire layers of graphene, not just the edges. This study theorized that the differences in char pore structural development between CO_2 gasification and combustion in air are therefore likely due to the timing and impact of micropores opening during gasification. During the char formation process, micropores may anneal shut or be plugged by molten ash, and later, during the gasification process, these pores may be opened as carbon is gradually consumed. In oxidation by O_2, micropores smaller than 10 Å do not increase in volume during conversion and are not available reaction surface area even at 653 K, but the larger pores increase greatly in volume and surface area, and correlate well with reactivity (Feng and Bhatia, 2003). In CO_2 gasification, the surface area of pores less than 10 Å increases dramatically during conversion, and the total pore volume correlates well with reactivity.

While these pore structures develop very differently in CO_2 or O_2 conversion, it is not clear that pore structural development and utilization are properly the purview of an annealing submodel. Certainly char morphology can, in some degree, be lumped together with annealing (micropores that anneal shut or molten ash that plugs pores), but there is no clear distinction between reactivity loss due to surface area loss vs activity reduction due to the destruction of active sites. This can be additionally complicated by "reversible" annealing. It is generally assumed that thermal deactivation is entirely irreversible, but in this case micropores may anneal shut during char formation and early gasification, but be reopened during later gasification (at roughly 20% conversion) (Feng and Bhatia, 2003). Thus, the active sites were first available within the micropores, then unavailable when the pores sealed, and then available again at about 20% conversion. It is also worth noting that virtually all of the annealing experimental data found in the literature show a peak in normalized mass loss rate at around 20-30% conversion. This may be due to the "annealing" of micropores, the rapid combustion of redeposited tar on the surface of the char, a peak in available surface area, or some other effect.

2.4.2 Model Forms for Annealing

2.4.2.1 Phenomenological Annealing Models

The many different types of thermally-induced changes outlined above have been the subject of a number of models with varying levels of detail. Because of the wide variety of mechanisms that may be responsible for char activity loss, the models do not necessarily agree on how to define annealing or which input values are needed. The simplest annealing models might be termed phenomenological models, in that they are conceptually satisfying, but embrace numerous questionable assumptions deliberately in highly simplified preliminary work to

quantify thermal deactivation. It is not necessary to exhaustively review all such published models here; instead, a representative example of a simple, low computation model from the literature is considered. One such model envisions the raw char and the annealed char as two different chemical species, and both species react with the reactive gases in the ambient environment (Senneca et al., 1997). This model was developed for gasification and involves three reactions (coal A → coal B, Coal A + CO_2 → 2CO, and Coal B + CO_2 → 2CO) and assumes:

1. The conversion of raw coal (coal A) to annealed coal (coal B) is irreversible. This is reasonable since (in post-pyrolysis annealing) it is generally observed that annealing reduces reactivity by decreasing the number of available reactive sites, which is highly thermodynamically favorable and thus not significantly reversible. If annealing is allowed to include pyrolysis, then many heteroatoms and reactive groups may be lost; this process is also irreversible in a reactive environment. In low temperature gasification or inert environments, the unreacted tar may well redeposit on the char surface, inducing a significant bias in subsequent reactivity measurements.
2. The gasification of both coal A and coal B is irreversible. This is also an excellent assumption.
3. The gasification kinetics of coals A and B are first order with respect to the *mass* of A and B respectively. This assumption is incorrect since it implies that either the entire coal mass is equally available to the gasification agent, or that the fraction of available mass is linearly proportional to the total mass. Either of these conditions ignore the reality of available surface area and potential diffusion limitations.

4. The annealing reaction is not influenced by either of the gasification reactions. As observed above, this may well be untrue for some stages of annealing if the gasifying agent forms activated complexes that hinder realignment of the turbostratic char structure. However, if these activated complexes are few, or the annealing is due to some other effect than carbon sheet rearrangement, then this assumption may be reasonable (Senneca et al., 2004).

5. The kinetics of annealing are first order with respect to the mass of coal A. This is possibly true, and in the absence of evidence to the contrary, an acceptable assumption.

The preceding assumptions lead to the following derivation, where r_A and r_B in Equations 2-15 and 2-16

$$-\frac{dm_A}{dt} = r_A m_A + r_{A\rightarrow B} m_A \qquad 2\text{-}15$$

$$-\frac{dm_B}{dt} = r_B m_B - r_{A\rightarrow B} m_A \qquad 2\text{-}16$$

are the reaction rates of coals A and B with CO_2, m_A and m_B are the current masses of each coal type, and t_{HT} is the amount of time the coal was exposed to some heat treatment in an inert atmosphere. In Equations 2-17 and 2-18,

$$r_A = k_A P_{CO_2}^{n_A} \qquad 2\text{-}17$$

$$r_B = k_B P_{CO_2}^{n_B} \qquad 2\text{-}18$$

k_A and k_B are temperature-dependent Arrhenius rate constants, but if temperature and CO_2 partial pressure remain constant throughout the conversion region of interest, r_A, r_B, and $r_{A\rightarrow B}$ are constant.

In a typical annealing experiment, the coal is initially treated at some temperature for a period of time t_{HT} in an inert gas. If the initial time, t=0, is considered to begin *after* the initial heat treatment (which is commonly the case in controlled experiments), then the initial conditions are as shown in Equations 2-19 and 2-20,

$$at\ t = 0, r_A = r_B = 0, \text{and } w_0 = m_A + m_B \qquad 2\text{-}19$$

$$at\ \ t = 0, m_A = m_{A_0} = w_o \exp(-r_{A\to B} * t_{HT}) \qquad 2\text{-}20$$

where w_o is the initial total mass of the char particle (potentially after heat treatment, but prior to any gasification). The second initial condition (Equation 2-20) results from integrating Equation 1 from 0 to t_{HT}. These initial conditions result in Equation 2-21,

$$\left[-\frac{df_A}{dt}\right]_t = r_B\left[1 - \frac{m_{A_0}}{w_0} + \frac{m_{A_0}}{w_0\left(1 + \frac{r_A}{r_{A\to B}} - \frac{r_B}{r_{A\to B}}\right)}\right]\exp(-r_B t)$$
$$+ \frac{m_{A_0}}{w_0}(r_A + r_{A\to B})\left[1 - \frac{1}{w_0\left(1 + \frac{r_A}{r_{A\to B}} - \frac{r_B}{r_{A\to B}}\right)}\right]\exp[(r_A + r_{A\to B})t] \qquad 2\text{-}21$$

the rate of conversion at time t, where f is the degree of conversion of solid carbon (starting at 0 and increasing to 1 at complete burnout). Note that no equation gives the rate of conversion from raw char to annealed char, $r_{A\to B}$. In this model, $r_{A\to B}$ is considered to be a regressed parameter, dependent only on particle temperature. If the particle temperature is held constant during heat treatment and conversion, then the parameter $r_{A\to B}$ may be regressed from Equation 2-22 (in the case of 1173 K, it was found to be 0.02 minute^{-1}).

$$\frac{df}{dt} = r_A \exp(-r_{A\to B} * t_{HT}) + r_B(1 - \exp(-r_{A\to B} * t_{HT})) \qquad 2\text{-}22$$

In general, the simplistic model above, despite several naïve assumptions, is able to match experimental data reasonably well for a single coal in a narrow window of conditions, but contains no parameters to include the experimentally observed changes for a wide range of coal types, heating rates, or peak treatment temperature. Obviously, this model also breaks down in conditions where any of the several fundamental assumptions listed above are substantially invalid. Again, the sample model discussed above was developed by Senneca et al. (1997), while several similar models are derived elsewhere (Salatino et al., 1999; Senneca and Salatino, 2002, 2011).

2.4.2.2 Advanced Annealing Models

Several authors (Hurt et al., 1998; Russell et al., 2000; Zolin et al., 2000) have also advanced more complicated models than those listed above; these models attempt to capture an increased level of physical detail over the phenomenological models. Again, it is not desirable to thoroughly examine each of these models. Instead, their common features are of interest. First, these models all used some form of distributed activation energy. In general, thermal annealing is the collection of processes that spontaneously occur to reduce the reactivity of a highly reactive raw coal particle to a relatively inert char particle. There is no uniform definition of which processes are specifically included in thermal annealing, though there is much excellent work (described in the prior section) investigating which chemical and physical processes occur. In general, all annealing processes are moving towards the thermodynamic minimum of a perfect carbon crystal, and they all have different activation energies. The wide range of annealing processes implies a distribution of activation energies, which suggests in turn that different portions of an activation energy distribution will be highlighted by experiments in different temperature ranges. That is, a given temperature will render reactions essentially instantaneous if

they are on the lower end of the distribution, while the reactions associated with the highest activation energies are immeasurably slow. Only a small subsection of the distribution of reactions will proceed on a time scale similar to the experiment, and experimental data over a wide range of conditions are necessary to characterize the annealing activation energy distribution in detail (D.B., 1971; Buch et al., 1978; McCarthy, 1982; Edwards, 1989).

This observation leads to a second difficulty common to the more advanced annealing models. No single activation energy distribution form is uniformly accepted, but the log-normal and gamma distributions are both used in various models (Hurt et al., 1998; Russell et al., 2000; Zolin et al., 2000). These distributions include very low values of the activation energy that would result in substantial activity loss even at room temperature. Obviously, these low activation energy processes are not observed, and the distribution must be truncated to avoid them. Additionally, some deactivation processes that do occur at lower temperature would be so rapid as to be essentially complete before any practical conversion temperature could be reached. These processes could be included as part of the truncation of the energy distribution in the absence of adequate data describing low-temperature annealing. Finally, the loss of reactivity in these annealing models must be modeled on a relative basis, because the combustion reactivity of raw coal at 300 K is indeterminate (i.e., if the temperature is sufficiently elevated for appreciable oxidation rates, annealing is already well advanced). Together, these difficulties require that the annealing model be used in conjunction with an appropriate initial value of the preexponential factor for the heterogeneous reaction rate (where appropriate in this case means self-consistent with reactivity data and the annealing model parameters). If the model is meant to apply to a variety of fuels, a submodel should be included to predict the nominal A_o (the preexponential factor for conversion of raw coal) as in Hurt et al. (1998). This may require some

explanation, and since the annealing model presented here is a direct extension from the model of Hurt et al. (1998), Hurt's model is an ideal representative of an advanced annealing submodel to explore in greater detail:

1. This annealing model is valid only with the specific preexponential submodel provided, and obviates the need for a truncated distribution (and avoids the question of where exactly the truncation should occur). Instead, the submodel provides A_o, which is then reduced according to a time-temperature profile by the annealing model
2. The model has the potential to capture both physical and chemical effects, and relies on annealing data obtained from inert environments. This assumes that an oxidizing environment would have minimal impact on the annealing process, which is likely a valid assumption in practical combustion cases that involve very rapid heating. The high heating rate drives rapid devolatilization and initially inhibits O_2 from reaching the surface, while the high temperature results in very rapid annealing.
3. All types of active sites are assumed to have the same *oxidation* kinetics. This is a necessary assumption given available data, but likely incorrect given the heterogeneous chemistry of coal. However, each type of active site is assigned a different *annealing* (not oxidation) activation energy.
4. All sites have the same annealing preexponential factor.
5. Annealing only affects the oxidation preexponential factor. This assumption is not precisely true, but if point three above is not too far wrong, it is a reasonable assumption.
6. All reactivity data are assumed to be measured in zone I or zone II reactivity ranges, where zone I is entirely kinetically limited and zone II experiences a mixture of kinetic and diffusion limitation. For zone I, the relative reactivity (the ratio of the annealed to raw

preexponential factors A_A/A_0) corresponds to the remaining fraction of active sites N_A/N_0. In zone II, the deactivation is proportional to $(N_A/N_0)^{1/2}$.

7. The deactivation model is fully defined by a preexponential factor and a lognormal distribution of activation energies. The lognormal distribution is defined in turn by a mean and a standard deviation. The values of these parameters were determined by fitting the data, but given the high uncertainty of the model, the parameters were found to occupy a broad parameter space with no clear, uniquely optimal solution. These parameters are assumed to be constant for all types of char and all preparation conditions, though Hurt et al. (1998) observed that this assumption is not entirely valid.

From the observations and assumptions above, Hurt et al. (1998) surmised that an appropriate oxidation preexponential factor model should have the functional form of Equation 2-23, and the Hurt model uses the specific form in Equation 2-24.

$$A_{ox} = \mathrm{f}[precursor, T(t)] \qquad 2\text{-}23$$

$$\ln(A_0) = 10.96 - 0.07136 * \mathrm{C} \qquad 2\text{-}24$$

The annealing model functional dependence was accomplished by apportioning the total (unknown) number of active sites N_0 in "i" bins each with a unique activation energy, where relative bin size was determined by the lognormal distribution. For the conditions and data used, 30 bins were found to be sufficient. The annealing model then became a series of i first order kinetic expressions, where N_i is the number of active sites in bin i, A_d is the preexponential factor of annealing, and $E_{d,i}$ is the activation energy of annealing associated with bin i as seen in Equation 2-25.

$$\frac{dN_i}{dt} = -A_d \exp\left(-E_{d,i}/\left(RT_p\right)\right) N_i \qquad 2\text{-}25$$

Again, the actual value of N_i is indeterminate (i.e., there is no way to count the number of actual active sites), so N_i is normalized by the equally indeterminate N_0. The model output then becomes the ratio of the number of active sites to the initial number of active sites, $N_A/N_0=f[T(t)]$, where the ratio is known to initially be equal to unity. Experimentally, this requires at least two reactivity data points so that the model output can be compared as a ratio of the two outputs, which cancels the unknowable N_0 from the equation and allows the model parameters to be fit to data.

N_i/N_0 is initially assumed to follow a log normal distribution as in Equation 2-26.

$$N\left(\ln(E_d)\,;\mu_{E_d},\sigma_{E_d}\right) = \frac{1}{\sigma_{E_d}\sqrt{2\pi}} \exp\left[-\frac{\left(\ln(E_d)-\mu_{E_d}\right)^2}{2{\sigma_{E_d}}^2}\right] \qquad 2\text{-}26$$

In Equation 2-26, $\ln(E_d)$ is considered the variable rather than E_d, and thus the normal distribution of $\ln(E_d)$, yields a log normal distribution of E_d, where μ_{Ed} and σ_{Ed} are the mean and standard deviation of the distribution, respectively. For any given value of activation energy for bin i ($E_{d,i}$), Equation 2-27 yields the ratio N_i/N_0 at t=0.

$$\frac{N_i(E_{d,i})}{N_0} = \frac{1}{\sigma_{E_d}\sqrt{2\pi}} \exp\left[-\frac{\left(\ln\left(E_{d,i}\right)-\mu_{E_d}\right)^2}{2{\sigma_{E_d}}^2}\right] \qquad 2\text{-}27$$

In the case of infinite bins, the fraction of active sites integrates to unity, while in a numerical approximation of i bins, Equation 2-28 sums to approximately unity.

$$\sum_i \Delta \ln(E_d) \left[\frac{N_i}{N_0}\right]_{initial} = \sim 1 \qquad 2\text{-}28$$

Equation 2-28 holds at t=0, but as time proceeds, the series of i ODEs (Equation 2-29, where $f_i=N_i/N_0$) reduces the value f_i, and the distribution of active sites deviates from lognormal to some irregular distribution.

$$\frac{df_i}{dt} = -A_d \exp\left(-E_{d,i}/\left(RT_p\right)\right) f_i \qquad 2\text{-}29$$

The sum of f_i at any time > 0 is some value less than unity, and, at fully kinetically-limited conditions, is directly proportional to the relative reactivity of the partially annealed char at a given time t.

2.5 Summary and Conclusions

The CBK model and its offshoots incorporate a comprehensive range of observed coal combustion and char conversion phenomena. However, combustion of solids is a complex, multi-faceted process, and continuing research has yielded new data to refine and extend past approaches. In particular, many of the key submodels in the CBK family of comprehensive models likely require extension to correctly respond to the extreme conditions found in oxy-coal combustion.

3 OBJECTIVE AND TASKS

The objective of this research is to improve and extend the state of the art for detailed coal char conversion in the gas and temperature regimes most relevant to oxy-coal combustion. The research presented here is in support of massively parallel computational fluid dynamics (CFD) simulations to accelerate and optimize the deployment of next-generation coal combustion systems.

3.1 Tasks

The following tasks were completed in this project:

1. Identify an appropriate comprehensive char conversion model from the current state of the art (Ch. 2)
2. Identify relevant data to evaluate models (Ch. 2, 5, 6, and 7)
3. Analyze the submodel and parameter sensitivity of the best available model in relevant (oxy-coal) conditions (Ch. 5)
4. Propose theory-based improvements to sensitive sub-models (Ch. 5, 6, and 7)
5. Generate and implement improved submodels (Ch. 6 and 7)
6. Analyze results (Ch. 8)
7. Propose CFD implementation (Ch. 8)

The remainder of this dissertation discusses the details of accomplishing the preceding tasks. Chapter 4 describes computational tools vital to this work. This chapter is admittedly hard

to digest, but it provides philosophical, conceptual, and mathematical underpinnings for the work outlined in Chapters 5-8, and is vital for interested parties to replicate or continue the work of those chapters. Chapter 5 is a thorough, global sensitivity analysis that highlighted the parameters of the combustion submodels that would most profitably be refined. The balance of the dissertation (Chapters 6-9) is largely devoted to creating and implementing the improvements implicated by Chapter 5. In particular, Chapter 6 is a discussion of the development of a much improved thermal annealing model, while the implementation of the thermal annealing model and several additional submodels into the central coal conversion model is presented in Chapter 7. Validation and discussion of the completed model are presented in Chapter 8. Finally, Chapter 9 is a summary of important developments and future work.

4 COMPUTATIONAL TOOLS

Since the work reported here is entirely modeling, a summary of the most useful computation tools is presented here. This chapter aims to clarify the mathematical underpinnings of modeling techniques, and to facilitate future replication and extension of any part of the modeling work described in the following chapters. Several of the computational tools are mathematically complex so many details pertinent to this chapter are given in Appendix A, or described in the literature (McKay et al., 1979; Sacks J., 1989; Welch et al., 1992; Kennedy, 2000; Kennedy and O'Hagan, 2001; Santner, 2003; Higdon et al., 2004; Higdon et al., 2008; Storlie et al., 2015; Gattiker et al., 2016; Gattiker, 2017). The following tools are applied to achieve the key goals of the dissertation. This dissertation aims to a) evaluate the state of the art in coal combustion modeling, b) highlight areas most in need of improvement, c) create improved combustion submodels from the aggregate of literature data, d) implement model improvements, and e) validate the final model. Specifically, the computational tools described here:

1. Optimize complicated models not amenable to straight-forward regression. This optimization is applied to coal kinetic models and thermal char deactivation models.
2. Propose space-filling experimental designs of high-dimensional spaces that must be explored or sampled in the course of calibration and uncertainty quantification.

3. Generate statistical emulators or surrogate models. Such models have the sole function of accepting any set of inputs and model parameters and producing one or more model outputs. The surrogate model executes very quickly and allows the expensive, physics-based model to be explored in relatively short order.

4. Explore a parameter space and accept or reject any region of the parameter space based on model emulations and experimental data.

5. Offer insight into model discrepancy (i.e., the systematic mismatch between the model and data).

4.1 MATLAB

MATLAB is a high-level scripting language with a well-developed set of computational tool boxes. The bulk of the work in this dissertation was coded in MATLAB, but the majority of the code uses only elementary commands such as variable assignment, various kinds of loops, and common mathematical and trigonometric functions. The only significant exceptions are the Latin Hyper-cube design and the fmincon optimization routine, available from the MATLAB Statistical Toolbox and Optimization Toolbox, respectively.

4.2 The "fmincon" Function

The fmincon MATLAB function is a relatively user-friendly optimization routine that optimizes a model based on gradients in the output of an objective function induced by changes to the input to the model. To give a trivial example, a line modeled by y=m*x+b might have an objective function that measures the sum-squared error between a collection of data points for given values of m and b. The parameters m and b would change at each iteration of fmincon,

following the gradient of the parameter space. In such a trivial case, fmincon would rapidly find the global minimum of the objective function, which could be analytically obtained from traditional linear regression. In more complicated cases with an expensive model or a high-dimensional parameter space, fmincon can take much longer to find a minimum, and sufficiently complicated parameter spaces include numerous local minima.

The fmincon routine accepts, at a minimum, an objective function and an initial values vector as inputs. The objective function is user-generated, and accepts the initial value vector as an input, calls any number of scripts and functions, and yields a scalar output to be minimized. Additionally, fmincon accepts optional upper and lower bounds, matrices and vectors for both linear equalities and linear inequalities (as constraints), and functions as non-linear constraints. Finally, fmincon includes an options string to specify values such as tolerance, maximum iterations, etc. The optimization function is prone to "sticking" in local minima and exiting due to exceptionally shallow gradients in parameter space, but the use of strategic initial values and log transforms of parameters generally overcomes these difficulties. Details on the algorithm employed by fmincon are available elsewhere (Byrd et al., 1999; Byrd et al., 2000; Waltz et al., 2006).

4.3 lhsdesign

In designing a computational experiment, sample values must be determined for both model inputs (values that would be measured or set in the course of a physical experiment, such as temperature or mass flow rate) and parameter values (potential values of model parameters that are not considered known, such as activation energy). First, the range of permissible values for each input and parameter was prescribed and used to set up a Latin hypercube sampling scheme. The hypercube sampling scheme accepts as inputs the allowed range and probability

distribution of each parameter. The experiment is then designed by dividing the range of parameter space into a specified number of equally probable intervals, and one parameter value is chosen at random from each interval. The randomly chosen value is stored for the next step of the experimental design. For example, if 10 runs were desirable, the parameter space would be divided into 10 intervals. In the case of a uniform probability distribution, each of the 10 intervals would be of equal "length" in parameter space, while in the case of a normal distribution on the parameter space, the intervals near the mean parameter value would be much "shorter" than the intervals in the tail. Because each interval contributes exactly one parameter value, most of the samples would cluster around the mean, and the low probability sample space would not be well explored.

The sampling process is executed for each parameter and input, and the values are then systematically paired to be optimally space filling (McKay et al., 1979). The result is a matrix in which each column "j" contains randomly ordered, unbiased, space-filling samples from the range of parameter (or input) "j", and each row "i" is a set of all necessary input values and model parameters for a single computational experiment. The number of columns equals the number of parameters plus the number of inputs, and the number of rows is the number of computational experiments to be performed.

The Latin hypercube is a p-dimensional analogue of the Latin square. In the Latin square, there are only two parameters, and in Figure 4-1, an example of n=5 is shown for parameters A and B with a uniform probability distribution. Each **X** is located within a two dimensional subsection of parameter space, and the exact values of the ordered pair at each **X** is chosen randomly from within the subsection. The location of the **X**'s (i.e., choosing which n of the n^2 subsections of parameter space will be occupied) is done by the Latin square (or hypercube

algorithm) such that no single row or column contains more than one **X**. This has been observed to be analogous to placing n rooks on an nxn chess board without allowing any two rooks to pose a danger to each other. Note that this design is more space-filling than randomly selecting five points from the entire joint parameter space.

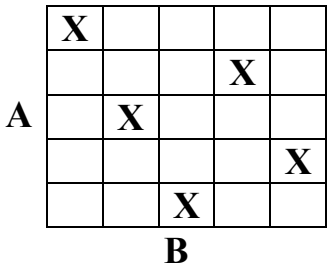

Figure 4-1 – Sample Latin square (Latin Hypercube where p=2 and n=5).

4.4 Gaussian Process Models for Simulation Analysis (GPMSA)

The Gaussian Process Models for Simulation Analysis (GPMSA) is a set of computer model analysis tools written at Los Alamos National Laboratories. The tool set is "aimed at *emulating* a computer model of a system being studied, *calibrating* this computer model to observations of the system, and giving *predictions* of the expected system response (Gattiker, 2017)."

4.4.1 Gaussian Processes

A Gaussian Process (GP) is defined as follow: for any set S, a GP on S is a set of random variables $\{Z_t : t \in S\}$ such that, for any set of indices $n \in \mathbb{N}$, $\{Z_{t\_1}, \ldots Z_{t\_n}\}$ is a multivariate Gaussian distribution. An example may render the definition more intuitive. By way of introduction, a random variable is a map between potential outcomes and a numerical value. These outcomes or realizations may be numerical (such as the selection of a real number from a random distribution), or non-numerical such as the iconic case of a coin toss (where the outcome "heads" maps to the value 1, and the outcome tails maps to 0). Note that the probability density (or mass)

function (PDF or PMF) is not a part of the map between outcomes and numerical values, but instead defines the probability of a given outcome. The following example is perhaps the simplest non-trivial example of a GP. In the example, let S be the entire set of real numbers in one dimension ($\mathbb{R}$) so that t is a subset of S, let the random variable Z_t be defined as in Equation 4-1, and for the specific example, choose the following four values as the subset of t: {-0.7, -0.3, 0.2, 0.9}. Equation 4-1 is the random variable (or map) between outcomes of ω and numerical values, where ω is a number drawn from the standard normal PDF.

$$Z_t = t * \omega \tag{4-1}$$

The Gaussian Process (i.e., the subset of four random variables) form a multivariate-normal. In this case, the GP is a four dimensional normal distribution fully defined by a vector of four means, and a 4x4 covariance matrix. Each realization of the GP is a vector of four values, while numerous samples both outline a univariate normal PDF for each Z_{t_n} with some mean and variance, *and* established the covariance between any two Z_{t_n}. Figure 4-2 shows a single realization of the GP (one sample from ω), while Figure 4-3 shows 500 samples from ω. The blue lines are linear interpolations between the realizations of the random variable, all of which pass through the origin. Mathematically, this is apparent from Equation 4-1, which (for any given sample from ω) is simply the equation for a line of slope ω and the intercept set equal to zero, while from the standpoint of a GP, the random variable Z_0 would yield zero for any sample from the PDF, so Z_0 would have the PDF N(0,0). In fact, in this case, the entire vector of mean values is zero, which can be inferred from the symmetry of ω or visually observed in Figure 4-3.

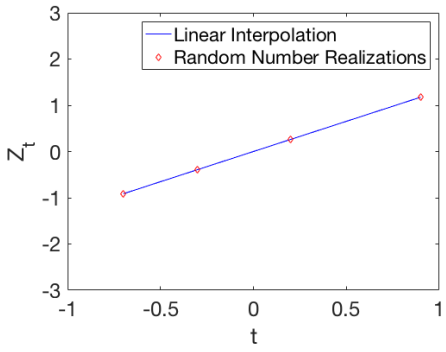

Figure 4-2 – Single realization of the Gaussian Process.

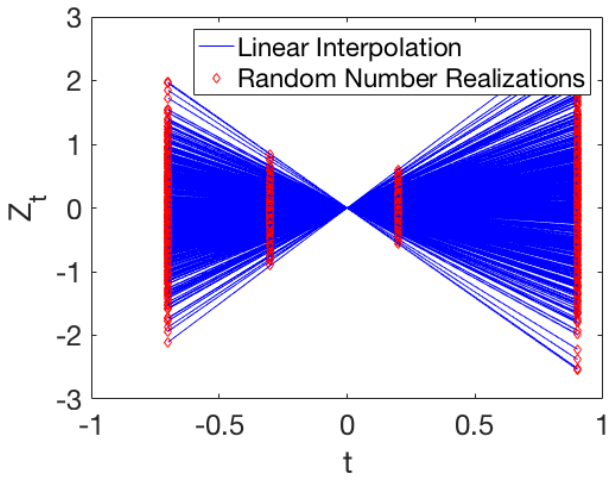

Figure 4-3 – 500 realizations of the Gaussian Process.

Mathematically, it is immediately apparent that Equation 4-1 yields a line for any given draw of ω, and superficially, it appears that the GP is not multi-variate at all, but instead a single sample from a standard normal that fully defines a line. However, the GP is in fact four dimensional, and for a single, four dimensional sample to contain four points exactly on a line, they must be drawn as a single sample from a multi-variate normal PDF constrained by the right covariance matrix. This matrix can be estimated from results in Figure 4-3, and exactly defined by the proper kernel function. Both approaches are shown, as they provide valuable insight. The diagonal of Table 4-1 shows the estimated variance for each univariate marginal distribution after a sample of 5,000 points from ω, while the off-diagonals show the covariance computed

between the univariate distributions. Table 4-2 (computed from the kernel function) shows that the estimates from Table 4-1 are converging on the true variances and covariances. Equation 4-2 is the kernel function for a linear GP (the kernel function generates the covariance matrix), while the subsequent equations derive the kernel function in the single-dimensional case from the definition of covariance (Equation 4-3).

$$\mathrm{cov}\left(\mathrm{Z}_{t_i}, \mathrm{Z}_{t_j}\right) = E\left[\left(\mathrm{Z}_{t_i} - E[\mathrm{Z}_{t_i}]\right)\left(\mathrm{Z}_{t_j} - E\left[\mathrm{Z}_{t_j}\right]\right)\right] \quad 4\text{-}2$$

$$\mathrm{cov}\left(\mathrm{Z}_{t_i}, \mathrm{Z}_{t_j}\right) = E\left[\mathrm{Z}_{t_i}\mathrm{Z}_{t_j}\right] - E[E[\mathrm{Z}_{t_i}]\mathrm{Z}_{t_i}] - E\left[E\left[\mathrm{Z}_{t_j}\right]\mathrm{Z}_{t_j}\right] + E\left[E[\mathrm{Z}_{t_i}]E\left[\mathrm{Z}_{t_j}\right]\right] \quad 4\text{-}3$$

Equation 4-4 expands the covariance terms, while Equation 4-5 simplifies 4-4 by taking advantage of the fact that the expected value of all Z_{t_n} is zero in this case.

$$\mathrm{cov}\left(\mathrm{Z}_{t_i}, \mathrm{Z}_{t_j}\right) = E\left[\mathrm{Z}_{t_i}\mathrm{Z}_{t_j}\right] = E[t_i\omega * t_j\omega] = t_i t_j E[\omega^2] \quad 4\text{-}4$$

Equation 4-6 shows (from a common form of the definition of the variance), that the variance of ω is ω^2, which leads directly to Equation 4-7.

$$\mathrm{var}(\omega) = E[\omega^2] - (E[\omega])^2 = E[\omega^2] = \sigma^2 = 1 \quad 4\text{-}5$$

$$\mathrm{cov}\left(\mathrm{Z}_{t_i}, \mathrm{Z}_{t_j}\right) = t_i t_j \quad 4\text{-}6$$

Comparing Equation 4-7 to the kernel function (Equation 4-2) they are seen to be identical, and to match Table 4-2.

The Gaussian process may be considered an alternative strategy for modeling a line. Rather than a single best fit line with confidence intervals on the line and the parameters, the GP has no specific parameters or value; instead, given a vector of input space and a region of output space, the GP quantifies the probability of the region of output space. Qualitatively, a region of

output space close to the best-fit line would have a high probability density, while a region of output space far from the data (and best-fit line) would have very low probability.

Table 4-1 – Calculated mean and covariance from 5000 samples of ω.

	Z_{t_1}	Z_{t_2}	Z_{t_3}	Z_{t_4}	**Mean**
Z_{t_1}	0.488	0.209	-0.139	-0.627	-0.0078
Z_{t_2}	0.209	0.0896	-0.0597	-0.269	-0.0033
Z_{t_3}	-0.139	-0.0597	0.0398	0.179	0.0022
Z_{t_4}	-0.627	-0.269	0.179	0.806	0.010

Table 4-2 – Exact theoretical mean and covariance.

	Z_{t_1}	Z_{t_2}	Z_{t_3}	Z_{t_4}	**Mean**
Z_{t_1}	0.490	0.210	-0.140	-0.630	0
Z_{t_2}	0.210	0.0900	-0.0600	-0.270	0
Z_{t_3}	-0.140	-0.0600	0.0400	0.180	0
Z_{t_4}	-0.630	-0.270	0.180	0.810	0

On a practical note, multivariate normal samples with a known covariance and mean may be obtained from a series of independent samples from the standard normal. This is done via a singular value decomposition (in MATLAB [**A,S,B**]=svd(**Σ**), where **Σ** is the covariance matrix). Following the svd, a matrix, **M**, is obtained by **M**=**A***sqrt(**S**), and a multivariate normal sample is then obtained by **M** multiplied by a vector of samples from the standard normal (**v**) added to a vector of mean values from the multivariate normal (**μ**) (**MVN_s**=**M***v+**μ**).

4.4.2 Bayesian Calibration

Bayesian calibration does not necessarily employ GPs, but Bayes' Law is an essential element of GPMSA, so it is discussed here, and a simple, non-GP example is given. Bayes' Law itself is an almost trivial statement of probability law, as seen in Equations 4-8 through 4-10.

$$P(A \cap B) = P(B \cap A) \tag{4-7}$$

$$P(A \cap B) = P(A|B)P(B) \tag{4-8}$$

$$P(A|B)P(B) = P(B|A)P(A) \tag{4-9}$$

$$P(A|B) = \frac{P(B|A)P(A)}{P(B)} \tag{4-10}$$

This derivation utilizes only the commutative property of probabilities and a definition of conditional probability. The result (Equation 4-10) is known as Bayes' Law, and the terms P(A|B), P(B|A), P(A), and P(B) are known respectively as the posterior, the likelihood, the prior of A and the prior of B. In discussions of model calibration, Bayes' Law is better couched in terms y (model output), **x** (model input), and **θ** (model parameters for both the physical model and the statistically machinery) as in Equation 4-11, where **θ** is the vector containing all model parameters (both for the physical model and the internal, statistical parameters).

$$f_{\Theta|Y}(\boldsymbol{\theta}|\mathbf{y}) \propto f_{Y|\Theta}(\mathbf{y}|\boldsymbol{\theta}) f_{\Theta}(\boldsymbol{\theta}) \tag{4-11}$$

Equation 4-11 merits considerable explanation. First, Equation 4-11 is composed of pdfs of the posterior, the likelihood, and the prior of **θ**, and omits the prior probability distribution of y. Second it is a proportionality, not strictly an equation. Note that the capital letters designate a random variable (i.e., the map between an event (with some pdf) and a corresponding numerical value) while the lower case letters indicating specific realizations or outcomes (a particular vector of parameter values (**θ**) or data points (y)). The following bullets detail the terms of Equation 4-11:

- The prior of y ($f_Y(y)$) is effectively a scaling factor that would constrain the left-hand side probability distribution to integrate to unity (as required for a pdf). However, the prior of y physically corresponds to the pdf of the experimental data, which is not generally accessible.

Fortunately, the calibration of a model searches for the most likely parameter values, given the data and prior beliefs regarding parameter values, so relative likelihood given any sets of parameters is retained, regardless of any scaling factor. Thus, knowledge of f_Y is not necessary for practical application.

- The prior of $\boldsymbol{\theta}$ ($f_\Theta(\boldsymbol{\theta})$) physically represents prior beliefs on the joint pdf of every model parameter and every internal parameter. As a matter of practical convenience, the joint pdf is typically assumed to be uncorrelated, and each parameter effectively has its own pdf, which is often simply the uniform pdf over some range of physically feasible space as determined by a domain expert. In reality, the model form typically dictates some correlation between model parameters, which should ideally be accounted for. The aforementioned internal parameters are those parameters that are necessary to execute the calibration, but not part of the mathematical model meant to capture some physical phenomenon. An example is given in Equation 4-12, where σ_i is an internal parameter; see the next bullet point for an explanation for Equation 4-12.

$$f_{Y|\Theta}(\mathbf{y}|\boldsymbol{\theta}) = \prod_{i}^{n} N(y_i; \mu_i(x), \sigma_i) \qquad 4\text{-}12$$

- The likelihood function ($f_{Y|\Theta}(\mathbf{y}|\boldsymbol{\theta})$) (in this case, Equation 4-12) is often the most difficult to compute from a practical standpoint. Physically, the function quantifies the question, "How likely are the data, given the numerical values of the current parameter vector $\boldsymbol{\theta}$?" In other words, if specific values are plugged into a model, how likely are those parameters to explain (or fit) the data. The answer to the goodness of fit question must include information about the noise or observational error in the data. Equation 4-12 quantifies the likelihood (and captures the observation error) with commonly employed assumptions: the data points

are independent, so the probability of all observations is the product of the probability of each observation (the observation y_i has no bearing on the observation y_{i+1}), identically distributed (the observation error distribution is the same for all y_i), and normally distributed (fully defined by the normal pdf equation with some μ and σ). The parameter σ_i is an internal parameter if it cannot be reliably estimated from other information, which is to say it is necessary to compute the likelihood function, but is not known, and must be calibrated against the data along with the other parameters in $\boldsymbol{\theta}$. It represents the standard deviation of the normally distributed observation error for observation y_i, and if the errors are considered to be identically distributed, the value of σ_i is constant for all i. On the other hand, μ_i is typically formulated as a function of $\boldsymbol{\theta}$. When evaluating any vector of model parameters (a subset of vector $\boldsymbol{\theta}$), the model will predict a specific value given the values of vector $\boldsymbol{\theta}$ and the experimental inputs associated with data point y_i (the predicted value is then designated as μ_i). Since the goal is to evaluate the likelihood of the parameter values in $\boldsymbol{\theta}$ for the specific model in question, the output of model under the conditions of y_i with specific values of $\boldsymbol{\theta}$ is a reasonable mean. If the probability density ($N(y_i;\mu,\sigma)$) of y_i under conditions i with the specific values of $\boldsymbol{\theta}$ is very low, then the experimental value of y_i is several standard deviations away from the model prediction (the mean of the normal pdf), and the values of $\boldsymbol{\theta}$ do not result in a model that represents the data well. Note that if σ is considered an internal parameter to be calibrated, it requires a prior pdf. This prior is often not based on knowledge of the actual observational error (which is unknown, otherwise σ would have a fixed value). Instead, it is typically a prior that favors small values, under the assumption that the

experiments resulted in reasonably consistent observations with pains taken to minimize error.

- Finally, the posterior pdf of the parameters given the data ($f_{\Theta|Y}$) is the product of the likelihood of the data given the parameters and the prior parameter probability. This can be calculated simultaneous or sequentially for multiple experiments or multiple data points in the same experiment. The result is the same, but the prior in the sequential case is the posterior of the immediately preceding data point (i.e., the prior of θ for point y_{i+1} is the posterior for point y_i). The posterior is a joint pdf of dimensionality equal to the length of $\boldsymbol{\theta}$), and samples from the posterior can be inserted into the model to generate model predictions with quantified uncertainty, as in Equation 4-13, where $y_{p,i,j}$ is the predicted output for the conditions of data point i and using parameters from sample j, η is the model output (or emulator output) for the sample parameters and experimental inputs, and ε_i is the observational error. Numerous samples build what amounts to an error bar conditional on $\mathbf{x}_i$ and $\boldsymbol{\theta}_j$.

$$y_{p,i,j} = \eta(\mathbf{x}_i, \boldsymbol{\theta}_j) + \varepsilon_j \qquad 4\text{-}13$$

Additionally, the calibration process may include some discrepancy term δ, which models the difference between reality and model predictions as a function of experimental inputs. Ideally, the model should be constructed to perfectly reflect reality, but in all practical applications this is not possible. As a simple example, ballistic motion can be captured by integrating the acceleration of an object with respect to time (one integration obtains the velocity equation, while two integrations yields the position equation). In many contexts, the integration neglects drag force as a matter of convenience, but this always introduces some error, which should be reflected in δ. In this case, δ would generally be small at low velocity values and large

as high velocity increases the magnitude of drag forces. In general, the calibrated model would have some form as in Equation 4-14. In general, all future predictions should include the discrepancy, and if the discrepancy is large, the model is effectively reduced to an empirical model without intrinsic physics.

$$y_{p,i,j} = \eta(\mathbf{x_i}, \boldsymbol{\theta_j}) + \delta(\boldsymbol{x_i}) + \varepsilon_j \qquad 4\text{-}14$$

4.4.3 Gaussian Processes for Model Emulation

In general, statistical model emulation seeks to capture the relationship between model inputs and outputs without requiring the computational expense of models containing high levels of physical detail. This allows a simulation scientist to explore expensive models in a timely manner, using relatively few runs from a high-cost computational experiment. Statistical surrogate models or emulators are especially useful in evaluating model predictions where no input/output pairs are given from the computational experiment. See Welch et al. (1992) and Sacks et al. (1989) for further discussion on the subject of emulators relevant to GPMSA. Gaussian processes are a popular and powerful tool for statistical emulation because they have the potential for enormous flexibility with relatively few parameters and they naturally incorporate uncertainty in model output. Gaussian processes are fully defined by a vector of mean values and a covariance matrix, so defining an emulator is conceptually as simple as arriving at the relevant mean and covariance. In some well-behaved cases, such as a linear model of p dimensions, the mean may be immediately obvious, and the covariance matrix can be generated from a kernel function. The kernel for a one-dimensional, linear covariance matrix for n data points on the domain $-1 \leq x \leq 1$ is shown in Equation 4-15, where **x** is the independent variable vector of length n, and i and j are used as indices in the covariance matrix.

$$Cov(i,j) = \mathrm{x}_i x_j \qquad 4\text{-}15$$

More complex cases require a more complex kernel or a covariance function tuned to the specific scenario and physical model. In the case of GPMSA, η is a statistical emulator (specifically a GP), and both δ and ε are similarly constructed GPs. The sum of the three GPs is also a GP, and an appropriate sample from the posterior distributions of **θ** in conjunction with any input values in the domain yields a model prediction including model and observational uncertainty as shown in Equation 4-14. The GPMSA emulators for η, δ, and ε are fully defined by mean and covariance matrices as shown below. Further details are available elsewhere (Higdon et al., 2008; Storlie et al., 2015; Gattiker et al., 2016; Gattiker, 2017). Equation 4-16 differs subtly from Equation 4-15 in that the model predictions for the ith input and jth sample of **θ** is not the prediction of interest.

$$\mathrm{y}_{e,i} = \eta(\mathbf{x_i}, \boldsymbol{\theta}^*) + \delta(\boldsymbol{x_i}, \mathbf{IP_\delta}) + \varepsilon_i(\mathbf{IP_\varepsilon}) \qquad 4\text{-}16$$

Instead, Equation 4-16 is an emulator that captures model behavior for the vector **x** for the ith set of input conditions at some fixed vector **θ*** that includes the model parameters and the emulator internal parameters. GP emulators require internal parameters, which are represented in Equation 4-16 by IP. The emulator could also use samples from the posterior of **θ*** (the vector of parameters **and** internal parameters for η) to generate estimates of uncertainty, and η(**x**,**θ**), δ(**x**$_i$), and ε_i in Equation 4-14 may well be emulators, in which case Equations 4-14 and 4-16 are identical. In GPMSA, η is expressed in Equation 4-17, where p is the number of input parameters, u indicates that the parameters are part of the GP for η, K_j is the jth basis function or principle component (meant to capture the output of the original, expensive model), and w_j is a weighting factor.

$$\eta(\mathbf{x_i}, \boldsymbol{\theta}^*) = \sum_{j=1}^{p_u} K_j w_j(\boldsymbol{x_i}, \boldsymbol{\theta}^*) \quad 4\text{-}17$$

The weighting factor is a GP and can be defined by a vector of means set to 0, and a covariance matrix given in Equation 4-18, where q is the number of total model parameters (parameters for both the original model and internal parameters for the GP emulator).

$$\Sigma_j(\boldsymbol{x_i}, \boldsymbol{\theta_i}^*, \boldsymbol{x_l}, \boldsymbol{\theta_l}^*) = \frac{1}{\lambda_j} \prod_{k=1}^{p} \rho_{jk}^{4(x_{ik}-x_{lk})^2} * \prod_{k=1}^{q} \rho_{j(p+k)}^{4(\theta_{ik}-\theta_{lk})^2} + \frac{1}{\lambda_{w_{Os}}} \quad 4\text{-}18$$

Note that $\boldsymbol{\theta}^*$ acquired a subscript in Equation 4-18 to account for the possibility that the emulator is being used in calibration, and that $\boldsymbol{\theta}^*$ is therefore not fixed, but a sample from the parameter prior distribution. In Equation 4-18, the subscripts i and l indicate covariance between two different experimental input settings, while the subscript j indicates a particular basis function or principle component, and the subscript k cycles through the length of the input vectors ($\mathbf{x}$ or $\boldsymbol{\theta}$). Other parameters (λ_j, λ_{W_Os}, and ρ) are explained in the next section.

The GP for $\delta(\mathbf{x_i}, IP_\delta)$ can be written in a similar manner as in Equation 4-19, where D_j is the j^{th} principal component or basis function and v_i is a multivariate normal weighting factor with 0 mean and a covariance function of the form of Equation 4-18.

$$\delta(\mathbf{x_i}, \mathbf{IP_\delta}) = \sum_{j=1}^{p_v} D_j v_j(\boldsymbol{x_i}, \mathbf{IP_\delta}) \quad 4\text{-}19$$

Finally, $\varepsilon(IP_\varepsilon))$ is a GP with mean 0 and covariance as shown in Equation 4-20, where Σ^{e_i} may be either the identity matrix or specified by the user.

$$\mathrm{cov}(\mathbf{IP_{i,\varepsilon}}) = \frac{1}{\lambda_y} \Sigma^{e_i} \quad 4\text{-}20$$

4.4.4 Gaussian Processes for Model Calibration

In principle, Bayesian calibration with GPs is identical to the Bayesian calibration with the simple model shown in Section 4.4.2, though the details of execution differ. In particular, the priors and hyper-priors of internal parameters becomes very complex, and the form of the likelihood function is far less neat. In the case of GPMSA the core internal parameters are referred to as β, ρ, λ_{w_Os}, and λ_n, each of which has several instances and their own hyper-priors.

GPMSA requires model parameters and prior distributions as inputs. In addition, internal parameters are required for GPMSA to function as it explores the parameter space and generates a posterior distribution of the model parameters, model discrepancy, and observational uncertainty. The internal parameters are not fixed values; instead they each have their own prior distribution (called hyper-priors) which is adjusted during the calibration process. The exact form of the hyper-priors is unimportant for this discussion, but in general, they are chosen to promote small values of the GP variance where the data and model form allow. The parameter λ, if large, results in a small value of $1/\lambda$, which promotes a small variance in component j of the GP, so the hyper-prior favors large values of λ. Similar statements may be made regarding λ_{w_Os}, but $1/\lambda_{w\_Os}$ represents a nugget rather than a variance scale, and is equal to zero, except on the diagonal of the covariance matrix. A nugget is some small variance added to the GP prediction of any data point to emphasize mathematically that there is always some level of uncertainty, even at "known" points for training the GP. In practical terms, the nugget prevents a zero uncertainty situation, which is physically unrealistic and computationally untenable. Finally, ρ and β are related as shown in Equation 4-21.

$$\rho = \exp(-\frac{\beta}{4}) \qquad 4\text{-}21$$

Substituting the right-hand-side of Equation 4-21 for ρ in Equation 4-18 yields the most common form of the covariance function, but ρ is easier to work with in the GPMSA code. In either case, these parameters may be regarded as length scale parameters; in other words, they indicate the degree to which different points in input space impact the corresponding points in output space as a function of the Euclidean distance between the two points in input space.

The methods outlined in Section 4.4 were applied particularly in Chapter 6 and additional results (for amine-based carbon capture) may be found in found in Appendix B. In general, the layers of models and submodels were unpacked from their "black-box" configuration, emulated by a collection of GPs, and calibrated via Bayesian inference on the parameters used in both the models and the GPs. Because the models are intended to be physically and theoretically sound, and not merely an empirical model that fits the data, the ultimate result of the calibration is not the only (or even primary) goal. Instead, the discrepancy function offers insight into how the model fails to match reality, and indicates which inputs are most important in reconciling the discrepancy by adjusting the model form to include further physics.

As a final note, the likelihood function itself is not given here, both because it is extremely intricate and lengthy, and because any reader interested in that level of detail would do far better to thoroughly peruse the literature references in an effort to reconstruct highly advanced model analysis machinery.

5 SENSITIVITY ANALYSIS[2]

This chapter describes a sensitivity analysis of the CCK model in oxy-coal conditions using the version of the CCK model developed by Shurtz (2011), with slight modifications. The CCK model was then modified to improve the submodels identified in this sensitivity analysis. The modified CCK code is described in Chapter 7.

5.1 Introduction

Oxy-coal combustion radically changes the environment that coal particles experience, which presents unprecedented difficulties for comprehensive carbon conversion models intended and tuned for more conventional firing. It is therefore reasonable to expect any comprehensive coal combustion model to produce substantially erroneous predictions when extrapolated to the extremes of oxy-coal combustion. In this chapter, a state of the art carbon conversion code (Carbon Conversion Kinetics or CCK) was thoroughly examined in a global sensitivity analysis, with all parameters being simultaneously adjusted. The CCK code was chosen since it contains a high degree of physical detail in several submodels for char conversion via CO_2, H_2O, and O_2 gasification (the prominent reactions in oxy-coal combustion). The sensitivity analysis on this code was used to identify the most influential submodels in oxy-fuel conditions, which can in turn guide future research and submodel improvements. To execute a sensitivity analysis,

[2] This chapter was modified from published work: Holland, T. and T. H. Fletcher, "Global Sensitivity Analysis for a Comprehensive Char Conversion Model in Oxy-fuel Conditions," *Energy & Fuels,* **30**, 9339-9350 (2016).

representative conditions are needed. The next section of this chapter briefly outlines the relevant experimental data, followed by a section that summarizes the CCK model, and finally two sections that describe the sensitivity analysis.

5.2 Experimental

To conduct a relevant sensitivity analysis, the CCK model was run at conditions related to real-world application. Here, the most applicable conditions are the oxy-coal combustion environment, so experimental data from the literature were chosen as a reference point at useful conditions. The experimental data also allowed the kinetic parameters to be optimally fit and fixed, so that the subsequent sensitivity analysis is most relevant at oxy-coal conditions with the kinetics of the specific coals in question, though the results of the sensitivity analysis are believed to be broadly applicable. The experimental data referenced here were collected by Shaddix and Molina (2009) and Geier et al. (2012) at gas temperatures of 1400-1800°C and O_2 mole fractions of 0.12 to 0.36. These data are fully detailed in section 8.2.

5.3 Char Conversion Modeling

Several char conversion models in the literature include complex submodels that attempt to capture the most important chemistry and transport effects of char conversion. The code used here is an extension of the Carbon Conversion Kinetics (CCK) code (Shurtz, 2011; Shurtz and Fletcher, 2013) with minor adjustments to make the code functional in the extremes of oxycoal combustion. These modifications include a more stable temperature solver with informed initial guess values that result in rapid convergence times, step-size independence, and successful model execution at extremely high temperature (appropriate for highly elevated O_2 concentrations) or high H_2O and CO_2 concentration environments. Predecessors of the CCK

code are listed in section 7.1.2. Like other previous versions of the CBK code, CCK includes the kinetic mechanism shown in Equations R1-R8 to model the oxidation and gasification of carbon. Note that in this mechanism the C(O) complexes in reactions R3, R5, and R7 represent distinct species with separate reactant pools, as indicated by their subscripts. This means that gasification via O_2, CO_2, and H_2O all have different pathways, and do not share the same C(O) complex pools as a common reactant (i.e.; if R1 were to be very rapid and produce a high concentration of the $C(O)_\alpha$ complex, this complex would not facilitate R5 or R7, nor hinder R4 or R6). This reaction formulation is in accordance with Liu and Niksa (2004). The CCK code also includes the energy balance, Thiele modulus, multicomponent gas diffusion, random pore model, and CO/CO_2 production ratio models shown in Table 7-1, and a coal swelling submodel (shown in Table 5-1). The extended CCK code contains over 300 input parameters that include effects such as reaction kinetics, pore diffusion, thermal annealing, ash layer build-up, particle size distribution, and distributed activation energies. The object of this chapter is to statistically determine the most sensitive parameters of this model in oxy-fuel combustion environments to optimally target further research and model improvement for those parameters.

Table 5-1 – CCK submodels.

Sub-Model Name	***Model Form***
Surface Reactions (Shurtz and Fletcher, 2013)	$2C + O_2 \rightarrow C(O)_\alpha + CO$ $(R1)$ $C + O_2 + C(O)_\alpha \rightarrow C(O)_\alpha + CO_2$ $(R2)$ $C(O)_\alpha \rightarrow CO$ $(R3)$ $CO_2 + C \leftrightarrow C(O)_\delta + CO$ $(R4)$ $C(O)_\beta \rightarrow CO$ $(R5)$ $C + H_2O \leftrightarrow C(O)_\beta + H_2$ $(R6)$ $C(O)_\beta \rightarrow CO$ $(R7)$ $C + 2H_2 \rightarrow CH_4$ $(R8)$

Table 5-1 Continued

Sub-Model Name	***Model Form***
Langmuir-Hinshelwood-type Reactions (Shurtz and Fletcher, 2013)	$R_{C-O_2} = \frac{k_1 k_2 P_{O_2}^{1+n_1} + k_1 k_3 P_{O_2}}{k_1 P_{O_2} + \frac{k_3}{2}}$ 5-1 $R_{C-CO_2} = \frac{k_4 P_{CO_2}}{1 + \frac{k_4}{k_5} P_{CO_2} + \frac{k_{4r}}{k_5} P_{CO} + \frac{k_6}{k_7} P_{H_2O} + \frac{k_{6r}}{k_7} P_{H_2}}$ 5-2 $R_{C-H_2O} = \frac{k_8 P_{H_2O}}{1 + \frac{k_4}{k_5} P_{CO_2} + \frac{k_{4r}}{k_5} P_{CO} + \frac{k_6}{k_7} P_{H_2O} + \frac{k_{6r}}{k_7} P_{H_2}}$ 5-3
Particle Swelling (Niksa et al., 2003)	$\frac{d}{d_0} = 8.67 - 0.0833 * X_C \;\; if \; 89 \leq X_C \leq 92$ 5-4 $\frac{d}{d_0} = -0.0458 + 0.01459 * X_C \;\; if \;\; 72 \leq X_C \leq 89$ 5-5 $\frac{d}{d_0} = 1 \;\; if \; X_C < 72$ 5-6

5.4 Sensitivity Analysis Method

Sensitivity can be measured in many ways by such standards as output variance, absolute change in output, correlation of model inputs with model outputs etc. These measures do not necessarily give the exact same information, but they reveal, broadly, which input variables have the greatest impact on model output quantities of interest. In the analyses presented here, three methods were employed. The first is a simple correlation check, the second considers the magnitude of the change in the outputs induced by the change in the inputs, and the third examines the monotonicity of input/output relationships. The three methods were chosen because they could be applied with reasonable coding and computational effort (once the codes were written and validated, they consumed approximately one week of computational time crudely

parallelized on a Mac Pro, 2014 model), and yielded results at an adequate level of detail (i.e., the results of the sensitivity analysis were consistent between computational runs).

The three methods were applied by varying all parameters simultaneously, followed by a comparison of the input and output matrices. Depending on the comparison method, the sensitivity test assumed either linear or monotonic variation of inputs with outputs. The test also assumed that any given variable would induce roughly the same order of magnitude change in the outputs. These assumptions are not rigorously true, but the results presented below show they are adequate to rank the various submodels and parameters in order of importance. Also, it must be emphasized that the linearity assumption is far more valid than might initially be supposed. In this case, the values of the parameters are known, and each parameter is associated with a linear coefficient that can be determined via multiple linear regression. The regressed model remains linear as long as the coefficients do not have a multiplicative, exponential, or logarithmic relationship to each other. This is valid regardless of the fact that the parameter, when employed in the CCK model, can (and often does) undergo any number of nonlinear operations or transformations.

The sensitivity analysis is of general interest because some of the parameters used in comprehensive char conversion models may be used more as fitting parameters rather than measureable, physical quantities (Shaddix and Molina, 2009; Lewis et al., 2015). Such fitting parameters weaken the predictive capability of the model. For example, physical measurements of tortuosity are generally unavailable, so relevant parameters are often tuned to specific data sets. The CCK model includes several submodels with numerous parameters, many of which have second order and higher interactive relationships. A sensitivity analysis was therefore performed to rank the parameters in order of importance. Because of the many complex

interactions between model parameters, the sensitivity analysis was global, over the entire range of physically-reasonable parameter space, and with all parameters of interest varying simultaneously. This is the first time such an exhaustive global analysis has been applied to a comprehensive char conversion code. The results of this analysis identified prime candidates for model improvement, and these candidates generally have an equivalent submodel or parameter in other comprehensive char conversion codes, which allows the results shown here to apply broadly to conceptually-similar codes.

5.4.1 Determine the Fundamental Parameters

As a first step, the set of model parameters was reduced to fundamental parameters, defined as those that were not computed from other parameters. This reduced the number of parameters to approximately 50, and these were further reduced to 36 parameters by testing only the physically feasible range of the combined activation energies (E) and preexponential factors (A) for the relevant chemical kinetics. Allowing both E and A to vary freely and independently of each other would result in many cases where the reaction in question essentially did not occur, and many others where the reaction proceeded orders of magnitude too rapidly, rendering the analysis physically meaningless. Choosing a value for the first parameter in any set of correlated parameters reduces the physically reasonable range of the other parameters, but this effect is particularly import in the case of the Arrhenius form kinetics. The exponential form found in Arrhenius kinetics is a specific example of a mathematical form common even outside of kinetic systems and is shown in Equation 5-7.

$$y = a * \exp(b) \qquad 5\text{-}7$$

In general, the exponential term changes rapidly with small changes in the exponential parameter “b”, but “y” is relatively tightly constrained, which in turn sharply proscribes acceptable values of “a” once “b” is chosen. This complicates sensitivity analyses because often it is unknown exactly which bounds “y” should have, as is the case in this system of eight reaction equations interrelated by Langmuir-Hinshelwood type kinetics.

However, the analysis can still be executed in a useful manner. Because the analysis seeks to determine the importance of a given reaction pathway (not the importance of A or E individually), reducing kinetic parameters to one parameter per reaction does not limit the usefulness of the sensitivity analysis. Instead, the one free parameter is allowed a sufficient range to express all feasible values of “y” without allowing any physically meaningless pairs of “a” and “b” (or in the specific case of kinetics, A and E). The analysis in fact indicated that the most important parameters were often kinetic parameters. This is to be expected, and served as a useful final check of the analysis codes, but does not offer much in the way of new insight, so the kinetic parameters were optimized and fixed at stationary values. The kinetic parameters were therefore excluded from the sensitivity analysis. Though the kinetic parameters are highly sensitive, reliable, general correlations for coal oxidation and gasification kinetic parameters do not exist. Therefore, a precise, predictive code must fit the kinetic parameters using data relevant to the specific combustion scenario. The kinetic parameters for the surface reaction resulting from the optimization were held constant for the subsequent sensitivity analyses, reducing the number of parameters to 27. Note that the optimized kinetic parameters are not a unique solution (as is typically the case of all but the simplest optimizations), and that different nominal values of the fundamental parameters could shift the optimized kinetic values. However, no reasonable nominal values would significantly reduce the sensitivity of the kinetic parameters, and no

reasonable values of the kinetic parameters would result in a radically different sensitivity analysis.

Also note that the word "fit" here does not imply the simple linearization of a global equation that results in a slope and intercept that correspond to values of the activation energy and preexponential factor. Because of the great complexity of the model, the fit was obtained by fixing all parameter values except for the kinetic parameters of Equations R3 and R7, and using MATLAB© fmincon optimization software to minimize the error between the data and the model prediction, where the data were divided into particle size "bins" to minimize the error introduced by a range of particle sizes. All other kinetic parameters are directly related to the values of the parameters of R3 and R7, as in the other most recent iterations of CBK type codes (Niksa et al., 2003; Liu and Niksa, 2004; Shurtz and Fletcher, 2013). Examples of the fit of particle temperature data during char conversion in an oxy-fuel environment are shown in Figures 5-1 through 5-3. Table 5-2 shows the optimized kinetic parameters.

Table 5-2 – Optimized kinetic parameters.[3]

Coal Type	**$E_{A,7}$ (kJ/mol)**	**$E_{A,3}$ (kJ/mol)**	**A_7 (s^{-1})**	**A_3 (unitless)**
Black Thunder	239	151	1.00×10^{11}	6.64×10^{8}
North Antelope	248	152	1.75×10^{11}	3.62×10^{9}
Utah Skyline	230	156	5.00×10^{11}	2.42×10^{11}
Pittsburgh	259	161	1.16×10^{11}	6.64×10^{8}

The predictions show the particle temperature rise due to convective heating (devolatilization occurs during this period), a subsequent rise due to exothermic heterogeneous

[3] Note that because E's and A's are strongly correlated, these are only one of several sets of possible values where a larger (or smaller) E_A may be compensated for by a larger (or smaller) A value.

reaction, and then a sharp temperature decrease as the heterogeneous reaction is completed. Also note that the error

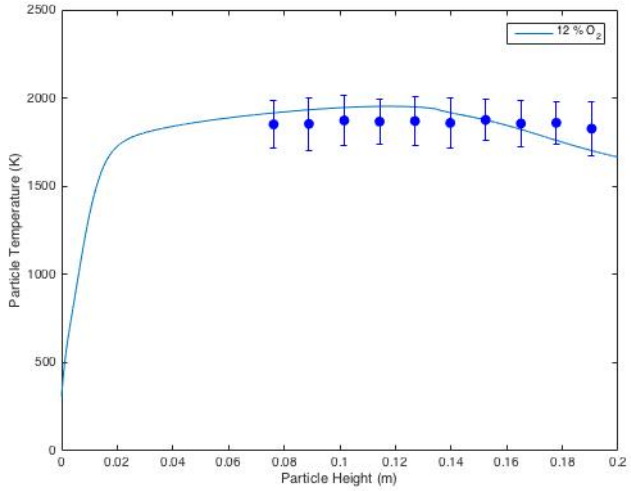

Figure 5-1 – Predicted (lines) and measured (points) particle temperatures of 90 µm initial char diameter North Antelope coal particles in 12% O_2.

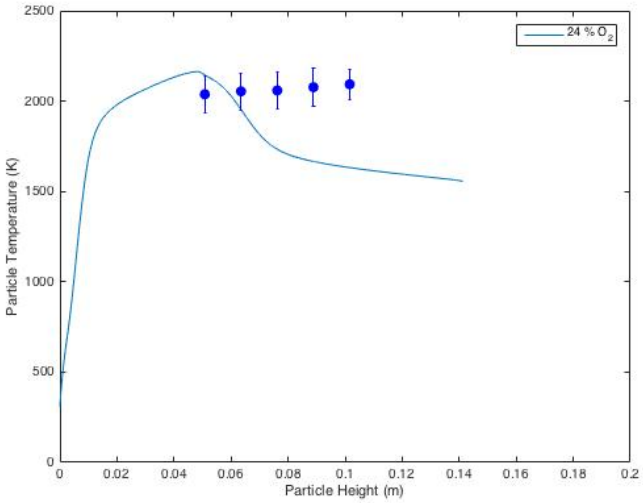

Figure 5-2 – Predicted (lines) and measured (points) particle temperatures of 90 µm initial char diameter North Antelope coal particles in 24% O_2.

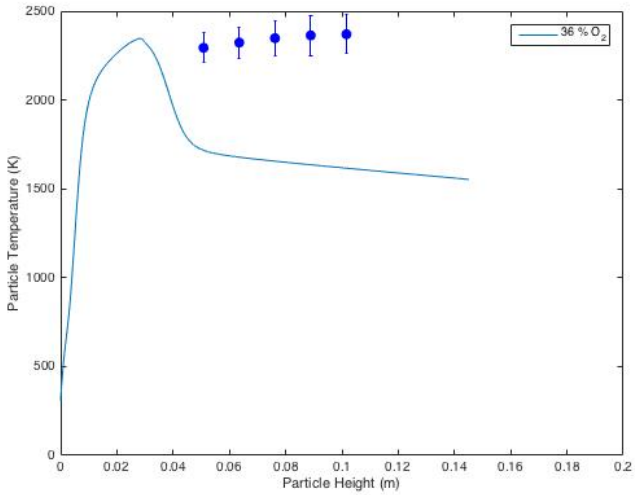

Figure 5-3 – Predicted (lines) and measured (points) particle temperatures of 90 µm initial char diameter North Antelope coal particles in 36% O_2.

bars in Figures 5-1 through 5-3 show two standard deviations from the mean data value; while the error bars are quite wide, this is a result a significant particle-to-particle variation rather than actual measurement error. That is, the particles vary substantially in diameter and ash content (and therefore combustion temperature), so the standard deviation bars actually show the range of roughly 95% of the data, rather than actual measurement error, which may be on the order of 25-50 K. The single, solid line is for one particle size and one ash fraction, while the error bars show the range of prediction curves expected for the entire range of ash content and particle sizes. The model fit to the data is (in high O_2 cases) quite poor, and the data do not show late-stage particle cooling as would be expected. The inadequate fit is partially due to particle-to-particle variation but mostly a result of inadequate treatment of oxy-fuel conditions by the model, and a potential skew introduced by the data collection system (particles that are too small or too cool are not detectable in this system). Similarly, the late-stage burnout particles are likely not observed because they have cooled below the detection threshold. Because the CCK code was not originally intended for oxycoal conditions, it is unsurprising that the sub-models are not entirely appropriate; thus, the main purpose of this chapter is to highlight the submodels most in

need of improvement. Figure 5-1 shows a very acceptable fit within the range of data (as might be expected with a more conventional O_2 concentration), while predictions in Figures 5-2 and 5-3 do not agree well with the data, indicating the need for substantial model changes especially at higher O_2 concentrations. The error bars represent the spread of approximately 95% of the data, and the data are found to have an approximately normal distribution with respect to the range of particle temperatures at any given observation height. The data also have a substantial spread in particle diameter despite the narrow, sieved size-cut, but the temperature range of approximately 300 K is far more substantial than would be expected from the variation in particle diameter, and in fact appears to be independent of diameter. Instead, it is likely due to substantial heterogeneity in coal ash content and chemistry. Data are from Geier et al. (2012).

5.4.2 Determine Parameter Ranges

The next step of the sensitivity analysis was to determine simulation input values for each parameter, along with a range of permissible values. The range of permissible values was used to set up a Latin hypercube sampling scheme. The hypercube accepts as inputs the allowed range and probability distribution of each parameter and creates a space filling design as described in section 4.3

The Latin hypercube design matrix was used to perform 10,000 experiments for 12 different sets of experimental conditions (i.e., 4 coals and 3 O_2 conditions). The sensitivity analysis was found to be well converged at this number of computer experiments. The very large number of parameters to be explored (and their exponentially greater pairwise and higher interactions) made for extremely noisy computational experiments, and 10,000 runs where necessary to clearly and consistently determine the pattern of sensitivity. The results of each set

of 10,000 experiments were evaluated using three methods: a simple scatter plot, a partial rank correlation coefficient, and a linear approximation. The scatter plot simply plots the values of a given parameter on the abscissa and the values of the output on the ordinate axis. Because of the large number of parameters, the resultant graphs were, unsurprisingly, entirely obscured by the noise described above, and hence the results are not shown. The other two methods are more robust and yielded satisfactory results, discussed below.

5.4.3 Linear Approximation Design

The modified linear approximation design followed the method described by Frenklach et al. (2005) and Box and Draper (1987), adjusted for a Latin hypercube set of experiments. The linear approximation was a global design as described by Saltelli et al. (2004; 2008) with the goal of prioritizing input parameters and a design space spanning the entire parameter space of each variable. The linear approximation method calculates an "importance measure" for each parameter, which roughly indicates the rate that a change in input induces a change in output. Here, the importance measure simply means a normalized score that indicates how influential a given parameter is in the model, on a scale from zero to one. The analysis entailed the following steps:

1. Determine physically reasonable ranges for each parameter. In this case, the ranges were determined from a combination of literature searches and past experience with char burnout modeling. The parameters of interest and their descriptions are given below in Table 5-3 with additional columns to include maximum and minimum allowed values.
2. Create an $n \times p$ input matrix $\mathbf{X}$ of experiments where each column contains the n input values for one particular variable needed to conduct n experiments. This was done with the

MATLAB© lhsdesign function to create a Latin hypercube of the parameters as described in section 4.3.

3. Execute the model once for each of the n experiments and store the outputs of interest. Here, the outputs were the total burnout of the particle and the temperature of the particle at each quartile of residence time.

4. Scale the input matrix **X** values so that they range between -1 and 1. This is accomplished by either linear or logarithmic scaling as appropriate, and is desirable to improve the numerical stability of computations involving large matrices.

5. Append a column of ones to matrix **X**, which accounts for the free parameter (the intercept) in a system of linear equations, and improves the linearized fit.

6. Solve for the importance measure **a** by multiple linear regression using **X*a** = **b**, where **X** is the n × p matrix of scaled inputs and **b** is the vector of n outputs from the n computational experiments. Each value in the vector **a** is normalized to range from 0 to 1, where higher numbers indicate greater importance for the corresponding parameter in matrix **X**.

The above procedure merits a number of comments and explanations. First, Table 5-3 shows the bounds of the various inputs to be varied in the global sensitivity analysis. In general, the bounds on any given parameter are wider than necessary to capture the variation of a single experiment, which allows them to capture the range of uncertainty seen in the body of char combustion research. Specific details are given where needed in the table. Also, the kinetic parameters are not shown, since they were initially determined to be highly sensitive parameters, and then fixed at optimized values for all of the analyses shown in this work.

Table 5-3 – Parameters of the sensitivity analysis.

Parameter	Description	Min	Max	Nominal
V_{ASTM}	ASTM volatiles; well known for common coals[4]	-1%	+1%	various
x_{ash}	Ash (dry basis); well known for common coals[4]	-1%	+1%	various
x_C	C (daf); well known for common coals[4]	-1%	+1%	various
x_H	H (daf); well known for common coals[4]	-1%	+1%	various
D_{P0}	Initial raw coal diameter (used mean value of a known size cut, and sufficient variation to capture the bulk of the size spread)[5]	-20%	+20%	various
E_A	Mean activation energy of char annealing from CBK (kcal/mol), with ranges chosen from the scatter in the data (Hurt et al., 1998)	1.6	3.7	2.8
E_C	Activation energy in the CO/CO_2 production ratio model. Wide uncertainty from CBK 8 (cal/mol). (Sun and Hurt, 2000)[5]	-50%	+50%	9,000
d_{grain}	Size of ash grains in the char particle (microns). (Hurt et al., 1998; Shurtz and Fletcher, 2013) These bounds are exceptionally wide because the parameter is thought to be relatively unimportant, and extreme cases test that theory.	0.1	10	5
V_{HT}	High-temperature volatile release.	1.1* V_{ASTM}	1.3* V_{ASTM}	1.2*V_{ASTM}
n_1	Oxidation reaction order (Liu and Niksa, 2004). The data show wide variation for this parameter, so the entire range is allowed.	0	1	1
P	Pressure of the combustion system (atm). The CCK code is most suited for roughly atmospheric pressure experiments.	0.9	1.1	1
φ_{af}	Ash-film porosity. (Hurt et al., 1998)	0	0.5	0.17
t_r	Char particle residence time (s). This was case specific, and largely of interest to observe the sensitivity of late burn out to the uncertainty in short residence times.	various	various	various
T_{P0}	Initial coal particle temperature (K). These values are room temperature for raw coal, and about 1300 K for cases when the model is initiated post devolatilization.	300	1500	300
α	Mode of burning parameter. Various conditions can span the entire range of the mode of burning. $\frac{\rho}{\rho_0} = \left(\frac{m}{m_0}\right)^{\alpha}$	0	1	various

[4] Absolute percent
[5] Relative percent

Table 5-3 continued

Parameter	Description	Min	Max	Nominal
λ_a	The thermal conductivity of the ash (cal/(cm*s*K). This value is likely unimportant, so an extreme range was used to test this theory.	0.001	0.01	0.005
ψ	A random pore model parameter. (Bhatia and Perlmutter, 1981) $$\frac{S}{S_o} = (1 - X) * \sqrt{(1 - \psi * \ln(1 - X))}$$	1	19	4.6
ρ_a	The density of the ash gm/cm^3.	2	3	2.65
ρ_c	The apparent density of the coal gm/cm^3.	1.2	1.4	1.3
σ_{EA}	Standard deviation of the log-normal activation energy distribution for char annealing (kcal/mol). (Hurt et al., 1998)	0.4	0.5	0.46
τ/f	A random pore model tortuosity parameter. (Shurtz and Fletcher, 2013)	1	24	12
d/d_0	Particle swelling (diameter/initial particle diameter).	0.9	1.1	various

Also note that the system is solved by linear regression, implying that each parameter has a linear impact on char burnout and particle temperature. This is not entirely true, resulting in a degree of fitting error, but each parameter was checked by performing a series of model executions where only the parameter in question was adjusted over its range while all others remained at their nominal values. In these computations, a straight line reasonably approximated the vast majority of changes in output vs. changes in input, and the exceptions were excluded from the analysis. Here, “reasonably” approximated by a line means that a linear fit was adequate to examine the sensitivity of the parameter, but not necessarily adequate to precisely track changes in output induced by the change to the input in question. Those few cases that were not reasonably linear together with those that were unsuitable for partial rank correlation (see below) constituted roughly 5% of the data, and were excluded from the analyses.

The multiple linear regression was used to solve Equation 5-8 where **X** is the n x p matrix of parameter values, **a** is the vector of importance measures for each of p parameters, and **b** is the vector of n outputs from the n computational experiments.

$$\boldsymbol{X} * \boldsymbol{a} = \boldsymbol{b} \tag{5-8}$$

The simplified case of a single computational experiment results in Equation 5-9, where the more traditional output y replaces the vector **b**.

$$x_1 a_1 + x_2 a_2 + \cdots x_p a_p = y \tag{5-9}$$

The partial derivative of y with respect to the i^{th} parameter yields Equation 5-10, which shows that the i^{th} importance measure is the derivative of the output with respect to the i^{th} parameter, or in other words the slope of the output in the direction of the i^{th} parameter.

$$\frac{\partial y}{\partial x_i} = a_i \tag{5-10}$$

On a normalized scale of inputs between -1 and 1, the importance measure is approximately a measure of how rapidly a change in the i^{th} input induces a change in the output y, and because the rate is constant over a scaled parameter space, it is also a measure of the magnitude of the total change in output.

In p dimensions (for the p parameters in the sensitivity analysis), Equation 5-11 is the solution to Equation 5-8, and is identical to setting the gradient of Equation 5-12 equal to zero, or minimizing the sum-squared-of-error in all p dimensions (where the error is the residual between the actual CCK output, and the linearized model prediction for the CCK output).

$$\boldsymbol{a} = (\boldsymbol{X}'\boldsymbol{X})^{-1}\boldsymbol{X}'\boldsymbol{b} \tag{5-11}$$

$$SSE = \sum_i r_i^2 = \sum_i (y_i - f(x_i, a))^2 \tag{5-12}$$

The solution vector **a** is therefore the best estimate of the importance measures in that it minimizes the difference between the regression predictions and the actual results of the model. The vector **a** is analogous to the slope of the change in output related to the change in input, but differs in that it captures some influence of the higher order effects of all other parameters (i.e., $\mathbf{a}_i$ is **not** the same as would be found by simply varying parameter i in isolation and finding the slope at the minimum and maximum of the allowed values of parameter i). Figure 5-4 is a block logic diagram of the sensitivity analysis process.

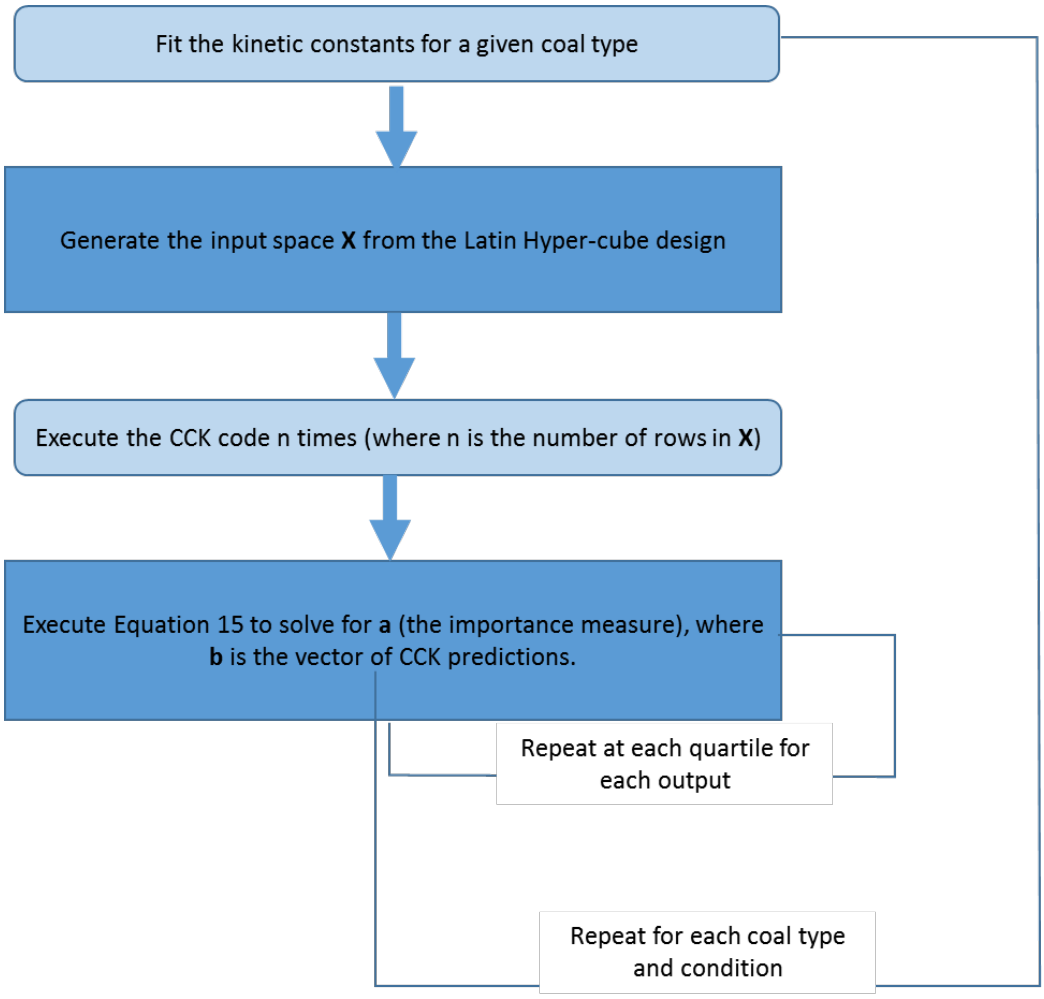

Figure 5-4 – Logic diagram to find the sensitivity measure for a given output.

5.4.4 PRCC

Partial rank correlation coefficients (PRCC), or Spearman correlation coefficients, establish the degree of monotonic relation between outputs and inputs after taking into account the effects of other input parameters, with +1 indicating perfectly monotonic, positive correlation, while -1 indicates perfectly monotonic anti-correlation (Gomero, 2012). PRC coefficients were found in three steps. First, the residuals were found by solving a series of multiple linear regressions where Equation 5-8 is solved repeatedly without one of the p columns (where each column contains values of one of the p parameters needed to execute the CCK code). This series of regressions results in a series of models, each missing one of the parameters. The difference between the predictions from the full model and the predictions from the model missing the i^{th} parameter are the i^{th} residuals, because they are the portion of the model that cannot be explained without the i^{th} parameter. Second, after the residuals are calculated, they are ranked by assigning the number 1 to the lowest valued residual, the number 2 to the second lowest value, and so forth until n (the integer number of experiments) is assigned to the highest value. This step is also applied to the predicted output of interest, **b** (burnout or particle temperature). The third and final step is to calculated the correlation coefficient for the residuals, as in Equation 5-13 (Marino et al., 2008).

$$\rho_{X,Y} = \frac{Cov(X,Y)}{\sigma_X \sigma_Y} \qquad 5\text{-}13$$

This sensitivity measure captures non-linear effects of the input parameters on the output, provided the effects are monotonic and the inputs have no significant correlation with each other. As mentioned above, the small fraction of the data that failed to meet these criteria was excluded from the analysis.

It is also worth noting that while the PRCC method is designed to rank the monotonic correlation of individual variables, it cannot perfectly discount the effects of other variables or the imperfect fit of the full model. The high number of replicates helps to overcome this noise, but a parameter that induces a small change in outputs will probably not have as high a sensitivity ranking as a parameter that induces an exponential shift, even if the smaller change is more perfectly monotonic, because the small change is far more likely to be lost in the noise. The PRCC measure is therefore somewhat of a measure of the magnitude of the change induced in an output parameter.

5.5 Results and Discussion

Simulations of four coals at each of three conditions for two different sensitivity tests of 27 parameters resulted in approximately 5,000 sensitivity measures, and a plethora of relevant comparisons. To make direct comparisons of all sensitivity measures, the linear approximation importance measures were normalized to range between 0 and 1, and the absolute value was taken of PRC coefficients, so they indicate only magnitude of importance, not correlation or anti-correlation. Relevant subsets of the sensitivity analysis are discussed below.

5.5.1 Total Sensitivity at Various O2 Concentrations

Table 5-4 shows the total sensitivity scores (the mean of all sensitivity scores over all experiments and conditions) of the seven most important variables in the CCK code at all coals at all conditions, for all outputs, and for a combination of both PRCC and linear approximation tests. It also shows the total sensitivity for each of the three O_2 levels tested.

Table 5-4 – Total sensitivity measures for all O_2 conditions and each individual condition.

Mean Sensitivity Measures		**Sensitivity for $y_{O2} = 0.12$**		**Sensitivity $y_{O2} = 0.24$**		**Sensitivity for $y_{O2} = 0.36$**	
Variable	**Importance**	**Variable**	**Importance**	**Variable**	**Importance**	**Variable**	**Importance**
E_A	0.74	E_A	0.76	E_A	0.72	E_A	0.75
n_1	0.51	n_1	0.55	n_1	0.51	n_1	0.48
d/d_0	0.27	d/d_0	0.40	d/d_0	0.22	α	0.22
α	0.20	d_{grain}	0.20	α	0.22	σ_{EA}	0.20
d_{grain}	0.20	t_r	0.18	d_{grain}	0.21	d_{grain}	0.19
σ_{EA}	0.18	α	0.18	σ_{EA}	0.17	d/d_0	0.17
t_r	0.14	σ_{EA}	0.17	t_r	0.12	t_r	0.11

The scores shown in the "Importance" column are the mean scores for the seven most important variables as measured from all the various combinations of conditions and analysis techniques. Note that although residence time (t_r) is not typically thought of as a model parameter, the quartile of residence time was included as a parameter in the sensitivity analysis to differentiate between sensitivity early in burnout and late in burnout. Residence time, along with the other six parameters shown in Table 5-4, is also the most sensitive in each individual analysis (with a minor exception discussed below). The same two variables are always of highest importance, and always have the same relative position: mean annealing activation energy (E_A) and the order of the oxidation reaction (n_1 in Equation 5-1). As such, these two parameters will be referred to as having primary importance, while the other five variables will be referred to as secondary, and the remaining 20 are considered to have tertiary importance. Though the seven most sensitive variables are the same in all analyses, and they share many common trends in sensitivity scores from one analysis to the next, there are several interesting differences in each group of analyses.

In the case of the analyses of each O_2 mole fraction shown in Table 5-4, the particle swelling/raw coal initial diameter (d/d_0) becomes less important as O_2 concentration increases.

The swelling and initial diameter parameters were lumped together because they are so closely linked in the CCK code, and in all other cases they parallel each other quite closely, but in the case of varying O_2 concentration, the decreased importance of d/d_0 is largely due to the decreased impact of the initial particle diameter. This decreased importance is due to higher O_2 concentrations rapidly consuming the bulk of the carbon, leaving an ash-rich char particle with less variability in particle size for most of the residence time. Similarly, the importance of residence time steadily decreases with O_2 concentration because the carbon is converted quite quickly at high O_2 levels, so late stage burnout has progressively less variability.

5.5.2 Sensitivity for All Coal Types and All Combustion Conditions

The subset of the sensitivity analyses for all coal types and combustion conditions are shown in Table 5-5, including the mean scores for sensitivity to particle temperature and burnout (averaged between PRCC and linear approximation tests), and the breakdown for the PRCC and linear approximation sensitivity tests (averaged between sensitivities for both burnout and particle temperature). The two outputs (burnout and particle temperature) are most sensitive to the same seven variables, but differ somewhat in the ordering of those variables. Note that the particle temperature predictions are considerably less sensitive than burnout predictions to E_A and d/d_0. The annealing parameters are likely more important in burnout because the kinetics they control determine how quickly the particle reaches low reactivity in late-stage burnout, but the relatively reactive particle in early burnout is both heated by initially rapid combustion and cooled by relatively high gasification rates, lessening the effects of high reactivity on particle temperature. Similarly, d/d_0 affects the surface area available, but while this affects burnout substantially, the combination of endothermic and exothermic reactions again lessens the reactivity effects on particle temperature. On the other hand, the mode of burning parameter (α)

is approximately 250% more important in particle temperature prediction than the burnout prediction, and the ash grain diameter is nearly four times more important. This is because α is indicative of the combustion regime (zone I, II, or III), which is fixed in the model for the entire system in the CCK model, but *should* be two substantially different values between the endothermic and exothermic reactions. Ash grain diameter (d_{grain}) is most important in late-stage burnout as the ash film model reduces reaction rates and allows other system parameters to significantly affect the temperature, while burnout is nearly complete in that region and not as heavily impacted.

Table 5-5 – Mean total sensitivity for particle temperature, burnout, PRCC, and linear approximation.

Sensitivity for Particle Burnout		**Sensitivity for Particle Temperature**		**Sensitivity for PRC Coefficients**		**Sensitivity for Linear Approximation**	
Variable	**Importance**	**Variable**	**Importance**	**Variable**	**Importance**	**Variable**	**Importance**
E_A	0.82	E_A	0.58	E_A	0.62	E_A	0.90
n_1	0.53	n_1	0.50	n_1	0.43	n_1	0.62
d/d_0	0.34	d_{grain}	0.31	d/d_0	0.26	d/d_0	0.28
σ_{EA}	0.21	α	0.29	α	0.16	d_{grain}	0.26
α	0.12	d/d_0	0.20	d_{grain}	0.15	α	0.24
t_r	0.11	t_r	0.17	σ_{EA}	0.13	σ_{EA}	0.23
d_{grain}	0.08	σ_{EA}	0.16	t_r	0.13	t_r	0.15

5.5.3 Subbituminous vs. High Volatile Bituminous Coals

Comprehensive char combustion codes should ideally function for all coal types, so it is particularly relevant to compare the prediction sensitivity for multiple coals and coal types. The data were for two high volatile bituminous and two subbituminous coals, and Table 5-6 compares their total importance measures and the breakdown between PRCC and linear approximation. The total importance is an average between the PRCC and linear approximation methods, weighted by the number of importance measures in each.

Table 5-6 – Mean total sensitivity for particle temperature and burnout using either the PRCC or linear approximation method for different coal types.

	Subbituminous Total	**Subbituminous PRCC**	**Subbituminous: Linear Aprx.**	**Bituminous Total**	**Bituminous PRCC**	**Bituminous: Linear Aprx.**
Variable	**Importance**	**Importance**	**Importance**	**Importance**	**Importance**	**Importance**
E_A	0.72	0.66	0.89	0.76	0.58	0.99
n_1	0.67	0.56	0.82	0.4	0.31	0.50
d/d_0	0.24	0.24	0.24	0.29	0.27	0.31
α	0.21	0.16	0.26	0.2	0.16	0.24
d_{grain}	0.20	0.15	0.27	0.2	0.14	0.25
σ_{EA}	0.17	0.15	0.19	0.19	0.12	0.26
t_r	0.13	0.12	0.14	0.14	0.13	0.16

The subbituminous and high volatile bituminous coals are striking in how closely they parallel each other in each of the three breakdowns above, with one exception. The subbituminous coal exhibits much higher sensitivity to the order of the oxidation reaction than the high volatile bituminous coals, probably because the subbituminous coal is more reactive and oxidation is the dominant conversion reaction. Note that in the CCK code, oxidation is governed by a Langmuir-Hinshelwood type reaction in which n_1 is the reaction order of one of the three reactions that constitute the oxidation reaction expression. Coal conversion data suggest that n_1 should be between 0 and 1, with the value depending on the reaction temperature. In a global reaction expression, the value of n_1 would change according to the combustion regime, while in the CCK code, the Langmuir-Hinshelwood expression adjusts the weight of the term containing n_1 depending on conditions to appropriately capture the change in apparent order (Hurt and Calo, 2001b; Niksa et al., 2003).

Table 5-6 also highlights a difference between the PRCC and linear approximations also seen in Table 5-6; the linear approximation generally gives markedly higher sensitivity measures than the PRCC method. This is not unexpected since the two sensitivity tests do not measure the

same thing, so they should not have exactly the same sensitivity. The linear approximation test is reporting the rate that the outputs change due to a change in a given input, while the PRCC method is reporting the degree of monotonic behavior in the change induced in an output by a change in input, and also indicates the rough magnitude of that change (because small changes are likely to get lost in the noise). The two methods together give a more complete view of the model, and here indicate that the rate of change is generally slightly greater than the monotonicity of the change.

5.5.4 Sensitivity at Quartiles of Residence Time

The life of a coal particle in an oxycoal system includes a period of heating/devolatilization, rapid initial reaction, potential additional heating or cooling depending on relative concentrations of reactive gases, and late-stage burnout. It is reasonable to expect different model parameters to be important at different burnout stages, so Table 5-7 summarizes the model sensitivity at each quartile of residence time.

Table 5-7 – Sensitivity scores by quartile of residence time.

Quartile 1		**Quartile 2**		**Quartile 3**		**Quartile 4**	
Variable	**Importance**	**Variable**	**Importance**	**Variable**	**Importance**	**Variable**	**Importance**
E_A	0.73	E_A	0.72	E_A	0.77	E_A	0.76
n_1	0.59	n_1	0.52	n_1	0.48	n_1	0.46
d/d_0	0.40	d/d_0	0.29	α	0.23	α	0.22
d_{grain}	0.18	α	0.21	d_{grain}	0.21	d_{grain}	0.21
α	0.16	d_{grain}	0.20	σ_{EA}	0.20	σ_{EA}	0.20
σ_{EA}	0.15	σ_{EA}	0.19	d/d_0	0.19	t_r	0.19
t_r	0.10	t_r	0.11	t_r	0.15	d/d_0	0.18

The sensitivity scores in Table 5-7 show a slight trend for model sensitivity to n_1 to decrease at later quartiles, which, as alluded to above, is unsurprising since most of the carbon has been consumed as burnout progresses, giving other model parameters relatively greater

importance. The residence time on the other hand shows the opposite trend; total residence time becomes more and more important at later quartiles. Most striking, however, is the change induced by particle swelling. The sensitivity to d/d_0 is quite large for the first and second quartiles but less important in late stages of burnout, which also is to be expected since the bulk of the carbon is eaten away at high t_r, leaving an ash-rich particle. Note that the first quartile included a minor exception to the sensitivity trends, and showed that the O_2 concentration (which was allowed to vary up to 10% of the total O_2 mole fraction) had a sensitivity measure of 0.12, displacing residence time (t_r) from the list of most important variables. However, the importance value for t_r in the first quartile was left in the table for comparative purposes.

5.6 Conclusions and Recommendations

A sensitivity analysis of an advanced char conversion model (CCK) was performed based on data for two subbituminous and two high volatile bituminous coals in an oxycoal environment. The results were analyzed using a linear approximation sensitivity analysis method and the partial rank correlation coefficients method. These analyses revealed the expected importance of kinetic parameters. However, after the kinetic values were found from an optimized fit with data, the subsequent set of analyses found that the next two most important parameters were the activation energy of char annealing (E_A) and a reaction order (n_1). Five other parameters were found to be of secondary importance: initial char diameter (d/d_0), ash grain size (d_{grain}), distribution of the activation energy for annealing (σ_{EA}), the quartile of residence time (t_r) distinguishing early burning behavior from late burning behavior, and the mode of burning parameter (α) which controls diameter and density change. These seven variables are prime candidates for future research to improve the accuracy and predictive power of the CCK char conversion code (and comprehensive char codes in general). These results imply a need to

carefully quantify and minimize the uncertainty in the seven most sensitive variables. The following bullet points summarize conclusions and recommendations with respect to each of the most influential parameters.

1. Both thermal annealing submodel parameters are in the top seven parameters, and the mean activation energy is consistently the most sensitive variable. Also, the annealing submodel currently in use is extremely rapid and does not distinguish between active sites, despite evidence that the active complex for each of the three main carbon conversion paths may be distinct (Hurt et al., 1998; Liu and Niksa, 2004). The initial rapid pace of the annealing submodel is not necessarily problematic, since it is a result of a somewhat unrealistic distributed activation energy. The most advanced annealing submodels use a distribution of activation energies to capture the numerous reactions involved in thermal annealing, and these submodels are largely reconcilable with each other (Senneca and Salatino, 2002), but they include unrealistic tails in the distribution. In the case of the activation energy employed in CBK and its offshoots, the log-normal distribution has a portion of annealing reactions with such low activation energies that they occur instantaneously. This problem could be solved by truncating the distribution, but there is no clear-cut truncation point, and since the distribution is consistent, it does not invalidate the model as a whole, as long as the gasification preexponential factors are calibrated in conjunction with the annealing parameters. However, the same sub-model has appeared in successive models without necessarily accounting for the relation between initial preexponential factors and annealing model parameters. The particular annealing model in CBK and its successors is presented by Hurt et al. as formulated by Suuberg (Suuberg, 1990; Hurt et al., 1998), and, contrary to the enormous impact seen in the sensitivity analysis, past

experience has shown relatively small influence due to annealing, especially in late burnout (Shim and Hurt, 2000; Sun and Hurt, 2000). Furthermore, the current annealing model fails to account for the dominant effects of peak particle temperature, particle heating rate, and coal precursor. These preparation conditions and differences in coal chemistry radically change the annealing activation energy distribution (Shim and Hurt, 2000; Senneca and Salatino, 2006), but the prior model has no method to incorporate this information, and was developed prior to sufficient available data to reasonably predict changes in the reaction pathway based on preparation conditions. It is likely that a new or extended annealing model is needed so that char annealing occurs along a more realistic path and distinguishes between gasification and oxidation reactive sites. A new annealing model is discussed in the next Chapter.

2. The global oxidation reaction order (n_1) likely changes depending on the temperature regime, but should lie between 0 and 1 (Niksa et al., 2003; Geier et al., 2012). The three-step oxidation model can switch between the different reaction orders at various temperatures, so despite the sensitivity of this parameter, it seems to be appropriately treated in the current Langmuir-Hinshelwood type kinetic scheme.

3. The residence time (t_r), while important, is experimentally measured or an input from the simulation, and does not rely on submodels, so it should of course be carefully measured, but does not impact the model construction. It was explored as a sensitive parameter only to observe how important uncertainty in residence time might be. Given that char burnout experiments tend to have relatively low burnout and short residence times (except in TGA systems), the high sensitivity of this parameter to small changes is worth noting.

4. The ash inhibition submodel originally outlined by Hurt et al. (1998) is currently used in the CBK offshoots and depends on the ash grain size (d_{grain}). This submodel relies on building on an ash film, which immediately begins to reduce the combustion rate. However, a more sophisticated model developed by Niu and Shaddix (2015) allows ash to build a film and to diffuse back into the carbon core and effectively dilute the carbon in later stages of burnout. This model may be more realistic and better explain late-stage burnout data.

5. The mode of burning parameter (α) describes the changes in diameter and density, and is related to combustion regime. Currently, the model uses only one regime for all reactions and the entire computation, which gives contradictory results for either gasification or oxidation occurring simultaneously. The mode of burning parameter is very commonly used in carbonaceous particle combustion models to describe the shrinking particle and decreasing particle density, but the value of α is given as a constant throughout burnout. Haugen et al. (2014), developed a much more realistic model that uses the effectiveness factor to appropriately weight mass loss between the particle exterior surface and the interior surface (diameter vs density change). All combustion models that have sufficient detail to capture changing particle size and density would be improved by similarly allowing that change to depend on the effectiveness factor, which varies throughout burnout. In the case of oxycoal, this modification is especially impactful because CO_2 and H_2O reactions are more important than in conventional air-fired coal combustion, and gasification reactions have very different effectiveness factors than the oxidation reaction.

6. The swelling and initial diameter require a better swelling model, such as the model developed by Shurtz et al. (2012) to allow for high heating rates and pressure. Currently the swelling model in the CCK code is quite crude and does not adequately account for radical

changes in swelling with coal type and char preparation conditions. Also, any comprehensive combustion model is likely to be too expensive to directly include in a CFD model, so the swelling model will likely be used to train global models to the specific conditions in question. Because pulverized coal has a distribution of particle sizes, the training code should be run for a series of size bins, sufficiently refined so that particle size is no longer a significant source of uncertainty in the trained global model.

6 COAL CHAR ANNEALING

6.1 Introduction

In this chapter, thermal annealing is used as an umbrella term to include both the radical changes in char reactivity due to coal pyrolysis and the lesser (but still substantial) reactivity loss induced by thermal treatment of the post-pyrolysis char. These effects may include reactivity loss due to changes in coal morphology (swelling, changes in pore structure, molten ash that physically plugs pores) and a shift in coal chemistry (cross-linking, loss of reactive groups, rearrangement of char carbon structure, loss of inorganic catalytic activity etc.). Such a broad definition of annealing is adopted because, at the temperatures of practical coal combustion, it may well be infeasible to separate the numerous effects since they occur on similar time scales and may be better viewed as continuous rather than discrete events (Senneca and Salatino, 2002). The model developed in this chapter is inspired and supported by an exhaustive literature review, found in Chapter 2. The remainder of this chapter briefly outlines experimental data tabulated from numerous literature reports, describes development of an annealing model with appropriate physical dependencies, shows a calibration of the model using the tools discussed in Chapter 4, and discusses the success and implications of the new model.

6.2 Experimental

The annealing model employed in CBK has been frequently reused in comprehensive char conversion models. The CBK annealing model was first calibrated to the relative paucity of

experimental data available at the time, i.e., five papers published between 1973 and 1996 (Jenkins et al., 1973; McCarthy, 1982; Radovic et al., 1983b, a; Beeley et al., 1996). The older data taken over a large time span resulted in highly diverse experimental methods, making it quite difficult to arrive at a single, consistent comparison. For example, particle sizes varied greatly, the reaction regime may have been zone I or zone II, measures of reactivity were not uniform, treatment temperatures were generally hundreds of Kelvin lower than practical combustion conditions, and some of the precursors were carbon sources other than coal. Also, except for the most recent paper listed (Beeley et al., 1996), the data were obtained using exceptionally low heating rates (well below 1 K/s) and long heat treatment times (up to 2 hours). These data are potentially useful for the regimes they were taken in, but more recent data show clearly that the most dramatic and dynamic annealing occurs in the first tens or hundreds of milliseconds, implying that annealing models should focus on (or at least include) short timescale data. Fortunately, much data have been collected on the millisecond to second timescale in the two decades since Hurt et al. (1998) published the CBK model; unfortunately, the bulk of these data lack one or more crucial model input or output, such as a reasonably well-defined heating rate, comparable reactivity measurements, or a recorded proximate and ultimate analysis, etc. Nevertheless, the literature contains several times more applicable data now than at the advent of the CBK model, which implies the potential for a more broadly applicable, less uncertain annealing model. The data discussed here were obtained from a detailed search of the literature.

6.2.1 Data for Annealed Char Reacting with O_2

The bulk of available char annealing data pertain to the reactivity of annealed char in O_2. The relevant experiments were carefully designed to take reactivity data in zone I to examine the

intrinsic reactivity of various annealed chars in a broad range of preparation conditions. All of the data points listed below included a proximate and ultimate analysis (see Table 6-1).

Table 6-1 – Ultimate analysis and ASTM volatiles for char precursors in O_2 (wt% daf).

Coal Name (Reference)	C	H	O	N	S	V_{ASTM}
Beulah Zap (Shim and Hurt, 2000)	73.2	4.4	20.6	1.0	0.82	42.0
Pocahontas (Shim and Hurt, 2000)	89.8	5.0	3.4	1.2	0.78	19.2
Illinois 6 (Shim and Hurt, 2000)	78.2	5.5	9.8	1.3	5.40	45.5
South African (Senneca et al., 2004)	80.7	4.5	12.7	1.5	0.73	27.4
Cerrejon (Feng et al., 2003b)	81.8	5.2	11.9	1.8	0.75	40.1
Pocahontas (Russell et al., 2000)	91.8	4.5	1.7	1.3	0.51	19.5
Pittsburgh 8 (Russell et al., 2000)	85.0	5.4	6.9	1.7	0.91	41.7
Tillmanstone (Cai et al., 1996)	91.4	4.4	2.2	1.3	0.70	18.1
Pittsburgh 8 (Cai et al., 1996)	83.2	5.3	9.0	1.6	0.90	41.7
Lindby (Cai et al., 1996)	81.0	5.3	11.0	1.7	1.00	37.5
Illinois 6 (APCS)(Cai et al., 1996)	77.7	5.0	13.5	1.4	2.40	47.4
Illinois 6 (SBN)(Cai et al., 1996)	75.6	5.8	14.5	1.4	2.70	47.0
South African (Bar-Ziv et al., 2000)	80.7	4.5	12.7	1.5	0.73	27.4
High Volatile Bituminous (Naredi and Pisupati, 2008)	80.3	6.0	11.0	1.4	1.00	44.4
Pittsburgh 8 (Gale, 1994; Gale et al., 1995, 1996)	85.0	5.4	6.9	1.7	0.91	41.7
Blind Canyon (Gale, 1994; Gale et al., 1995, 1996)	81.3	5.8	10.9	1.6	0.37	48.1
Beulah Zap (Gale, 1994; Gale et al., 1995, 1996)	74.1	4.9	19.1	1.2	0.71	49.8
South African (Senneca et al., 1997)	82.5	4.6	13.2	1.5	0.73	27.4
South African (Salatino et al., 1999)	82.7	4.5	12.7	1.5	0.73	27.4
Shenfu (Wu et al., 2008)	80.1	5.5	12.3	1.8	0.22	40.6
Rhur (Senneca et al., 1998)	81.0	5.0	10.5	2.1	1.20	32.9
South African (Bar-Ziv et al., 2000)	80.7	4.5	12.7	1.5	0.73	27.4
High Ash Indian (Jayaraman et al., 2015)	72.8	4.7	19.9	1.8	0.83	50.0

Table 6-2 illustrates details on the *initial* heating rate (HR) of the coal particles, the peak temperature achieved (T_p) , and the high temperature treatment time (HTT). In addition, annealing models require a reference char to calculate the relative loss of activity; thus Table 6-2 includes similar data for the reference char as well. The data table also includes a calculated value for p_0 (an NMR structural parameter discussed in the model development section), the measured char **relative** reactivity (MC_R), and the model predicted **relative** char reactivity (PC_R).

Because the reactivities are relative to some reference char, they are unitless. Note Table 6-2 is a subset of the entire data set that is found in Appendix C.

Table 6-2 – Detailed experimental data for char reactivity in O_2.[6]

Coal name	PC_R	MC_R	p_0	HR (K/s)	T_p (K)	HTT (s)	Ref HR (K/s)	Ref T_p (K)	Ref HTT (s)
Pittsburgh 8	1.50	2.08	0.52	1e4	1673	2	1e4	2073	2
Pittsburgh 8	1.42	2.03	0.52	1e4	1673	5	1e4	2073	2
Pittsburgh 8	1.48	2.84	0.52	1e4	1873	0.15	1e4	2073	2
Pittsburgh 8	1.37	2.03	0.52	1e4	1873	0.5	1e4	2073	2
Pittsburgh 8	1.21	1.39	0.52	1e4	1873	2	1e4	2073	2
Pittsburgh 8	1.15	1.30	0.52	1e4	1873	5	1e4	2073	2
Pittsburgh 8	0.53	0.14	0.53	1e3	1773	2	5e3	1273	2
Pittsburgh 8	0.83	0.68	0.53	5	1273	2	5e3	1273	2
Pittsburgh 8	0.93	0.77	0.53	50	1273	2	5e3	1273	2
Pittsburgh 8	1.66	1.80	0.52	3.3e4	1106	0.49	6.6e4	1627	0.135
Pittsburgh 8	1.34	0.80	0.52	5.4e4	1333	0.28	6.6e4	1627	0.135

The data used to calibrate the model were, as mentioned above, exceptionally detailed. Additionally, these data were required to have a reactivity measurement that could be legitimately compared to the compilation of the data as a whole, which most commonly meant that the reactivity was given as a rate of change of normalized mass (i.e., the derivative of the degree of carbon conversion, f, with respect to time). This derivative was taken post-heat treatment in uniform conditions. Ideally, a complete particle time-temperature profile during heat-up would also be available, but given the extremely short time scale, it is not generally possible to solve the relevant energy balance at such a precise level. Instead, the estimated initial heating rate is used, as is common practice in coal-related models that involve heating rate as a

[6] PC_R indicates the model prediction of the reactivity ratio between a data point and a reference point (unitless), while MC_R indicates the measured ratio. HR indicates the estimated initial heating rate, and HTT indicates the treatment time.

parameter. Finally, the data were generally taken between 30 and 70 % char conversion (after devolatilization).

The 70 % conversion boundary was chosen because the later stages of burnout are not fully understood. Senneca et al. (1998) observed that particle reactivity from different particle preparation conditions often converged in late-stage burnout, while Hurt et al. (1998) noted that burnout rates changed dramatically in the final ~15% of char consumption. It has been variously theorized that this is due to factors such as complete annealing, ash inhibition, rising experimental uncertainty near complete burnout, or a small fraction of exceptionally inert macerals. A full discussion of these effects is beyond the scope of the present work, but in all cases, late-stage burnout data is likely to include non-annealing effects. Alternatively, if annealing really is complete, then there is no purpose in training an annealing model to match irrelevant data, although this seems unlikely to be the case, given that the annealed chars have never been observed to anneal to a perfect graphite crystal. Also, the trend of convergent reactivities is more based on extent of conversion rather than any factors expected to influence annealing, and the reactivity measurements are made at temperatures much lower than the heat-treatment, which implies very little further annealing during the low-temperature burnout.

As for the lower bound, the annealing model was trained only to data of at least 30% conversion, where char conversion begins to be measured post-pyrolysis. The first 30% of conversion data is excluded due to observed “early-stage” effects. The data show a trend of initially increasing reactivity, regardless of preparation conditions, in the first few percent of conversion, with a peak typically at ~20-30% carbon conversion. As discussed in the literature review, this could be due to plugged pores reopening, adsorbed oxygen complexes releasing from the surface, highly reactive tar that had redeposited on the char surface, a peak in char

surface area as pores expand, or a combination of many factors. This early stage is not well explored, and is complicated by numerous effects, so it was deemed inappropriate to select "early-stage" data for the training set. As a final note on data selection, a few of the data sources included numerous data points at a single preparation condition. Rather than give this handful of experiments undue statistical weight, the replicate points were averaged together. This could be considered poor statistical practice in that a portion of the data is eliminated, but in this case the wide variety of data collection systems certainly introduces various biases that the model cannot (and should not) account for. An overwhelming number of data points with a particular bias is therefore likely to prove detrimental to the model overall, even though the replicates would prove informative about the variance within that single experiment.

6.2.1 The Error Factor

To accurately assess model success, a quantity termed "error factor" is defined. The error factor is the larger of the ratio of model prediction to experimental measurement or the reciprocal of that same ratio. The result is the factor by which the prediction differs from the measurement, and by taking the larger value, under-prediction is treated on equal footing with over-prediction (i.e., a ratio of PC_R/MC_R of 0.1 or 10 are both penalized in the objective function as being a full order of magnitude off).

6.2.2 Data for Annealed Char Reacting with CO_2 or H_2O

In recent years, thermal deactivation of coal char with respect to CO_2 and H_2O has garnered some interest. Relatively few data are available relevant to annealing during gasification, but those rate data that met the same criteria as the analogous O_2 rate data are given below. Almost all of the data are for CO_2 reactivity, but the set from Jayamaran et al. (2015)

includes a handful of experiments with steam. Table 6-3 contains the relevant proximate and ultimate analysis, while a table similar to Table 6-2 contains a selection of CO_2 and H_2O reactivity and preparation condition data, and is found in Appendix C.

Table 6-3 – Ultimate analysis and volatiles for annealed char precursors in CO_2 (wt% daf).

Coal Name (reference)	C	H	O	N	S	V_{ASTM}
South African (Senneca et al., 1997)	82.5	4.6	13.2	1.46	0.73	27.4
South African (Salatino et al., 1999)	82.7	4.5	12.7	1.46	0.73	27.4
Shenfu (Wu et al., 2008)	80.1	5.5	12.3	1.83	0.22	40.6
Rhur (Senneca et al., 1998)	81.0	5.0	10.5	2.10	1.20	32.9
South African (Bar-Ziv et al., 2000)	80.7	4.5	12.7	1.46	0.73	27.4
High Ash Indian (Jayaraman et al., 2015)	72.8	4.7	19.9	1.79	0.83	50.0

6.3 O_2 Reactivity Model Development, Results, and Discussion

6.3.1 Conceptual Development

Considering the aggregate picture presented by the literature review section (see Chapter 2) and the experimental data, it is clear that coal annealing depends heavily on the precursor, heating rate, treatment time, and peak temperature. The literature review also clearly highlights several of the most prominent thermal deactivation processes (loss of heteroatoms, carbon structure reordering, ash fusion etc.). Such diverse physical and chemical changes cannot be adequately captured by a single activation energy, at least not for a broad array of preparation conditions and precursors. Unfortunately, neither data nor computational power are available in sufficient quantity to rigorously model the vast diversity of annealing processes, so a distributed activation energy similar to the most advanced past models still seems like the most viable path forward. The literature also implies that an annealing model should only affect the preexponential factor in combustion kinetics, and is ambivalent on the subject of reactivity loss

of O_2 vs. CO_2. Taken together, the literature points toward a model of the same kind implemented by Hurt et al. (1998), with the possible addition of an identical model form (with appropriate parameter values) for CO_2 activity loss. The CBK annealing submodel is an excellent starting point, but lacks a more subtle point found in recent literature. The annealing model as a whole depends on time, peak temperature, and heating rate, with the expectation that precursor differences fall under the purview of an additional submodel, while the actual distribution of activation energies is fixed for all coals and preparation conditions. Both the annealing literature and a basic understanding of coal combustion indicate that this is an oversimplification. The activation energy distribution simply states the relative abundance of various deactivation pathways. The following examples briefly describe why this distribution depends heavily on precursor and preparation conditions:

- In the case of the precursor, coals have widely varying chemical structures, sometimes even when their elemental composition is nearly identical. This variation can be observed not only between different coal seams, but also within the same seam to some degree. A different chemical structure implies a different distribution of annealing pathways.
- In the case of peak temperature, consider a coal with high catalytic ash content. This ash may limit pyrolysis or encourage graphite crystal growth by catalyzing crosslinking or carbon crystal rearrangement, as discussed in the literature review. In such a case, the ash will fuse, eliminating the catalyzed deactivation pathway, if and only if a sufficient peak temperature is attained. A catalyst is defined, in part, by lowering the activation energy of a reaction pathway, so a loss of a catalyst certainly changes the correct form of the distribution of annealing activation energies.

- In the case of heating rate, the importance of initial heating rate on pyrolysis is well established. As the extent of pyrolysis shifts for various heating rates, the chemistry of the newly formed char necessarily adjusts as well. Again, different char chemistry unavoidably leads to a different activation energy distribution.

Since annealing depends on so many variables, the lognormal activation energy employed in CBK and its many successors is intrinsically flawed. This lack of generality was unavoidable given the data available to Hurt et al. (1998), and while relevant data have multiplied, they are far from sufficient to construct a perfect annealing model. However, given the arguments of more recent literature and data, it is perhaps possible to extend the CBK annealing model to include the effects of coal type, heating rate, and peak temperature. Below, Equation 6-1 represents the log-normal distribution of the activation energy, which is divided into i "bins" with i activation energies (i=100 was found to be adequate).

$$N\left(\ln(E_d)\,;\mu_{E_d},\sigma_{E_d}\right) = \frac{1}{\sigma_{E_d}\sqrt{2\pi}}\exp\left[-\frac{\left(\ln(E_d)-\mu_{E_d}\right)^2}{2{\sigma_{E_d}}^2}\right] \qquad 6\text{-}1$$

N_i in Equations 6-2 and 6-3 is the number of active sites with an annealing activation energy equal to the energy associate with bin i; with infinite bins, N_i/N_o (where N_o is the total number of active sites) would integrate to unity, but (as shown in Equation 6-3), this is only approximated with i bins.

$$\frac{N_i(E_{d,i})}{N_0} = \frac{1}{\sigma_{E_d}\sqrt{2\pi}}\exp\left[-\frac{\left(\ln\left(E_{d,i}\right)-\mu_{E_d}\right)^2}{2{\sigma_{E_d}}^2}\right] \qquad 6\text{-}2$$

$$\sum_i \Delta\ln(E_d)\left[\frac{N_i}{N_0}\right]_{initial} = \sim 1 \qquad 6\text{-}3$$

Equation 6-4 is an Arrhenius rate expression where $f_i=N_i/N_o$, the fraction of active sites in bin i.

$$\frac{df_i}{dt} = -A_d \exp\left(-E_{d,i}/\left(RT_p\right)\right) f_i \qquad 6\text{-}4$$

The expression is integrated over a time-temperature profile to arrive at a fraction of remaining reactivity, rather than an actual value for post-annealing reactivity. This is because the initial reactivity and N_o are not obtainable experimentally. In contrast to the CBK annealing model (see Section 2.4.2), the mean and standard deviation of the activation energy used here, along with the preexponential factor (Equations 6-5 through 6-7) become functions of coal type, heating rate (HR), and peak temperature experienced during heat treatment (T_{peak}).

$$\mu_{E_d} = \mathrm{f}(T_p, \text{Precursor}, \text{HR}, \text{reactive gas}) \qquad 6\text{-}5$$

$$\sigma_{E_d} = \mathrm{f}\left(T_p, p_0, \text{HR}, \text{reactive gas}\right) \qquad 6\text{-}6$$

$$A_d = \mathrm{f}\left(T_p, p_0, \text{HR}, \text{reactive gas}\right) \qquad 6\text{-}7$$

In the equations above, p_0 represents a coal-type effect based on chemical structure. While p_0 ranges only between 0 and unity (see Figure 6-1), the majority of coals fall in a range with roughly 30% variation; the model form uses scaled parameters so that the 0-1 range of p_0 is not overwhelmed by the ~1000-2000 K range that influences the T_{peak} parameter.

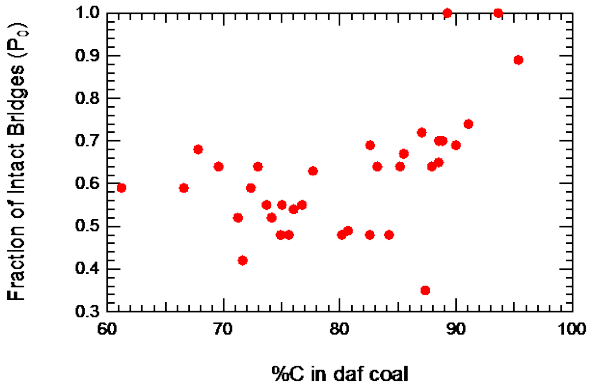

Figure 6-1 – Measured values of p_0 for a variety of coals.

6.3.2 Model Calibration and Optimization

Having arrived at a theoretical dependency for an extended annealing model, finding the functional form relies on a statistical calibration tool, insight from past annealing experiments, a good deal of trial and error, and an optimization routine. The statistical calibration tool is complex, and numerous publications have been devoted to various iterations, applications, and development of the method. This method is explained only in the briefest, most conceptual manner here, with further details available elsewhere (Sacks J., 1989; Welch et al., 1992; Kennedy and O'Hagan, 2001; Gattiker, 2017) as well as in Chapter 4. The calibration can be broken into six steps, as demonstrated in Figure 6-2. The first two steps consist of understanding the physical phenomena in question and coding a relevant model. Step 1 simply involves building a physical intuition that allows the investigator to create a reasonable model and produce well-founded expectations for how the model will behave, and how model parameters are interrelated. Step 2 is often an Edisonian attempt to capture observations in an acceptably simple model, guided by the intuition developed in step 1. The latter four steps require an extended explanation, given in the following four subsections. These steps are experimental design (for a computational experiment), model emulation, model calibration, and model results analysis. Note that Equation 6-8 show a generic model form for Bayesian statistical calibration.

$$y_i = \eta(\mathbf{x_i}, \boldsymbol{\theta}) + \delta(\mathbf{x_i}) + \varepsilon_i \quad 6\text{-}8$$

In Equation 6-8, η is a model that depends on both experimental inputs and model parameters (typically, η is the statistical emulation of the model designed in step 2). Similarly, δ is a function that reflects the discrepancy between model and reality (i.e. it tracks errors introduced by imperfect assumptions), and ε is the noise observed in experimental data.

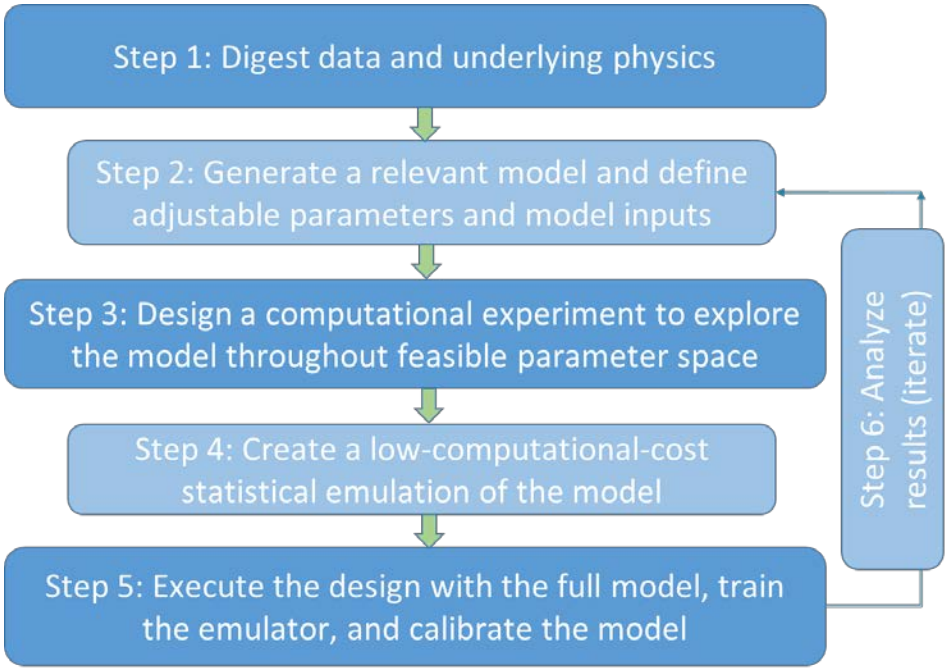

Figure 6-2 – Logic map of the model calibration process

6.3.2.1 Computational Experimental Design

See Section 4.3 and Appendix C.

6.3.2.2 Statistical Model Emulation

The calibration procedure requires exploration of model behavior throughout the allowable ranges of inputs and parameters. This allows the calibration machinery to reject

unsuitable parameter space by assigning a low probability to poorly performing regions of the sampled space. However, numerous executions of the model are required, and most computational models incur a non-trivial computational cost in the case of even moderately high-dimensional parameter spaces. Here, model execution costs may be as low as fractions of a second and still considered non-trivial, depending on available computation resources, so models that require weeks or months are certainly not feasible. This difficulty is circumvented by implementing a statistical emulator, trained by the results of the computational experiment designed in the previous section. An emulator accepts any set of inputs and parameters, and produces outputs that approximate the full model. The emulator result is computed very quickly, and includes an estimate of output uncertainty. The full annealing model was executed with 400 sets of inputs and parameters from the Latin hypercube design discussed above, and the corresponding inputs and outputs were used to train a Gaussian process emulator, as described in detail elsewhere (Sacks J., 1989; Welch et al., 1992; Kennedy and O'Hagan, 2001). In essence, the Gaussian process is a multivariate normal distribution fully defined by a vector of mean values and a covariance matrix. In principle, the values of the mean and covariance are trained to model outputs such that the Gaussian process can predict the model output for any given set of inputs and model parameters. In practice, this may be only partially successful due to poor mathematical behavior in the model. Such problematic cases include, for example, a model where large, irregular shifts in output correspond to small adjustments in the inputs, or due to a poorly explored model parameter space. The emulator is represented in Equation 6-8 as $\eta(\mathbf{x_i},\boldsymbol{\theta})$, while the other two terms (δ and ε) are additional Gaussian processes.

6.3.2.3 Model Calibration

The terms ε_i and $\delta(\mathbf{x_i})$ represent the model discrepancy and experimental error, respectively. The experimental error is a collection term for observational error, variation between experiments, potential experimental bias, etc., and is used to quantify the uncertainty inherent in the experimental data. In annealing experiments, this uncertainty is relatively large. The discrepancy term quantifies the ways in which the model fails to match reality, even after all sources of experimental error are accounted for. It enhances the model calibration process by analyzing the difference between the model predictions and experiment, and describing where the model fails, to what degree, and with respect to which inputs.

This may be illustrated with the well-known model for ballistic motion in Equation 6-9, which is derived by integrating the acceleration due to gravity twice with respect to time.

$$x(t) = \frac{1}{2}gt^2 + c_1 t + c_2 \qquad 6\text{-}9$$

Here c_1 and c_2 are the constants of integration and represent initial velocity and position, respectively. Assuming c_1 and c_2 are both zero, the model reduces to $x(t)=g/2*t^2$, and perfectly captures the position of a falling object in a vacuum. If such a model were to be calibrated, experimental observations will be imprecise, leading to a non-zero ε_i. On the other hand, if the experiments did not take place in a vacuum, the results would become increasingly erroneous as the drag force increases, but is not accounted for. This discrepancy between model and reality would be revealed and attributed to the input, (i.e., time). This is because the lack of drag force induces no error at t=0. Instead the error is observed when velocity is non-zero, and is exacerbated as velocity increases with time. The low dimensionality of this trivial example is amenable to graphical inspection. Simply plotting the data with respect to time would show

model discrepancy. Model discrepancy in the case of the falling object also lends itself well to diagnosis via physical intuition, in that drag force is a daily experience that can easily be conceptualized. In fact, it is counterintuitive that a feather and a bowling ball fall at the same velocity in a vacuum, because daily experience is not a vacuum. Similarly, physical phenomena models beyond the range of direct human experience are often counter intuitive, and thus difficult to visualize and diagnose, especially when they incorporate a high-dimensional parameter space. Such models benefit from a quantified model misfit with respect to parameters and inputs.

6.3.2.4 Calibration Results and Analysis

In the interest of brevity, the details of the statistical analysis are not given. To summarize, the analysis found the CBK annealing model to be overwhelmingly uncertain, which is in fact consistent with the statement by Hurt et al. (1998) in the publication of the original annealing model. The model uncertainty was substantially reduced by applying a greater wealth of data, a better exploration of parameter space, and a coal structural parameter as a dummy input, but considerable uncertainty remained. The dummy parameter had no impact on the model whatsoever, but it did allow the statistical machinery to attach a discrepancy to the input, and indicate the level of functional dependence an annealing model *should* have. The subsequent analysis indicated that the time-temperature profile and the coal structural parameter were by far the largest sources of discrepancy between the model and the data. This was quantified in an internal statistical parameter for the covariance matrix of the discrepancy (δ) term. The covariance parameter necessary to capture the discrepancy due to precursor structure and the time-temperature profile were each about a factor of five greater than discrepancy in other parameters.

The insights from the statistical calibration tools and the observations of the literature review led to a campaign of informed trial and error to uncover the model functional form (step 6 in Figure 6-2); this ultimately reduced the model uncertainty and average prediction error substantially. The extended annealing model is executed precisely as the prior CBK annealing model (see Section 2.4.2), with all changes successfully confined to the annealing activation energy distribution and the annealing preexponential factor. The model was inspired by literature implications for functional dependence on heating rate, T_{peak}, and the precursor chemical structure, but balanced with a need to minimize the total number of parameters that would effectively be relegated to fudge factors in an over-parameterized optimization. Note however, that despite considerable model improvement, annealing is still an umbrella term for numerous processes that include enormous variability. The current model performs well, given the current data, but substantial improvements could be made by both specifying which processes should fall under the auspices of annealing, and conducting sharply focused research on the specified processes.

Equations 6-10 through 6-14 describe the final functional form of the preexponential parameter for annealing (A_d), the mean annealing activation energy (μ_{Ed}), and the standard deviation for the annealing activation energy distribution (σ_{Ed}).

$$if\ HR < 10^4 \qquad A_d = \frac{p0 * A_{d,0}}{\ln(HR + 2.7)} \tag{6-10}$$

$$if\ HR \geq 10^4 \qquad A_d = \frac{p0 * A_{d,0}}{\ln(10^4)} \tag{6-11}$$

$$if\ T_p \leq 1500 \qquad \ln(\mu_{E_d}) = \mathrm{a} * p_0 + \mathrm{b} + T_p * c/1000 \tag{6-12}$$

$$if\ T_p > 1500 \qquad \ln(\mu_{E_d}) = \mathrm{a} * p_0 + b \tag{6-13}$$

$$\ln(\sigma_{E_d}) = \frac{ln(\sigma_0)}{p0} \qquad 6\text{-}14$$

Equations 6-10 and 6-11 express the heating rate dependence on the original number of active sites. Cai et al. (1996) found that higher heating rates increased the reactivity of a char considerably with all other preparations conditions held constant. The natural log of the heating rate captured the reactivity increase well up to about 10^4 K/s, after which a plateau was reached for all coals tested. The increase in activity is speculatively attributed to an increase in micropores during increasingly rapid devolatilization. This implies that the annealing model is perhaps not the ideal submodel to include this information, but in general, comprehensive char combustion codes do not include a submodel to address preparation condition-based pore development. Therefore, the umbrella of annealing with built-in preparation condition dependence is the most appropriate submodel available. Any model employing an estimate of porosity based on heating rate would be well served to eliminate the heating rate dependence of the annealing preexponential factor. Note that the heating rate dependence is located in the denominator because A_d describes how rapidly annealing proceeds. If the surface area increases by some factor "F", the number of active sites is expected to increase by the same factor "F" (assuming uniform active site density). This is captured in the annealing submodel by reducing the rate of site destruction by "F," where F=ln(HR+2.7) (note that F reduces to ~1 at very low heating rates). This is not mathematically identical to increasing the number of sites by "F," but the number of active sites was normalized to unity as is appropriate for a lognormal probability density function, and it is undesirable to disrupt the normalization. Since the annealing model is far from mathematically perfect in any case, it was deemed conceptually adequate to adjust the preexponential factor to decrease the rate of reactivity loss instead. Finally, the structural parameter p_0 is included, where p_0 specifies the fraction of intact bridges in the coal pseudo-

monomer. The intact bridge fraction is experimentally found via NMR, or derived from a correlation via the proximate and ultimate analysis as described by Genetti et al. (Genetti, 1999; Genetti et al., 1999). There are four NMR parameters commonly used to describe coal structure, all of which appear strongly correlated with each other and were found equally suitable for a coal structural parameter. The NMR parameter p_0 was chosen to represent coal structure after only moderate success with the simple ratio of carbon to hydrogen from the ultimate analyses. The C/H ratio does not distinguish between radically different coal structures with a similar elemental composition. The NMR structural parameter approach has been successfully employed elsewhere (Shurtz et al., 2011; Holland and Fletcher, 2017).

Equations 6-12 and 6-13 are a straightforward linear model to predict the mean (μ_{E_d}) of the log-normal activation energy distribution, given coal structure and peak temperature, with the addition of some constant, "b." The only subtlety is that the peak temperature dependence may be profitably turned off at peak temperatures above 1500 K, where the literature observed many T_{peak} effects were no longer relevant. In fact, a series of models that employed the T_{peak} term *above* 1500 K (and turned off "c" *below* 1500 K) found that the optimal value of "c" was driven towards zero (i.e., T_{peak} is not an important parameter input for the mean activation energy above 1500 K). Equation 6-14 predicts the standard deviation of the distribution, and, together with Equations 6-12 and 6-13, fully defines the log-normal activation energy distribution. The model standard deviation was found to be relatively constant with respect to T_{peak} and heating rate, with a direct dependence on char precursor. The functional dependence of σ_{EA} on precursor only is reasonable as a given coal should have some distribution of activation energies, but T_{peak} and HR likely shift the center of that distribution more than they adjust the range. Once μ_{Ed} and σ_{Ed} are defined, the log-normal distribution is known. After the log normal distribution is defined, it is

split into a bimodal distribution in accordance with numerous observations of two distinct annealing regimes in the literature (see Chapter 2). This is done by the factors B_f and B_r, which are both optimized values, so the actual location of the bimodal trough is also determined by optimization. The factors B_f and B_r split the log normal distribution by isolating the activation energies in the range $\mu_{Ed} - B_f < \mu_{Ed} < B_f + \mu_{Ed}$. The density of active sites within that range is divided by B_r. In other words, B_f indicates the breadth of a trough in the bimodal distribution (centered on the mean), and B_r determines the depth of the trough. The formerly log-normal distribution is then renormalized, which maintains the total number of initial active sites, but allows for a bimodal distribution with an optimized weight between the two regimes.[7]

Figure 6-3 below is a sample log normal distribution that shows the fraction of active sites in any given bin. The exact mean and variance of the distribution depends on heating rate, precursor NMR parameters, and peak temperature. Figure 6-4 shows an irregular, bimodal distribution after parameters B_r and B_f are applied and the distribution is renormalized. The second figure has two striking features. First, the majority of the low activation energy sites vanish. This is not a problem in either of the two distributions, because the original log normal distribution resulted in a highly exaggerated rate of initial annealing, which was compensated for by using an excessively high initial preexponential value, as discussed in the literature review. The reduced initial annealing of the second figure dispenses with the need for an excessive initial preexponential factor. The second notable feature is that the second peak of the distribution is highly irregular. This indicates that, after the very rapid initial annealing, the remaining activated

[7] The bimodal distribution factors B_f and B_r are mathematically applied as shown in the script "match_reactivity." They are referred to as t_f and t_r respectively.

annealing processes have a large number of active sites at a high activation energy, so the remaining annealing processes will be relatively gradual.

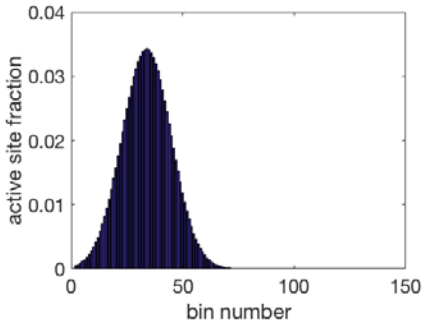

Figure 6-3 – Sample log normal distribution of the fraction of active sites in any given bin.

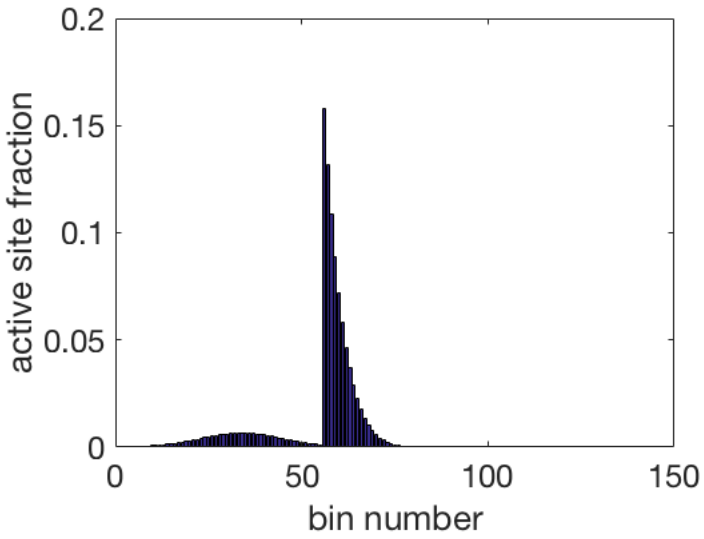

Figure 6-4 – Sample "bimodal" distribution after applying the parameters B_r and B_f and renormalizing the distribution.

6.3.3 Model Optimization

Once a reasonable model form was developed, the model parameters were optimized. The optimization routine was coded using fmincon in MATLAB, which traversed the bounded parameter space of the model in an attempt to minimize an objective function. Thus, the annealing data are not fit via a standard linear regression. In fact, the model parameters cannot be directly regressed because even the conceptual form of the model is far from linear in its

parameters, and even if the model could be linearized, such a mathematical transform would render a regression statistically invalid. Instead, the optimization routine finds a narrow subsection of parameter space containing numerous local minima, many of which lead to approximately the same model output. Any vector of parameter spaces that leads to a reasonable local minimum is valid, and finding the absolute minimum in a high dimensional, non-linear parameter space is essentially impossible. Instead, the optimization is carried out by implementing various parameter bounds and constraints, and initializing the optimization from different locations in parameter space. Each optimization required roughly 12 hours on a standard work station, and after dozens of optimizations approximately 1/3 failed (settled on a local minimum that was clearly far from the global minimum) and 2/3 succeeded (located local minima that were all roughly equal, and presumed to be near the global minimum). Table 6-4 gives the values of the annealing model parameters used in the results section. The optimization routine yields a single local minimum. Here, the routine was executed numerous times with different initial values in the parameter space, and in about half of all cases a local minimum in the objective function was found within 5 % of the objective function value produced by the parameters in Table 6-4. In almost all other cases, the objective value was within 50 % of the superior local minima, and there were a handful of optimization failures. The particular values in Table 6-4 were chosen because they were the lowest found, but in this model there are numerous essentially equivalent local minima, and an infinite number of surrounding points that are equivalent for any practical purpose. Note that the parameters a and b are on similar scales, while c (relating to the influence of peak particle temperature) is roughly and order of magnitude smaller. Since the temperature and NMR parameters were scaled to be similar, this indicates the

relatively low impact of peak particle temperature, which is expected, since most the available data are at relatively high temperature.

Table 6-4 – Annealing model parameter values.

Parameter	Value	Units
$A_{d,0}$	$9.71x10^{11}$	s^{-1}
B_f	45.55	kcal/mol
B_r	176.66	-
a	0.46	ln(kcal/mol)
b	1.77	ln(kcal/mol)
c	$7.32x10^{-2}$	ln(kcal/mol)/K
$\ln(\sigma_o)$	0.65	ln(kcal/mol)

6.4 Model Execution Results and Discussion

The final annealing model predicts the relative reactivity of a char compared to some reference char, as discussed previously. This is because reactivity is measured directly, but the number of active sites (either initial or final) cannot be measured. Instead, by taking the ratio of reactivity in two annealed chars in a zone 1 combustion regime, the ratio of final active sites can be determined. Therefore, each set of annealing data has a single char designated as a reference, and the data points are the ratio of the reactivity between each char and the designated reference char. The annealing model is considered to be performing well when the measured relative reactivity is close to the predicted relative reactivity. Because the model parameters were optimized, an objective function was required to quantify "close." Because the annealing data covered a very wide range of coals and conditions, the quantitative objective function was difficult to write, and the results cannot be conveniently displayed. Simply plotting the measured and predicted reactivities on the ordinate axis (with an index on the abscissa) resulted in an unreadable mess due to the variation in scale between experiments. Ultimately, it was decided that several measures of model success should be included. A log-scale parity plot is shown in

Figure 6-5, partially to show all of the O_2 data in one compact location, and partially because the original CBK annealing model results were displayed on a log parity plot. A linear parity plot has the dual difficulties of requiring a very large axis to display the outlier points from the Hurt model, while simultaneously compressing the majority of the points into a tight region not amenable to visual inspection. The log-scale plot on the other hand, can be quite misleading and give the impression that the extended annealing model developed in the present work is only a minor improvement over the prior model. Note that, in accordance with the discussion in the model development section, the **relative** reactivity is used in Figure 6-5 because the actual degree of activity loss can only be observed as a ratio between two chars that received different heat treatments. Thus, every data set includes a reference char with a measured reactivity, and the ratio of reactivities between the reference char and any other char in the data set is the (unitless) relative reactivity.

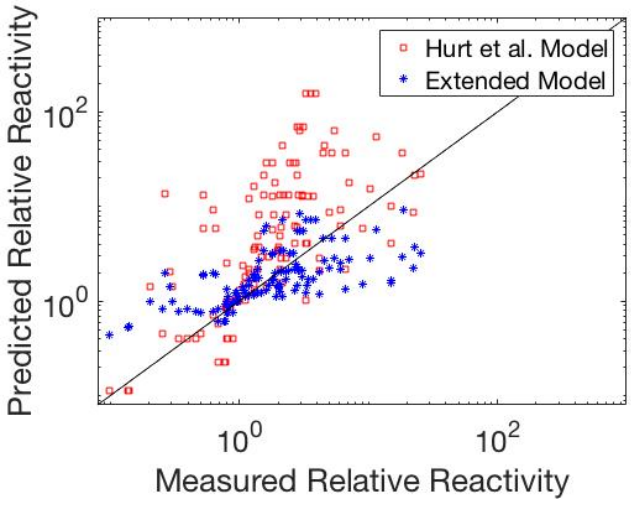

Figure 6-5 – Parity plot of measured and predicted relative reactivities in O_2 for two models.

In contrast, Table 6-5 includes the results of the sum-squared error as an equally misleading measure. Superficially, the sum squared error indicates that the extended model is ~2 orders of

magnitude superior to the prior model, but in reality a relatively small handful of points result in enormous error. The best measure of model success, both for an optimization objective function and for reasonable model comparison, is referred to in Table 6-5 as the error factor (which is a quantity defined and described in detail in the experimental section). Table 6-5 includes the mean and range of the error factor for entire body of data as well as several subsets. This breakdown shows that the extended model is certainly an improvement, but the improvement is closer to a factor of four than a factor of 100. Additionally, the quartile breakdown shows that the extended model performs well across the board with only a small handful of egregious failures, while the CBK annealing model has numerous large errors in all but the best performing quartile. Note that, while it would be desirable to compare the original CBK annealing model directly to the extended annealing model, the extended annealing model requires more detailed information that was not available in the referenced literature for the Hurt model, so direct comparison is impossible.

Table 6-5 – Measures of model success.

	Hurt et al. Model			**Extended Model**		
Model Quantification	**Mean**	**Minimum**	**Maximum**	**Mean**	**Minimum**	**Maximum**
Sum Squared Error	$1.45 \times 10^{5*}$	N/A	N/A	2.43×10^{3}*	N/A	N/A
Error Factor: All Points	**6.08**	**1.00**	**51.97**	**2.24**	**1.00**	**9.96**
Error Factor: Least Successful Quartile	17.28	7.00	51.97	4.44	2.30	9.96
Error Factor: Most Successful quartile	1.13	1.00	1.25	1.10	1.00	1.20
Error Factor: Central Quartiles	2.78	1.25	6.50	1.63	1.21	2.27

* This is a scalar value, not a mean.

On average, the extended annealing model predictions differ by a factor of about 2.24 from measured values. An average error of 124% is far from an optimal model, but in comparison to past work (with an average error of 508%), it is a significant improvement (a factor of ~4). It is worth noting that carbon sources are notorious for enormous variability in their respective reactivities. In fact, it seems likely that the umbrella of effects referred to as annealing are responsible for such a large range of reactivities. There are insufficient replicates in the data for a detailed statistical analyses of variance within individual data sets, but a brief examination of the few replicates or pseudo-replicate data points is enlightening. Among these data (Senneca et al., 1998; Senneca and Cortese, 2014), the variation between replicates ranges from roughly 20-50%. Thus, 124% error is not at all unreasonable, and is in fact a substantial stride towards mitigating the vast uncertainty of coal combustion rate modeling, perhaps even to the extent that a coal-general kinetic correlation is feasible if derived in conjunction with a comprehensive char conversion model.

6.4.1 Model Predictivity

The present annealing model was developed with a minimal number of adjustable parameters specifically to avoid a large number of "fudge factors" that would fit virtually any data set while having very low predictive power. However, a model with few parameters is no guarantee of predictive power. As observed above, the annealing model employed in CBK and its successors often predicted annealing quite far from experimental data, probably because the model was calibrated using relatively few data points from a narrow selection of precursors and preparation conditions. Given that a substantial amount of uncertainty remains in the current annealing model, it was entirely possible that the new model would suffer from a similar handicap. Therefore, several data points were initially excluded from the optimization objective

function to test the model predictivity. In general, the model predicted the new points with remarkable success, and when the model parameters were re-optimized with all data points, the new data had a minimal impact on the overall model calibration. One such data set is shown below in Figure 6-6 (data collected by Jayaraman et al. (2015) for a high-ash Indian coal). The ordinate axis is the relative reactivity NOT the error factor. The error factor (calculated as described above) in this case ranged from 1.00-1.12, with a mean of 1.08. In general, any ratio less than ~2 is considered quite good in the context of reactivity loss. The abscissa is potentially misleading in that up to six input variables influence each data point (the heating rate, treatment time, and peak temperature for the char particle, and the same three variables for the reference char). However, the peak temperature of the char particle is most likely to both change and have a dramatic impact between points, so it was deemed the best variable for the abscissa in the absence of six-dimensional plotting software. Nevertheless, the apparent replicates are not actually identical data points.

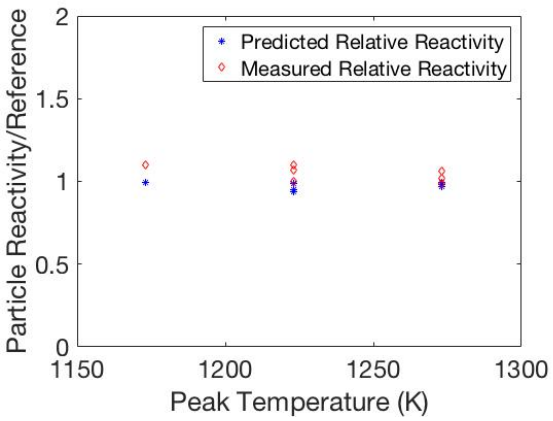

Figure 6-6 – Model predictions compared to experimental measurements of an Indian coal (data were not used to calibrated model).

At first glance, Figure 6-6 can be misleading. It is natural to intuitively view the annealing values close to unity as uninformative. However, an annealing value near unity does

NOT indicate a lack of annealing. Instead, it indicates that the annealing of the data point and the annealing of the reference char were very similar. Figure 6-6 is therefore an exceptional example of model success in that it tracks annealing quite well even at conditions or treatment times that are very similar. The predictions and data are not identical, and the predictions have a slight but consistent negative bias, which indicates that the annealing model is not exact, but it is correctly responding to subtle changes in heat treatment.

Additional comparisons of predictions and measured data (and associated error factors) are shown in Figure 6-7 and Table 6-6. In all cases, the ordinate access is the relative reactivity NOT the error factor. The error factor mean and range are reported in Table 6-6. Panels (a) and (b) both show data from experiments with Pittsburgh 8 coal, but from two different investigators. Panels (c) through (f) show a variety of other coals over the range of experimental data. In general, the model predictions are quite good, with obvious outliers at the lowest heat treatment temperatures. The poor predictions at low temperature are much worse than the average predictions, and while they are undesirable, they are not unexpected. The raw coal precursors are quite diverse, and low heat treatment temperatures do not allow the chars to progress as far towards the thermodynamic minimum of a perfect graphite crystal. Also, low-temperature heat treatments likely do not fuse the ash. The chemical identity of the ash is rarely characterized, so it is not reflected in the annealing model. This creates additional model uncertainty for low-temperature char preparation because ash has fusion-dependent chemical and physical effects on the coal. More importantly, the low-temperature heat-treatment implies a drastically different devolatilization process, which significantly alters the chemistry of the char. Ultimately, the low-temperature predictions are of far less practical importance, and are not cause for significant concern in practical char conversion models.

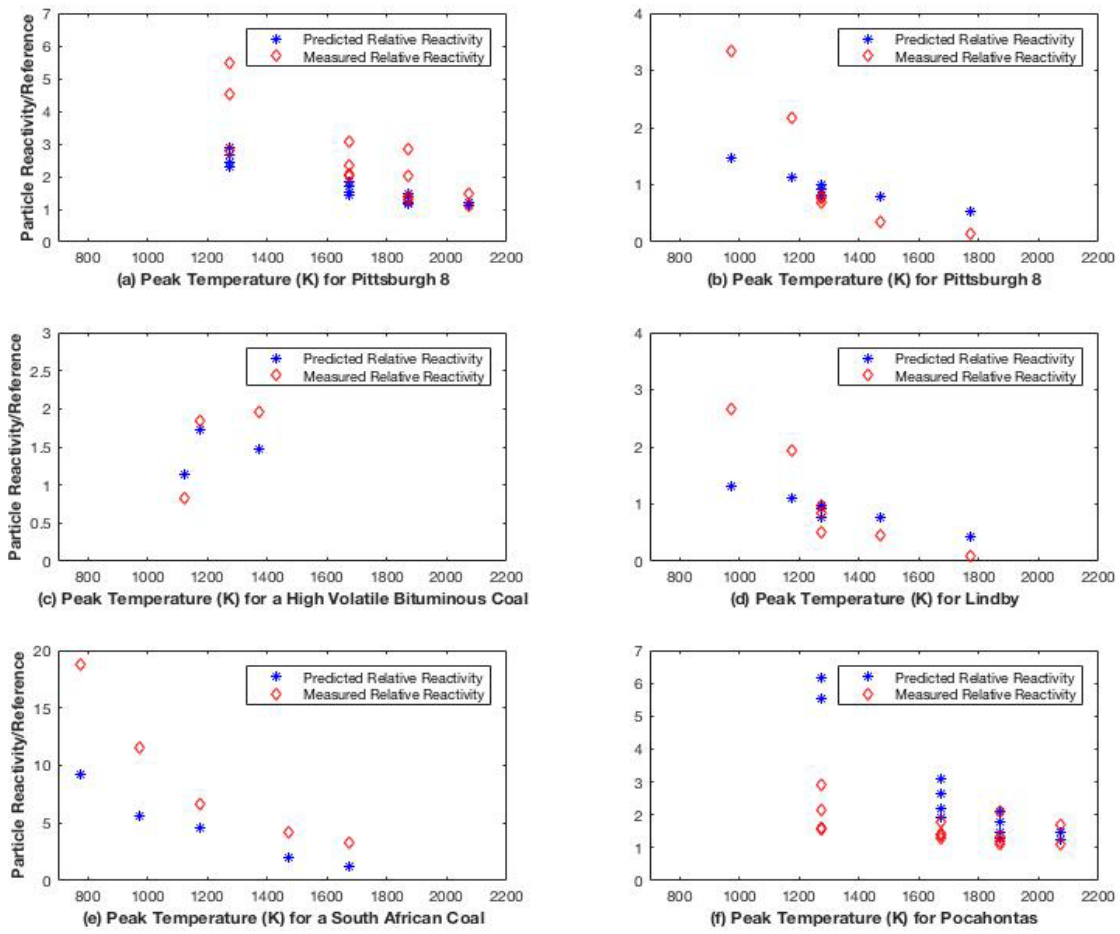

Figure 6-7 – Predicted and measured changes in reactivity due to annealing for diverse coals.

Table 6-6 – Error factors associated with a diverse selection of coals.

Coal	Min Error Factor	Max Error	Mean Error
Pittsburgh 8 (Russell et al., 2000)	1.01	1.92	1.41
Pittsburgh 8 (Cai et al., 1996)	1.20	3.84	2.00
HVB (Naredi and Pisupati, 2008)	1.06	1.37	1.26
Lindby (Cai et al., 1996)	1.01	4.50	1.92
South African (Bar-Ziv et al., 2000)	1.44	2.73	2.06
Pocahontas (Russell et al., 2000)	1.00	3.84	1.95

6.4.2 Model Failure

Despite the general success of the model in fitting data (and predicting data it had not yet been calibrated to), there were a number of model failures (5.1%), defined as model predictions

greater than a factor of five from the experimental data. Among these failures, all but a single point of data had several things in common. First, all of the data points in question came from two authors (Gale, 1994; Shim and Hurt, 2000), and both of these authors formed their char in an entrained flow reactor. The data sets from both authors appeared to have a very high variance, in that supposedly similar experiments led to widely different results without a definite trend; however, the actual variance cannot be computed, as replicates are not given. Third, both sets of experiments sampled data on a short time scale, and fourth, both authors obtained a number of points that agreed remarkably well with model predictions, both before and after the questionable data was included in the optimization routine. Finally, both data sets included coals that were used by other authors in annealing experiments, with vastly different results.

It is possible that the annealing model is simply unable to predict flat flame burner chars. However, given that many of the chars in the same data sets were predicted very accurately, it seems far more likely that the short time scale and sampling limitations in an entrained flow reactor led to noisy data. A sample of the worst model failures and adjacent successes to supposedly similar experiments is given in Figure 6-8 (data from Shim and Hurt (2000)).

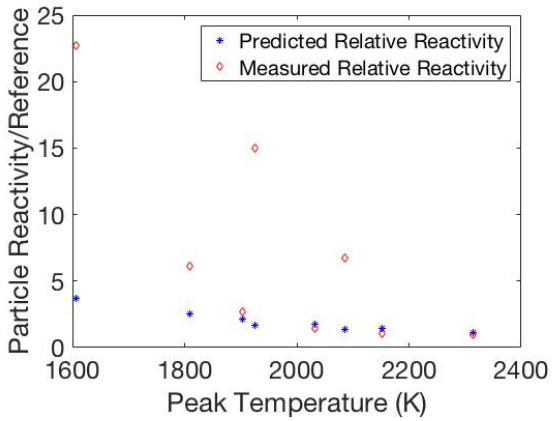

Figure 6-8 – Model predictions of the Shim and Hurt data set, both failures and exceptional successes.

6.4.3 Sample Model Predictions

While the extended annealing model was broadly successful in reducing the variability of char reactivity due to preparation and combustion conditions, there was one large data set that consistently failed. The failure was not large in terms of error factor, as with the handful of anomalous, erratic points. Instead, it was a consistent failure to track a subtle trend in char reactivity with treatment time in a Chilean coal (Feng et al., 2003b). Figure 6-9 shows that the model does reasonably well predicting the degree of annealing in an absolute sense, but an additional dimension of treatment time shows that the model remains essentially constant with the very small changes in treatment time. This was ultimately determined to be the reason that the statistical calibration tool found substantial model discrepancy with treatment time. Physically, it is caused by the approximation of the initial heating time-temperature profile. Because detailed data are not available to reasonably estimate the time-temperature profile, the initial heating rate is used as a crude substitute. In general, the estimate is sufficient, but when the heating time is a significant portion of the total annealing time, the error can become noticeable. This error was further verified by attempts to fit only the data in Figure 6-9 without any other experimental data, but the results were not improved, even when several different model functional forms were attempted. Also, when the data were excluded from the objective function, the annealing model predictions did not change notably (and still gave the reasonable predictions seen below). Conversely, when the data of Figure 6-9 were included with all other data, model predictions were also not significantly influenced; the extended annealing model simply cannot fit the subtle trend of a data set with very short treatment times in the absence of a more accurate heating profile.

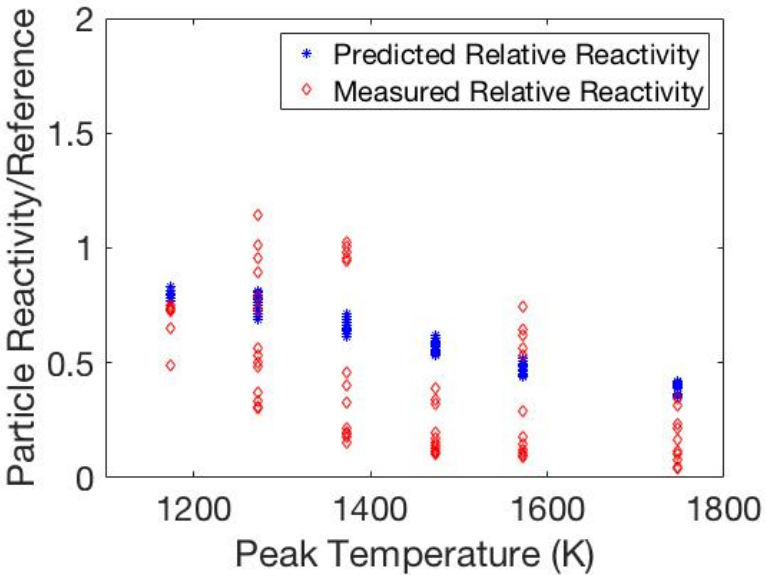

Figure 6-9 – Model predictions and experimental data for Cerrejon coal.

6.4.4 CO_2 Model Development and Results

The literature implied that activity loss to CO_2 gasification potentially proceeds along different kinetic pathways than O_2 annealing. By extension, steam reactivity reduction may also behave differently than combustion annealing. In general, CO_2 and steam may be neglected as reactants in pulverized coal combustion, but the extended annealing model is intended to function in an oxy-fuel setting as well, where CO_2 and H_2O may have appreciable influence on the combustion process. Therefore, it seemed prudent to tabulate CO_2 annealing data and attempt a similar calibration for an alternative annealing model form, or at least determine alternative parameter values if the same functional form turned out to be adequate. However, as a matter of curiosity, the O_2 calibrated annealing model was applied directly to the CO_2 and steam data, and in general performed astonishingly well considering the lack of calibration. It must be noted that there was relatively little CO_2 data available, and that one large set of data fit extremely well, forcing the mean error factor down. However, the results in Table 6-7, Figure 6-10, and Figure 6-11 clearly show that, within the limits of available data, the model is able to predict CO_2 and

H_2O annealing adequately even with the parameters calibrated to O_2 annealing. Figure 6-10 contains data for a South African Coal, which was also used in several of the O_2 data sets, although the CO_2 experiments were from a different lead author and institution (Bar-Ziv et al., 2000). This may well have improved the uncalibrated model prediction in the case of South African coal, but the uncalibrated model was also successful with other coals in the CO_2 environment. If the O_2 experiments allowed for successful CO_2 model inference, that strongly supports using the same annealing model form and parameters for both O_2 and CO_2 activity loss. Recall that Figure 6-10 shows the model predictions, not the error factor, so the model is actually performing even better than the plot implies. Figure 6-11 represents the sole H_2O data set available (Jayaraman et al., 2015). The small sample size limits inference, but the model appears to perform exceptionally well. In the absence of addition annealing data for char reactivity to steam, it seems reasonable to assume that H_2O active sites are lost at a similar rate and comparable processes as the active sites for both O_2 and CO_2.

Table 6-7 – Uncalibrated CO_2 and H_2O extended model annealing predictions.

Model Quantification	Mean	Minimum	Maximum
Sum Squared Error	268*	N/A	N/A
Error Factor: All Points	1.66	1.00	4.96
Error Factor: Least Successful Quartile	2.84	2.05	4.96
Error Factor: Most Successful quartile	1.04	1.00	1.08
Error Factor: Central Quartiles	1.37	1.09	2.02

* This is a scalar value, not a mean.

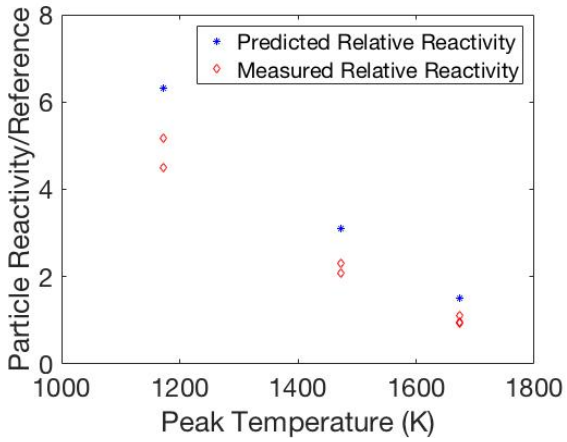

Figure 6-10 – CO_2 Annealing data and uncalibrated predictions for a South African coal.

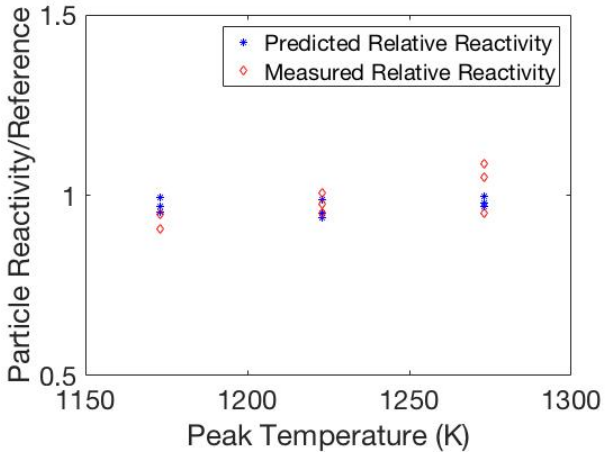

Figure 6-11 – H_2O Annealing data and uncalibrated model predictions for an Indian Coal.

6.4.5 Model Implications

As has been noted in Chapter 2, the literature indicates that the vast bulk of annealing occurs very rapidly, followed by a much more moderate loss of reactivity due to heat-treatment. The model has been designed to reflect this trend, which is thought to be due to initial, dramatic annealing during pyrolysis, and a lesser degree of annealing during subsequent heat-treatment. The annealing model therefore offers flexibility (when employed in a comprehensive coal conversion model) to allow char combustion predictions over a broad array of combustion conditions. However, no effective, coal-general kinetic correlation exists, so data are generally

required to tune a rate constant. If data are available to tune kinetic constants, the initial annealing effects are embedded in the data, while the subsequent annealing effects may or may not be negligible, depending on coal type and combustion conditions. Thus the annealing model may be circumvented entirely in certain conditions, but is of considerable utility in comprehensive coal conversion models. In particular, the model shown here has been successfully employed in just such a comprehensive model to explain data over a broad range of conditions (Holland and Fletcher, 2017).

Perhaps even more importantly, the literature data used in this work clearly show several orders of magnitude in char reactivity change due to char preparation condition, and both the data and the model show trends (at high T_{peak}) of converging char reactivities for diverse precursors. The historical failure of coal-general kinetic correlations has depended in large part upon many orders of magnitude of variation in the body of literature data between char reactivities, while no pattern between proximate and ultimate analysis and char reactivity is readily discernible. The enormous impact of preparation condition on char reactivity (and the great inconsistency in char preparation methods in the literature) certainly account for a portion of char reactivity variability. It is possible that preparation conditions even accounts for the bulk of observed variability, at least at practical (high T_{peak}) combustion conditions. If so, the present annealing model could potentially account for the preparation condition variability, and allow for a coal-general kinetic correlation based on structural parameters or the proximate/ultimate analysis.

6.5 Summary and Conclusions

A thermal annealing model functional form was developed based on observations supported by multiple authors, experimental methods, and detection systems. Qualitatively, coal char annealing is found to depend heavily on the time-temperature profile, the initial particle heating rate, the peak particle temperature, and the parent coal chemical structure as indicated by the NMR parameters. Trends in functional form dependence were quantified by optimizing a number of model forms for the annealing activation energy distribution to fit a broad array of literature data. The resulting model was shown to be a significant improvement; average error decreased to roughly a factor of two rather than a factor of five as compared to the preceding annealing model. The improvement is largely due to a model form that accounts for coal chemical structure, heating rate, and T_{peak}, as well as a much larger data set. Note that both the predicted degree of annealing, and the annealing activation energy distribution depend heavily on heating rate, T_{peak}, and chemical structure. Model functional dependency on HR and T_{peak} were previously included implicitly in the model form, which integrated a reaction rate at a specific temperature for a relevant increment of time. However, a more realistic model must incorporate explicit dependence of the annealing activation energy distribution on HR, T_{peak}, and chemical structure. For example, ash fusion occurs solely as an effect of T_{peak}. Ash fusion in turn affects several annealing and char conversion pathways, such as catalyzing carbon crystallite rearrangement. If the ash fuses, a catalytic annealing pathway is eliminated, and the distribution of activation energies should shift accordingly. Similar arguments can be made for other annealing effects such as devolatilization, coal morphology, and coal precursor.

The annealing model was trained by a selection of 25 different data sets and 167 data points. Some data sets were initially excluded to test model predictivity; the model was found to

predict the excluded data approximately as well as the training data. The model shows rapid decreases in char reactivity during heat-up and devolatilization before significant char oxidation occurs. The model generally matches the decrease in reactivity best at temperatures above 1200 K (and especially above 1800 K), which was expected. The dependence on coal type was modeled using a chemical structure parameter measured by solid-state NMR spectroscopy.

While the average error factor was greatly reduced, much of the remaining error is due to a relatively few outliers with data at low values of T_{peak}. The weaker model results at low temperature are thought to be due to both greater diversity and poorer char characterization (i.e., annealing is far from complete, and the chars may have unfused ash, catalytic effects, residual volatiles, greater crosslinking etc.). Bearing in mind the disproportionate error in low-temperature experiments, and given that practical combustion occurs are temperatures in the range of ~2000-2300 K, the annealing model presented here works especially well in practical circumstances.

It was shown that annealing data relevant to CO_2 gasification is predicted at an acceptable level by the annealing model trained from O_2 oxidation reactivity data. This result is somewhat surprising as the limited literature data imply that O_2, CO_2, and H_2O active sites may all be different (Liu and Niksa, 2004). However, because current knowledge of coal reaction pathways is woefully incomplete, this result is certainly not impossible. The single set of available H_2O gasification data (with sufficient experimental detail for this model), is also predicted quite well by the annealing model trained to O_2 oxidation data.

Despite model improvements, there is still considerable work that could be done to improve the annealing model. Such work includes data for an even broader array of coals, data collected over a large range of temperatures and heating rates with very short treatment times,

and data that allow more detailed predictions of the initial time-temperature profile (prior to a fixed temperature soak time). There are also numerous other questions of interest that may prove more difficult to address. These questions include disentangling the coal swelling models and pore development from thermal annealing, a broader study of char ash content on thermal annealing (examining both ash quantity and chemical identity), and further investigation into early and late burnout effects. Late burnout effects are not related to annealing, but tend to obscure char reactivity (for example pore networks that are initially blocked during the metaplast phase, but quickly become available surface area at a low level of char conversion).

Finally, it should be emphasized that this annealing model, like most prior literature models, impacts only the conversion rate law preexponential factor by decreasing the number of active sites available. It was implemented directly in a comprehensive coal char conversion model with the parameters derived in this work (with a remarkable level of success) (Holland and Fletcher, 2017). However, the comprehensive model typically requires that key kinetic parameters be fit to data, since it lacks an effective coal-general reactivity correlation. This is a ubiquitous weakness in char conversion models, but it should be noted that the annealing model will impact the preexponential factor, so optimization or regression of kinetic coefficients for any char conversion model should take place *after* implementing the char annealing model.

7 FULL CCK MODEL DEVELOPMENT[8]

7.1 Introduction

This chapter outlines the development of the Carbon Conversion Kinetics Oxy-coal model (CCK/oxy). The model is intended to support computational fluid dynamics (CFD) modeling of oxy-coal boilers either for the retrofit of existing boilers or the construction of new oxy-coal fired power plants by providing a detailed code that can predict the temperature and burnout profiles of coal particles in a hot, oxidative environment. The detailed model could also be used to train low computational cost, reduced-order models to accurately describe a specific scenario. In the following sections, the model is conceptually and mathematically developed from a series of literature sources and original work, followed by a brief overview of available data applicable to the oxy-coal scenario.

7.1.1 Model Summary

The CCK/oxy model is motivated by the inability of past comprehensive models to fit data taken in oxy-fuel conditions. This failure has been observed in previous work by Holland and Fletcher (2016) (see Chapter 4) and by McConnel and Sutherland (2016). While the model development of this section was guided by a sensitivity analysis of the Carbon Conversion Kinetics (CCK) model (see Chapter 5), that sensitivity analysis strongly implied that the most

[8] This chapter was modified from published work: Holland, T. and T. H. Fletcher, "Comprehensive Model of Single Particle Pulverized Coal Combustion Extended to Oxy-Coal Conditions," *Energy & Fuels,* **31**, 2722-2739 (2017).

influential model parameters were the same parameter subset in all cases, almost entirely independent of combustion conditions or coal type. Therefore, the most sensitive parameters in the CCK model are expected to retain their sensitivity in the CCK/oxy extension under a wide variety of conditions. Though the sensitivity analysis used approximately half of the same data cited in the experimental section, the sensitivity analysis only indicated which submodels were most influential. In this chapter, those models are updated based solely on recent research and literature observations, including the annealing model discussed in Chapter 6, and completely independent of the char burnout data. Thus, this model was constructed to more precisely capture the physics of char burnout and not merely to fit the selected data set. The char burnout data influenced the model only in the final stage of kinetic parameter calibration. A list of sensitive parameters is given in Chapter 5. Figure 7-1 is a logic map of CCK/oxy execution, while Table 7-1 shows the main equations of the model. The model is currently configured for an entrained flow reactor (specifically the flat flame burner referenced in Section 2), so minor modifications may be necessary for other reactor types. It is also worth noting that this model does not consider a reactive boundary layer, but instead incorporates a single-film model. In the single-film model, the reactive gases are allowed to diffuse entirely from the boundary layer without gas phase reaction (i.e., there is a transport boundary layer, but not a reactive boundary layer). The single film model compared more favorably than a double-film model (a reactive boundary layer model with an infinitely thin flame sheet between two non-reactive films) when compared to a fully resolved reactive boundary layer code that was thoroughly investigated elsewhere (Hecht et al., 2012).

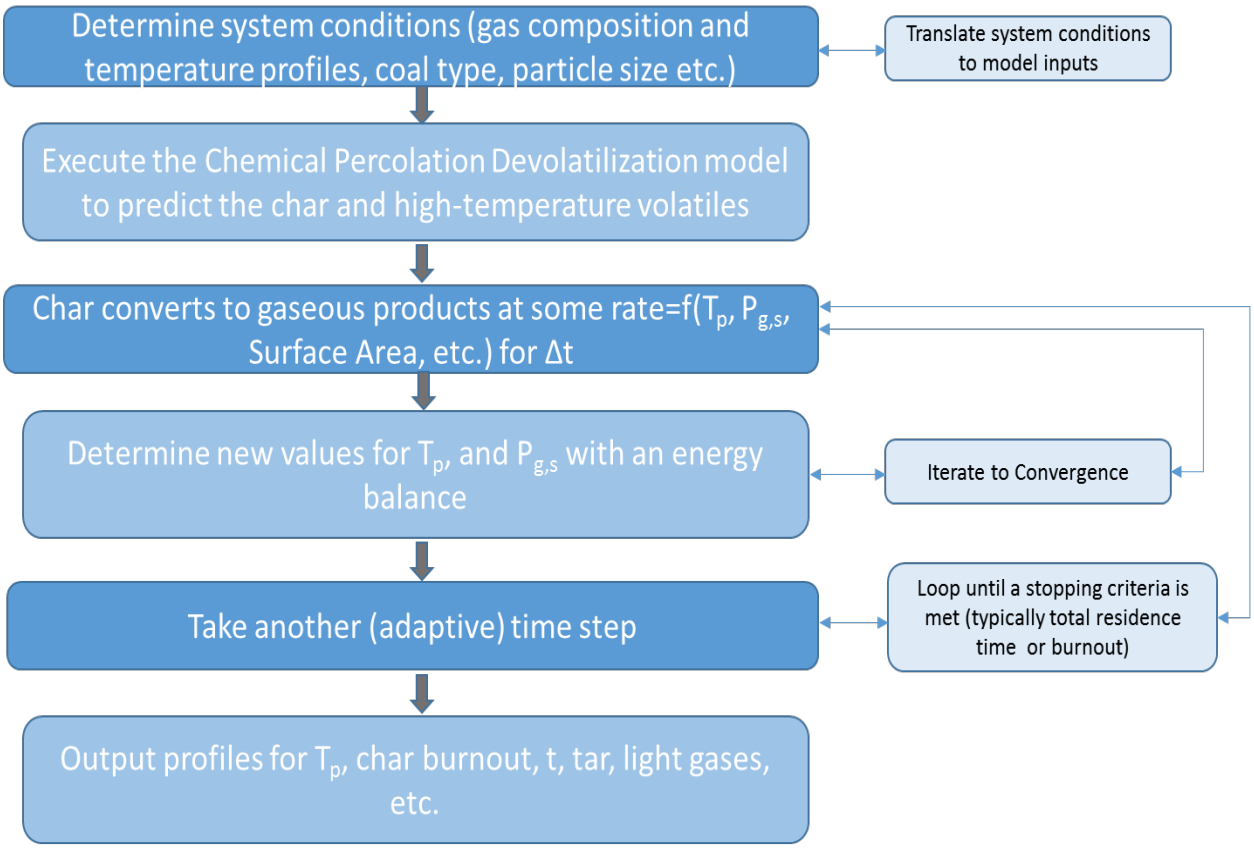

Figure 7-1 – Logic Map of CCK/Oxy Execution.

Table 7-1 – CCK/oxy Submodels.

Sub-Model Name	**Model Form**
Particle Energy Balance[9]	$m_p C_p \frac{dT_p}{dt} = hA_p(T_g - T_p) + \sigma\varepsilon_p A_p(T_s^4 - T_p^4) + \sum_i r_{p,i}\Delta H_{rxn,i}$ 7-1
Surface Reactions (Shurtz and Fletcher, 2013)	$2C + O_2 \rightarrow C(O)_\alpha + CO$ (R1) $C + O_2 + C(O)_\alpha \rightarrow C(O)_\alpha + CO_2$ (R2) $C(O)_\alpha \rightarrow CO$ (R3) $CO_2 + C \leftrightarrow C(O)_\beta + CO$ (R4) $C(O)_\beta \rightarrow CO$ (R5) $C + H_2O \leftrightarrow C(O)_\gamma + H_2$ (R6) $C(O)_\gamma \rightarrow CO$ (R7) $C + 2H_2 \rightarrow CH_4$ (R8)

[9] All of the heat of reaction is applied to the char particle, and Eq. 13 dictates the ratio of CO to CO_2

Table 7-1 Continued

Sub-Model Name	Model Form
Langmuir-Hinshelwood-type Reactions (Shurtz and Fletcher, 2013)	$R_{C-O_2} = \frac{k_1 k_2 P_{O_2}^2 + k_1 k_3 P_{O_2}}{k_1 P_{O_2} + \frac{k_3}{2}}$ 7-2 $R_{C-CO_2} = \frac{k_4 P_{CO_2}}{1 + \frac{k_4}{k_5} P_{CO_2} + \frac{k_{4r}}{k_5} P_{CO} + \frac{k_6}{k_7} P_{H_2O} + \frac{k_{6r}}{k_7} P_{H_2}}$ 7-3 $R_{C-H_2O} = \frac{k_8 P_{H_2O}}{1 + \frac{k_4}{k_5} P_{CO_2} + \frac{k_{4r}}{k_5} P_{CO} + \frac{k_6}{k_7} P_{H_2O} + \frac{k_{6r}}{k_7} P_{H_2}}$ 7-4
Thermal Annealing (Hurt et al., 1998)[10]	$\frac{df_i}{dt} = -f_i A_d \exp\left(\frac{E_A}{RT_p}\right)$ 7-5
Thiele Modulus	$\phi_i = \frac{d_p}{2}\sqrt{\frac{\rho_C \upsilon_i (n_i + 1) R_{i,s}}{2 D_{eff,i} C_{i,s}}}$ 7-6
Effectiveness Factor	$\eta_j = \frac{1}{\phi_j}\left[\coth\left(3\phi_j - \frac{1}{3\phi_j}\right)\right]$ 7-7
Multi-component Diffusion	$D_{i,mix} = \frac{1 - y_i}{\sum_{j=1, j\neq i}^{Species} \frac{y_j}{D_{i,j}}}$ 7-8
Random Pore Model (Bhatia and Perlmutter, 1981)	$\frac{A_p}{A_{p,0}} = (1 - x) * \sqrt[2]{1 - \psi * \ln(1 - x)}$ 7-9
High Heating Rate Particle Swelling (Shurtz et al., 2011)	$\frac{d}{d_0} = s_{var}\left(\frac{\dot{T}_{base}}{\dot{T}}\right)^{c_{HR}} + s_{min}$ 7-10
Low Heating Rate Particle Swelling (Shurtz et al., 2011)	$\left(\frac{d}{d_0}\right)_{LHR} = m * \log(\dot{T}) + b$ 7-11
Devolatilization Model	The CPD model is complex. Some detail is given below, and further details are referenced.
Gas Property Models (McBride et al., 2002; Rowley et al., 2010)	Polynomials from tabulated data used to calculate gas phase thermal conductivity and heat capacity as a function of temperature and molar composition.

[10] The annealing model is a complex set of statements to determine E_A and A_d. Details are given below.

Table 7-1 Continued

NMR Parameter Correlation (Genetti, 1999; Genetti et al., 1999)	$NMR_p = c_1 + c_2X_C + c_3X_C^2 + c_4X_H + c_5X_H^2 + c_6X_O + c_7X_O^2 + c_8X_{VM} + c_9X_{VM}^2$ 7-12
Mode of Burning (Haugen et al., 2014; Haugen et al., 2015)	$\frac{d\rho_p}{dt} = \frac{dm_p}{dt}\frac{\eta}{V_p}$ 7-13
CO/CO_2 ratio (Skokova, 1997; Sun and Hurt, 2000)	$\frac{CO}{CO_2} = A_c\exp(\frac{E_c}{R * T_p})$ 7-14

7.1.2 Previous Models

Several char conversion models include complex submodels that attempt to capture the most important chemistry and transport effects of char conversion. The code used here is an extension of the Carbon Conversion Kinetics (CCK) code (Shurtz, 2011; Shurtz and Fletcher, 2013) with numerous additions to make the code functional and accurate in the extremes of oxycoal combustion. These modifications include a more stable temperature solver with informed initial guess values that result in rapid convergence times, step-size independence, and successful model execution at extremely high temperature (appropriate for highly elevated O_2 concentrations) or high H_2O and CO_2 concentration environments. A number of key submodels were also revised or replaced to more nearly approximate the physics of heterogeneous char conversion. Predecessors of the CCK code include Carbon Burnout Kinetics - extended (CBK/E) (Niksa et al., 2003), and Carbon Burnout Kinetics – gasification (CBK/G) (Liu and Niksa, 2004) codes (which grew out of the Carbon Burnout Kinetics or CBK code (Hurt et al., 1998)).

CBK/E utilizes a 3-step char oxidation reaction with O_2 (reaction equations R1-R3) first introduced by Hurt and Calo, (2001a) while CBK/G introduced a 5-step gasification model with CO_2, H_2O, and H_2 (R4-R5). CCK combined these two equation sets into a single, 8-step mechanism theoretically capable of handling the common gasification species (optionally at high

pressure) within a single model (Shurtz and Fletcher, 2013). Note that in the 8-step mechanism shown in Table 7-1, the C(O) complexes in reactions R3, R5, and R7 represent distinct species with separate reactant pools, as denoted by the subscripts α, β, and γ. The above models successfully described the details of char conversion for oxidation, gasification, and pressurized gasification, but they were neither designed for, nor tested at the unusual gas compositions and combustion temperature found in oxy-coal combustion. Further details of the CCK and CBK-type models are available elsewhere (Hurt et al., 1998; Niksa et al., 2003; Liu and Niksa, 2004; Shurtz, 2011; Shurtz and Fletcher, 2013).

7.1.3 Practical Model Execution Considerations

The next several sub-sections outline the work done to improve the most influential submodels of the CCK/oxy code. While it is tempting (and often effective) to adjust some of the numerous uncertain parameters in the char combustion code until a desirable fit to data is obtained, this method of tuning to data results in a code that is often less predictive and less broadly applicable. Thus, with the goal of producing a combustion code with the widest possible applicability, the CCK/oxy model as a whole was not tuned to the specific data used here until the final optimization of the kinetic parameters. Instead, each submodel is in general compliance with char conversion theory and a subset of data related to the specific function of the submodel (i.e.; the swelling submodel was tuned to data that only related to swelling, etc.). The CCK/oxy model still contains several uncertain parameters related to such values as char tortuosity or ash grain size; since these values are generally unavailable for specific coals, default values are used.

Prior to revising submodels, several practical issues had to be resolved in code execution. These same issues are quite likely to arise in any attempt to modify a char combustion code from conventional to oxy-coal conditions, and are therefore worth mentioning briefly.

First, oxy-coal systems tend to have a higher O_2 concentration to compensate for the slower diffusivity of O_2 through CO_2 and the cooling effects of endothermic gasification reactions. The high O_2 concentrations can lead to very high local char combustion temperatures, and the high temperature, abundant O_2, and concentrated CO_2 and H_2O form an ambient environment that converts solid carbon very rapidly. Because char conversion codes are typically numerical solutions of sequential time steps, the reactant surface partial pressure is used throughout the time step, and the especially intense conditions of oxy-fuel are not likely to be fully grid-converged in models that functioned well at conventional conditions. The second issue is a direct consequence of the first; unrealistically fast carbon conversion leads to excessive temperature spikes that diverge rapidly from experimental data. The solution to both of these issues was an adaptive time step tied to the particle temperature change. In the initial particle heating phase, when gasification and combustion reactions are negligible, the particle is permitted to change temperature significantly in a single time step, but if the magnitude of change is too great, then the step is retaken with a smaller time step. In the current model, 10 K in a single time step is found to be more than sufficiently restrictive to ensure grid convergence in the cold region. When the particle is hot enough to react at a meaningful rate, the time step is instead tied to the ability of the particle to rapidly converge to a new temperature and surface reactant concentration via diffusion and the particle energy balance (which leads to much smaller time steps). Together, the adaptive time step was effective in maintaining grid convergence and reasonably rapid model execution.

The final practical code execution issue resulted from O_2, CO_2, and H_2O all becoming important reactants in the oxy-coal environment. The balance between exothermic oxidation and endothermic gasification makes the energy balance difficult to converge even before attempting to match the model to data. More robust solver constraints and a relatively conservative and adaptive guess function for the new particle temperature ameliorated this issue, but there are still significant combinations of kinetic parameter space that lead to physically absurd results or outright model failure. It is impractical to search the entire kinetic parameter space as part of the optimization routine, but infeasible to put simple constraints on an irregularly shaped, high-dimensional kinetic parameter space. The details of the kinetics are discussed below, but the simple, practical solution was to explore the kinetic parameter space with a space-filling design. In this case, a Latin Hyper-cube design (McKay et al., 1979) was used, and an alternative pathway detected and reported non-physical parameter sets. This method was insufficient to wholly avoid physically infeasible space, but it did reveal the contours of several "valleys" of parameter space that contained local minima for an optimization objective function. By using these valleys as starting points for the final optimization, local minima were located with minimal intrusion into unphysical parameter space, and optimization routines became practical to execute.

7.1.4 The Chemical Percolation Devolatilization Code

The chemical percolation devolatilization (CPD) model (Grant et al., 1989; Fletcher et al., 1992) calculates the time-dependent release of volatiles as a function of coal type, heating rate, temperature, and pressure. The mechanism for thermal decomposition in the CPD model is directly related to the initial chemical structure, and the rates for cleavage of bonds between aromatic clusters are modeled. A Bethe lattice along with percolation lattice statistics is used to

relate the number of cleaved bridges to the fraction of clusters that are not attached to the lattice. A flash calculation is used to relate vapor pressure to the amount of released tar vs. the amount of metaplast remaining in the particle. Crosslinking of metaplast to the char particle is also modeled.

The CPD code was recoded into a compatible format and linked to the CCK/oxy code to allow a complete prediction of the coal particle in a given set of circumstances. With a single set of inputs to describe the ambient environment, CCK/oxy produces a prediction that tracks the coal particle from raw coal, through initial heating and devolatilization, and throughout gasification and complete burnout (unlike any prior comprehensive coal conversion model). Because the thermal annealing kinetics are quite rapid, it is generally thought to be sufficient to execute the devolatilization code in the absence of annealing, and then to allow annealing to begin at the same time as combustion (despite most annealing actually taking place during the devolatilization phase). This is valid only if the consumption of char is negligible during devolatilization, *and* if the annealing of the char "catches up" before significant amounts of char are converted. Both assumptions are reasonable in typical combustion regimes, but this assumption was tested here by intertwining the annealing with the devolatilization model and the char conversion model. No significant difference was manifested when allowing annealing and devolatilization to occur sequentially vs. the more physically appropriate (but computationally onerous) concurrent computation of devolatilization and the annealing submodels. Figure 7-2 is a sample case with Black Thunder coal in 36% O_2, where the temperature profiles differ between the two cases by approximately 0.04 K.

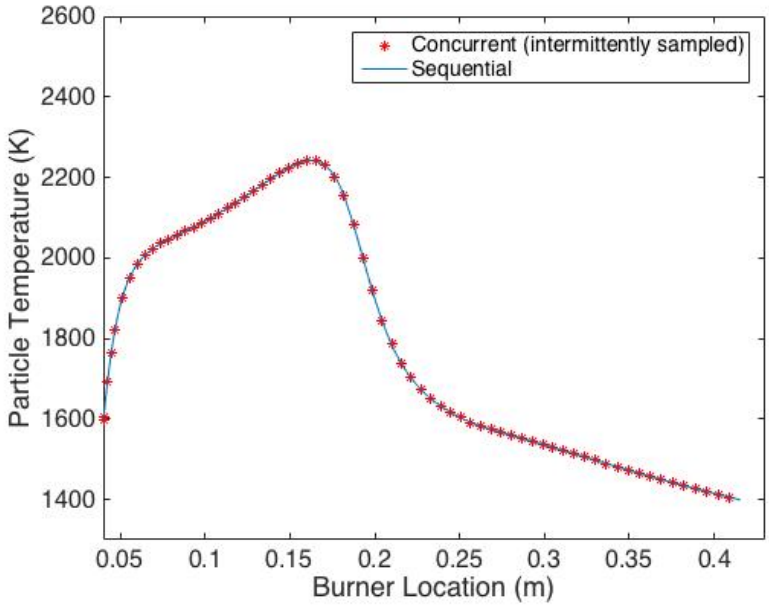

Figure 7-2 – Comparison of concurrent and sequential CPD and annealing models.

The CPD code and three other submodels employed in CCK/oxy (the kinetics, swelling, and annealing submodels) require information from the ^{13}C Nuclear Magnetic Resonance Imaging (NMR) parameters. These parameters contain important structural information about the coal, but they are not generally available for most coals. Therefore, to maintain a broad level of applicability, the NMR parameter correlations reported by Genetti et al. (Genetti et al., 1999) were used. These nonlinear correlations were developed to predict the NMR parameters of any coal based only on the widely available proximate and ultimate analysis, and are described briefly below, with more detail available elsewhere (Genetti, 1999; Genetti et al., 1999).

The NMR parameter correlations calculate five parameters of interest: M_δ, M_{cl}, $\sigma+1$, p_o, *and* c_o. These parameters are, respectively, the average molecular weight of the side chains attached to aromatic clusters, the average molecular weight of an aromatic cluster, the coordination number (that is, the number of attachments per cluster, or the sum of the number of

bridges and the number of side chains), the fraction of intact bridges, and the number of stable bridges. Here, stable typically refers to biaryl connections or cross-linking that is not readily decomposed during the complete devolatilization process. Together, these parameters provide substantial information about the irregular and generally unknown pseudo-monomer that makes up the backbone of the coal particle. The true values of these parameters dictate much of the coal chemistry, particularly the reactivity of the char and the behavior of the metaplast during heating and devolatilization (or even whether or not a metaplast forms at all). The correlations for these parameters were originally intended to provide coal general inputs for advanced devolatilization models such as CPD, but they can also offer valuable insights into models such as the annealing and kinetic models employed in flexible, comprehensive char conversion models. The correlations and their coefficients are shown in Equations 7-15 and 7-16 below and in Table 7-2 respectively.

$$Parameter = c_1 + c_2 X_C + c_3 X_C^2 + c_4 X_H + c_5 X_H^2 + c_6 X_O + c_7 X_O^2 + c_8 X_{VM} + c_9 X_{VM}^2 \quad 7\text{-}15$$

$$c_0 = \min[0.36, \max\{(0.118 * X_C - 10.1), 0\}] + \min[0.15, \max\{(0.014 * X_O - 0.175), 0\}] \quad 7\text{-}16$$

Table 7-2 – NMR parameter correlation coefficient.

	M_δ	M_{cl}	p_0	σ+1
c1	421.957	1301.41	0.489809	-52.1054
c2	-8.64692	16.3879	-0.00982	1.63872
c3	0.046389	-0.18749	0.000133	-0.01075
c4	-8.47272	-454.773	0.155483	-1.23688
c5	1.18173	51.7109	-0.02439	0.093194
c6	1.15366	-10.072	0.007052	-0.16567
c7	-0.0434	0.076083	0.000219	0.004096
c8	0.556772	1.36022	-0.01105	0.009261
c9	-0.00655	-0.03136	0.000101	-8.3E-05

7.1.5 Mode of Burning Parameter

Porous fuel particles are typically considered to gasify in one of three regimes or zones. They may be entirely kinetic limited (zone I), entirely film diffusion limited (zone II), or exhibit a mixture of internal diffusion and kinetic limitations (zone III). Kinetic limitations imply a relatively cool particle, which is not the case of coal char at practical combustion conditions. However, since gasification reactions with CO_2 and H_2O have enhanced importance in the oxy-fuel scenario, and because their associated gasification activation energies are much higher than that of combustion in O_2, kinetic limitations may well be expected to have a significant impact on char conversion in the oxy-coal scenario. Because the three regimes have very different implications for char consumption, the concept of a mode of burning parameter, α, has historically been used to balance the shrinking diameter with the decrease in density in accordance with the char conversion regime (film diffusion limited, kinetically limited, or mixed) (Smith, 1982; Hurt and Mitchell, 1991; Essenhigh, 1994). Equation 7-17 and 7-18 relate mode of burning, mass, density, and diameter, where α=0 indicates constant density and thus a complete film diffusion limitation, while α=1 implies constant diameter with kinetic limitation.

$$\frac{\rho}{\rho_0} = \left(\frac{m}{m_0}\right)^{\alpha} \qquad 7\text{-}17$$

$$\frac{m}{m_0} = \left(\frac{m}{m_0}\right)^{\alpha}\left(\frac{d}{d_0}\right)^{3} \qquad 7\text{-}18$$

In conventional, air-fired char combustion an α value of 0.2 is recommended (Mitchell et al., 1992; Hurt et al., 1998).

In the construction of the CCK model, it was intended that the model should be run at either combustion conditions or gasification conditions, while oxy-coal combines the high

temperature and O_2 conditions of combustion with the high CO_2 (and sometimes H_2O) concentration of gasification. Thus, while the CCK code could match data well with a simple heuristic to determine α, the CCK/oxy model is a significantly more complicated situation. Moreover, oxy-coal might have a very wide range of O_2 concentrations, depending on the specific application, which in turn leads to a broad range for particle temperature that heavily influences the value of α relevant to gasification. Finally, global coal combustion models (and CCK) simply designate a mode of burning as a constant for a given instance, but in reality the balance between diameter loss and density decrease is far from static during char particle burnout. Given the sensitivity of the CCK model to α (Holland and Fletcher, 2016), it was necessary to significantly improve the mode of burning implementation in CCK/oxy using a variation on a method derived and applied by Haugen et al. (2014; 2015). This method is derived in detail elsewhere (Haugen et al., 2014), but the key results are shown in Equations 19 through 22.

$$\frac{dr_p}{dt} = 0 \qquad 7\text{-}19$$

$$\frac{d\rho_p}{dt} = \frac{dm_p}{dt}\frac{1}{V_p} \qquad 7\text{-}20$$

$$\frac{dr_p}{dt} = \frac{dm_p}{dt}\frac{1-\eta}{4\pi r_p^2 \rho_p} \qquad 7\text{-}21$$

$$\frac{d\rho_p}{dt} = \frac{dm_p}{dt}\frac{\eta}{V_p} \qquad 7\text{-}22$$

The equations above were obtained using the Thiele modulus relevant to a first-order, irreversible reaction at steady state, and also assumed a relatively large value of the Thiele modulus such that the effectiveness factor could be approximated by Equation 23.

$$\eta \approx \frac{3}{\phi} \qquad 7\text{-}23$$

In reality, the order of the combustion reaction is a matter of controversy that depends both on how the kinetic system of equations is framed and on the temperature regime; also the effectiveness factor may not be small for gasification reactions. However, the method shown in the equations below is considerably superior to a single, fixed value of α, and establishes a conceptually sound relation between the changes in particle diameter and density for the reactive regime of the oxidative gases.

The first pair of equations above indicate that up to some point of burnout, the outermost layer of char becomes more and more porous, but is not yet fully consumed (i.e.; the char particle has not yet begun to shrink). This implies that the rate of change of mass (as determine from the kinetic and transport equations) is proportional to the rate of change of density, and that the constant of proportionality is the volume of the char particle (which does not change until the radius begins to shrink). The appropriate time point to switch between the first and second set of equations is referred to as time τ, and it depends on gas temperature and composition, as well as the reactivity of the specific coal. The value of τ is computed numerically in CCK/oxy as the time when the outermost char layer of differential thickness has decreased to $\rho(R,\tau)=0$, as derived by Haugen et al (2014). Once τ is reached, the second equation pair replaces the first. The second pair of equations balances the loss in particle diameter with the loss in density via the effectiveness factor as computed from the Thiele modulus. In the case of a near zero effectiveness factor, the particle is diffusion limited and the radius change represents the entire mass loss of the particle, while the density is essentially constant. In the case of $\eta=1$, the char particle is kinetically limited, and the diameter is essentially constant. These equations are

exactly true under the assumptions used in the derivation (first-order, irreversible kinetics modeled by the Thiele modulus at steady state, and a small effectiveness factor). The assumptions are not entirely valid in the case of char particle conversion, and there is also the issue of multiple reactions with different effectiveness factors. However, the concept of determining mode of burning via effectiveness factor is intuitively sound, and a considerable improvement over using a heuristic to fix the mode of burning parameter for the entire reaction. In CCK/oxy, the effectiveness factors for reaction with O_2, CO_2, and H_2O are computed at each time step, and then they are weighted according to the fraction of carbon consumption that is due to each reaction. The weighted effectiveness factor for a given time step is used to compute the change in density for that time step, and the change in density is then used in conjunction with the computed conversion of carbon (from the kinetic and gas diffusion submodels) to compute the diameter decrease for the time step. This second step is necessary because, as mentioned above, some of the assumptions in the derivation of Equations 7-18 through 7-21 are only approximations in the reality of char combustion. Thus, Equation 7-21 for the change in radius is superseded by enforcing the law of conservation of mass, which corrects for the inconsistency introduced by the approximations of the derivation.

In the interest of displaying the impact of this submodel, Figure 7-3 shows profiles for the weighted effectiveness factor, char conversion, and normalized T_p. It is not as meaningful to make a direct comparison between shifting values of α because (aside from the extremes or 0 and 1) α does not have an intuitive meaning. Furthermore, α should change due to changes in both the effectiveness factor and the fraction of total internal area vs total surface area (e.g., if the particle is a non-porous sphere, kinetic limitation and film diffusion limitation would be identical as far as the mode of burning is concerned). Because the simplified model of Equation 7-17 does

not account for (or disentangle) the impact of effectiveness factor or changing porosity on α, the weighted effectiveness factor is a more interesting output. Note that the effectiveness factor first drops precipitously during the rapid initial particle heating, as would be expected as the reaction quickly shifts from fully kinetically limited at low particle temperatures to largely diffusion limited at higher temperatures. The initial decline leads to the first and most severe minimum effectiveness factor, as the random pore model makes more surface area available, but the heated particle isn't able to take significant advantage of it. The effectiveness factor then enters a nearly stable region with relatively minor fluctuations and a local maximum and a local minimum due to the interactions of the random pore model, the energy balance, the cooling ambient gas, and gradually changing char reactivity. Finally, as the particle enters what is typically acknowledges as late burn-out (about 85% conversion), the effectiveness factor rises rapidly as the heavily annealed particle drops to a regime of mostly kinetic limitation.

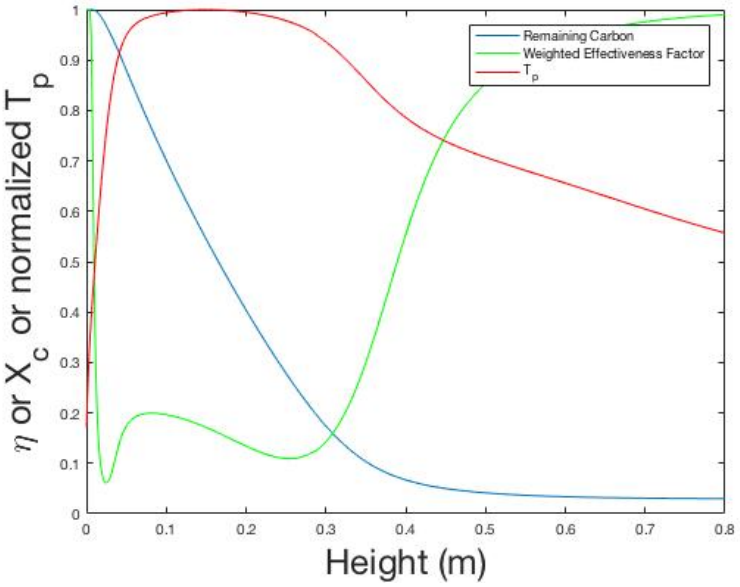

Figure 7-3 – Effectiveness factor, remaining carbon fraction, and normalized T_p for Black Thunder coal in 12% O_2. In this plot, T_p is normalized by the maximum T_p for convenience in plotting.

7.1.6 Particle Swelling Model

The swelling submodel employed in the CCK model is shown in Equations 24-26, and is overly simplistic.

$$\frac{d}{d_0} = 8.67 - 0.0833 * X_C \text{ if } 89 \leq X_C \leq 92 \quad 7\text{-}24$$

$$\frac{d}{d_0} = -0.0458 + 0.01459 * X_C \text{ if } 72 \leq X_C \leq 89 \quad 7\text{-}25$$

$$\frac{d}{d_0} = 1 \text{ if } X_C < 72 \quad 7\text{-}26$$

The most advanced swelling models attempt to capture the physics of bubble formation (Oh et al., 1989; Yang et al., 2014, 2015), but are impractical because they are computationally expensive, complicated to implement, and may not be applicable to a wide range of coals. Most importantly, until recently (Yang et al., 2014, 2015), these swelling models did not follow the observed swelling trends at the extremely high heating rates (10^4-10^6 K/s) relevant to practical coal combustion systems (Yu et al., 2004). This is true of all swelling models that neglect the functional dependence on heating rate, and is presumably because the extreme heating rates drive the volatiles from the particle very rapidly (Niksa et al., 2003; Kidena et al., 2007). The rapid loss of volatiles leads to a very short time-frame for bubble formation, and when the rate of bubble growth exceeds the rate of metaplast relaxation, the bubbles "pop" leading to an entirely different swelling regime (Gale et al., 1995). The swelling model implemented in CCK failed properly incorporate coal structure or heating rate dependence, and is shown in Equations 24-26, where X_C is the wt% carbon in the parent coal on a daf basis

The swelling model implemented in CCK/oxy incorporates information about the coal structure and type as well as heating rate dependence, with the structural parameters predicted

from the NMR correlations mentioned previously. Both the coal type and heating rate heavily impact the swelling behavior (Kidena et al., 2007). The newly implemental model was developed by Shurtz et al. (2011; 2011) and a brief description of equations and applicability is given below, with details of the swelling model development given elsewhere (Shurtz, 2011; Shurtz et al., 2011). The swelling ratio is given by Equation 27, where s_{var}, c_{HR}, and s_{min}, and described by the correlations in Table 7-3 and Equation 7-28.

$$\left(\frac{d}{d_0}\right)_{HHR} = s_{var}\left(\frac{\dot{T}_{base}}{\dot{T}}\right)^{c_{HR}} + s_{min} \qquad 7\text{-}27$$

$$s_{min} = (FC_{ASTM} + A_{ASTM})^{1/3} \qquad 7\text{-}28$$

Table 7-3 – High Heating Rate Swelling Model Parameter Correlations.

Correlation	Applicable Range
$s_{var} = 1.69\frac{\sigma+1}{M_\delta} - 0.0309$	$0.018 \leq \frac{\sigma+1}{M_\delta} < 0.207$
$s_{var} = -3.37\frac{\sigma+1}{M_\delta} + 1.01$	$0.207 \leq \frac{\sigma+1}{M_\delta} \leq 0.301$
$s_{var} = 0$	$\frac{\sigma+1}{M_\delta} < 0.018$ *or* $\frac{\sigma+1}{M_\delta} > 0.301$
$c_{HR} = -191\left(\frac{\sigma+1}{M_\delta}\right)^2 + 68.9\frac{\sigma+1}{M_\delta} - 5.16$	$0.106 < \frac{\sigma+1}{M_\delta} < 0.254$
$c_{HR} = 0$	$\frac{\sigma+1}{M_\delta} < 0.106$ *or* $\frac{\sigma+1}{M_\delta} > 0.254$

$\dot{T}$ is the maximum heating rate that the particle experiences during the heat-up and swelling process (in K/s, as estimated via the energy balance). This maximum rate occurs at initial heating, when the cold particle experiences the greatest temperature gradient with its surroundings. Table 7-3 (reproduced from Shurtz et al. (2011)) gives the value for other variables

of interest, as well as their range of applicability. Here σ+1 indicates the coordination number, M_δ refers to the average molecular weight of the side chains, HHR applies to the high heating rate regime, and FC_{ASTM} and A_{ASTM} are the American Society for Testing and Materials values for ash and fixed carbon content, respectively. $\dot{T}_{base}$ is set at $5.8x10^4$ K/s.

The preceding equations and parameters introduce the vital elements of heating rate and coal structure into the coal particle swelling model. Coal structure in particular is introduced via correlations with the NMR parameters calculated from the correlations in section 7.1.4, which allows for superior correlation than the less informative parameters of the proximate and ultimate analysis used previously. Equations 27 and 28 are intended for heating rates of at least $8.3x10^3$ K/s, and have been shown to fit data taken at relevant heating rates and atmospheric pressure (Shurtz et al., 2011). The CCK/oxy implementation of the swelling model also incorporates a plugin for adding in the influence of high-pressure on swelling (developed by Shurtz and Fletcher and detailed elsewhere (2013)). For lower heating rates, Shurtz et al. (2011) developed a piecewise correlation, described in Appendix C.

7.1.7 Gasification and Oxidation Kinetic Parameters[11]

The reaction steps R1-R8 (shown earlier in Table 7-1) each have an associated activation energy and preexponential factor for a total of 20 kinetic parameters (including two reverse reactions). This kinetic scheme was given in the CCK model as a combination of the combustion kinetic scheme from CBK/E and the five gasification reactions from CBK/G. A system of only eight reactions is a very simplistic skeletal mechanism, but it has proven sufficiently flexible to

[11] The preexponential factors are heavily impacted by a greatly extended thermal annealing model, which is described in Chapter 6.

fit a broad sampling of combustion and gasification data (Liu and Niksa, 2004; Shurtz and Fletcher, 2013). It is typically sufficient to fit only the four kinetic parameters involved in R3 and R7 (A_3, E_3, A_7, and E_7), where R3 is the principal combustion reaction and R7 is the principal gasification reaction. The rest of the kinetic parameters are either fixed at nominal values or tied to the kinetic parameters of R3 and R7 via correlations developed with CBK/G (Liu and Niksa, 2004). In the present work, it was desirable for the sake of future work to: 1) investigate the potential for coal-general kinetic correlations, and 2) determine the number of fitting parameters needed to fit the data. To that end, eight kinetic parameters were optimized instead of the usual four. Equations 7-29 and 7-30 contain four of the parameters,

$$A_3 = a_3 M_\delta + b_3 \qquad 7\text{-}29$$

$$A_7 = a_7 M_\delta + b_7 \qquad 7\text{-}30$$

which are used in a simple correlation for determining the preexponential factor based on a coal specific NMR-based chemical structure parameter, where M_δ is the average mass of a side chain in the initial chemical structure of the coal. This correlation is almost certainly overly simplistic, and is intended as a first step to investigate the viability of chemical structure parameters in coal-general kinetic correlation. The other parameters are the activation energies for R1-3, and R7. The variables E_1 and E_2 generally remain at their default values without harming model fit, but in this case, they allowed the optimization to test the usefulness of additional model flexibility. Specifically, the ultimate and elusive goal of coal combustion modeling has been a coal-general correlation capable of predicting reasonable combustion kinetics for any coal from only proximate and ultimate analysis data, and it was desirable to test the feasibility of advancing that goal.

After all of the preceding submodels were updated or added to the CCK/oxy model, the eight kinetic parameters were optimized. It is important to note that this optimization is not a fit of the kinetic parameters as is typically observed with a single, linearized reaction equation fit to a set of rate data. Instead, the entire space of 8 parameters was given bounds and, optionally, given both linear and nonlinear constraints. An initial guess value was provided for each parameter, and the optimization algorithm fmincon (from the MATLAB Optimization Toolbox) explored the constrained parameter space to minimize the error of an objective function.

7.2 Summary and Conclusions

In this chapter, an extended carbon conversion kinetic model was developed. The model is generally intended to predict single particle coal combustion rates and particle time-temperature profiles, and specifically designed for the extreme conditions of oxy-coal combustions. The model is a synthesis and culmination of several prior comprehensive coal combustion models, none of which were able to model oxy-fuel conditions with any degree of accuracy. In addition to input from prior comprehensive models, several submodels were developed or adapted from the literature to improve the accuracy of the CCK/oxy model over any previous comprehensive coal model. These additional submodels include:

1. The Chemical Percolation Devolatilization (CPD) model, which was translated from legacy Fortran codes and allowed to proceed in parallel with the combustion model (rather than the traditional series of models). It was confirmed that no significant differences exist between the two model execution options under the high heating rate conditions used in this study. It is therefore advisable to execute the CPD and CCK/oxy models in series for computational efficiency and simplicity. Also, prior comprehensive coal combustion models

were only capable of modeling the coal char conversion, but with the addition of CPD, CCK/oxy models coal conversion from raw coal through all conversion processes to complete burnout.

2. The mode of burning parameter model, which has traditionally been a static value determined by a heuristic for the combustion regime and ambient atmosphere, was updated to change at every time-step. The new mode of burning parameter was modeled via a rigorously derived, first-principles based effectiveness factor model adapted from the literature.

3. The updated particle swelling model replaced an outdated swelling model that ignored the massive impact of heating rate on particle swelling. The former model also relied on a simple carbon mole fraction correlation to determine swelling. This is particularly problematic as coals with similar elemental composition are known to have very different softening and swelling behaviors. The current model was taken from extensive work in the literature and includes the impact of heating rate as well as a series of coal structural correlations. The new model also includes options for high-pressure effects on particle swelling.

4. The thermal annealing model was found to be the most sensitive submodel by far in work documented in Chapter 4 and was the focus of a thorough literature review and model development in Chapters 2 and 6. The revised annealing model incorporates changes in the annealing activation energy distribution due to heating rate, peak particle temperature, and coal precursor, all of which were necessary but neglected components of the prior model.

8 FULL CCK/OXY MODEL RESULTS[12]

8.1 Introduction

The prior chapter developed a new coal conversion model in two steps. First, numerical and model execution issues from CCK that caused the CCK/oxy model to fail in the extremes of the oxy-coal environment were eliminated. Second, the most sensitive submodels were replaced with updated, more physically realistic submodels. Because the models are simply more refined, rather than specific to the oxy-coal environment, improvements realized by the updated model are valid in gasification, air-fired, and oxy-coal conditions. This chapter compares the relatively limited oxy-coal data to the CCK/oxy model, after optimizing the kinetic parameters as described in Chapter 7. These comparisons are intended to answer (or at least provide insight) for several questions:

(a) Can the CCK/oxy model predict oxy-coal data?

(b) Can the CCK/oxy predictions be extrapolated to limited data scenarios?

(c) Can CCK/oxy predictions from one O_2 condition be reasonably extrapolated?

(d) Can CCK/oxy predictions from conventional firing conditions be extrapolated to oxy-coal conditions?

(e) Is a coal general correlation even remotely feasible?

[12] This chapter was modified from published work: Holland, T. and T. H. Fletcher, "Comprehensive Model of Single Particle Pulverized Coal Combustion Extended to Oxy-Coal Conditions," *Energy & Fuels,* **31**, 2722-2739 (2017).

(f) Is it reasonable to use CCK/oxy predictions as a CFD submodel training tool?

8.2 Experimental

To conduct a relevant comparison, the model was executed at conditions related to real-world application. Here, the most applicable conditions are the oxy-coal combustion environment, so experimental data from the literature were chosen for comparison at useful conditions. The experimental data also allowed the model kinetic parameters to be calibrated. The model was then compared both to the calibration data and similar data not used in the calibration. The experimental data referenced here were collected by Shaddix and Molina (2009) and Geier et al. (2012). The reactor consisted of a burner-stabilized flat flame, a quartz chimney for gas and particles to flow through, and a coal particle inlet in the center of the burner. The particle temperatures were measured with a 2-color pyrometry system and the particle diameters and velocities were measured by imaging of the particle emission. No burnout data from probe measurements were available from this data set. The coal particle flow rate was sufficiently low that particles did not affect each other or the bulk gas composition. The data were for two subbituminous coals (Black Thunder and North Antelope) and two high volatile bituminous coals (Utah Skyline and Pittsburgh seam (Bailey)) which were subjected to conditions of 14 or 16% H_2O; 12, 24, or 36% O_2; and the balance CO_2, at gas temperatures ranging from approximately 1400-1800 K. The proximate and ultimate analyses of the coals and a summary of experimental conditions are given in Table 8-1 and Table 8-2.

The char particles were in the reactor for up to approximately 0.2 seconds (post devolatilization), and on the order of 1,000 particle data triplets of temperature, location, and diameter were collected for each condition. These data were used in a related sensitivity analysis

of the Carbon Conversion Kinetics (CCK) model (2016) to determine which model parameters were most sensitive when coal is combusted at oxy-fuel conditions, and to target model updates and refinements. These updates were implemented, but it should be noted that the updates did not detract from the ability of the CCK code to predict char behavior in conventional oxidation and combustion scenarios. Instead, the additions to CCK extended the submodels to capture intense oxy-fuel conditions, while maintaining (and improving) predictive power in more traditional regimes.

Table 8-1 – Proximate and Ultimate Analysis of Coal Particles between 76 and 105 microns.

Coal	Moisture (% AR)	Ash (% AR)	Volatiles (% AR)	C (% daf)	H (% daf)	N (% daf)	S (% daf)
Black Thunder	9.34	4.84	42.34	68.96	5.00	0.97	0.45
Utah Skyline	1.69	10.2	40.79	79.4	6.09	1.67	0.59
Pittsburgh	0.47	6.95	35.89	81.26	5.55	1.54	2.16
North Antelope	10.83	5.54	39.64	72.12	5.45	1.00	0.35

Table 8-2 – Summary of Experiments for Char Particles between 53 and 125 microns.

Coal	O_2 Mol %	CO_2 Mol %	H_2O Mol %	Peak Particle Temp. (K)	Peak Gas Temp. (K)
Black Thunder	12	74	14	1732	1741
	24	62	14	1919	1710
	36	50	14	2147	1726
Pittsburgh	12	74	14	1889	1741
	24	62	14	2077	1710
	36	50	14	2248	1726
Utah Skyline	12	72	16	1954	1697
	24	60	16	2181	1700
	36	48	16	2564	1714
North Antelope	12	72	16	1931	1697
	24	60	16	2108	1700
	36	48	16	2414	1714

Table 8-3 shows a summary of parallel experiments conducted with N_2 diluent rather than CO_2. These data were not used in the calibration of the CCK/oxy model, but they were collected under parallel conditions in the same apparatus, for the same coal, and with the same size cuts. It is of interest to determine whether kinetic parameters calibrated solely in conventional conditions (21% O_2 and 79% N_2) can predict oxy-coal combustion data when using an advanced comprehensive model. If this turns out to be the case, then decades of coal combustion research are potentially useful in calibrating oxy-fuel combustion models. This is especially useful in the current state of the art where oxy-fuel combustion data are relatively limited, and detailed data including high heating rates, a reasonable time temperature profile, and an ambient gas composition profile are essentially non-existent.

Table 8-3 – N_2 parallel experiments.

Coal	O_2 Mol %	N_2 Mol %	H_2O Mol %	Peak Particle Temp. (K)	Peak Gas Temp. (K)
Black Thunder	12	74	14	1861	1677
	24	62	14	2128	1711
	36	50	14	2289	1753
Pittsburgh	12	74	14	1770	1677
	24	62	14	2154	1711
	36	50	14	2313	1753
Utah Skyline	12	72	16	2091	1690
	24	60	16	2325	1692
	36	48	16	2520	1712
North Antelope	12	72	16	2080	1690
	24	60	16	2357	1692
	36	48	16	2532	1712

8.3 Coal Particle Diameter Overview

In evaluating the results of the optimized kinetics in the next several sections, it should be noted that selecting the correct input value for the coal particle diameter was not as straightforward as expected. First, the data in question have a very wide range of particle

temperature values (independent of particle size); at any given observation height and particle diameter the particle temperatures range on the order of ±150 K from the mean. However, the trends in the data may be due to more than merely noisy data, and in fact the data may not actually be "noisy" at all in the traditional sense. Instead, they appear to indicate the actual temperature variation due to particle-to-particle variation in ash content and/or maceral character (actual noise was estimated to be in the range of ±25 to 50 K) (Mitchell et al., 1992). Second, the model clearly has a strong bias in that the CCK/oxy model frequently over- or under-predicts the data very strongly in early burnout, and then does the opposite as burnout progressed. Thus, even though the mean of the absolute error was occasionally near the range that can reasonably be ascribed to actual measurement noise, the systematic bias trends in the figures, in conjunction with the very large maximum error values, prompted a closer investigation of the data. The following four sections focus on a stepwise investigation into the true diameters of the observed particles, since this input is believed to be the primary source of lack of agreement between models and data. Results are shown in a stepwise fashion partially to improve readability, but mostly to show how gradually improved assumptions impact the results, which in turn isolates which assumptions eliminate the largest share of the disagreement.

The next several sections could easily give the erroneous impression that particle diameter was essentially used as a fitting parameter. This is not the case, and in fact all of the diameter values were decided based on available data, and only the kinetic parameters were adjusted to fit the data. Diameter values are an input parameter, but that parameter has some uncertainty in these experiments. The following sections gradually decrease that uncertainty by making progressively better use of available diameter data. This point is crucial to the validity of the results section (and the usefulness of any associated conclusions), so it is briefly summarized

here and reiterated in greater detail in each subsection.

- First, a uniform raw coal diameter of 95 microns was assumed. This was not based on the detailed diameter data available, but was a naïve first pass at selecting the diameter solely based on the rough mean of the nominally known particle size cut.
- Second, it was observed that the North Antelope and Utah Skyline coals have an observed particle diameter associated with every char particle. These data allow for a simple computation of the *char* mean diameter at every O_2 concentration condition, and imply that the resultant mean should be rounded up because the initial, post-swelling char particle diameter is somewhat larger than the partially-burned particle. The Black Thunder and Pittsburgh coals do not include diameter data, but their mean diameter sizes can be extrapolated from the North Antelope and Utah Skyline coals, respectively, on the tenuous justification that they are the same coal ranks. Naturally this means there is greater uncertainty in the mean diameters of the Black Thunder and Pittsburgh coals.
- Because the data often show a near step-change in burnout, it is reasonable to attempt to model the data with only two diameters per O_2 condition. The diameters of Black Thunder and Pittsburgh coals must be extrapolated here as well, though it is slightly less straightforward in this case. The complexity arose because burner location is the driving factor behind observed average particle diameters, and the measurements for the four coals were not performed at the exact same heights, so additional extrapolation was required.

- Finally, a diameter value was assigned to every coal at every observation height and condition. For the North Antelope and Utah Skyline coals, this was easily done from the detailed data. In the case of the Black Thunder and Pittsburgh coals, the extrapolation was not considered sufficient for a high level of detail. Instead the extrapolated values were

rounded, which sometimes resulted in sequences of 2-3 points with the same rounded diameter value. This was done to emphasize that the rounded values are not precisely known, but it is not thought that the small differences would have a notable impact on the model fit. More details are given in the following sections.

8.4 CCK/oxy Optimization with a 95 μm Initial Diameter

The data described in the experimental section of Chapter 7 include particle temperature data, but do not include information on the degree of char burnout. Therefore, the comparison was made by providing the CCK/oxy model with all of the inputs of the experiment (gas concentration and temperature profiles, coal specific details etc.), and plotting the CCK/oxy prediction of the particle temperature profile vs burner height, together with the measured mean particle temperature at each height where data were collected. The coals all had a nominal size cut ranging from 76-106 μm, but sieving is imperfect and coal particles may fragment during combustion, so the distribution is actually considerably wider than the nominal cut and expected to be skewed. Therefore, a rough mean of 95 μm was estimated as the input particle diameter for the results in this section. Kinetic parameters were fit to the data of Shaddix and coworkers (Shaddix and Molina, 2009; Geier et al., 2012), and the results are shown in Figure 8-1 and Table 8-1. The choice of diameter turned out to be naïve and substantially incorrect, as seen by the lack of agreement between the model and the data in Figure 8-1 and Table 8-4. The performance of the CCK/oxy code is, however, an enormous improvement over the errors observed from the original CCK model (see Figures 5-1 to 5-3) (Holland and Fletcher, 2016). Figure 8-1 and all subsequent figures modeling coal conversion have several common features. First, the model initially heats up at a rate determined by the energy balance. As the particle heats, it begins to react with the ambient gases, which raises the particle temperature further,

especially for the high O_2 concentration conditions. As the particle becomes more porous, it burns more rapidly and increases in temperature to some peak temperature. After the peak temperature, the particle rapidly decreases in temperature in a near-extinction phenomenon, and then exhibits a slow decline in particle temperature as the ambient gas cools. Note that many of the model prediction lines are truncated in the figures of this chapter to facilitate plot reading.

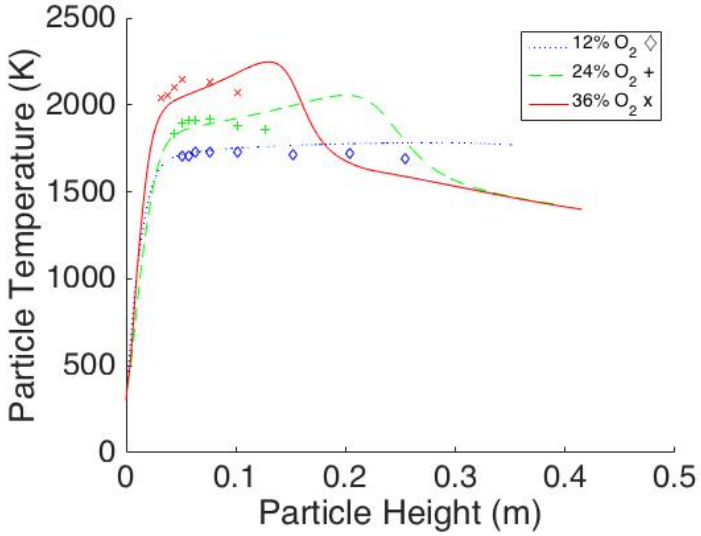

(a) Black Thunder coal

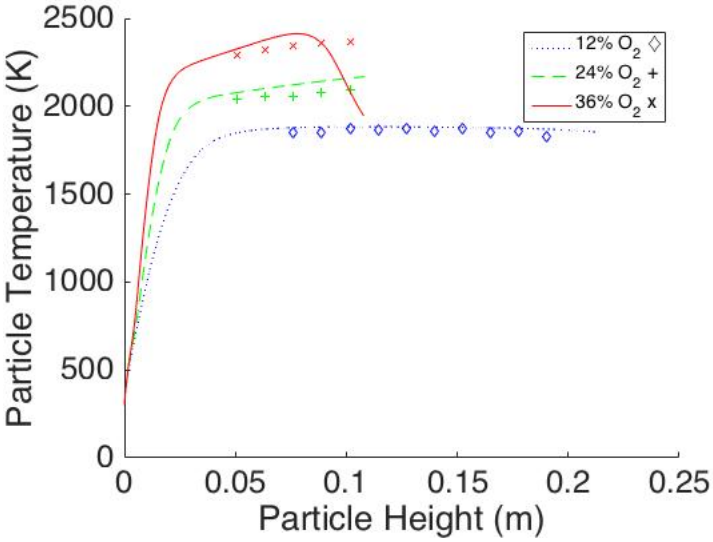

(b) North Antelope coal

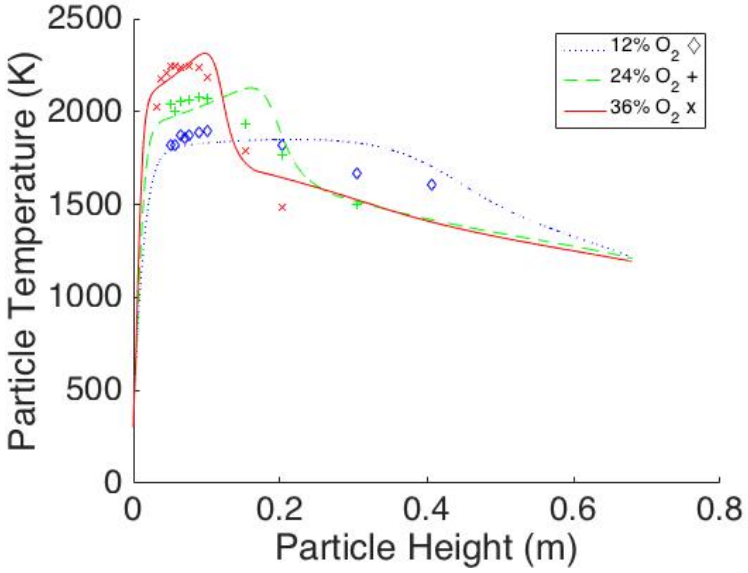

(c) Pittsburgh 8 coal

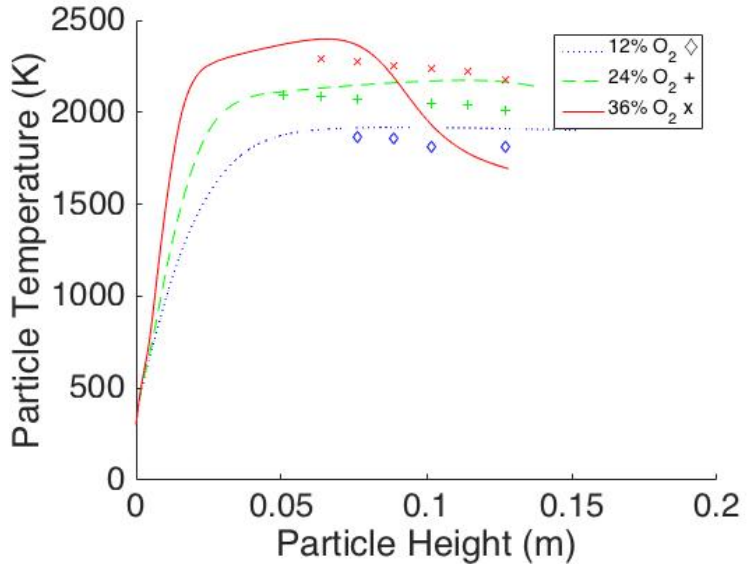

(d) Utah Skyline coal

Figure 8-1 – Comparison of CCK/oxy model calculations with coal data from Shaddix and coworkers (Shaddix and Molina, 2009; Geier et al., 2012) using the measured particle diameters.

Table 8-4 – Mean absolute error and max error using an initial char diameter of 95 μm.

Black Thunder	Mean Absolute Error (K)	Max Error (K)	Pittsburgh 8	Mean Absolute Error (K)	Max Error (K)
12 % O_2	33	92	12 % O_2	62	161
24 % O_2	45	101	24 % O_2	68	188
36 % O_2	79	113	36 % O_2	66	162
North Antelope			**Utah Skyline**		
12 % O_2	20	43	12 % O_2	79	107
24 % O_2	56	66	24 % O_2	91	153
36 % O_2	85	268	36 % O_2	246	479

8.5 CCK/oxy Optimization with a Condition-dependent Initial Diameter

While the CCK/oxy model was a gratifying improvement over past models, the previous section still shows significant lack of agreement between the model and the data. Fortunately, the data collection system was able to measure the diameter and temperature of individual particles at pre-determined heights in the burner. Table 8-5 and Table 8-6 show the mean of particle diameter and temperature for each height for two of the coals, but the other two coals reported only the average temperature data, which are shown in Table 8-7 and Table 8-8. The more complete data for Utah Skyline and North Antelope coals have several implications for the behavior of the experiment. First, the cohort of particles observed at a given height is NOT the same cohort as observed at lower burner heights. The burner height is adjusted between experiments, so the individual particles are different specific particles, but more importantly, the average characteristics of an observed particle change based on observation height. This is because of at least four competing effects:

1. The detection method relies on the light emitted by burning particles, so some particles simply are not detected. A particle is most likely to be detected if it is large and hot (and thus emitting a relatively large quantity of light).

2. Small particles tend to burn hotter than larger particles, but have less surface area and thus emit less total light than a larger particle of the same temperature.

3. As particles burn, the smaller particles reach near extinction relatively quickly, becoming invisible to the detection system. This increases the average diameter of the detected particles and decreases the number of particles detected. This effect is especially important for the very small particles that are below the nominal size cut (either from fragmentation or from imperfect sieving).

4. Large particles take longer to burn out into the undetectable range because they have both greater mass and a larger surface area to emit light, but while they persist into later burnout, they decrease in diameter, which decreases the average diameter of the detected particles.

Table 8-5 – Utah Skyline data summary.

12% O_2						
Height (cm)	7.62	8.89	10.16	12.70		
Avg. D_p (μm)	106	102	96	98		
Avg. T_p (K)	1864	1857	1810	1815		
Number of Points	231	184	1078	198		
24% O_2						
Height (cm)	5.08	6.35	7.62	10.16	11.43	12.70
Avg. D_p (μm)	96	97	102	103	106	107
Avg. T_p (K)	2092	2088	2071	2049	2038	2013
Number of Points	195	233	214	180	195	100
36% O_2						
Height (cm)	6.35	7.62	8.89	10.16	11.43	12.70
Avg. D_p (μm)	111	120	119	124	123	122
Avg. T_p (K)	2290	2272	2256	2239	2219	2180
Number of Points	859	295	201	162	75	29

Table 8-6 – North Antelope data summary.

12% O_2										
Height (cm)	7.62	8.89	10.16	11.43	12.70	13.97	15.24	16.51	17.78	19.05
Avg. D_p (μm)	86	89	88	88	91	86	96	96	94	103
Avg. T_p (K)	1851	1853	1873	1867	1870	1859	1876	1854	1860	1826
Number of Points	176	149	131	151	100	59	54	52	31	19
24% O_2										
Height (cm)	5.08	6.35	7.62	8.89	10.16					
Avg. D_p (μm)	92	96	96	97	100					
Avg. T_p (K)	2038	2054	2059	2077	2093					
Number of Points	191	211	293	129	37					
36% O_2										
Height (cm)	5.08	6.35	7.62	8.89	10.16					
Avg. D_p (μm)	100	106	110	96	92					
Avg. T_p (K)	2294	2323	2348	2363	2370					
Number of Points	200	200	157	105	23					

Bearing the above effects in mind, it is not easy to immediately apply simple trends to the data, but some approximations are certainly necessary to input a more accurate particle size into the CCK/oxy model so that the comparison between data and model is legitimate. One obvious trend is the change in observed particle diameter between conditions. In general, more intense conditions have a larger average particle diameter, most likely because the high O_2 concentration rapidly consumes the smallest particles. Therefore, as a second step, each condition was assigned a different average particle diameter (shown in Table 8-9), with a different diameter for each O_2 condition. This approach is not fully correct, but it is regarded as a worthwhile experiment to partially separate the particle cohort variability between different conditions, while later steps further separate the cohort variability between burner heights. The results are shown in Figure 8-2 and Table 8-10.

Table 8-7 – Black Thunder data summary.

12% O_2								
Height (cm)	5.08	5.715	6.35	7.62	10.16	15.24	20.32	25.40
Avg. T_p (K)	1703	1708	1726	1732	1725	1715	1718	1690
24% O_2								
Height (cm)	4.45	5.08	5.715	6.35	7.62	10.16	12.70	
Avg. T_p (K)	1837	1894	1913	1914	1919	1879	1859	
36% O_2								
Height (cm)	3.18	3.81	4.45	5.08	7.62	10.16		
Avg. T_p (K)	2038	2052	2103	2147	2135	2072		

Table 8-8 – Pittsburgh 8 data summary.

12% O_2									
Height (cm)	5.08	5.715	6.35	7.00	7.62	8.89	10.16		
Avg. T_p (K)	1822	1824	1872	1855	1873	1889	1898		
24% O_2									
Height (cm)	5.08	5.715	6.35	7.62	8.89	10.16			
Avg. T_p (K)	2037	2006	2054	2066	2077	2067			
36% O_2									
Height (cm)	3.18	3.81	4.45	5.08	5.715	6.35	7.62	8.89	10.16
Avg. T_p (K)	2028	2179	2207	2242	2248	2237	2245	2238	2186

Table 8-9 – Average particle diameter (μm) assigned for each O_2 condition.

O_2 Condition	**Black Thunder**	**North Antelope**	**Utah Skyline**	**Pittsburgh 8**
12% O_2	100	100	100	100
24% O_2	105	105	110	115
36% O_2	110	110	125	125

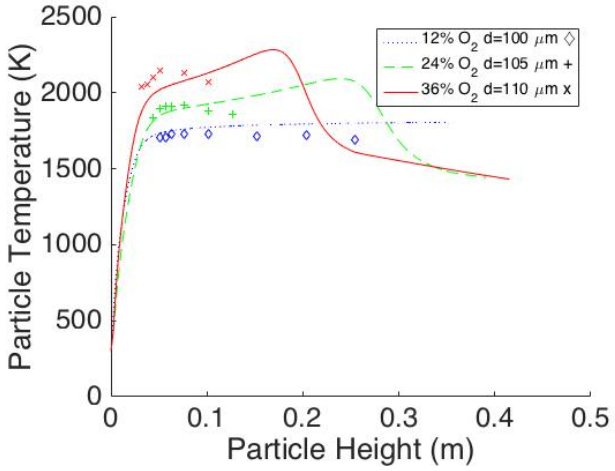

(a) Black Thunder Coal

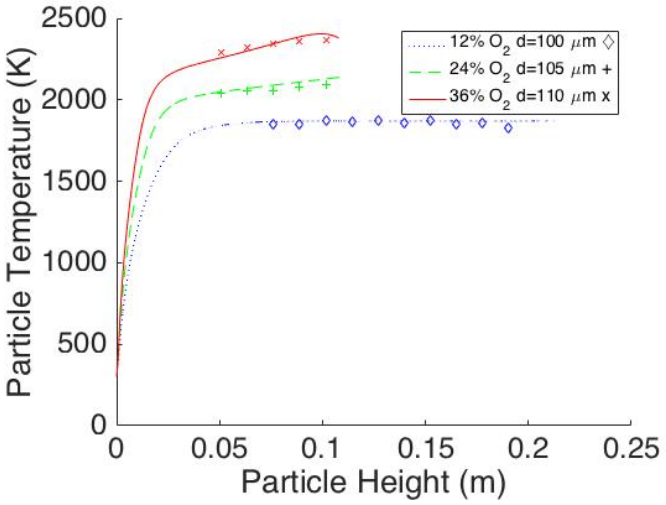

(b) North Antelope Coal

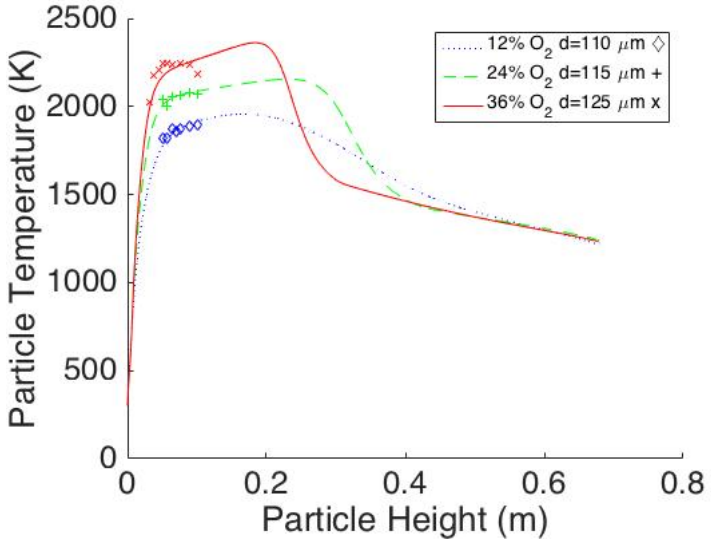

(c) Pittsburgh 8 Coal

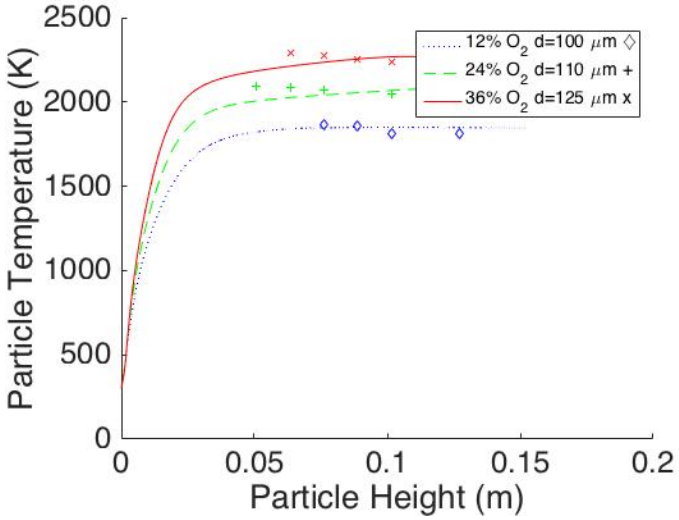

(d) Utah Skyline Coal

Figure 8-2 – Comparison of CCK/oxy performance with a single particle diameter for a given coal and O_2 condition.

Table 8-10 – Mean absolute error and max error using one diameter for each O_2 condition.

Black Thunder	**Mean Absolute Error (K)**	**Max Error (K)**	**Pittsburgh 8**	**Mean Absolute Error (K)**	**Max Error (K)**
12 % O_2	52	109	12 % O_2	19	49
24 % O_2	44	96	24 % O_2	14	30
36 % O_2	106	174	36 % O_2	56	108
North Antelope			**Utah Skyline**		
12 % O_2	12	43	12 % O_2	25	40
24 % O_2	24	34	24 % O_2	53	87
36 % O_2	26	39	36 % O_2	41	77

In general, the results are much improved over the more naïve assumption of a single particle diameter applied to all conditions, but there is still substantial bias due to the cohort variability even within a single O_2 condition. This is especially true of the Black Thunder coal and of the 36% O_2 condition for Pittsburgh 8 coal. The difficulties in these two coals is unsurprising because the diameter data are not available for these two coals, so the values used are only approximate, based on the data from the other two coals. The 36% O_2 condition is particularly uncertain because the lowest observed burner height was much lower for these two

coals. The Black Thunder and Pittsburgh coals also show a clear peak in particle temperature, followed by a slight decrease in particle temperature as burner height continues to increase. The drop in average particle temperature is not nearly sufficient to indicate near-extinction. Instead, it is quite consistent with and the temperature drop expected from slightly larger particles at the same conditions, further implying a need for a more detailed diameter profile.

8.6 CCK/oxy Optimization with two Diameters per O_2 Condition

Examining the data in Tables 8-2 and 8-3, a pattern in particle diameter is readily discernable. These trends show that in general, measured particle size either gradually increases, or, in the most intense burnout, particle size increases to a peak and then decreases. This is thought to be because, after a peak in particle size, diameter loss due to burnout becomes dominant; unsurprisingly, the size of the particles at peak diameter corresponds well with the size of the large end of the particle size cut (after accounting for predicted swelling). The trends led to the assumption that the data could largely be captured by each coal and O_2 condition were assigned two diameters per condition, as shown in Figure 8-3 and Table 8-11.This begins to incorporate the variability between particle cohorts that the data show at different observation heights. Note that the smaller diameter is modeled the line that heats up faster and to a higher temperature.

In the case of the 12% O_2 environment, the North Antelope coal was assigned diameter values from the mean of the data, rounded up. The diameters are rounded because the data are too noisy to provide an actual mean diameter down to the micron level, but rounded up because any given particle decreases in size with increasing burnout. Because there are few sharp jumps in particle diameter, it is likely that this diameter loss is gradual and not overwhelming until later

burnout. The Utah Skyline diameters were assigned in the same manner as the North Antelope, but the Black Thunder and Pittsburgh 8 data do not include the necessary detail. However, the North Antelope and Black Thunder coals are both subbituminous, so the diameter profile from the North Antelope was applied to the Black Thunder coal (extrapolated to the observed burner heights of the Black Thunder coal). This is an extrapolation made on tenuous grounds, but the data are insufficient for a better estimate, and the constraint of the known size cut keeps the extrapolation reasonable. The Pittsburgh 8 coal diameter is assigned in a similar manner from Utah Skyline (both are high volatile bituminous coals). The results are shown in Figure 8-3 and Table 8-12. The low mean and peak error values between model fit and measured particle temperature indicate a vast improvement over prior model predictions.

*Table 8-11 – Two diameter profiles for each condition.**

Coal Type	**Black Thunder**			**North Antelope**			**Pittsburgh 8**			**Utah Skyline**		
O_2 %	**12**	**24**	**36**	**12**	**24**	**36**	**12**	**24**	**36**	**12**	**24**	**36**
Height (cm)	**Diameter (µm)**			**Diameter(µm)**			**Diameter (µm)**			**Diameter (µm)**		
3.18			90						105			
3.81			90						105			
4.45		90	90						105			
5.08	90	90	90		100	105	98	100	105		100	
5.72	90	90					98	100	105			
6.35	90	90			100	105	98	100	115		100	115
7.00							98					
7.62	90		110	95	105	110	98	100	115	105	100	115
8.89				95	105	110	98	105	115	105		115
10.16	105	115	110	95	105	110	98	105	115	100	110	125
11.43				95							110	125
12.70		115		95						100	110	125
13.97				95								
15.24	105			100								
16.51				100								
17.78				100								
19.05				100								
20.32	105											
25.40	105											

*Diameters are only shown at locations where measurements were performed.

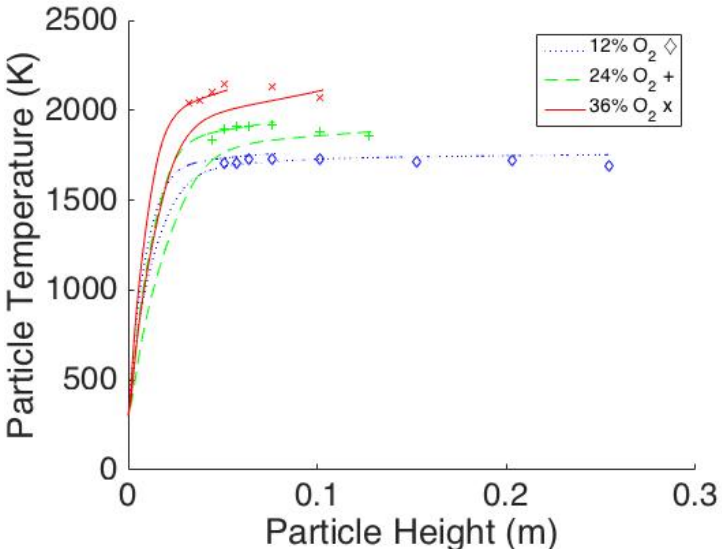

(a) Black Thunder Coal

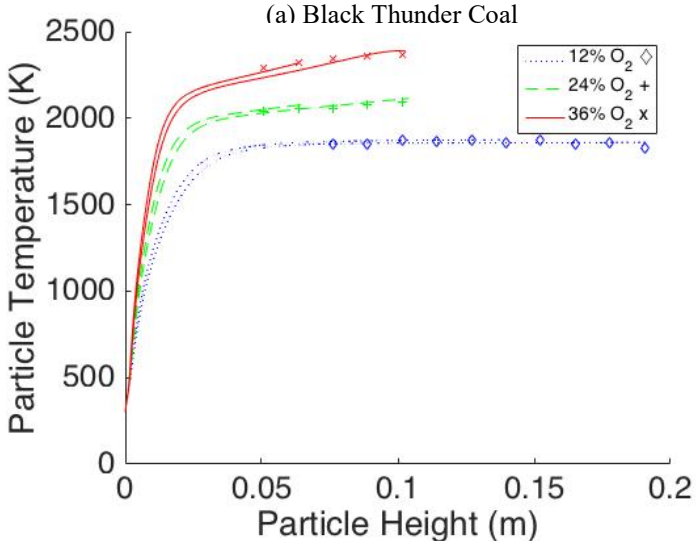

(b) North Antelope Coal

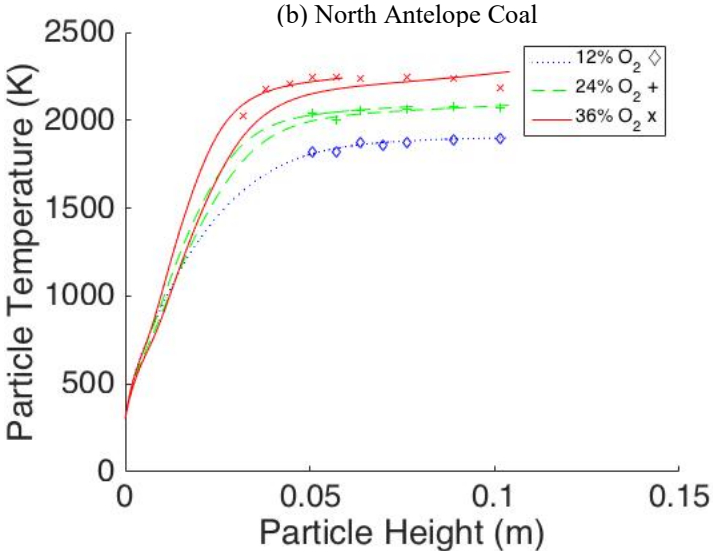

(c) Pittsburgh 8 Coal

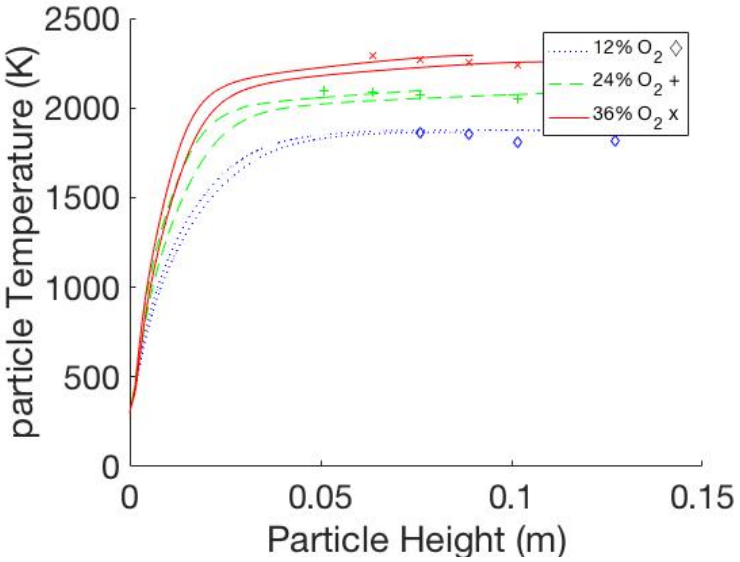

(d) Utah Skyline Coal

Figure 8-3 – CCK/oxy prediction with two particle diameters for each coal and O_2 condition.

Table 8-12 – Two diameters per O_2 condition.

Black Thunder	**Mean Absolute Error (K)**	**Max Error (K)**	**Pittsburgh 8**	**Mean Absolute Error (K)**	**Max Error (K)**
12 % O_2	29	63	12 % O_2	11	18
24 % O_2	16	36	24 % O_2	14	40
36 % O_2	32	82	36 % O_2	31	85
North Antelope			**Utah Skyline**		
12 % O_2	11	34	12 % O_2	33	66
24 % O_2	15	20	24 % O_2	37	81
36 % O_2	17	29	36 % O_2	29	48

8.7 Multiple Diameter Profiles

The results of the previous section are quite promising, and are as good as can be reasonably expected for coal particle predictions. All of the mean absolute error values are within the expected noise due to measurement error (±50 K), as are the majority of the maximum error values. The trends in error due to O_2 condition have largely disappeared, showing that much of the condition-based bias is accounted for, and the maximum values that fall outside the range of noise would easily be swallowed in the broad distribution of particle-to-particle variation.

However, unless the data are skewed, it is not expected to have so many maximum error values outside of range of the noise. Furthermore, the plots show some minor trends in the CCK/oxy model first over-predicting and then under-predicting systematically. The relatively large maximum errors imply a skew, and the systemic prediction error also indicates that some bias remains between the different observation heights. The data do not allow a complete profile of the exact actual particle diameter that should be used as an input for a given height (due to the competing effects outlined in the previous section), but they do allow more detailed estimates than shown thus far.

In this section, different diameters are allowed for comparison with data from each measurement height. In general, the diameter profiles shown in Table 8-13 are taken directly from the diameter profiles of the observed data (in the case of North Antelope and Utah Skyline), or extrapolated from the North Antelope and Utah Skyline diameter profiles (in the case of Black Thunder and Pittsburgh 8). These profiles have small increases in diameter added to the initial diameters of later-burnout particles, where the data imply that some diameter loss has occurred, because CCK/oxy accepts the **initial** diameter as an input, so where there is evidence that the diameter has decreased from the initial value, the decrease should be taken into account. In the case of a full profile of diameters, the CCK/oxy model accepts the initial diameter as an input, and integrates in time to create a complete time-temperature-location profile for each individual data point, with the goal of matching the comparable point of the predicted profile to the actual data point. Note that while the profiles are reasonable given the coal size cut, predicted swelling, and expected diameter loss due to burn out, the late-burnout diameters are a slight extrapolation. The specific profiles of each coal have a few points worth noting:

1. The extrapolated profile for Black Thunder and Pittsburgh 8 were simply set at a lower bound of 90 and 95 μm respectively. Those coals were observed at much lower heights than the North Antelope and Utah Skyline coals, but, given the particle size cut, it is unreasonable that the average particle diameter would continue to follow a sharp downward trend at low observation heights. Interestingly, the results in this section imply that the lower bound on the Pittsburgh coal should have been 105 microns, which is certainly a reasonable value given the uncertainty of the very early observation heights.

2. In general, the North Antelope profiles are directly from the data with small increases of between 2 and 6 μm added to the **initial** diameter for those data after the temperature data are observed to "peak." At that point, it is assumed that diameter loss has become more important than the higher observability and longevity of larger particles, which causes the mean diameter to gradually decrease or not increase sharply enough. In the last two points of the 36% O_2 condition, the mean particle size dropped quite substantially because of the rapid burnout of the intense condition. Here, 15 microns were added, to bring the value approximately to the peak observed size.

3. The Pittsburgh 8 coal is a rounded extrapolation from Utah Skyline as in the previous section, but more gradation was to allow than a mere two diameters per condition. Also, the 12% O_2 condition in Utah Skyline is too narrow and noisy to be overly informative, so there was no justification for a particular profile for Pittsburgh 8. Instead, the Pittsburgh 8 12% O_2 input was left fixed at 98 microns.

4. The Utah Skyline coal 12% O_2 environment is an anomaly in that it begins with a relatively high diameter and then decreases both diameter and particle temperature markedly. By examining the relevant data closely, it seems likely that fragmentation is to blame. The

first two observation heights have relatively high proportion of large particles. However, at the third observation height, the data show a significant increase in very small particles when the opposite trend is generally expected (and observed in the remaining data). This is shown in Table 8-5 with a sudden spike in the number of observed particles at the third burner height (a factor of 5 increase over the previous burner height, completely out of character with the rest of the data). Additionally, the third observation height shows a substantial increase of small, cold particles, either because the particles are nearing burnout or because fragmentation delayed ignition. Given that the data imply fragmentation, it would perhaps be more correct to exclude the skewed data (both the extraordinarily large particles and their fragments) but for the sake of consistency in this section and with past sections, this was not done.

5. Like North Antelope, the Utah Skyline particle diameter in 36% O_2 is observed to peak and then decrease, so the original diameter of the cohort is crudely estimated to be between 4 and 8 microns higher than the observed diameter, based on the amount of post-peak decrease and the range of observed diameters.

6. Because each observation height and condition are associated with a complete diameter prediction in the following figures, the lines were truncated for clarity. In general, a coal particle follows stages of heat-up, a peak/plateau temperature until 70-85% burnout, followed by a near-extinction event and slow burnout. The model accurately predicts all stages of burnout, but the late stages of burnout are not shown in the following figures to avoid an unreadable mess of partially overlapping model predictions.

Table 8-13 – Multiple diameter profiles.

Coal Type	Black Thunder			North Antelope			Pittsburgh 8			Utah Skyline		
O_2 %	12	24	36	12	24	36	12	24	36	12	24	36
Height (cm)	Diameter (µm)			Diameter(µm)			Diameter (µm)			Diameter (µm)		
3.18			90						95			
3.81			90						95			
4.45		90	90						100			
5.08	90	90	90		92	100	98	95	105		96	
5.72	90	90					98	98	110			
6.35	90	90			96	106	98	98	110		97	111
7.00							98					
7.62	90		105	86	96	110	98	100	120	106	102	120
8.89				89	101	111	98	100	120	103		119
10.16	95	105	115	87	106	106	98	105	125	101	107	124
11.43				88							112	127
12.70		115		91						103	115	128
13.97				85								
15.24	105			96								
16.51				98								
17.78				97								
19.05				107								
20.32	105											
25.40	115											

The results of using the multiple diameter profiles are shown in Figure 8-4 and Table 8-14. In general, the mean error is only slightly improved, but systematic bias is nearly eliminated and maximum errors now fall in the range of measurement error, with two notable exceptions.

First, the Pittsburgh 8 coal has an enormous maximum error that is introducing a skew into the entire data set, especially in the 36% O_2 environment. This is because the extrapolation of coal diameter to the very low observation heights for the Pittsburgh 8 data appears to be incorrect. In the extrapolation, the 36% O_2 Pittsburgh 8 data were assigned diameters as low as 95 microns, because the observations began much earlier than Utah Skyline (where the lowest

diameter was observed to be 111 microns). By updating the values to be in-line with the known early burnout values at the Utah Skyline 36% O_2 condition, the mean absolute error was reduced to 36 K and the maximum error decreased to 65 K. The sum squared of error also decreased by more than 50% all without re-optimization, because the single point in question contained more error than the sum of the entire data at all three O_2 conditions. Because of the dominant weight of that one point introducing a large skew in the optimization objective function, re-optimization greatly reduced the skew at 36% O_2 for the Pittsburgh 8 coal and reduced the mean and maximum absolute errors in the 36% O_2 Pittsburgh 8 data to 21 and 42 K respectively, effectively eliminating one of the two remaining sources of notable bias.

The other notable bias is, not coincidentally, in the same data set with the other maximum error beyond the range of measurement noise. The 24% O_2 environment for Utah Skyline coal has a bias from one of several possible sources: bias in model prediction due to imperfect submodels, inappropriate extrapolation for the initial diameter inputs, a skew in the data, etc. The extrapolation on the data seems the mostly likely culprit, and it must be emphasized that **all** of the diameter profiles in this section are, to some degree, an extrapolation. However, the extrapolation is quite reasonable to within a few microns given the data trends, and since the profiles were set prior to optimization, not adjusted post-optimization to match the CCK/oxy model, it is likely that any coal initial diameter profile following the observed trends in the data would be able to obtain a very satisfactory fit. This conclusion is strongly implied by the great improvement in allowing different diameters for each condition, and further allowing two diameters per condition to capture the broadest strokes of the diameter profile, while there is only a modest improvement with a complete diameter profile.

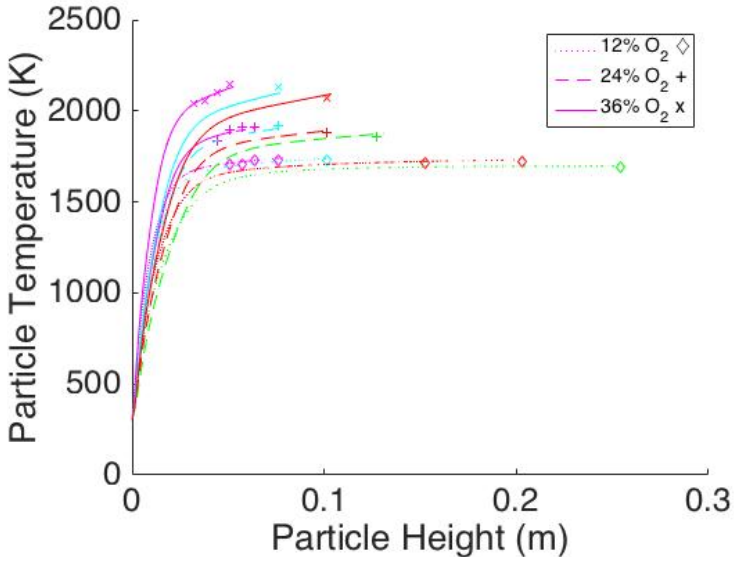

(a) Black Thunder Coal

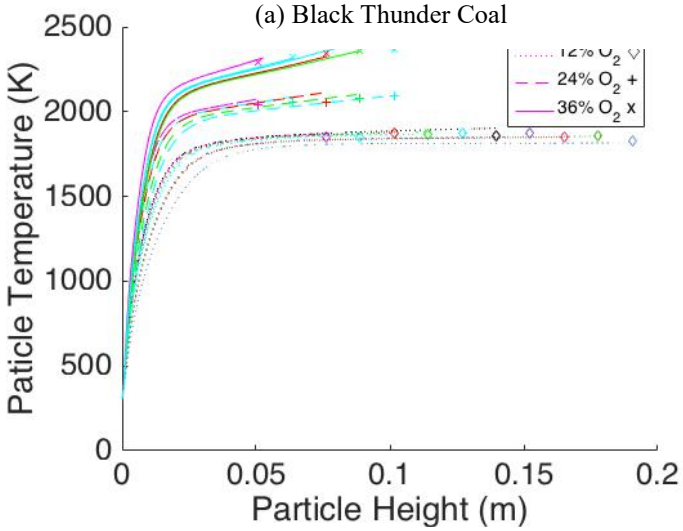

(b) North Antelope Coal

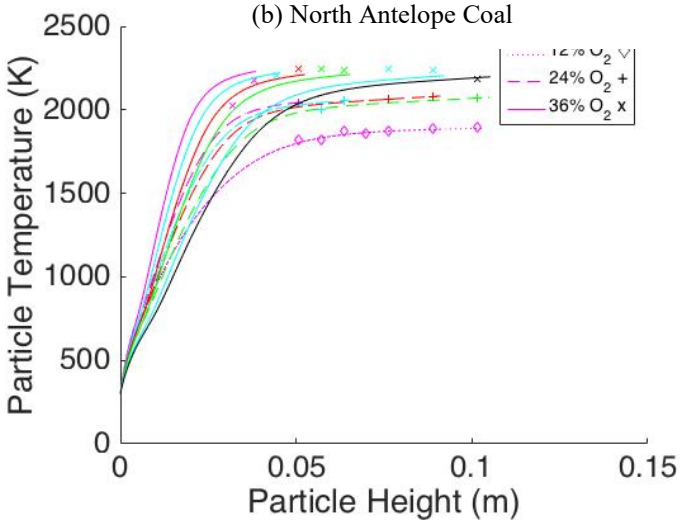

(c) Pittsburgh 8 Coal

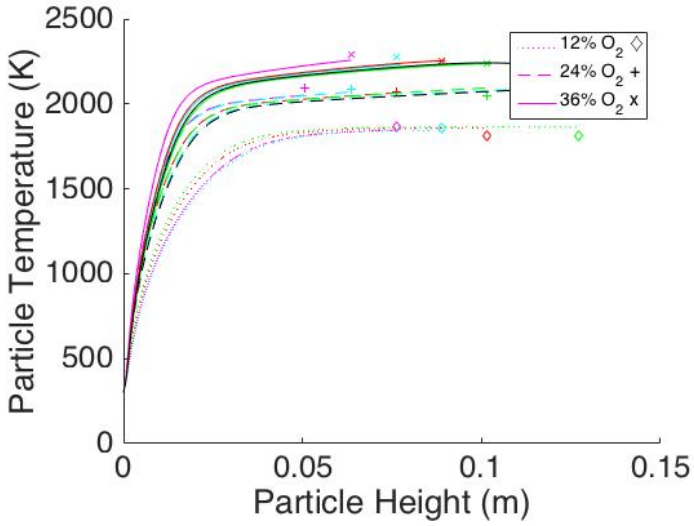

(d) Utah Skyline Coal

Figure 8-4 – Comparison of four coals in oxy-coal conditions with a complete char particle diameter profile to experimental data.

Table 8-14 – Difference between calculations with multiple diameter profile and measured particle temperatures.

Black Thunder	**Mean Absolute Error (K)**	**Max Error (K)**	**Pittsburgh 8**	**Mean Absolute Error (K)**	**Max Error (K)**
12 % O_2	9	14	12 % O_2	11	22
24 % O_2	16	26	24 % O_2	9	37
36 % O_2	18	40	36 % O_2	49	157
North Antelope			**Utah Skyline**		
12 % O_2	13	43	12 % O_2	33	48
24 % O_2	28	52	24 % O_2	41	81
36 % O_2	13	27	36 % O_2	17	44

8.8 Late Burnout

It should be noted that the Pittsburgh 8 data also included a selection of data points at far higher observation heights than any of the other data. Predicting the relevant diameters would have been an extreme extrapolation, so they were excluded from the optimization, but they are shown below in Figure 8-5 and Table 8-15 (a discussion of relevant kinetics follows in the next section).

Initial diameter values were selected such that CCK/oxy precisely predicted the measured mean particle temperature (upper and lower particle diameter bounds were also plotted for reference). These diameters were not selected on any basis other than that they fit the measured mean particle temperature at a given height, in contrast to all prior work in this chapter. The diameters required to match the temperature data are uniformly unfeasible for such late burnout given the rest of the data, but this is in fact exactly what would be expected. The particles that survive to late burnout are either exceptionally persistent or they are in a near-extinction regime or near-burnout as discussed by Sun and Hurt (2000). Persistent particle are likely larger particles that have a particular ash content and/or maceral character that requires a longer residence time to consume. In the case of near-extinction or burnout, the particles have experienced a very significant and rapid transition to a nearly inert particle that is heated almost entirely by ambient conditions (rather than exothermic oxidation). CCK/oxy accurately predicts both states, and it is seen in the rapid decrease of the particle temperature profile (corresponding to roughly the last 15% of burnout), followed by a long, slow decline in particle temperature.[13] Because the transition between burning and near-extinction is quite rapid, and the particles are far from uniform in their burning characteristics, it is quite unlikely that the observation height would happen to be appropriate to observe a significant number of particles mid-transition. Instead, the observations are an average of particles that are just barely hot enough to be detected, and particles that continue to burn. This average is weighted by the proportion of particles that are near burnout vs. those still burning rapidly, and that weight shifts (as expected) toward near-burnout for progressively longer residence times. Also as expected, this shift is more rapid for more intense O_2 environments. In short, the Pittsburgh 8 late burnout data support the

[13] The slow decline is due largely to the continual decrease in ambient gas temperature with height in the particular experimental setup.

validity of the kinetic optimization done on earlier burnout data, and all but one of the particles fall within an appropriate diameter window (as determined by the reference diameter sizes) and show a reasonable weighted average.

The largest disagreement between the model and the data in Figure 8-5 is the last point in the 36% O_2 environment. No diameter input into CCK/oxy, no matter how small, intersects that point, indicating that it is essentially completely converted, and the relevant energy balance is that of an inert particle. This in turn means that the kinetic submodel in CCK/oxy is no longer relevant to that particle. Instead only the energy balance is relevant, and no set of coal-specific inputs into CCK/oxy allow the energy balance prediction to intersect the point in question, which leaves two potential conclusions: 1) Some of the commonly accepted energy balance assumptions are incorrect in this case (true, but probably not significant), or 2) the gas temperature profile and/or environmental wall temperature profile are slightly incorrect (also true in some degree, and more significant).

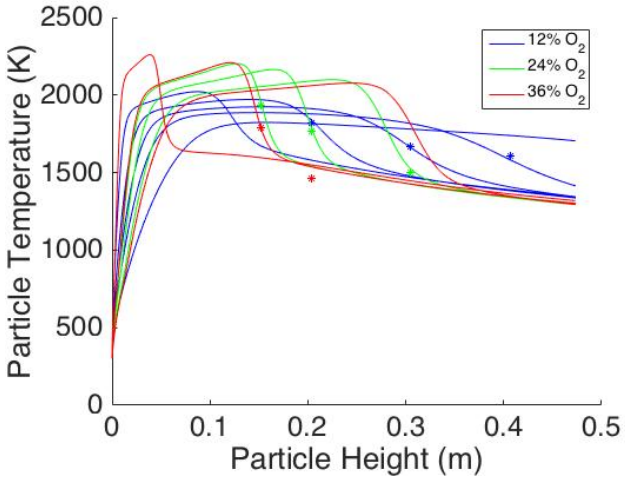

Figure 8-5 – CCK/oxy model calculations with late burnout Pittsburgh 8 coal data from Shaddix and coworkers (Shaddix and Molina, 2009; Geier et al., 2012) using the measured particle diameters.

Table 8-15 – Diameter values that match late burnout predictions of particle temperature.

Diameter Designation	12% O_2	24% O_2	36% O_2
Lower Diameter Bound (μm)	60	60	60
Diameter Match (μm)	77	93	91
Diameter Match (μm)	89	104	
Diameter Match (μm)	100		
Upper Diameter Bound (μm)	125	120	125

8.9 Kinetic Parameter Results

The optimized values of the kinetic parameters for this data set are given in Table 8-16. These values represent a local minimum in the kinetic parameter space, and are not unique values. This is expected and in fact unavoidable in any skeletal reaction mechanism because each reaction (R1-R8) represents an umbrella reaction for an enormous number of similar reactions involving the complex carbon chemistry of the char, and consequently, the kinetic parameters have little physical meaning. Even a perfectly correct, physically meaningful model will have an infinite number of feasible parameter sets located in a "valley" in parameter space because of the noise in the experimental data. In the case of highly auto-correlated parameters (such as A and E in the Arrhenius form), the "valley" in parameter space takes on a distinctive shape, and in the case of high dimensional parameter space in a model with limited physical meaning and correlated parameters, the single "valley" becomes many, exceptionally narrow, "valleys" each with a local minimum. This is the case of all but the simplest kinetic schemes, and there is no analytical solution to find either a local or absolute minimum, so optimization algorithms are used instead to find a local minimum. The location of the local minimum will depend on the initial guess value, but as long as appropriate constrains are set, the minimum of one "valley" is as valid as another. The optimization routine was executed from several different initial guess values, and generally found an equivalent "valley." In the small fraction of cases where the

optimization ended in a substantially different local minima, failure was obvious from the results of the objective function, and the failed optimization was discarded.

Table 8-16 – Kinetic parameters optimizations.

Parameter	Black Thunder	North Antelope	Pittsburgh 8	Utah Skyline
k_3 (mol/cm^3)	2.18×10^{10}	1.39×10^{10}	2.13×10^{8}	2.39×10^{10}
k_7 (mol/cm^3)	1.21×10^{9}	1.60×10^{9}	3.63×10^{8}	7.28×10^{9}
$E_{R,3}$ (kJ/mol)	117	117	180	130
$E_{R,7}$ (kJ/mol)	210	240	267	272

The kinetic parameters in Table 8-16 apportion carbon consumptions between the three reactive gases (O_2, CO_2, and H_2O) as seen in Table 8-17. There are two trends of interest: first, with the exception of Pittsburgh 8, the carbon consumption due to O_2 increases with higher O_2 concentration, which is unsurprising. Second, and somewhat surprising, the very high levels of O_2 do not completely marginalize the conversion due to CO_2. This is likely due to the relative magnitudes of the temperature-dependent exponential term in the relevant gasification and combustion Arrhenius equations. The high activation energy of the gasification reactions makes the exponential terms in the rate equation increase more rapidly with temperature than for the combustion reaction, and hence the gasification reactions stay significant at the high particle temperatures reached by the high O_2 concentrations.

Table 8-17 – Conversion fraction due to each gas (particle diameter of 100 microns)

O_2 Condition	**Black Thunder**			**North Antelope**			**Pittsburgh 8**			**Utah Skyline**		
	O_2	CO_2	H_2O	O_2	CO_2	H_2O	O_2	CO_2	H_2O	O_2	CO_2	H_2O
12%	0.72	0.25	0.03	0.82	0.16	0.02	0.89	0.09	0.02	0.82	0.15	0.03
24%	0.79	0.18	0.03	0.85	0.13	0.02	0.87	0.11	0.02	0.82	0.14	0.03
36%	0.83	0.15	0.03	0.86	0.11	0.02	0.87	0.11	0.03	0.85	0.12	0.04

8.10 Extrapolation from 12% O_2 Data

The literature data used here are of exceptional quality and detail, with a very wide range of O_2 concentrations and parallel experiments using both CO_2 and N_2 as the gas diluent. Unfortunately, this level of detail and O_2 range is unusual, so it is desirable to determine whether or not the CCK/oxy model is effective when extrapolating from only a single O_2 concentration, rather than the entire span of the O_2 range. The 12% case was chosen for the single condition optimization because, while it is the least informative about the effects of extreme conditions, the overwhelmingly most common literature scenario is a relatively low O_2 concentration. The following kinetic parameter optimizations were performed using the same diameter profiles shown in Table 8-13, but only the four data sets from the 12% O_2 environment were used. The resultant kinetic parameters were then used to extrapolate to the 24% and 36% O_2 conditions for their respective coals. Kinetic parameter values are given in Table 8-18. The results are shown in Figure 8-6 and Table 8-19, while the bullet points below highlight several important points of the results:

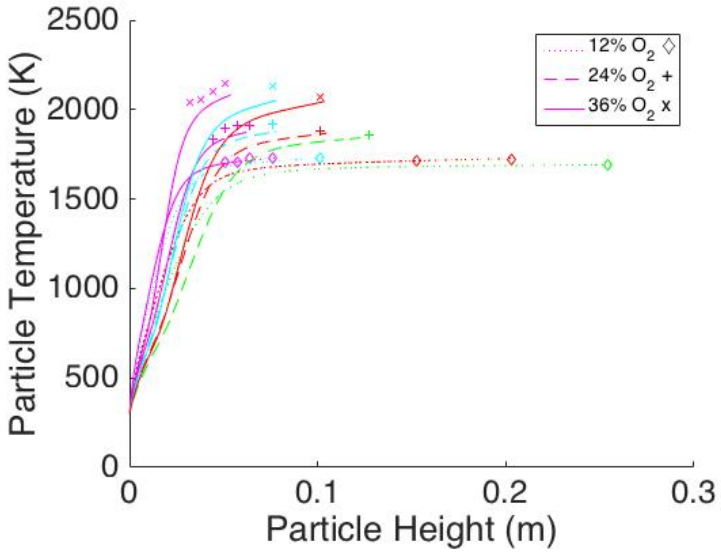

(a) Black Thunder coal

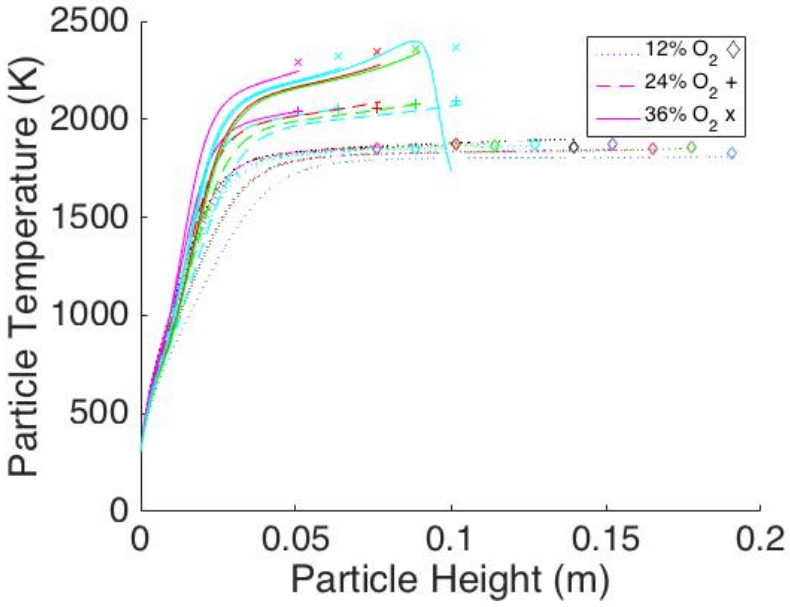

(b) North Antelope coal

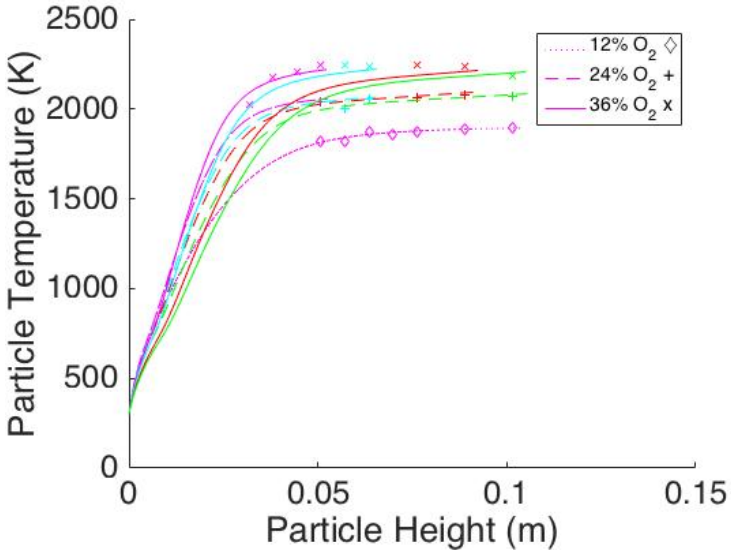

(c) Pittsburgh 8 coal

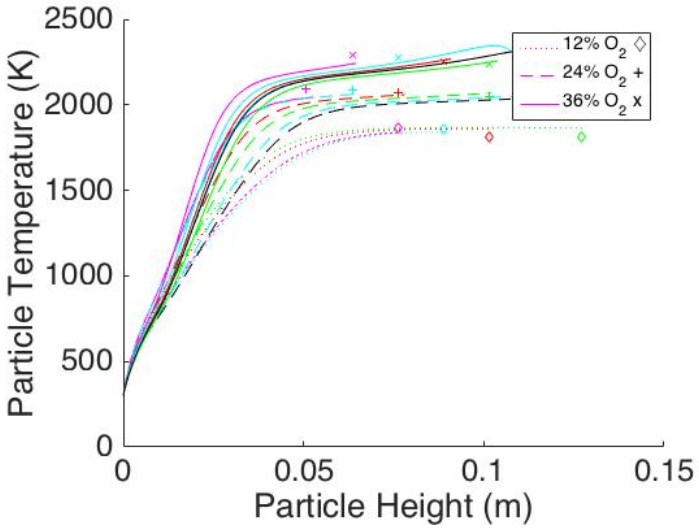

(d) Utah Skyline coal

Figure 8-6 –Predictions in oxy-coal conditions from 12% O_2 data only.

Table 8-18 – Kinetic parameters of the 12% O_2 oxy-coal system.

Parameter	Black Thunder	North Antelope	Pittsburgh 8	Utah Skyline
k_3 (mol/cm^3)	5.06×10^8	1.00×10^8	1.90×10^8	6.54×10^7
k_7 (mol/cm^3)	6.37×10^8	4.71×10^8	4.23×10^9	1.16×10^8
$E_{R,3}$ (kJ/mol)	178	180	180	180

Table 8-19 – Absolute errors from an optimization using only 12% O_2 data in an oxy-fuel environment.

Black Thunder	**Mean Absolute Error (K)**	**Max Error (K)**	**Pittsburgh 8**	**Mean Absolute Error (K)**	**Max Error (K)**
12 % O_2	5	11	12 % O_2	9	16
24 % O_2	38	58	24 % O_2	17	46
36 % O_2	69	92	36 % O_2	31	58
North Antelope			**Utah Skyline**		
12 % O_2	13	39	12 % O_2	35	53
24 % O_2	11	29	24 % O_2	31	60
36 % O_2	49	69	36 % O_2	49	89

1. Only the activation energy and preexponential factor of R3 were optimized in this case. This was done because a brief exploration of the gasification parameters showed that any reasonable set of gasification kinetic parameter values gave equivalent results at both the

12% O_2 gas composition *and* at the higher concentrations. It was observed that the optimization routine provided no significant inference regarding the gasification parameter values, because the gradient in the gasification dimensions of parameter space was close to zero for the 12% O_2 data (i.e., the gasification reaction was exceptionally weak relative to the noise at low temperature conditions). While the gasification kinetic parameters are certainly important for the 24 and 36% O_2 conditions, little could be inferred about them from the 12% optimization, so they were fixed at the values found in the previous optimization.

2. Because optimizations in complex parameter spaces very often only find local minima, each kinetic parameter optimization was executed four times with widely different initial guess vectors. The resultant values were sometimes quite different in individual optimizations of k_3 and E_3 (as expected in a complex space of many "peaks" and "valleys"), but the total rate constant and the goodness of fit (from the sum squared of error of the objective function) were in excellent agreement. The figures below were generated using one of the four sets of results (chosen at random), and the values in Table 8-19 are averages of the replicate results.

3. In evaluating the usefulness of the extrapolations shown below, two distinct questions must be asked, and this evaluation endeavors to answer only one of the two. First, it is of interest to know if the extrapolated curves have the correct shape and magnitude. In this case, that means: 1) are the particle predictions roughly the correct temperature, and 2) does the shape of the prediction curve follow the shape of the data. The second question of interest determines how well the time axis from data corresponds to the extrapolated predictions. It is necessary to decouple these two questions because even the most minor shift in the time axis can cause a large shift in temperature for very early or very late particle burnout, which gives

extremely misleading results. For example, the first data point of the Black Thunder coal in the 36% O_2 extrapolation is offset from the data by approximately 2 milliseconds, which results in an error between prediction and data of roughly 160 K, which far exceeds any of the other error values in the extrapolation. Furthermore, that two milliseconds of time disappear with a slight shift of diameter or gas temperature profile (well within the range of uncertainty), and the true particle temperatures span a wide range due to slight variations in maceral character, heat capacity, or particle shape.

4. A more accurate evaluation acknowledges that there is significant variation in the exact timing of initial particle heat-up and in the exact time of particle near-extinction. The small variation on the time axis is entirely within the variation of particle size and character, and the resulting large temperature change from such a small variation emphasizes the impact and importance of describing the char particles as a distribution rather than a point estimate. To accurately answer the question of prediction trends and magnitude, the first point of the Black Thunder coal and the last point in the Utah Skyline coal from the 36% O_2 environment are not included in the average error values in Table 8-19.

5. The North Antelope and Black Thunder temperature extrapolations were observed to consistently under-predict the data by a small amount. This is due to a slight imbalance between the gasification and combustion carbon conversion pathways. However, as described in point 1 above, other reasonable value of the gasification kinetics neither exacerbate nor correct this deficiency, so it is thought that the noise of 12% O_2 data can be better accommodated with slightly less aggressive combustion kinetics than the value suggested by the entire body of data. These less aggressive kinetics have a very small positive impact on the 12% data under optimization simply because of random chance in a

small data sample. In the extrapolation to the entire data set, this translates to a small negative impact on the rest of the data set. No immediate solution presents itself; small, uniform data samples are simply of less value that larger, more diverse samples.

6. On the whole, the results show that the extrapolation from low O_2 concentration up to very extreme concentrations was remarkably successful, and the CCK/oxy model may be expected to function over an exceptionally wide range of conditions. This strongly implies that the submodels effectively capture the necessary physics to make CCK/oxy a powerful predictive tool. However, it must be emphasized that the data here are a relatively small sample size of only four coals, and the current results would benefit from further validation with a wider range of data. Also, it is highly desirable to collect as much data at as many conditions as possible to minimize the type of bias observed in the Black Thunder and North Antelope results.

8.11 Extrapolation from 12% N_2 Data

Because oxy-coal combustion has only become a popular research topic relatively recently, most literature data are not only obtained over a relatively narrow (and low) O_2 range, but are also almost always in a conventional regime using N_2 as the diluent. The CCK/oxy model would therefore be of most use if it could reasonably be calibrated from data collected at conventional conditions. Fortunately, the literature oxy-coal data used here were collected in parallel with data of the same coals at the same O_2 concentration. The two experimental conditions differed only in that the second set of experiments used N_2 as the diluent. In general, the method outlined in Section 8.10 applies to the optimizations that resulted in Figure 8-7 and Table 8-21 but differences and important similarities are highlighted below: The optimizations in this section were carried out using N_2 data and conditions as inputs to the CCK/oxy model, but the plots and

tables are extrapolations that took the kinetic parameters obtained from the 12% N_2 data optimizations, and applied them to all three O_2 conditions in the oxy-fuel environment.

1. Table 8-20 shows the diameter values relevant to this set of experiments.
2. As in Section 8.10, four replicate optimizations were run for each set of data, and all had excellent agreement with each other except for of one of the Utah Skyline replicates. This exception found a local minimum substantially farther from the minima found by the other three replicates (i.e., the optimization routine failed to find a reasonable optimum in one instance), and the results from the exception were discarded.
3. The Pittsburgh coal data were unique in that the particle temperatures in N_2 diluent were actually substantially lower than the particle temperatures in CO_2 diluent. This one data set is inconsistent with theory, past experience, and all of the other 23 experimental data sets referenced here. The author of the paper containing the inconsistent Pittsburgh coal data theorized that this was because the gas temperature profile (which cannot be perfectly regulated) was colder in the N_2 environment than in the CO_2 environment (Shaddix and Molina, 2009). This is true, but even when accounting for the difference in profile temperature, the particles in the N_2 environment are predicted to be roughly 50 K hotter than the CO_2 environment, due to slower O_2 diffusion and an endothermic gasification reaction in the CO_2 environment. In the N_2 environment data, the particles were roughly 150 K *colder* than in the CO_2 environment for Pittsburgh coal. Adding in the prediction that they should be 50 K hotter, the total discrepancy is on the order of 200 K. Lacking a reasonable explanation for these anomalous data, the Pittsburgh coal data from the N_2 experiment are not shown here.

4. As before, the first point of the Black Thunder data and the last point of the North Antelope data are slightly off-set in time, and not included in the averages for Table 8-21.

5. The Black Thunder and North Antelope coals have the same bias towards under-prediction of the particle temperature as before, and are in general quite similar to the predictions from the extrapolations based on the 12% O_2 in oxy-fuel conditions. This implies that there is no significant reaction O_2-char reaction mechanism change between oxy-coal and conventionally fired coal.

6. The N_2 Utah Skyline coal results did not extrapolate well to the oxy-fuel data, which could indicate either: 1) that there *is* a mechanism change between the oxy-coal and conventional environments, 2) the N_2 Utah Skyline data are erroneous, or 3) that the exceptionally small N_2 Utah Skyline data set (only 3 data collection heights) is insufficient to accurately capture the combustion kinetics. The last point (option 3) is thought to be the most likely explanation.

Table 8-20 – Diameter profiles for N_2 experiments.

Coal Type	**Black Thunder**	**North Antelope**	**Utah Skyline**
O_2 %	**12**	**12**	**12**
Height (cm)	**Diameter (µm)**	**Diameter(µm)**	**Diameter (µm)**
4.45	100		
5.08	100		
5.72	100		
6.35	100	94	
7.62	100	98	102
8.89		96	99
10.16		92	99
11.43		94	
12.70	110	97	

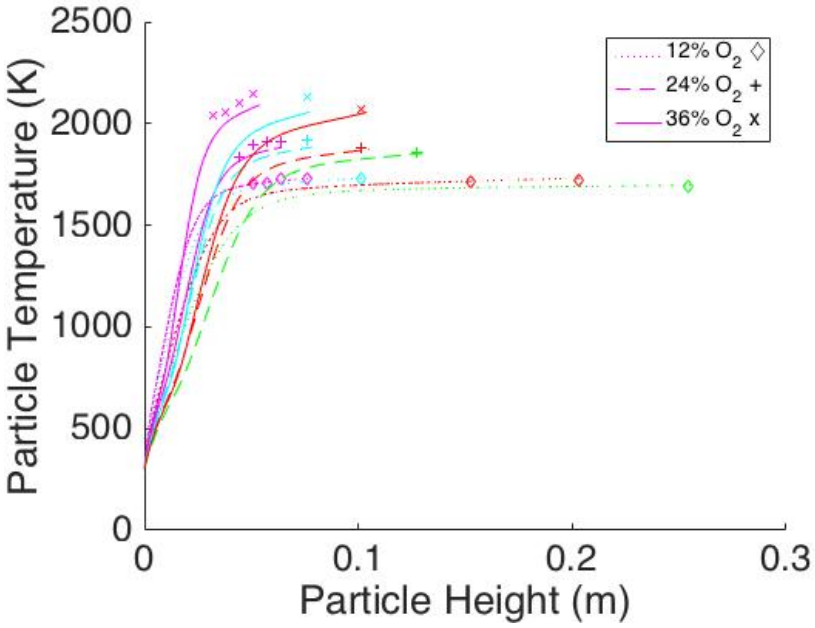

(a) Black Thunder coal

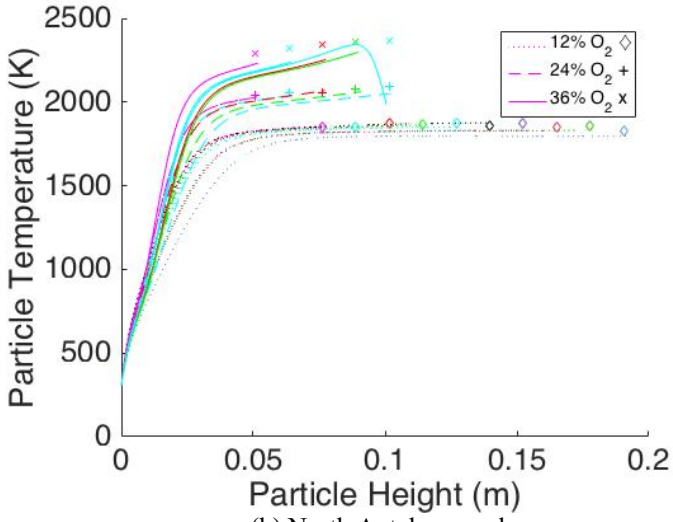

(b) North Antelope coal

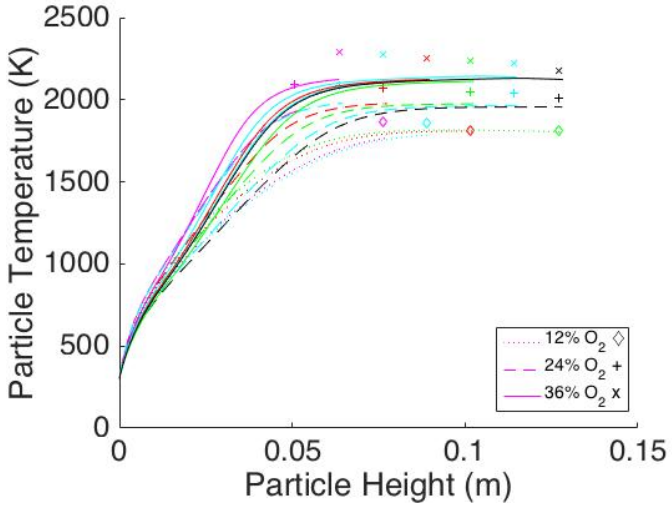

(c) Utah Skyline coal

Figure 8-7 – Predictions in conventional conditions from 12% O_2 data only.

Table 8-21 – Absolute errors from an optimization using only 12% O_2 data in a conventional coal environment.

Black Thunder	**Mean Absolute Error (K)**	**Max Error (K)**	**Pittsburgh 8**	**Mean Absolute Error (K)**	**Max Error (K)**
12 % O_2	5	15	12 % O_2	N/A	N/A
24 % O_2	31	50	24 % O_2	N/A	N/A
36 % O_2	57	84	36 % O_2	N/A	N/A
North Antelope			**Utah Skyline**		
12 % O_2	19	44	12 % O_2	55	114
24 % O_2	19	43	24 % O_2	109	190
36 % O_2	83	102	36 % O_2	135	181

On the whole, the extrapolation from conventional data at low O_2 concentrations to the full range of oxy-fuel data has some promise, but is far from conclusive. Further validation (additional data) is needed. Kinetic parameters are given in Table 8-22.

Table 8-22 – Kinetic parameters for the 12% O_2 condition in conventional air-fired regime.

Parameter	**Black Thunder**	**North Antelope**	**Pittsburgh 8**	**Utah Skyline**
k_3 (mol/cm^3)	1.00×10^8	1.00×10^8	N/A	2.21×10^6
k_7 (mol/cm^3)	2.20×10^9	1.00×10^8	N/A	9.41×10^6
$E_{R,3}$ (kJ/mol)	175	180	N/A	179

8.12 Simultaneous Optimization of Multiple Data Sets

This section was inspired by the promising results of the other sections. The CCK/oxy model appears to be a great improvement over past models in both oxy-coal and conventional conditions. This is attributed to the more exacting convergence tolerances, numerous improvements in key submodels, and especially the vast improvement in the annealing submodel. The annealing submodel is key to predicting changes in coal conversion kinetics in the wide variety of preparation conditions relevant to coal kinetics experimental data. These data include such divergent conditions that, lacking an excellent annealing model, there is little hope of reconciling multiple experiments simultaneously. However, with the current CCK/oxy model yielding promising predictions for extrapolated severe combustion conditions, and the marked improvement of the annealing model, it is reasonable to attempt a coal-general kinetic correlation. Such a coal-general model would ideally require only the most commonly available coal data as inputs (i.e., the proximate and ultimate analysis), but would certainly benefit from the additional structural information contained in NMR parameters. In this section, the simplest and most naïve attempt at a coal-general kinetic correlation is tested. It is expected to be far from adequate, but the attempt provides a valuable foundation for future model forms. Figure 8-8 shows the results of optimizing Equations 8-1 and 8-2 for Utah Skyline, Black Thunder, and North Antelope coals, while the Pittsburgh 8 coal predictions are an extrapolation.

$$A_3 = a_3 M_\delta + b_3 \qquad 8\text{-}1$$

$$A_7 = a_7 M_\delta + b_7 \qquad 8\text{-}2$$

The results are approximately the same when optimizing any three of the four oxy-coal data sets used in this chapter. Clearly, the results are far from the excellent predictions given by optimizing the kinetic parameters directly, but they are not hopeless. In general, only the 36% O_2

condition is extremely far from the data, and it is not unreasonable to suggest that reworking the kinetic scheme, and attempting other kinetic correlation forms (based on NMR parameters) would yield acceptable results. Equations 8-1 and 8-2 (repeated from section 7.1.7) contain four of the parameters, which are used in a simple correlation for determining the preexponential factor based on a coal specific NMR-based chemical structure parameter, where M_δ is the average mass of a side chain in the initial chemical structure of the coal. The coal structural parameters may be predicted from a correlation for NMR parameters from the proximate and ultimate analysis (Genetti, 1999; Genetti et al., 1999).

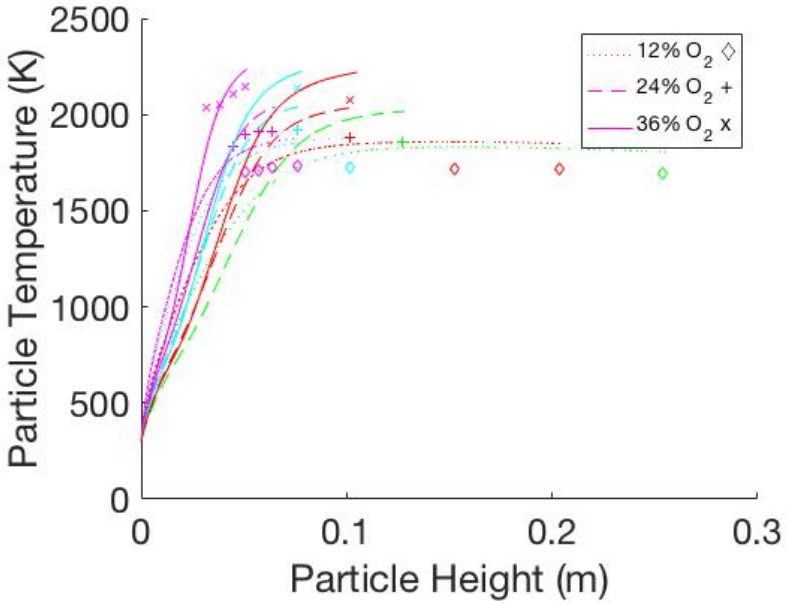

(a) Black Thunder Coal

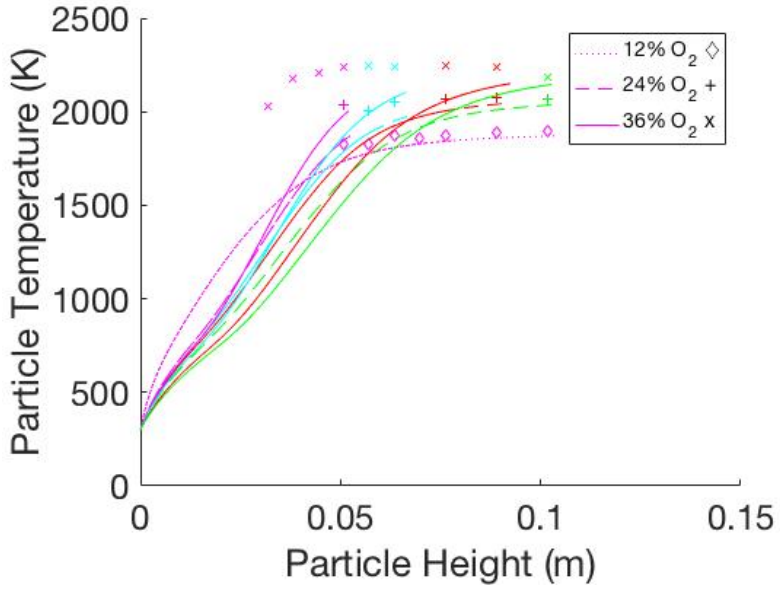

(b) North Antelope Coal

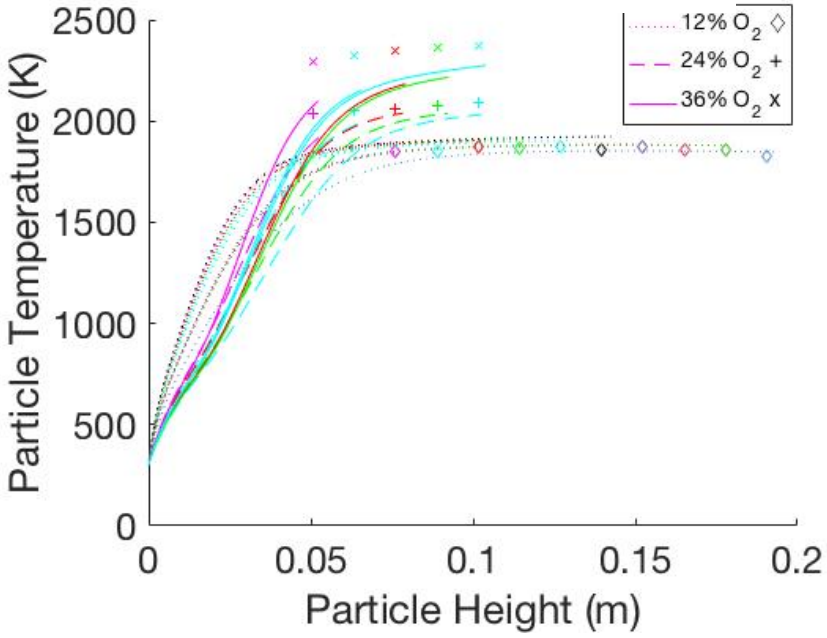

(c) Pittsburgh 8 Coal

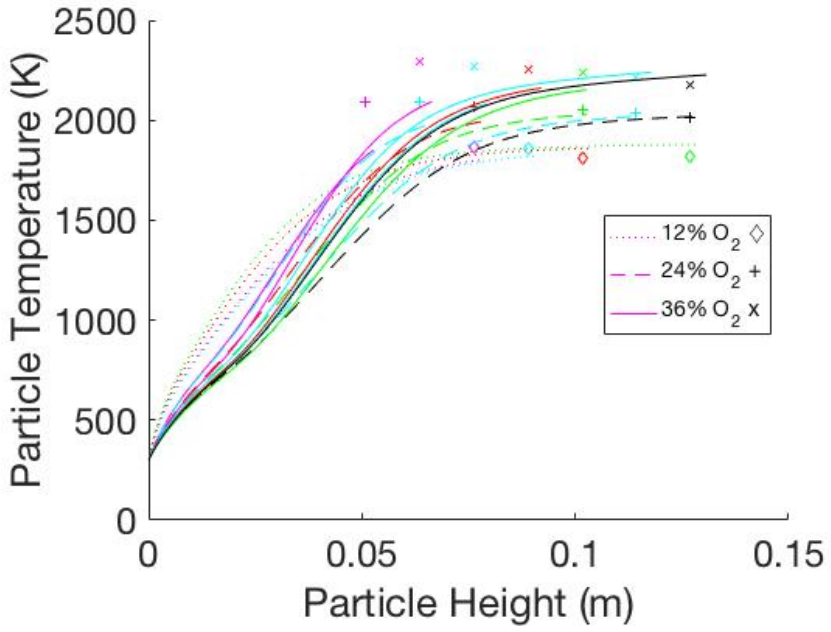

(c) Utah Skyline Coal

Figure 8-8 – Representative plots of particle temperature profiles optimized using a simplified coal-structural correlation.

8.13 Summary and Conclusions

An extended comprehensive coal char conversion model (Carbon Conversion Kinetics) was evaluated in the extremes of oxy-coal combustion environments. Specifically, the model was validated and explored by optimizing the model oxidation and gasification parameters to match a selection of the available oxy-coal data from the literature. The validation revealed:

1. The CCK/oxy model matched the available data extremely well, with enormous improvement over past attempts using the CCK model.(Holland and Fletcher, 2016; McConnel and Sutherland, 2016) The CCK/oxy model was able to simultaneously fit all O_2 conditions for a given coal with a single set of kinetic parameters. This was largely due to improvements in the devolatilization, swelling, and mode of burning models, as well as more exacting numerical solutions. The thermal annealing model is also exceptionally sensitive, but it is so tightly coupled to the kinetic preexponential factor that the submodel has minimal

impact when optimizing the kinetic parameters of a single coal in a narrow range of heating rates and peak temperatures. Instead, the annealing model is vitally important to any attempt to create coal-general kinetic correlations or in exploring widely varying heating rate and peak temperature regimes with a given coal.

2. The CCK/oxy model, when optimized to the 12% O_2 oxy-coal data **only**, made reasonable extrapolations to 24 and 36% O_2 conditions.

3. The CCK/oxy model, when optimized to the 12% O_2 conventional fired condition, made reasonable extrapolations to all levels of oxy-coal firing in two of three cases. These results are inconclusive, but imply that data collected in conventional firing conditions may be useful in determining kinetic parameters relevant to oxy-coal scenarios.

4. In oxy-fuel conditions, several competing effects complicate the combustion regime. These effects are mainly due to high concentrations of gasification reactants (especially CO_2), high temperatures that accompany enhanced O_2 levels, and a balance between endothermic and exothermic reactions. The CCK/oxy model predictions are (as anticipated): 1) that O_2 combustion is by far the dominant reaction pathway, 2) that gasification becomes relatively less important at more intense oxygen conditions, and 3) that gasification becomes relatively more important at high temperature. The last two effects are in competition, and the second effect proved dominant here.

5. The ability of the CCK/oxy model to match combustion data using an oversimplified correlation for coal combustion and gasification kinetics was briefly explored. The results showed that the correlation was not sufficiently detailed (as expected), but that there is significant potential for future work. In aggregate, the results of this chapter indicate that CCK/oxy is a remarkable improvement in capturing coal combustion physics, and the new

submodels may allow a much larger portion of the literature data to be simultaneously compared in the same model to finally create a coal-general kinetic correlation.

Finally, as the present work was intended to support predictive boiler design via computational fluid dynamics simulation, a brief suggestion for CFD application was outlined. In this work, it was observed that both particle diameter distributions and particle reactivity distributions are vitally important to accurate model predictions. As CFD work ideally models the entirety of both distributions, accurate descriptions of both distributions must be estimated as closely as possible. This estimation is problematic when data are collected via radiant particle detection, because certain subsections of the activity and size distribution fall below the lower temperature and size limit of detectability.

9 SUMMARY AND CONCLUSIONS

This work was intended to create a comprehensive coal-char conversion model suitable for oxy-coal conditions. The new model was intended to incorporate a high level of physical detail with the particular goal of using the highly detailed model to train situation-specific, low-cost surrogate models. The desired model (CCK/oxy) was created by 1) applying an exceptionally detailed sensitivity analysis, 2) extending or replacing key submodels with more physically realistic models (including models developed through original research), and 3) validating the new model in a broad selection of relevant conditions.

9.1 Sensitivity Analysis

A thorough global sensitivity analysis was performed on the CCK code, which allowed all fundamental parameters to vary simultaneously and produced several thousand sensitivity measures that together comprised a holistic view of model parameter dependence. The analysis was the first full-model sensitivity test for a comprehensive coal conversion code, and it successfully confirmed expected, intuitive results (i.e., the importance of kinetic parameters and particle diameter). More importantly, several other parameters were found to be sensitive beyond what simple intuition could account for, especially the mode of burning parameter and the annealing submodel. The analysis was broadened by including four different coal types at three widely disparate sets of combustion conditions, and the most sensitive parameters were found to be highly consistent and broadly applicable to any physically realistic, comprehensive coal

conversion code. Most importantly, the sensitivity analysis targeted the submodels and parameters most in need of further research and modeling efforts, which in turn guided the balance of the work reported here.

9.2 Coal Char Annealing

A new coal char thermal annealing submodel was developed to include physically observed functional dependence on heating-rate, peak particle temperature, and coal precursor. The char annealing submodel was consistently shown (in the sensitivity analysis) to be of dominant importance in char conversion, and a detailed literature review revealed the massive impact of char preparation conditions (especially heating rate, peak char temperature, and coal precursor) on char annealing and reactivity. A new annealing model was developed that included the effects of heating rate, peak char temperature, and coal precursor. The error between the new model and the available data was a factor of three better than the previous model in the literature. Predicting the reactivity of a given char has been an insurmountable obstacle in coal combustion modeling for decades, and it is quite possible that the much improved char annealing model will prove to be the final piece of the puzzle in a coal-general kinetics correlation, which would arguable be considered the “Holy Grail” of coal conversion modeling.

9.3 CCK/oxy Model Development

The CCK model was greatly extended in accordance with the sensitivity analysis. The model was rewritten to incorporate more robust convergence, an auto-adaptive time-step, and the capacity to predict char conversion even in the extreme conditions of oxy-coal combustion. The new model (CCK/oxy) is fully valid in all conditions where CCK functioned, and was also shown to be exceptionally accurate in oxy-coal conditions that the previous CCK model

completely failed to predict. The CCK/oxy model was even found to perform relatively well when only the least informative fraction of the data was used to train model parameters; this successful extrapolation strongly implies that the relevant physics are properly represented. The CCK/oxy model was further tested in a range of conventional combustion and high O_2/N_2 conditions, with promising results. This implies that the CCK/oxy model has sufficient physical detail to use data from widely varying physical sources in tuning coal specific kinetic parameters for conditions far removed from the data. It also implies that CCK/oxy has the potential to be a critical tool in completing the decades-old search for a coal general kinetic correlation by bringing a vast array of data under the purview of a single model.

9.4 CCK/oxy Model Results

In validating the CCK/oxy model against literature data, several important results were obtained. First, and most apparent, was the exceptional improvement in model/data fit. The process of validation also showed the high model sensitivity to initial particle diameter and the importance of properly accounting for the detection system bias. The diameter sensitivity can be well accounted for by an appropriate coal particle distribution, but the detection system may be unique between any two experimental setups, and care must be taken to make and "apples-to-apples" comparison. In the case of the literature data used here, the detector observed only those particles that were sufficiently large and hot, which created a progressive bias at later burnout as more and more of the particle distribution was rendered undetectable. Fortunately, the data were highly detailed, and the degree of bias was clearly recorded in the data. Finally, it was shown that not only could the model extrapolate to widely different temperature, O_2, and diluent gas ranges, but the model success is such that it predicts observed late stage burnout effects that could not be explicitly modeled due to the lack of detail in a subset of the literature data.

9.5 Future Work

As mentioned above, the reactivity of coal has been a matter of research and controversy for decades, but since the CCK/oxy model submodels are sufficient to capture the broadest impacts of preparation and combustion conditions, it is quite possible that the hunt for a coal-general kinetic correlation is no longer out of reach. With sufficient literature data, a coal general kinetic correlation should be attempted by linking a subset of the 20 kinetic parameters to correlations that depend on coal structural parameters, such as measured by NMR spectroscopy. The form of such correlations would be a matter of both careful analysis as well as trial and error.

The work reported here pertains exclusively to atmospheric pressure char conversion, but pressurized systems potentially enable massive capital-cost savings. The CCK/oxy model is set-up to accept pressure as an input, and the swelling submodel is prepared for a minor change to include an advanced pressure submodel. These small changes could allow the CCK/oxy model to be extended to high-pressure conditions, though it would perhaps be necessary to invest considerable effort to rework the 8-step reaction mechanism.

REFERENCES

Álvarez, L., M. Gharebaghi, J. M. Jones, M. Pourkashanian, A. Williams, J. Riaza, C. Pevida, J. J. Pis and F. Rubiera, "CFD modeling of oxy-coal combustion: Prediction of burnout, volatile and NO precursors release," *Applied Energy,* **104**, 653-665 (2013).

Aris, R., "Reactions in continuous mixtures," *Aiche Journal,* **35**(4), 539-548 (1989).

Astarita, G., "Lumping nonlinear kinetics - Apparent Overall Order of Reaction," *Aiche Journal,* **35**(4), 529-532 (1989).

Bar-Ziv, E., A. Zaida, P. Salatino and O. Senneca, "Diagnostics of carbon gasification by Raman microprobe spectroscopy," *Proceedings of the Combustion Institute,* **28**, 2369-2374 (2000).

Beeley, T., J. Crelling, J. R. Gibbins, R. Hurt, M. Lunden, C. K. Man, J. Williamson and N. Y. C. Yang, "Transient high-temperature thermal deactivation of monomaceral-rich coal chars," *Proceedings of the Combustion Institute,*(26th), 3103-3110 (1996).

Bhatia, S. K. and D. D. Perlmutter, "A random pore model for fluid-solid reactions. 1. isothermal, kinetic control," *AIChE J,* **26**(3), 379-386 (1980).

Bhatia, S. K. and D. D. Perlmutter, "A random pore model for fluid-solid reactions. 2. diffusion and transport effects," *AIChE J,* **27**(2), 247-254 (1981).

Box, G. and N. Draper, Empirical Model-Building and Response Surfaces, USA, John Wiley & Sons (1987).

Buch, T., J. A. Guala and A. Caneiro, "Oxyreactivity of doped sucrose carbon," *Carbon,* **16**(5), 377-383 (1978).

Burnham, A. K. and R. L. Braun, "Global kinetic analysis of complex materials," *Energy & Fuels,* **13**(1), 1-22 (1999).

Byrd, R. H., M. E. Hribar and J. Nocedal, "An interior point algorithm for large-scale nonlinear programming," *Siam Journal on Optimization,* **9**(4), 877-900 (1999).

Byrd, R. H., J. C. Gilbert and J. Nocedal, "A trust region method based on interior point techniques for nonlinear programming," *Mathematical Programming,* **89**(1), 149-185 (2000).

Cai, H. Y., A. J. Guell, I. N. Chatzakis, J. Y. Lim, D. R. Dugwell and R. Kandiyoti, "Combustion reactivity and morphological change in coal chars: Effect of pyrolysis temperature, heating rate and pressure," *Fuel,* **75**(1), 15-24 (1996).

Chen, L., M. Gazzino and A. Ghoniem, "Characteristics of pressurized oxy-coal combustion under increasing swirl number," Clean Coal AND Fuel Systems. International Technical Conference. 35th 2010., Clearwater, FL (2010).

Chen, L., S. Z. Yong and A. F. Ghoniem, "Oxy-fuel combustion of pulverized coal: Characterization, fundamentals, stabilization and CFD modeling," *Progress in Energy and Combustion Science,* **38**, 156-214 (2012).

Chui, E. H., M. A. Douglas and Y. Tan, "Modeling of oxy-fuel combustion for a western Canadian sub-bituminous coal," *Fuel,* **82**, 1201-1210 (2003).

Cloke, M., T. Wu, R. Barranco and E. Lester, "Char characterisation and its application in a coal burnout model," *Fuel,* **82**, 1989-2000 (2003).

D.B., F., "Chemistry and Physics of Carbon," Kinetic Model of Carbon Burnout, New York, Marcel Dekker, **7:** 1 (1971).

Davis, K. A., R. H. Hurt, N. Y. C. Yang and T. J. Headley, "Evolution of char chemistry, crystalinity, and ultrafine structure during pulverized-coal combustion," *Combustion and Flame,* **100**(1-2), 31-40 (1995).

DoE, "AOE2014 Early Release Overview," Annual Energy Outlook, 1000 Independance Ave. SW Washington D.C., U.S. Department of Energy (2013).

Dugas, R. E., "Carbon dioxide absorption, desorption, and diffusion in aqueous piperazine and monoethanolamine," Chemical Engineering, UT Austin (2009).

Edwards, I. A. S., "Chapter 1 - Structure in carbons and carbon forms," Introduction to Carbon Science, Eds., Butterworth-Heinemann**:** 1-36 (1989).

EIA, "Annual Energy Review 2011," Annual Energy Review, 1000 Independance Ave. S.W. Washington D.C., U.S. Energy Information Administration (2012).

Essenhigh, R. H., M. K. Misra and D. W. Shaw, "Ignition of coal particles - a review," *Combustion and Flame,* **77**, 3-30 (1989).

Essenhigh, R. H., "Influence of initial particle density on the reaction mode of porous carbon particles," *Combustion and Flame,* **99**(2), 269-279 (1994).

Fei, H., S. Hu, J. Xiang, L. S. Sun, P. Fu and G. Chen, "Study on coal chars combustion under O_2/CO_2 atmosphere with fractal random pore model," *Fuel,* **90**, 441-448 (2011a).

Fei, H., L. S. Sun, S. Hu, J. Xiang, Y. Song, B. Wang and G. Chen, "The combustion reactivity of coal chars in oxyfuel atmosphere: Comparison of different random pore models," *Journal of Analytical and Applied Pyrolysis,* **91**, 251-256 (2011b).

Feng, B. and S. K. Bhatia, "On the validity of thermogravimetric determination of carbon gasification kinetics," *Chemical Engineering Science,* **57**(15), 2907-2920 (2002).

Feng, B., S. K. Bhatia and J. C. Barry, "Structural ordering of coal char during heat treatment and its impact on reactivity," *Carbon,* **40**(4), 481-496 (2002).

Feng, B. and S. K. Bhatia, "Variation of the pore structure of coal chars during gasification," *Carbon,* **41**(3), 507-523 (2003).

Feng, B., S. K. Bhatia and J. C. Barry, "Variation of the crystalline structure of coal char during gasification," *Energy & Fuels,* **17**(3), 744-754 (2003a).

Feng, B., A. Jensen, S. K. Bhatia and K. Dam-Johansen, "Activation energy distribution of thermal annealing of a bituminous coal," *Energy & Fuels,* **17**(2), 399-404 (2003b).

Fletcher, T. H., A. R. Kerstein, R. J. Pugmire, M. S. Solum and D. M. Grant, "Chemical percolation model for devolatilization .3. Direct use of C-13 NMR data to predict effects of coal type," *Energy & Fuels,* **6**(4), 414-431 (1992).

Frailie, P., "Modeling of carbon dioxide absorbing/stripping by aqueous methyldiethanolamine/piperazine," Chemical Engineering, UT Austin (2014).

Freeman, S. A., "Thermal degradation and oxidation of aqueous piperazinefor carbon dioxide capture," Chemical Engineering, UT Austin (2011).

Frenklach, M., A. Packard and R. Feeley, Modeling of Chemical Reactions, Elsevier Science (2005).

Fulk, S. M., "Measuring and modeling aerosols in carbon dioxide capture by aqueous amines," Chemical Engineering, UT Austin (2016).

Gale, T. K., "Effects of pyrolysis conditions on coal char properties," Mechanical Engineering, Brigham Young University (1994).

Gale, T. K., C. H. Bartholomew and T. H. Fletcher, "Decreases in the swelling and porosity of bituminous coals during devolatilization at high heating rates," *Combustion and Flame,* **100**(1-2), 94-100 (1995).

Gale, T. K., C. H. Bartholomew and T. H. Fletcher, "Effects of pyrolysis heating rate on intrinsic reactivities of coal chars," *Energy & Fuels,* **10**(3), 766-775 (1996).

Gattiker, J., K. Myers, D. Higdon and B. Williams, "Handbook of uncertainty quantification," Eds. H. Ghanem, Owadhi, New York, Spring (2016).

Gattiker, J., Myers, K., Williams, B., Higdon, D., Carzolio, M., & Hoegh, A. , "Gaussian process-based densitivity analysis and bayesian model calibration with GPMSA," Handbook of Uncertainty Quantification, Eds. H. Ghanem, Owadhi, Springer**:** 1-41 (2017).

Gavalas, G. R., "A random capillary model with application to char gasification at chemically controlled rates," *Aiche Journal,* **26**(4), 577-585 (1980).

Geier, M., C. R. Shaddix, K. A. Davis and H. S. Shim, "On the use of single-film models to describe the oxy-fuel combustion of pulverized coal char," *Applied Energy,* **93**, 675-679 (2012).

Genetti, D., "An advanced model of coal devolatilization based on chemical structure," Chemical Engineering, Brigham Young University (1999).

Genetti, D., T. H. Fletcher and R. J. Pugmire, "Development and application of a correlation of C-13 NMR chemical structural analyses of coal based on elemental composition and volatile matter content," *Energy & Fuels,* **13**(1), 60-68 (1999).

Gomero, B., "Latin hypercube sampling and partial rank correlation coefficient analysis applied to an optimal control problem," Masters, Mathematics, University of Tennessee, Knoxville (2012).

Gonzalo-Tirado, C., S. Jiménez and J. Ballester, "Gasification of a pulverized sub-bituminous coal in CO2 at atmospheric pressure in an entrained flow reactor," *Combustion and Flame,* **159**, 385-395 (2012).

Grant, D. M., R. J. Pugmire, T. H. Fletcher and A. R. Kerstein, "Chemical model of coal devolatilization using percolation lattice statistics," *Energy & Fuels,* **3**(2), 175-86 (1989).

Hampartsoumian, E., M. Pourkashanian, D. T. Trangmar and A. Williams, "Effect of the porous structure of char on the rate of gasification," *Abstracts of Papers of the American Chemical Society,* **197**, 73-FUEL (1989).

Haugen, N. E. L., M. B. Tilghman and R. E. Mitchell, "The conversion mode of a porous carbon particle during oxidation and gasification," *Combustion and Flame,* **161**(2), 612-619 (2014).

Haugen, N. E. L., R. E. Mitchell and M. B. Tilghman, "A comprehensive model for char particle conversion in environments containing O_2 and CO_2," *Combustion and Flame,* **162**(4), 1455-1463 (2015).

Hecht, E. S., C. R. Shaddix, M. Geier, A. Molina and B. S. Haynes, "Effect of CO_2 and steam gasification reactions on the oxy-combustion of pulverized coal char," *Combustion and Flame,* **159**, 3437-3447 (2012).

Hecht, E. S., C. R. Shaddix and J. S. Lighty, "Analysis of the errors associated with typical pulverized coal char combustion modeling assumptions for oxy-fuel combustion," *Combustion and Flame,* **160**, 1499-1509 (2013).

Hecker, W. C., K. McDonald, W. Reade, M. Swensen and R. Cope, "Effects of burnout on char oxidation kinetics," *Symposium (International) on Combustion,* **24**(1), 1225-1231 (1992).

Hendrickson, T. A., Synthetic Fuels Data Handbook, Denver, CO, Cameron Engineers, Inc. (1975).

Higdon, D., M. Kennedy, J. C. Cavendish, J. A. Cafeo and R. D. Ryne, "Combining field data and computer simulations for calibration and prediction," *Siam Journal on Scientific Computing,* **26**(2), 448-466 (2004).

Higdon, D., J. Gattiker, B. Williams and M. Rightley, "Computer model calibration using high-dimensional output," *Journal of the American Statistical Association,* **103**(482), 570-583 (2008).

Hilliard, M. D., "A predictive thermodynamic model for an aqueous blend of potassium carbonate, piperazine, and monoethanolamine for carbon dioxide capture from flue gas," Chemical Engineering, UT Austin (2008).

Holland, T. and T. H. Fletcher, "Global sensitivity analysis for a comprehensive char conversion model in oxy-fuel conditions," *Energy & Fuels,* (2016).

Holland, T. and T. H. Fletcher, "Comprehensive model of single particle pulverized coal combustion extended to oxy-coal conditions," *Energy & Fuels,* (2017).

Hurt, R., J. K. Sun and M. Lunden, "A kinetic model of carbon burnout in pulverized coal combustion," *Combustion and Flame,* **113**, 181-197 (1998).

Hurt, R. H., J. P. Longwell and A. F. Sarofim, "Gasification reactivity of chars from low rank coal lithotypes," *Fuel,* **65**, 451-452 (1986).

Hurt, R. H. and R. E. Mitchell, "On the combustion kinetics of heterogeneous char particle populations," ACS Division of Fuel Chemistry, 202 (1991).

Hurt, R. H., A. F. Sarofim and J. P. Longwell, "Role of microporous surface-area in uncatalyzed carbon gasification," *Energy & Fuels,* **5**, 290-299 (1991).

Hurt, R. H. and J. R. Gibbins, "Residual carbon from pulverized coal-fired boilers .1. Size distribution and combustion reactivity," *Fuel,* **74**(4), 471-480 (1995).

Hurt, R. H., M. M. Lunden, E. G. Brehob and D. J. Maloney, "Statistical kinetics for pulverized coal combustion," *Symposium (International) on Combustion,* **26**(2), 3169-3177 (1996).

Hurt, R. H. and J. M. Calo, "Semi-global intrinsic kinetics for char combustion modeling," *Combustion and Flame,* **125**, 1138-1149 (2001a).

Hurt, R. H. and J. M. Calo, "Semi-global intrinsic kinetics for char combustion modeling," *Combustion and Flame,* **125**(3), 1138-1149 (2001b).

Jayaraman, K., I. Gokalp, E. Bonifaci and N. Merlo, "Kinetics of steam and CO_2 gasification of high ash coal–char produced under various heating rates," *Fuel,* **154**, 370-379 (2015).

Jenkins, R. G., S. P. Nandi and P. L. Walker, "Reactivity of heat-treated coals in air at 500 degrees C," *Fuel,* **52**(4), 288-293 (1973).

Kennedy, M., O'Hagan A., "Supplementary details on bayesian callibration of computer models," University of Sheffield, University of Sheffield (2000).

Kennedy, M. C. and A. O'Hagan, "Bayesian calibration of computer models," *Journal of the Royal Statistical Society Series B-Statistical Methodology,* **63**, 425-450 (2001).

Khatami, R., C. Stivers and Y. A. Levendis, "Ignition characteristics of single coal particles from three different ranks in O_2/N_2 and O_2/CO_2 atmospheres," *Combustion and Flame,* **159**, 3554-3568 (2012).

Kidena, K., T. Yamashita and A. Akimoto, "Prediction of thermal swelling behavior on rapid heating using basic analytical data," *Energy & Fuels,* **21**(2), 1038-1041 (2007).

Kim, D., S. Choi, C. R. Shaddix and M. Geier, "Effect of CO_2 gasification reaction on char particle combustion in oxy-fuel conditions," *Fuel,* **120**, 130-140 (2014).

Kuhr, C., Ehmann M, Rehfeldt S, Bergins C, Maier J, S. G. and S. Wu, "Modeling of char combustion in CO_2/O_2 and N_2/O_2 atmospheres," The 35th international technical conference on clean coal and fuel systems, Clearwater, FL (2010).

Laurendeau, N. M., "Heterogeneous kinetics of coal char gasification and combustion," *Progress in Energy and Combustion Science,* **4**, 221-270 (1978).

Lewis, A. D., T. M. Holland, N. R. Marchant, F. E. G., D. J. Henley, E. G. Fuller and T. H. Fletcher, "Steam gasification rates of three bituminous coal chars in an entrained-flow reactor at pressurized conditions," *Energy & Fuels,* (2015).

Lewtak, R. and A. Milewska, "Application of different diffusion approaches in oxy-fuel combustion of single coal char particles," *Fuel,* **113**, 844-853 (2013).

Liu, G. S. and S. Niksa, "Coal conversion submodels for design applications at elevated pressures. Part II. Char gasification," *Progress in Energy and Combustion Science,* **30**, 679-717 (2004).

Liu, Y. H., M. Geier, A. Molina and C. R. Shaddix, "Pulverized coal stream ignition delay under conventional and oxy-fuel combustion conditions," *International Journal of Greenhouse Gas Control,* **5**, S36-S46 (2011).

Marino, S., I. B. Hogue, C. J. Ray and D. E. Kirschner, "A methodology for performing global uncertainty and sensitivity analysis in systems biology," *Journal of Theoretical Biology,* **254**(1), 178-196 (2008).

McBride, B., M. Zehe and S. Gordon, "NASA Glenn Coefficients for Calculating Thermodynamic Properties of Individual Species," Cleveland, Ohio, John H. Glenn Research Center**:** 291 (2002).

McCarthy, D. J., "Some Effects of Overheating and carbon bunr-off on the performance of fluidized-bed combustors," *Fuel,* **61**(3), 298-302 (1982).

McConnel, J. and J. Sutherland, "The effect of model fidelity on prediction of char burnout for single-particle coal combustion," *Proceedings of the Combustion Institute,* (2016).

McKay, M. D., R. J. Beckman and W. J. Conover, "A comparison of three methonds for selecting values of input variabls in the analysis of output from a computer code," *Technometrics,* **21**(2), 239-245 (1979).

Mitchell, R. E., R. H. Hurt, L. L. Baxter and D. R. Hardesty, "Compilation of Sandia coal char combustion data and kinetic analyses. Milestone report," Livermore, Ca, Sandia National Laboratories**:** 615 (1992).

Murty, H. N., D. L. Biederman and E. A. Heintz, "Kinetics of graphitization—II. Pre-exponential factors," *Carbon,* **7**(6), 683-688 (1969).

Nagle, J. and R. F. Strickland-Constable, "Oxidation of carbon between 1000°C and 2000°C," Fifth Carbon Conference, Pennsylvania State University, 1 (1962).

Naredi, P. and S. V. Pisupati, "Interpretation of char reactivity profiles obtained using a thermogravimetric analyzer," *Energy & Fuels,* **22**(1), 317-320 (2008).

Naredi, P. and S. Pisupati, "Effect of CO2 during coal pyrolysis and char burnout in oxy-coal combustion," *Energy and Fuels,* **25**, 2452-2459 (2011).

Nguyen, B.-T. N., "Amine volatility in CO_2 capture," Chemical Engineering, UT Austin (2013).

Nikolopoulos, N., A. Nikolopoulos, E. Karampinis, P. Grammelis and E. Kakaras, "Numerical investigation of the oxy-fuel combustion in large scale boilers adopting the ECO-Scrub technology," *Fuel,* **90**, 198-214 (2011).

Niksa, S., G. S. Liu and R. H. Hurt, "Coal conversion submodels for design applications at elevated pressures. Part I. devolatilization and char oxidation," *Progress in Energy and Combustion Science,* **29**, 425-477 (2003).

Niu, Y. Q. and C. R. Shaddix, "A sophisticated model to predict ash inhibition during combustion of pulverized char particles," *Proceedings of the Combustion Institute,* **35**, 561-569 (2015).

Nozaki, T., S. I. Takano, T. Kiga, K. Omata and N. Kimura, "Analysis of the flame formed during oxidation of pulverized coal by an O_2-CO_2 mixture," Energy, **22** (1997).

Oh, M. S., W. A. Peters and J. B. Howard, "An experimental and modeling study of softening coal pyrolysis," *Aiche Journal,* **35**(5), 775-792 (1989).

Osafune, K. and H. Marsh, "Gasification kinetics of coal chars in carbon dioxide," *Fuel,* **67**(March), 384-388 (1987).

Ponzio, A., S. Senthoorselvan, W. H. Yang, W. Blasiak and O. Eriksson, "Ignition of single coal particles in high-temperature oxidizers with various oxygen concentrations," *Fuel,* **87**, 974-987 (2008).

Qiao, Y., L. A. Zhang, E. Binner, M. H. Xu and C. Z. Li, "An investigation of the causes of the difference in coal particle ignition temperature between combustion in air and in O_2/CO_2," *Fuel,* **89**, 3381-3387 (2010).

Radovic, L. R., P. L. Walker and R. G. Jenkins, "Effect of lignite pyrolysis conditions on calcium-oxide dispersion and subsequent char reactivity," *Fuel,* **62**(2), 209-212 (1983a).

Radovic, L. R., P. L. Walker and R. G. Jenkins, "Importance of carbon active-sites in the gasification of coal chars," *Fuel,* **62**(7), 849-856 (1983b).

Rathnam, R. K., L. K. Elliott, T. F. Wall, Y. Liu and B. Moghtaderi, "Differences in reactivity of pulverised coal in air (O_2/N_2) and oxy-fuel (O_2/CO_2) conditions," *Fuel Processing Technology,* **90**, 797-802 (2009).

Rowley, R. L., W. V. Wilding, J. L. Oscarson, Y. Yang and N. F. Giles, "DIPPR® data compilation of pure chemical properties," (2010). Last accessed

Russell, N. V., J. R. Gibbins, C. K. Man and J. Williamson, "Coal char thermal deactivation under pulverized fuel combustion conditions," *Energy & Fuels,* **14**(4), 883-888 (2000).

Sacks J., W., W.J., Mitchell, T.J. and Wynn, H.P. , *Statistical Science,* **4**, 409-423 (1989).

Sahu, R., Y. A. Levendis, R. C. Flagan and G. R. Gavalas, "Physical-properties and oxidation rates of chars from 3 bituminous coals," *Fuel,* **67**(2), 275-283 (1988).

Salatino, P., O. Senneca and S. Masi, "Assessment of thermodeactivation during gasification of a bituminous coal char," *Energy & Fuels,* **13**(6), 1154-1159 (1999).

Saltelli, A., S. Tarantola, F. Campolongo and M. Ratto, Sensitivity Analysis in Practice: A Guid to Assessing Scientific Models, Wiley (2004).

Saltelli, A., M. Ratto, T. Andres, F. Campolongo, J. Cariboni, D. Gatelli, M. Saisana and S. Tarantola, Global Sensitivity Analysis: The Primer, Hoboken, NJ, John Wiley & Sons (2008).

Santner, T. J., Williams, B.J., and Notz, W.I. , Design and analysis of computer experiments, New York, Springer (2003).

Scheffknecht, G., L. Al-Makhadmeh, U. Schnell and J. Maier, "Oxy-fuel coal combustion-A review of the current state-of-the-art," *International Journal of Greenhouse Gas Control,* **5**, S16-S35 (2011).

Senneca, O., P. Russo, P. Salatino and S. Masi, "The relevance of thermal annealing to the evolution of coal char gasification reactivity," *Carbon,* **35**(1), 141-151 (1997).

Senneca, O., P. Salatino and S. Masi, "Microstructural changes and loss of gasification reactivity of chars upon heat treatment," *Fuel,* **77**(13), 1483-1493 (1998).

Senneca, O. and P. Salatino, "Loss of gasification reactivity toward O_2 and CO_2 upon heat treatment of carbons," *Proceedings of the Combustion Institute,* **29**, 485-493 (2002).

Senneca, O., P. Salatino and S. Masi, "Heat treatment-induced loss of combustion reactivity of a coal char: the effect of exposure to oxygen," *Experimental Thermal and Fluid Science,* **28**(7), 735-741 (2004).

Senneca, O., P. Salatino and S. Masi, "The influence of char surface oxidation on thermal annealing and loss of combustion reactivity," *Proceedings of the Combustion Institute,* **30**, 2223-2230 (2005).

Senneca, O. and P. Salatino, "Overlapping of heterogeneous and purely thermally activated solid-state processes in the combustion of a bituminous coal," *Combustion and Flame,* **144**(3), 578-591 (2006).

Senneca, O., P. Salatino and D. Menghini, "The influence of thermal annealing on oxygen uptake and combustion rates of a bituminous coal char," *Proceedings of the Combustion Institute,* **31**, 1889-1895 (2007).

Senneca, O. and P. Salatino, "A semi-detailed kinetic model of char combustion with consideration of thermal annealing," *Proceedings of the Combustion Institute,* **33**, 1763-1770 (2011).

Senneca, O. and L. Cortese, "Kinetics of coal oxy-combustion by means of different experimental techniques," *Fuel,* **102**, 751-759 (2012).

Senneca, O. and L. Cortese, "Thermal annealing of coal at high temperature and high pressure. Effects on fragmentation and on rate of combustion, gasification and oxy-combustion," *Fuel,* **116**, 221-228 (2014).

Shaddix, C. R. and A. Molina, "Particle imaging of ignition and devolatilization of pulverized coal during oxy-fuel combustion," *Proceedings of the Combustion Institute,* **32**, 2091-2098 (2009).

Shibaoka, M., Y. Ohtsuka, M. J. Wornat, C. G. Thomas and A. J. R. Bennett, "Application of microscopy to the investigation of brown-coal pyrolysis," *Fuel,* **74**(11), 1648-1653 (1995).

Shim, H. S. and R. H. Hurt, "Thermal annealing of chars from diverse organic precursors under combustion-like conditions," *Energy & Fuels,* **14**(2), 340-348 (2000).

Shurtz, R., "Effects of pressure on the properties of coal char under gasification conditions at high initial heating rates," Chemical Engineering, Brigham Young University (2011).

Shurtz, R. C., K. K. Kolste and T. H. Fletcher, "Coal Swelling Model for High Heating Rate Pyrolysis Applications," *Energy & Fuels,* **25**(5), 2163-2173 (2011).

Shurtz, R. C., J. W. Hogge, K. C. Fowers, G. S. Sorensen and T. H. Fletcher, "Coal swelling model for pressurized high particle heating rate pyrolysis applications," *Energy & Fuels,* **26**(6), 3612-3627 (2012).

Shurtz, R. C. and T. H. Fletcher, "Coal char-CO_2 gasification measurements and modeling in a pressurized flat-flame burner," *Energy & Fuels,* **27**, 3022-3038 (2013).

Skokova, K. A., "Selectivity in the carbon-oxygen reaction," Pennsylvania State University (1997).

Smith, I. W., "The combustion rates of coal chars: A review," *Symposium (International) on Combustion,* **19**, 1045-1065 (1982).

Smith, P. J., "The UQ-predictive multidisciplinary simulation center for high efficiency electric power generation with carbon capture," The University of Utah, Salt Lake City, UT (2012).

Smoot, D. L. and P. J. Smith, Coal Combustion and Gasification, New York, Plenum Press (1985).

Storlie, C. B., W. A. Lane, E. M. Ryan, J. R. Gattiker and D. M. Higdon, "Calibration of computational models with categorical parameters and correlated outputs via Bayesian

smoothing spline ANOVA," *Journal of the American Statistical Association,* **110**(509), 68-82 (2015).

Sun, J. K. and R. H. Hurt, "Mechanisms of extinction and near-extinction in pulverized solid fuel combustion," *Proceedings of the Combustion Institute,* **28**, 2205-2213 (2000).

Suuberg, Fundamental Issues in Control of Carbon Gasification Reactivity, Mulhouse, France, Centre de Recherches sur la Physico-Chimie des Surface Solides (1990).

Suuberg, E. M., M. Wojtowicz and J. M. Calo, "Some aspects of the thermal annealing process in a phenol-formaldehyde resin char," *Carbon,* **27**(3), 431-440 (1989).

Toporov, D., P. Bocian, P. Heil, A. Kellermann, H. Stadler, S. Tschunko, M. Förster and R. Kneer, "Detailed investigation of a pulverized fuel swirl flame in CO_2/O_2 atmosphere," *Combustion and Flame,* **155**, 605-618 (2008).

Tremel, A., T. Haselsteiner, M. Nakonz and H. Spliethoff, "Coal and char properties in high temperature entrained flow gasification," *Energy,* **45**(1), 176-182 (2012).

Tremel, A. and H. Spliethoff, "Gasification kinetics during entrained flow gasification - Part I; Devolatilisation and char deactivation," *Fuel,* **103**, 663-671 (2013).

Vleeskens, J. M., Nandi, B. N., "Burnout of Coals - Comparative bench-scale experiments on pulverized fuel and fluidized-bed combustion," *Fuel,* **65**, 797-802 (1986).

Wall, T., Y. H. Liu, C. Spero, L. Elliott, S. Khare, R. Rathnam, F. Zeenathal, B. Moghtaderi, B. Buhre, C. D. Sheng, R. Gupta, T. Yamada, K. Makino and J. L. Yu, "An overview on oxyfuel coal combustion-State of the art research and technology development," *Chemical Engineering Research & Design,* **87**(8A), 1003-1016 (2009).

Waltz, R. A., J. L. Morales, J. Nocedal and D. Orban, "An interior algorithm for nonlinear optimization that combines line search and trust region steps," *Mathematical Programming,* **107**(3), 391-408 (2006).

Wang, W., K. M. Thomas, R. M. Poultney and R. R. Willmers, "Iron-catalyzed graphitization in the blast-furnace," *Carbon,* **33**(11), 1525-1535 (1995).

Waters, B. J., R. G. Squires and N. M. Laurendeau, "Morphological development and intrinsic reactivity for combustion of 2 cicroporous carbon chars," *Combustion Science and Technology,* **62**, 187-209 (1988).

Welch, W. J., R. J. Buck, J. Sacks, H. P. Wynn, T. J. Mitchell and M. D. Morris, "Screening, predicting, and computer experiments," *Technometrics,* **34**(1), 15-25 (1992).

Wu, S. Y., J. Gu, X. Zhang, Y. Q. Wu and J. S. Gao, "Variation of carbon crystalline structures and CO2 gasification reactivity of Shenfu coal chars at elevated temperatures," *Energy & Fuels,* **22**(1), 199-206 (2008).

Xu, Q., "Thermodynamics of CO_2 loaded aqueous amines," Chemical Engineering, UT Austin (2011).

Yang, H., S. Li, T. H. Fletcher and M. Dong, "Simulation of the swelling of high-volatile bituminous coal during pyrolysis," *Energy & Fuels,* **28**(11), 7216-7226 (2014).

Yang, H., S. Li, T. H. Fletcher and M. Dong, "Simulation of the swelling of high-volatile bituminous coal during pyrolysis. Part 2: Influence of the maximum particle temperature," *Energy & Fuels,* **29**(6), 3953-3962 (2015).

Yu, J., K. Zhou and W. Ou, "Mass transfer coefficients considering effects of steam in oxy-fuel combustion of coal char," *Fuel,* **111**, 48-56 (2013).

Yu, J. L., J. Lucas, T. Wall, G. Liu and C. D. Sheng, "Modeling the development of char structure during the rapid heating of pulverized coal," *Combustion and Flame,* **136**(4), 519-532 (2004).

Zolin, A., A. Jensen and K. Dam-Johansen, "Kinetic analysis of char thermal deactivation," *Proceedings of the Combustion Institute,* **28**, 2181-2188 (2000).

Zolin, A., "Reactivity of solid fuels," Chemical and Biochemical Engineering, Technical University of Denmark (2001).

Zolin, A., A. Jensen and K. Dam-Johansen, "Coupling thermal deactivation with oxidation for predicting the combustion of a solid fuel (vol 125, pg 1341, 2001)," *Combustion and Flame,* **126**(3), 1746-1746 (2001).

Zolin, A., A. D. Jensen, P. A. Jensen and K. Dam-Johansen, "Experimental study of char thermal deactivation," *Fuel,* **81**(8), 1065-1075 (2002).

APPENDICES

A. Computational Tools

B. Solvent UQ results

C. Additional Chapter Sections

D. CCK/oxy Codes

E. Annealing Codes

A. COMPUTATIONAL TOOLS FOR UNCERTAINTY QUANTIFICATION

A.1 Analytical and Semi-analytical Uncertainty Quantification

Most commonly, uncertainty quantification (UQ) is accomplished through a collection of disparate ad hoc methods such as a brute force method (such as using the most extreme feasible values of each parameter or input to find the greatest cumulative error), a p-value, or simple confidence intervals. All uncertainty quantification techniques have weaknesses which must be carefully managed, but the most common techniques are popular for their simplicity, often misused, and tend to imply far greater uncertainty that the data require. The models developed in this dissertation primarily employed two UQ methods: an analytical (or semi-analytical) joint confidence region, or a Bayesian calibration. The analytical joint confidence region is readily derived from the foundation of linear regression.

A.1.1 Linear Regression

Linear regression is a process of finding the best estimate of a model that is linear in its parameters. A model in this context is typically a single equation that accepts experimental inputs as independent variables, and yields a dependent variable comparable to experimental input, as in Equation A-1. In Equation A-1, the i^{th} experimental observation corresponds to the i^{th} prediction, and the associated experimental inputs. Both $\mathbf{x_i}$ and $\boldsymbol{\beta}$ may be vectors of any length. The input vector ($\mathbf{x_i}$) may be different experimental observations or the same observation, reused

with other parameters. In the case of linear regression, $f(\mathbf{x_i},\boldsymbol{\beta})$ requires linearity in its parameters *only*. That is, each element of vector $\boldsymbol{\beta}$ is multiplied by the corresponding element of vector $\mathbf{x_i}$, but $\boldsymbol{\beta}$ is not subjected to any nonlinear transformation, or multiplied by any other element of $\boldsymbol{\beta}$. In real experiments, there is always some degree of observational error and some level of model imperfection, so any regression involving more data points than parameters will have a degree of error between observation (y_i) and prediction ($f(\mathbf{x_i},\boldsymbol{\beta})$). This i^{th} error or residual is usually squared to ensure a consistently positive value, as in Equation A-2, and the sum of squared residuals is used as a common measure of "goodness of fit" as in Equation A-3.

$$y_i = f(\boldsymbol{x}_i, \boldsymbol{\beta}) + \mathrm{r}_i \qquad \text{A-1}$$

$$r_i^2 = (f(\boldsymbol{x}_i, \boldsymbol{\beta}) - y_i)^2 \qquad \text{A-2}$$

$$SSR = \sum_i^n (f(\boldsymbol{x}_i, \boldsymbol{\beta}) - y_i)^2 \qquad \text{A-3}$$

This measure of model success equates minimizing the SSR to the best estimate of the true but unknown parameter vector $\boldsymbol{\beta}$. To minimize the SSR, the gradient of the sum of squares *parameters* (not independent variables) must be set to zero for each of j dimensions, as is shown for one β_j in Equation A-4. While Equation A-4 applies to any regression that accepts the sum squared error as the measure of success, it simplifies to Equation A-5 in the case of a model linear in all j elements of $\boldsymbol{\beta}$, because y_i and all terms in $f(\mathbf{x_i},\boldsymbol{\beta})$ are constant with respect to β_j except the term involving β_j. In Equation A-5, f_j is merely a map of the independent variable to the form used in the model (for example, it could be a log transform, an exponent, multiply by unity, or simply set the value of $x_{i,j}$ to unity as in parameter "b" of the common linear form y=m*x+b). By letting the entries of the matrix X be the transformed independent variables, Equation A-5 may be written as Equation A-6, where $\mathbf{b}$ is the specific vector that sets Equation A-6 to 0. By rearrangement,

Equation A-6 leads to Equation A-7, and rewriting to matrix notation yields Equation A-8, which finally yields the common form of Equation A-9, which is the analytical, unique solution to setting the gradient of the sum squared error to 0. This solution is the best estimate of **b** as defined here.

$$\frac{\partial SSR}{\partial \beta_j} = \sum_i^n \frac{\partial r^2}{\partial \beta_j} = 2\sum_i^n r\frac{\partial r}{\partial \beta_j} = 2\sum_i^n (f(\boldsymbol{x}_i, \boldsymbol{\beta}) - y_i)\frac{\partial (f(\boldsymbol{x}_i, \boldsymbol{\beta}) - y_i)}{\partial \beta_j} = 0 \quad \text{A-4}$$

$$\frac{\partial SSR}{\partial \beta_j} = \sum_i^n (f(\boldsymbol{x}_i, \boldsymbol{\beta}) - y_i)\big(f_j(x_i)\big) = 0 \quad \text{A-5}$$

$$\sum_i^n \left(\sum_k^m X_{i,k}\boldsymbol{b} - y_i\right)\left(X_{i,j}\right) = 0 \quad \text{A-6}$$

$$\sum_i^n \left(\sum_k^m X_{i,j}X_{i,k}\boldsymbol{b}\right) = \sum_i^n \left(X_{i,j}y_i\right) \quad \text{A-7}$$

$$\boldsymbol{X^T X b} = \boldsymbol{X^T Y} \quad \text{A-8}$$

$$\boldsymbol{b} = \left(\boldsymbol{X^T X}\right)^{-1}\boldsymbol{X^T Y} \quad \text{A-9}$$

Having obtained a solution for the parameter best estimates, the next step of common uncertainty quantification is to compute the confidence intervals. All work from this point on implicitly assumes data normality and homoscedasticity, as well as independent, identically distributed, unbiased data. These assumptions are likely never true, but they are often an adequate approximation. Under the prior assumptions, the confidence interval may be calculated by first calculating the covariance matrix of the parameters, and the relevant value from the t-distribution. The t-distribution is well known and available in most standard regression packages, and the parameter covariance matrix is also readily obtained. Equation A-10 is the definition of the covariance for the estimators of the true value of **β**, and by expanding the right hand side of Equation A-10 and recalling that the expected value of an estimator is a constant (the true value

of the estimator), Equation A-10 simplifies to Equation A-11. Extending the definition in Equation 4-10 and the simplification from Equation 4-11 to p dimensions, yields Equation 4-12 in matrix notation, which will resolve the apparent difficulty of requiring the unknown **β** in Equation A-11. Note that var(**b**) yields a matrix with variance on the diagonals and the covariance on the off-diagonals. Equation A-13 substitutes **b** with the right hand side of Equation A-9 and Equation A-14 substitutes **Y** with the matrix form of the right hand side of Equation A-1. Equation A-15 expands A-14, and then Equation A-16 simplifies $(\boldsymbol{X^TX})^{-1}\boldsymbol{X^TX}$ to the identity matrix. Equation A-17 expands the square, A-18 applies the linearity of expectations and takes advantage of the fact that only $\mathbf{r_i}$ is non-constant (and $E[\boldsymbol{r_i}]=0$). Finally, Equation A-19 is simplified to A-23 by recalling that $(\mathbf{AB})^{\mathbf{T}}=\mathbf{B}^{\mathbf{T}}\mathbf{A}^{\mathbf{T}}$, $\boldsymbol{X^TX}$ is symmetric, and thus equal to its transpose, and that $E[\boldsymbol{r_i^2}]=\sigma^2$. This gives the equation for the covariance matrix. The confidence interval is simply an appropriate number of standard errors from the best estimate of the parameter. For example, a 95% confidence interval is 1.96 standard errors (for the entire population), where a standard error is given by Equation A-23. Thus, the confidence interval is given by Equation A-24, assuming the data are only a sample of the populations.

$$cov(b_i, b_j) = E[(b_i - E[b_i])(b_j - E[b_j])] \quad \text{A-10}$$

$$cov(b_i, b_j) = E[b_i * b_j] - E[b_i]E[b_j] = \; E[b_i * b_j] - \beta_i\beta_j \quad \text{A-11}$$

$$var(\boldsymbol{b}) = E[\boldsymbol{b} * \boldsymbol{b'}] - E[\boldsymbol{b}]E[\boldsymbol{b'}] = E[\boldsymbol{b} * \boldsymbol{b'}] - \boldsymbol{\beta^2} \quad \text{A-12}$$

$$var(\boldsymbol{b}) = E\left[\left(\left(\boldsymbol{X^TX}\right)^{-1}\boldsymbol{X^TY}\right)^2\right] - \boldsymbol{\beta^2} \quad \text{A-13}$$

$$var(\boldsymbol{b}) = E\left[\left(\left(\boldsymbol{X^TX}\right)^{-1}\boldsymbol{X^T}\left((\boldsymbol{X\beta}) + \mathbf{r}_i\right)\right)^2\right] - \boldsymbol{\beta^2} \quad \text{A-14}$$

$$var(\boldsymbol{b}) = E\left[\left(\left(\boldsymbol{X^T X}\right)^{-1}\boldsymbol{X^T X\beta} + \left(\boldsymbol{X^T X}\right)^{-1}\boldsymbol{X^T}\mathbf{r}_i\right)^2\right] - \boldsymbol{\beta^2} \quad \text{A-15}$$

$$var(\boldsymbol{b}) = E\left[\left(\boldsymbol{\beta} + \left(\boldsymbol{X^T X}\right)^{-1}\boldsymbol{X^T}\mathbf{r}_i\right)^2\right] - \boldsymbol{\beta^2} \quad \text{A-16}$$

$$var(\boldsymbol{b}) = E\left[\boldsymbol{\beta^2} + 2\boldsymbol{\beta}\left(\left(\boldsymbol{X^T X}\right)^{-1}\boldsymbol{X^T}\mathbf{r}_i\right) + \left(\left(\boldsymbol{X^T X}\right)^{-1}\boldsymbol{X^T}\mathbf{r}_i\right)^2\right] - \boldsymbol{\beta^2} \quad \text{A-17}$$

$$var(\boldsymbol{b}) = E\left[\left(\left(\boldsymbol{X^T X}\right)^{-1}\boldsymbol{X^T}\mathbf{r}_i\right)^2\right] + \boldsymbol{\beta^2} - \boldsymbol{\beta^2} \quad \text{A-18}$$

$$var(\boldsymbol{b}) = E[(\mathbf{r_i})^2] * \left(\left(\boldsymbol{X^T X}\right)^{-1}\boldsymbol{X^T}\right)^2 \quad \text{A-19}$$

$$var(\boldsymbol{b}) = E[(\mathbf{r_i})^2] * \left(\left(\boldsymbol{X^T X}\right)^{-1}\boldsymbol{X^T}\right) * \left(\left(\boldsymbol{X^T X}\right)^{-1}\boldsymbol{X^T}\right)^T \quad \text{A-20}$$

$$\left(\left(\boldsymbol{X^T X}\right)^{-1}\boldsymbol{X^T}\right) * \left(\left(\boldsymbol{X^T X}\right)^{-1}\boldsymbol{X^T}\right)^T = \left(\left(\boldsymbol{X^T X}\right)^{-1}\boldsymbol{X^T}\right) * \left(\boldsymbol{X^T}\right)^T\left(\boldsymbol{X^T X}\right)^{-1^T} \quad \text{A-21}$$

$$\left(\left(\boldsymbol{X^T X}\right)^{-1}\boldsymbol{X^T}\right) * \left(\boldsymbol{X^T}\right)^T\left(\boldsymbol{X^T X}\right)^{-1^T} = \left(\boldsymbol{X^T X}\right)^{-1}\boldsymbol{X^T X}\left(\boldsymbol{X^T X}\right)^{-\mathbf{1}^T} = \left(\boldsymbol{X^T X}\right)^{-1} \quad \text{A-22}$$

$$var(\boldsymbol{b}) = \sigma^2 * \left(\boldsymbol{X^T X}\right)^{-1} \quad \text{A-23}$$

$$CI_i = \mathrm{b}_i \mp t_{stat} * var(\boldsymbol{b})_i \quad \text{A-24}$$

Often, the parameter confidence intervals (or even the model prediction confidence interval) signal the final stage of UQ, but the following linear joint confidence region shows that this is quite misleading. Equation 25 defines the joint confidence region of a linear model with p parameters. The F statistic is commonly used in the F-test for the equality of two variances, where two parameter sets for a model are considered statistically valid if the ratio of variances is less than or equal to the relevant F statistic. The value of the F statistic depends on the confidence level, but the overall confidence level of the joint confidence region is not known exactly. As an approximation, CI^p may be acceptable (i.e., a 95% confidence level for the F statistic would yield a joint confidence region at approximately the 0.95^2 confidence level for a

two parameter model). Equation A-25 is derived from the F-test as shown in Equations A-26 through Equation A-28. In Equation A-26, the left hand side is the ratio of two variances, and should therefore follow an F-distribution. The variance in the numerator is the difference in the sum squared errors between the best estimate parameters and some other proposed set of parameters, normalized the number of degrees of freedom (i.e., the number of parameters, p). The denominator is simply the estimate of the variance from the best-fit model, or the sum squared error of the best-fit model normalized by the number of degrees of freedom (i.e., the total number of data points minus the number of parameters, p, that had to be estimated). Equation A-27 simply rearranges Equation A-26, and Equation A-28 rewrites the left hand side of Equation A-27 with the matrix notation for a linear model with data matrix $\boldsymbol{X}$.

$$(\boldsymbol{\beta_s} - \boldsymbol{b})^T(\boldsymbol{X'X})(\boldsymbol{\beta_s} - \boldsymbol{b}) \leq \mathrm{F}_{stat}\mathrm{ps}^2 \quad \text{A-25}$$

$$\frac{\frac{SSR(\boldsymbol{\beta_s}) - SSR(\boldsymbol{b})}{p}}{\frac{SSR(\boldsymbol{b})}{n-p}} \leq \mathrm{F}_{stat} \quad \text{A-26}$$

$$SSR(\boldsymbol{\beta_s}) - SSR(\boldsymbol{b}) \leq p * \frac{SSR(\boldsymbol{b})}{n-p}\mathrm{F}_{stat} \quad \text{A-27}$$

$$(\boldsymbol{\beta_s} - \boldsymbol{b})^T(\boldsymbol{X'X})(\boldsymbol{\beta_s} - \boldsymbol{b}) \leq p * \frac{SSR(\boldsymbol{b})}{n-p}\mathrm{F}_{stat} \quad \text{A-28}$$

Figure A-1 shows the joint confidence region from the model y=mx+b, where the blue ellipse represents the joint confidence region, and the red square is the slightly extended space determined solely by the individual confidence regions (extended so as to avoid truncating the joint confidence region). Figure A-1 used a simple Monte Carlo method to select $\boldsymbol{\beta_s}$ 10,000 times. This was done to emphasize how much smaller even a two-dimensional, linear model joint confidence region is compared to the confidence intervals alone (i.e., how much the uncertainty

is over estimated), and to show how inefficient searching the entire confidence interval space could be. Higher dimensional joint confidence regions quickly decrease to a small fraction of the hyper-volume to be explored, and the uncertainty overestimation soon becomes completely unmanageable. In the case of a joint confidence region of a linear model, the ellipsoid can be found much more efficiently by sampling from a multivariate normal with the same mean and covariance as the parameter space (as in Figure A-2), or be computed analytically. This method captures total parameter uncertainty well, but with the caveat that the exact confidence level is slightly uncertain and that the model is assumed to be physically correct. The second assumption is almost never true, but in cases where it is not badly violated, the joint confidence region approach is excellent. Unfortunately, non-linear models do not have such a well behaved joint confidence region.

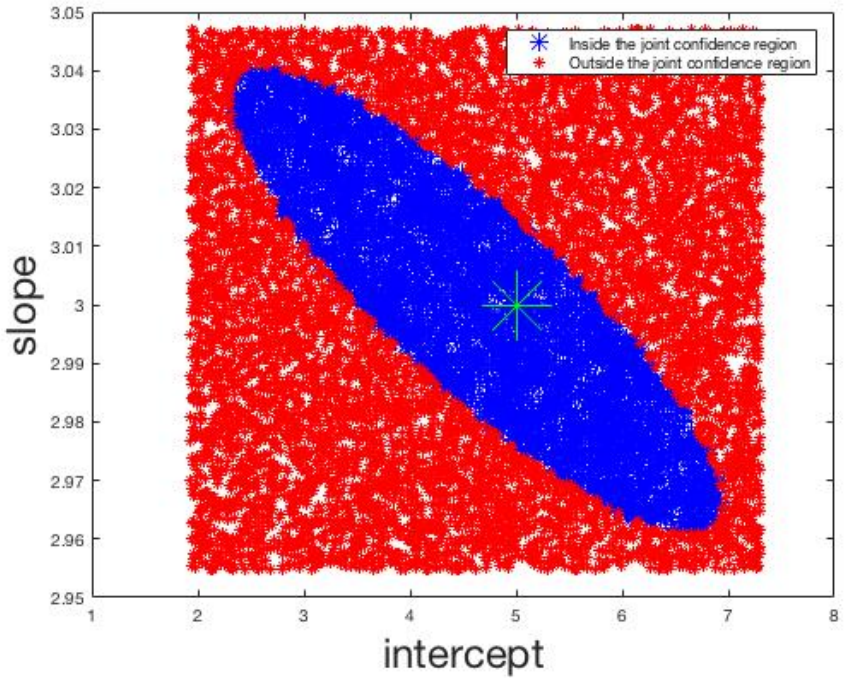

Figure A-1 – Joint confidence region of a simple linear model, random Monte Carlo method

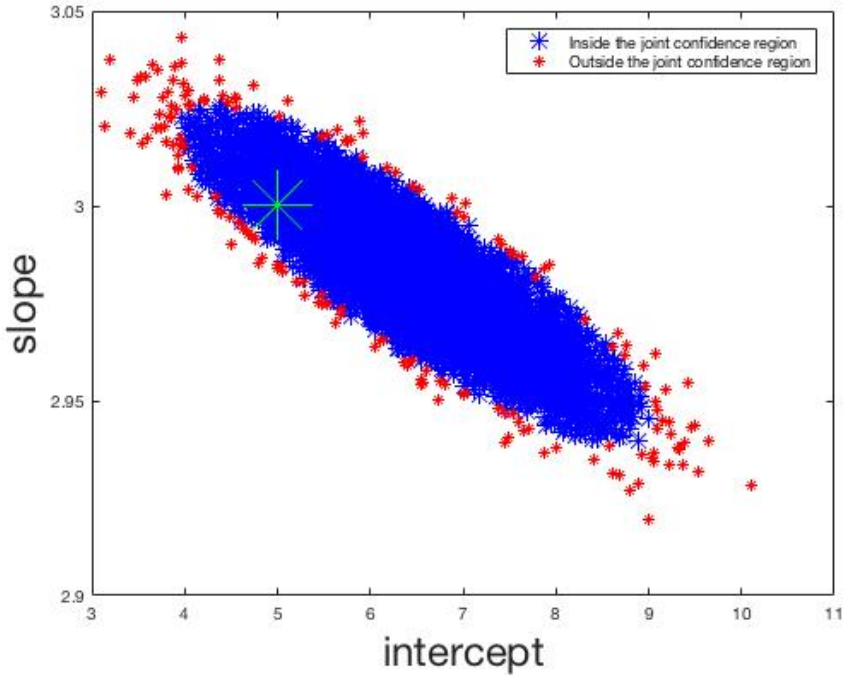

Figure A-2 – Joint confidence region of a simple linear model, multi-variate normal method

A.1.2 Nonlinear Regression

As stated above, Equation A-4 applies to any regression that accepts the sum squared error as the measure of success. However, for any model that is NOT linear in its parameters, the previous derivation does not hold. Instead, a solution requires somewhat more complicated approximation, an initial guess value for the parameters, and an iterative optimization approach. In simple cases, a reasonable initial solution can often be found, but it is far more cumbersome and there is a substantial possibility that the ultimate solution will not be the truly optimal solution. Also, like linear regression, the resulting best estimate of parameters does not address model discrepancy in any way, and in large models the non-linear joint confidence region in parameter space becomes exceptionally difficult to locate because it occupies only a very narrow, irregularly shaped region of parameter space, with no analytical solution. In multi-step models, the joint confidence region cannot be computed, and other methods must be attempted.

Such methods are even more important in the common case of non-linear or multi-step models, because the difficulty of exaggerated uncertainty may become even more extreme.

A.2 Gaussian Process Models for Simulation Analysis (GPMSA)

The Gaussian Process Models for Simulation Analysis (GPMSA) is a set of computer model analysis tools written at Los Alamos National Laboratories. The tool set is "aimed at *emulating* a computer model of a system being studied, *calibrating* this computer model to observations of the system, and giving *predictions* of the expected system response (Gattiker, 2017)."

A.2.1 Gaussian Processes

A Gaussian Process (GP) is defines as follow: for any set S, a GP on S is a set of random variables $\{Z_t : t \in S\}$ such that, for any set of indices $n \in \mathbb{N}$, $\{Z_{t\_1},...Z_{t\_n}\}$ is a multivariate Gaussian distribution. An example may render the definition more intuitive. By way of introduction, a random variable is a map between potential outcomes and a numerical value. These outcomes or realizations may be numerical (such as the selection of a real number from a random distribution), or non-numerical such as the iconic case of a coin toss (where the outcome "heads" maps to the value 1, and the outcome tails maps to 0). Note that the probability density (or mass) function (PDF or PMF) is not a part of the map between outcomes and numerical values, but instead defines the probability of a given outcome. The following example is perhaps the simplest non-trivial example of a GP. In the example, let t be the entire set of real numbers in one dimension ($\mathbb{R}$), let the random variable Z_t be defined as in Equation A-29, and for the specific example, choose the

following four values as the subset of t: {-0.7, -0.3, 0.2, 0.9}. Equation A-29 is the random variable (or map) between outcomes of ω and numerical values, where ω is a number drawn from the standard normal PDF.

$$Z_t = t * \omega \quad \text{A-29}$$

The Gaussian Process (i.e., the subset of four random variables) form a multivariate-normal. In this case, the GP is a four dimensional normal distribution fully defined by a vector of four means, and a 4x4 covariance matrix. Each realization of the GP is a vector of four values, while numerous samples both outline a univariate normal PDF for each Z_{t_n} with some mean and variance, *and* establishes the covariance between any two Z_{t_n}. Figure 4-2 shows a single realization of the GP (one sample from ω), while Figure 4-3 shows 500 samples from ω. The blue lines are linear interpolations between the realizations of the random variable, all of which pass through the origin. Mathematically, this is apparent from Equation A-29, which (for any given sample from ω) is simply the equation for a line of slope ω and the intercept set equal to zero, while from the standpoint of a GP, the random variable Z_0 would yield zero for any sample from the PDF, so Z_0 would have the PDF N(0,0). In fact, in this case, the entire vector of mean values is zero, which can be inferred from the symmetry of ω or visually observed in Figure 4-3.

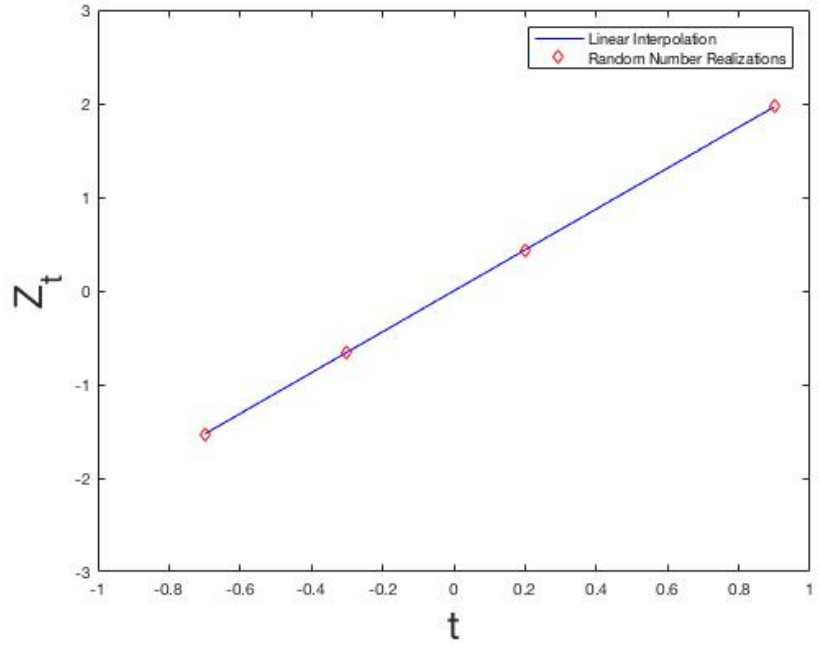

Figure A-3 – Single realization of the Gaussian Process

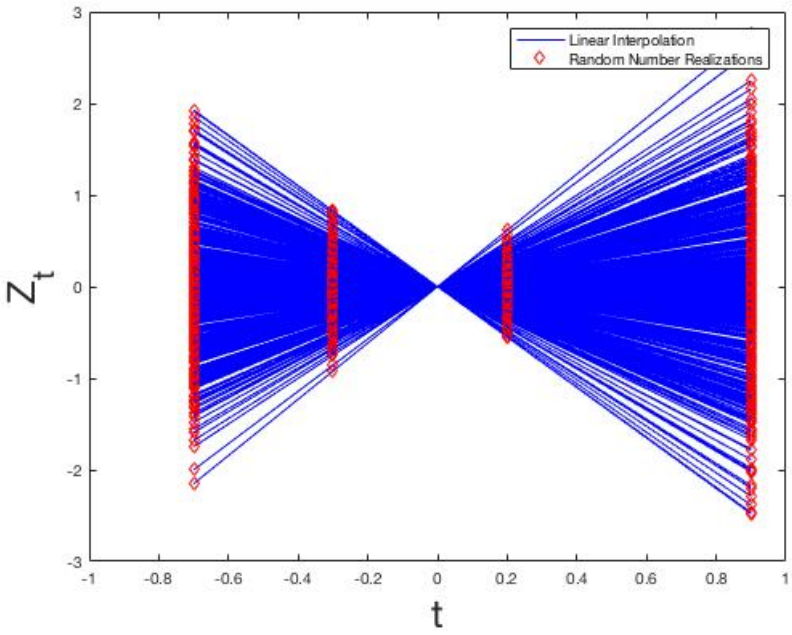

Figure A-4 – 500 realizations of the Gaussian Process

Mathematically, it is immediately apparent that Equation A-29 yields a line for any given draw of ω, and superficially, it appears that the GP is not multi-variate at all, but instead a single

sample from a standard normal that fully defines a line. However, the GP is in fact four dimensional, and for a single, four dimensional sample to contain four points exactly on a line, they must be drawn as a *single* sample from a multi-variate normal PDF constrained by the right covariance matrix. This matrix can be estimated from results in Figure 4-3, and exactly defined by the proper kernel function. Both approaches are shown, as they provide valuable insight. The diagonal of Table 4-1 shows the estimated variance for each univariate marginal distribution after a sample of 5,000 points from ω, while the off-diagonals show the covariance computed between the univariate distributions. Table 4-2 (computed from the kernel function) shows that the estimates from Table 4-1 are converging on the true variances and covariances. Equation A-30 is the kernel function for a linear GP (the kernel function generates the covariance matrix), while the subsequent equations derive the kernel function in the single-dimensional case from the definition of covariance (Equation A-31). Equation A-32 expands the covariance terms, while Equation A-33 simplifies A-32 by taking advantage of the fact that the expected value of all Z_{t_n} is zero in this case. Equation A-34 shows (from a common form of the definition of the variance), that the variance of ω is ω^2, which leads directly to Equation A-35. Comparing Equation A-35 to the kernel function (Equation A-30) they are seen to be identical, and to match Table 4-2.

The Gaussian process may be considered an alternative strategy for modeling a line. Rather than a single best fit line with confidence intervals on the line and the parameters, the GP has no specific parameters or value; instead, given a vector of input space and a region of output space, the GP quantifies the probability of the region of output space. Qualitatively, a region of output space close to the best-fit line would have a high probability density, while a region of output space far from the data (and best-fit line) would have very low probability.

Table A-1 – Calculated mean and covariance from 5000 samples of ω

	Z_{t_1}	Z_{t_2}	Z_{t_3}	Z_{t_4}	**Mean**
Z_{t_1}	0.488	0.209	-0.139	-0.627	-0.0078
Z_{t_2}	0.209	0.0896	-0.0597	-0.269	-0.0033
Z_{t_3}	-0.139	-0.0597	0.0398	0.179	0.0022
Z_{t_4}	-0.627	-0.269	0.179	0.806	0.010

Table A-2 – Exact theoretical mean and covariance

	Z_{t_1}	Z_{t_2}	Z_{t_3}	Z_{t_4}	**Mean**
Z_{t_1}	0.490	0.210	-0.140	-0.630	0
Z_{t_2}	0.210	0.0900	-0.0600	-0.270	0
Z_{t_3}	-0.140	-0.0600	0.0400	0.180	0
Z_{t_4}	-0.630	-0.270	0.180	0.810	0

$$\mathrm{k}(\mathbf{t_i}, \mathbf{t_j}) = \boldsymbol{t_i^T t_j} \tag{A-30}$$

$$\mathrm{cov}\left(\mathrm{Z}_{t_i}, \mathrm{Z}_{t_j}\right) = E\left[\left(\mathrm{Z}_{t_i} - E[\mathrm{Z}_{t_i}]\right)\left(\mathrm{Z}_{t_j} - E\left[\mathrm{Z}_{t_j}\right]\right)\right] \tag{A-31}$$

$$\mathrm{cov}\left(\mathrm{Z}_{t_i}, \mathrm{Z}_{t_j}\right) = E\left[\mathrm{Z}_{t_i}\mathrm{Z}_{t_j}\right] - E[E[\mathrm{Z}_{t_i}]\mathrm{Z}_{t_i}] - E\left[E\left[\mathrm{Z}_{t_j}\right]\mathrm{Z}_{t_j}\right] + E\left[E[\mathrm{Z}_{t_i}]E\left[\mathrm{Z}_{t_j}\right]\right] \tag{A-32}$$

$$\mathrm{cov}\left(\mathrm{Z}_{t_i}, \mathrm{Z}_{t_j}\right) = E\left[\mathrm{Z}_{t_i}\mathrm{Z}_{t_j}\right] = E[t_i\omega * t_j\omega] = t_i t_j E[\omega^2] \tag{A-33}$$

$$\mathrm{var}(\omega) = E[\omega^2] - (E[\omega])^2 = E[\omega^2] = \sigma^2 = 1 \tag{A-34}$$

$$\mathrm{cov}\left(\mathrm{Z}_{t_i}, \mathrm{Z}_{t_j}\right) = t_i t_j \tag{A-35}$$

On a practical note, multivariate normal samples with a known covariance and mean may be obtained from a series of independent samples from the standard normal. This is done via a singular value decomposition (in MATLAB [**A,S,B**]=svd(**Σ**), where **Σ** is the covariance matrix). Following the svd, a matrix, **M**, is obtained by **M**=**A***sqrt(**S**), and a multivariate normal sample

is then obtained by **M** multiplied by a vector of samples from the standard normal (**v**) added to a vector of mean values from the multivariate normal (**μ**) (**MVN_s=M*v+μ**).

A.2.2 Bayesian Calibration

Bayesian calibration does not necessarily employ GPs, but Bayes' Law is an essential element of GPMSA, so it is discussed here, and a simple, non-GP example is given. Bayes' Law itself is an almost trivial statement of probability law, as seen in Equations A-35 through A-39. This derivation utilizes only the commutative property of probabilities and a definition of conditional probability. The result (Equation A-39) is known as Bayes' Law, and the terms P(A|B), P(B|A), P(A), and P(B) are known respectively as the posterior, the likelihood, the prior of A and the prior of B. In discussions of model calibration, Bayes' Law is better couched in terms y (model output), x (model input), and θ (model parameters for both the physical model and the statistically machinery) as in Equation A-40, where θ is the vector containing all model parameters (both for the physical model and the internal, statistical parameters).

$$P(A \cap B) = P(B \cap A) \quad \text{A-36}$$

$$P(A \cap B) = P(A|B)P(B) \quad \text{A-37}$$

$$P(A|B)P(B) = P(B|A)P(A) \quad \text{A-38}$$

$$P(A|B) = \frac{P(B|A)P(A)}{P(B)} \quad \text{A-39}$$

$$f_{\Theta|Y}(\boldsymbol{\theta}|\mathbf{y}) \propto f_{Y|\Theta}(\mathbf{y}|\boldsymbol{\theta}) f_{\Theta}(\boldsymbol{\theta}) \quad \text{A-40}$$

Equation A-40 merits considerable explanation. First, Equation A-40 is composed of pdfs of the posterior, the likelihood, and the prior of **θ**, and omits the prior probability distribution of y. Second it is a proportionality, not strictly an equation. Note that the capital letters designate a

random variable (i.e., the map between an event of some pdf and a corresponding numerical value) while the lower case letters indicating specific realizations or outcomes (a particular vector of parameter values ($\boldsymbol{\theta}$) or data points (y)). The following bullets detail the terms of A-40:

- The prior of y ($f_Y(y)$) is effectively a scaling factor that would constrain the left hand side probability distribution to integrate to unity (as required for a pdf). However, the prior of y physically corresponds to the pdf of the experimental data, which is not generally accessible. Fortunately, the calibration of a model searches for the most likely parameter values, given the data and prior beliefs regarding parameter values, so relative likelihood given any sets of parameters is retained, regardless of any scaling factor. Thus, knowledge of f_Y is not necessary for practical application.

- The prior of $\boldsymbol{\theta}$ ($f_\Theta(\boldsymbol{\theta})$) physically represents prior beliefs on the joint pdf of every model parameter and every internal parameter. As a matter of practical convenience, the joint pdf is typically assumed to be uncorrelated, and each parameter effectively has its own pdf, which is often simply the uniform pdf over some range of physically feasible space as determined by a domain expert. In reality, the model form typically dictates some correlation between model parameters, which should ideally be accounted for. The aforementioned internal parameters are those parameters that are necessary to execute the calibration, but not part of the mathematical model meant to capture some physical phenomenon. An example is given in Equation A-41, where σ_i is an internal parameter; see the next bullet point for an explanation for Equation A-41.

$$f_{Y|\Theta}(\mathbf{y}|\boldsymbol{\theta}) = \prod_{i}^{n} N(y_i; \mu_i(x), \sigma_i) \qquad \text{A-41}$$

- The likelihood function ($f_{Y|\Theta}(y|\theta)$) (in this case, Equation A-41) is often the most difficult to compute from a practical standpoint. Physically, the function quantifies the question, "How likely are the data, given the numerical values of the current parameter vector **θ**?" In other words, if specific values are plugged into a model, how likely are those parameters to explain (or fit) the data. The answer to the goodness of fit question must include information about the noise or observational error in the data. Equation A-41 quantifies the likelihood (and captures the observation error) with commonly employed assumptions: the data points are independent, so the probability of all observations is the product of the probability of each observation (the observation y_i has no bearing on the observation y_{i+1}), identically distributed (the observation error distribution is the same for all y_i), and normally distributed (fully defined by the normal pdf equation with some μ and σ). The parameter σ_i is an internal parameter if it cannot be reliably estimated from other information, which is to say it is necessary to compute the likelihood function, but is not known, and must be calibrated against the data along with the other parameters in **θ**. It represents the standard deviation of the normally distributed observation error for observation y_i, and if the errors are considered to be identically distributed, the value of σ_i is constant for all i. On the other hand, μ_i is typically formulated as a function of **θ**. When evaluating any vector of model parameters (a subset of vector **θ**), the model will predict a specific value given the values of vector **θ** and the experimental inputs associated with data point y_i (the predicted value is then designated as μ_i). Since the goal is to evaluate the likelihood of the parameter values in **θ** for the specific model in question, the output of model under the conditions of y_i with specific values of **θ** is a reasonable mean. If the probability density ($N(y_i;\mu,\sigma)$) of y_i under conditions i with the specific values of **θ** is very low, then the experimental value of y_i is several standard

deviations away from the model prediction (the mean of the normal pdf), and the values of $\boldsymbol{\theta}$ do not result in a model that represents the data well. Note that if σ is considered an internal parameter to be calibrated, it requires a prior pdf. This prior is often not based on knowledge of the actual observational error (which is unknown, otherwise σ would have a fixed value). Instead, it is typically a prior that favors small values, under the assumption that the experiments resulted in reasonably consistent observations with pains taken to minimize error.

- Finally, the posterior pdf of the parameters given the data ($f_{\Theta|Y}$) is the product of the likelihood of the data given the parameters and the prior parameter probability. This can be calculated simultaneous or sequentially for multiple experiments or multiple data points in the same experiment. The result is the same, but the prior in the sequential case is the posterior of the immediately preceding data point (i.e., the prior of θ for point y_{i+1} is the posterior for point y_i). The posterior is a joint pdf of dimensionality equal to the length of $\boldsymbol{\theta}$), and samples from the posterior can be inserted into the model to generate model predictions with quantified uncertainty, as in Equation A-42, where $y_{p,i,j}$ is the predicted output for the conditions of data point i and using parameters from sample j, η is the model output (or emulator output) for the sample parameters and experimental inputs, and ε_i is the observational error. Numerous samples build what amounts to an error bar conditional on $\mathbf{x}_i$ and $\boldsymbol{\theta}_j$.

$$y_{p,i,j} = \eta(\mathbf{x}_i, \boldsymbol{\theta}_j) + \varepsilon_j \qquad \text{A-42}$$

Finally, the calibration process may include some discrepancy term δ, which models the difference between reality and model predictions as a function of experimental inputs. Ideally, the model should be constructed to perfectly reflect reality, but in all practical applications this is

not possible. As a simple example, ballistic motion can be captured by integrating the acceleration of an object with respect to time (one integration obtains the velocity equation, while two integrations yields the position equation). In many contexts, the integration neglects drag force as a matter of convenience, but this always introduces some error, which should be reflected in δ. In this case, δ would generally be small at small velocity values and large as high velocity increases the magnitude of drag forces. In general, the calibrated model would have some form as in Equation A-43.

$$y_{p,i,j} = \eta(\mathbf{x_i}, \boldsymbol{\theta_j}) + \delta(\boldsymbol{x_i}) + \varepsilon_j \qquad \text{A-43}$$

Because Bayesian statistical model calibration is not widely applied to the combustion field, Figure A-5 summarizes the concepts of statistical calibration from a second point of view. In Figure A-5, the prior distributions are informed by the data (the likelihood function is computed for both internal parameters and model parameters), and a new, posterior parameter space is produced, where parameter values that are likely to explain the data have a high probability density while parameter values that explain the data very poorly are assigned correspondingly low probability densities.

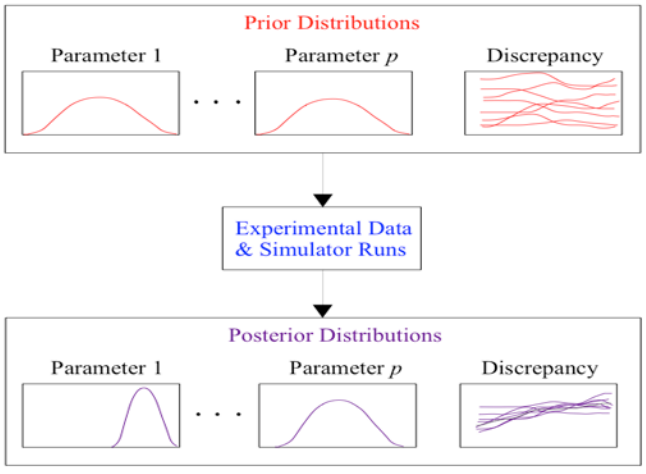

Figure A-5 – Graphical representation of model calibration with discrepancy

A.2.3 Gaussian Processes for Model Emulation

In general, statistical model emulation seeks to capture the relationship between model inputs and outputs without requiring the computational expense of physical models. This allows a simulation scientist to explore expensive models in a timely manner, using relatively few runs from a high-cost computational experiment. Statistical surrogate models or emulators are especially useful in evaluating model predictions where no input/output pairs are given from the computational experiment. See Welch et al. (Welch et al., 1992) and Sacks et al. (Sacks J., 1989) for further discussion on the subject of emulators relevant to GPMSA. Gaussian processes are a popular and powerful tool for statistical emulation because they have the potential for enormous flexibility with relatively few parameters and they naturally incorporate uncertainty in model output. Gaussian processes are fully defined by a vector of mean values and a covariance matrix, so defining an emulator is conceptually as simple as arriving at the relevant mean and covariance. In some well-behaved cases, such as a linear model of p dimensions, the mean may be immediately obvious, and the covariance matrix can be generated from a kernel function. The kernel for a one-dimensional, linear covariance matrix for n data points is shown in Equation A-44, where **x** is the independent variable vector of length n, and i and j are used as indices in the covariance matrix.

$$Cov(i,j) = \mathrm{x}_i x_j \qquad \text{A-44}$$

More complex cases require a more complex kernel or a covariance function tuned to the specific scenario and physical model. In the case of GPMSA, η is a statistical emulator (specifically a GP), and both δ and ε are similarly constructed GPs. The sum of the three GPs is also a GP, and an appropriate sample from the posterior distributions of **θ** in conjunction with any input values in the domain yields a model prediction including model and observational

uncertainty as shown in Equation A-43. The GPMSA emulators for η, δ, and ε are fully defined by mean and covariance matrices as shown below. Further details are available elsewhere (Higdon et al., 2008; Storlie et al., 2015; Gattiker et al., 2016; Gattiker, 2017). Equation A-45 differs subtly from equation A-43 in that the model predictions for the i^{th} input and j^{th} sample of $\boldsymbol{\theta}$ is not the prediction of interest. Instead, Equation A-45 is an emulator that captures model behavior for the vector $\mathbf{x}$ for the i^{th} set of input conditions at some fixed vector $\boldsymbol{\theta}^*$ that includes the model parameters and the emulator internal parameters. GP emulators require internal parameters, which are represented in Equation A-45 by IP. The emulator could also use samples from the posterior of $\boldsymbol{\theta}^*$ to generate estimates of uncertainty, and $\eta(\mathbf{x},\boldsymbol{\theta})$, $\delta(\mathbf{x}_i)$, and ε_i in Equation A-43 may well be emulators, in which case Equations A-43 and A-45 are identical. In GPMSA, η is expressed in Equation A-46, where p is the number of input parameters, u indicates that the parameters are part of the GP for η, K_j is the j^{th} basis function or principle component (meant to capture the output of the original, expensive model), and w_j is a weighting factor. The weighting factor is a GP and can be defined by a vector of means set to 0, and a covariance matrix given in Equation A-47, where q is the number of total model parameters (parameters for both the original model and internal parameters for the GP emulator). Note that $\boldsymbol{\theta}^*$ acquired a subscript in Equation A-47 to account for the possibility that the emulator is being used in calibration, and that $\boldsymbol{\theta}^*$ is therefore not fixed, but a sample from the parameter prior distribution. In Equation A-47, the subscripts i and l indicate covariance between two different experimental input settings, while the subscript j indicates a particular basis function or principle component, and the subscript k cycles through the length of the input vectors (x or θ). Other parameters (λ_j, λ_{W_Os}, and ρ) are explained in the next section.

$$y_{e,i} = \eta(\mathbf{x_i}, \boldsymbol{\theta}^*) + \delta(\boldsymbol{x_i}, \mathbf{IP_\delta}) + \varepsilon_i(\mathbf{IP_\varepsilon}) \quad \text{A-45}$$

$$\eta(\mathbf{x_i}, \boldsymbol{\theta}^*) = \sum_{j=1}^{p_u} K_j w_j(\boldsymbol{x_i}, \boldsymbol{\theta}^*) \quad \text{A-46}$$

$$\Sigma_j(\boldsymbol{x_i}, \boldsymbol{\theta_i}^*, \boldsymbol{x_l}, \boldsymbol{\theta_l}^*) = \frac{1}{\lambda_j} \prod_{k=1}^{p} \rho_{jk}^{4(x_{ik}-x_{lk})^2} * \prod_{k=1}^{q} \rho_{j(p+k)}^{4(\theta_{ik}-\theta_{lk})^2} + \frac{1}{\lambda_{w_{Os}}} \quad \text{A-47}$$

The GP for $\delta(\mathbf{x_i}, IP_\delta)$ can be written in a similar manner as in Equation A-48, where D_j is the j^{th} principal component or basis function and v_i is a multivariate normal weighting factor with 0 mean and a covariance function of the form of Equation A-47. Finally, $\varepsilon(IP_\varepsilon))$ is a GP with mean 0 and covariance (as shown in Equation A-49), where Σ^{e_i} may be either the identity matrix or specified by the user.

$$\delta(\mathbf{x_i}, \mathbf{IP_\delta}) = \sum_{j=1}^{p_v} D_j v_j(\boldsymbol{x_i}, \mathbf{IP_\delta}) \quad \text{A-48}$$

$$\mathrm{cov}(\mathbf{IP_{i,\varepsilon}}) = \frac{1}{\lambda_y} \Sigma^{e_i} \quad \text{A-49}$$

A.2.4 Gaussian Processes for Model Calibration

In principle, Bayesian calibration with GPs is identical to the Bayesian calibration with the simple model shown in Section 4.4.2, though the details of execution differ. In particular, the priors and hyper-priors of internal parameters becomes very complex, and the form of the likelihood function is far less neat. In the case of GPMSA the core internal parameters are referred to as β, ρ, λ_{w_Os}, and λ_n, each of which has several instances and their own hyper-priors.

GPMSA requires model parameters and prior distributions as inputs. In addition, internal parameters are required for GPMSA to function as it explores the parameter space and generates

a posterior distribution of the model parameters, model discrepancy, and observational uncertainty. The internal parameters are not fixed values; instead they each have their own prior distribution (called hyper-priors) which is adjusted during the calibration process. The exact form of the hyper-priors is unimportant for this discussion, but in general, they are chosen to promote small values of the GP variance where the data and model form allow. The parameter λ, if large, results in a small value of $1/\lambda$, which promotes a small variance in component j of the GP, so the hyper-prior prior favors large values of λ. Similar statements may be made regarding λ_{w_Os}, but $1/\lambda_{w\_Os}$ represents a nugget rather than a variance scale, and is equal to zero, except on the diagonal of the covariance matrix. A nugget is some small variance added to any data point the GP to emphasize mathematically that there is always some level uncertainty, even at "known" points for training the GP. In practical terms, the nugget prevents a zero uncertainty situation, which is physically unrealistic and computationally untenable. Finally, ρ and β are related as shown in Equation A-50. Substituting the right-hand-side of Equation A-50 for ρ in Equation A-47 yields the most common form of the covariance function, but ρ is easier to work with in the GPMSA code. In either case, these parameters may be regarded as length scale parameters; in other words, they indicate the degree to which different points in input space impact the corresponding points in output space as a function of the Euclidean distance between the two points in input space.

$$\rho = \exp(-\frac{\beta}{4}) \qquad \text{A-50}$$

As a final note, the likelihood function itself is not given here, both because it is extremely intricate and lengthy, and because any reader interested in that level of detail would do far better to thoroughly peruse the literature references in an effort to reconstruct highly advanced model analysis machinery. Some results using the techniques of this chapter are described briefly in

B. SOLVENT MODEL UNCERTAINTY QUANTIFICATION AND CALIBRATION

B.1 Introduction

A substantial amount of work was also done on what might be referred to as the inverse problem to Oxy-coal combustion. Oxy-coal systems were conceived to concentrate flue gas CO_2 to facilitate post-combustion carbon capture. Alternatively, air-fired systems could be used with a high-selectivity, solvent-based CO_2 capture system. The following work was done in collaboration with a number of organizations (including West Virginia University, NETL, LANL, LLNL, PNNL, General Electric, UT Austin etc.) under the umbrella of the Carbon Capture Simulation Initiative (CCSI). CCSI primarily focused on creating computational tools to accelerate the deployment of advanced technologies in industrial settings, and most of the following work supports that goal in direct collaborations between LANL, General Electric, WVU, and UT Austin. The work is less suitable for the body of the dissertation because of space constraints and intellectual property limitations.

B.2 General Electric Solvent Model

A General Electric proprietary solvent was used to create absorber/stripper simulations in Aspen Plus. Additionally, basic properties and chemistry submodels were created, modified, or calibrated from GE data. LANL's role revolved around calibration and uncertainty quantification of both submodels and process models. Model details, data, and results are not available for open

publication, but they closely resembled the details of the UT Austin solvent calibration detailed below.

B.3 UT Austin Piperazine Model Calibration and Uncertainty Quantification

B.3.1 Scope

- Receive model and data
- Dissect model to establish theoretical motivations and parameters to be calibrated
- Determine physically feasible ranges and prior distributions on model parameters
- Determine observational error in the data to the extent possible
- Calibrate the model to available data
- Quantify uncertainty
- Suggest model updates based on calibrated model/data discrepancy

B.3.2 Models

The UT Austin Piperazine model "Independence" is a collection of thermodynamic, kinetic, and heat and mass transfer submodel in the Aspen Plus framework. Some of the submodels are user models written in FORTRAN, but the majority are native Aspen submodels with user defined parameters. Ultimately, the uncertainty quantification (UQ) and calibration work will calibrate four layers of submodels: thermodynamics, kinetics, heat and mass transfer, and the full process model of a CO_2 absorber/stripper system. Further data and detailed descriptions are available elsewhere (Hilliard, 2008; Dugas, 2009; Freeman, 2011; Xu, 2011;

Nguyen, 2013; Fulk, 2016) Because the submodels contain numerous parameters calibrated to a large body of data, it is mathematically and computationally unfeasible to simultaneously calibrate all parameters in all submodels. Instead, the strategy of sequential calibration with carefully propagated uncertainty between submodels has been adopted. As of May 2017, the thermodynamic submodels and parameters have been identified and separately calibrated. Work is ongoing to propagate uncertainty between submodels. The thermodynamic submodels of interest are given below:

B.3.2.1 Electrolyte Non-Random Two Liquid Model (eNRTL)

The eNRTL model is an activity coefficient model native to Aspen plus with a number of internal parameters. It predicts activity coefficients based on molecular interactions in the liquid phase. The interactions fall into 3 categories (local, Pitzer-Debye-Huckle, and Born), and they are captured in the asymmetric Gibbs excess energy in Equation B-1, where the asterisk indicates the asymmetric convention (i.e., the related activity coefficient is $\gamma^* = \gamma / \gamma^{\infty}$). Equation B-2 show the relation between the asymmetric Gibbs excess energy and the asymmetric activity coefficient.

$$\boldsymbol{G_{Ex}^{*} = G_{Ex,lc}^{*} + G_{Ex,PDH}^{*} + G_{Ex,Born}^{*}} \qquad \text{B-1}$$

$$\boldsymbol{RT * ln(\gamma_i^{*}) = \frac{\partial G_{Ex}^{*}}{\partial n_i}} \qquad \text{B-2}$$

All three liquid interactions are represented by a number of complex expressions with numerous parameters. However, in this work, only the local contribution is considered for calibration and UQ, with other parameters being considered fixed in the present scope of work. The local Gibbs excess energy contribution is calculated via Equation B-3, where m, c, and a

denote molecule, cation, and anion respectively. The constituents of Equation B-3 are given by Equations B-4 through B-7. Because α is set by a heuristic (0.3 for molecule-molecule interactions, 0.2 for electrolyte-electrolyte or molecule-electrolyte interactions where the molecule is water, and 0.1 where the molecule is a solute), only the values of various types of τ need to be computed. The value "G" (shown in Equation B-6 for molecule-ionic pairs) represents differences in liquid component interaction that contribute to a non-ideal solution and thus a non-unity activity coefficient. Since the value of G is not often known, Equations B-6 is used to compute it, which in turn requires an alternative approach to obtain τ. Equations B-4, B-5, and B-7 are empirical correlations with (typically regressed) parameters that give τ as a function of temperature in K. Given the many pair-wise interactions in real systems, the total number of parameters to be regressed quickly becomes prohibitive, and often only the first one or two parameters in the empirical correlations are non-zero. See Table B-1 for additional details on parameter equations and locations in Aspen Plus, and note that $X_j=x_jC_j$, where x is the mole fraction and C is either z (the charge on the ion) or unity for molecules.

$$\frac{G^{*}_{Ex,lc}}{RT} = \sum_{m} X_m \frac{\sum_j X_j G_{jm}\tau_{jm}}{\sum_k X_k G_{km}} + \sum_{c} X_c \sum_{a'} \left(\frac{X_{a'}}{\sum_{a''} X_{a''}}\right) \frac{\sum_j G_{jc,a'c}\tau_{jc,a'c}}{\sum_k X_k G_{jc,a'c}}$$
$$+ \sum_{a} X_a \sum_{c'} \left(\frac{X_{c'}}{\sum_{c''} X_{c''}}\right) \frac{\sum_j G_{ja,a'c}\tau_{ja,a'c}}{\sum_k X_k G_{ja,a'c}} \qquad \text{B-3}$$

$$\tau_{mc,ac} = -ln\left[\sum_{a} \frac{X_a exp\left(-\alpha_{ca,m}\tau_{ca,m}\right)}{\sum_{a'} X_{a'}}\right] - \tau_{ca,m} + \tau_{m,ca} \qquad \text{B-4}$$

$$\tau_{m,ac} = A_{m,ac} + \frac{B_{m,ac}}{T} + C_{m,ac}\left(\frac{T^{ref} - T}{T} + ln\left(\frac{T}{T^{ref}}\right)\right) \qquad \text{B-5}$$

$$G_{mc,ac} = exp(-\alpha_{ca,m}\tau_{mc,ac}) \qquad \text{B-6}$$

$$\tau_{m,m'} = A_{m,m'} + \frac{B_{m,m'}}{T} + \cdots \quad \text{B-7}$$

In addition to the activity coefficient equations, the thermodynamic system in Independence requires self-consistency between submodels for Henry's constant, heat capacity, vapor-liquid equilibrium, and chemical equilibrium. The heat capacity and Henry's constant (Equation B-8) submodels are empirical, and typically only use two or three parameters of the between five and eleven available parameters. Models for C_p are shown in Table B-1, but are not shown with the other equations below because several different model forms are available. Regression data are proprietary and are omitted.

Equation B-9 is a form of the teenage vapor-liquid equilibrium equation, where the activity coefficient is referenced to the infinite dilution activity coefficient. Similarly, the Henry's constant replaces the vapor pressure of component i in the solvent (water), because the Henry's constant is conceptualized as the constant of direct proportionality between vapor-phase partial pressure of component i and liquid phase mol fraction of i ($H=P_i/x_i$). This is only valid at or near infinite dilution of component i, but by an abuse of theory Equation B-9 is serviceable. That is, γ^* is allowed to compensate for H, even though the activity coefficient is theoretically rooted in liquid-liquid non-idealities while Henry's constant is only valid at infinite dilution because of liquid non-idealities, but is conceptualized for largely non-condensable gases rather than all non-water components in a system. The form of H used here has units of pressure, but it is meant to be a proportionality constant, not a vapor pressure. This abuse is a convenience introduced because much of the data and a number of submodels were referenced to the infinite dilution state, and Aspen does not have another convenient way to compensate for the change in reference state (Hilliard, 2008).

Finally, the location of the ionic activity coefficient τ parameters are given in Table B-2, and Equations B-10 through B-13 show the equilibrium equation and the chemical equations used in Independence.

$$ln(H_{i,solvent}) = A_i + \frac{B_i}{T} + C_i ln(T) + D_i + \frac{E_i}{T^2} \quad \text{B-8}$$

$$y_i \phi_i P = x_i \gamma_i^* H_{i,H_2O} \quad \text{B-9}$$

$$-RT ln(K_{eq}) = \frac{\Delta G^o}{RT}$$

$$= \frac{\Delta G_0^o - \Delta H_0^o}{RT_0} + \frac{\Delta H_0^o}{RT} + \frac{1}{T}\int_{T_0}^{T} \frac{\Delta C_p^o}{R} dT - \int_{T_0}^{T} \frac{\Delta C_p^o}{RT} dT \quad \text{B-10}$$

$$2PZ + CO_2 \leftrightarrow PZH^+ + PZCOO^- \quad \text{B-11}$$

$$2PZCOO^- + CO_2 \leftrightarrow PZ(COO)_2^{2-} + H^+PZCOO^- \quad \text{B-12}$$

$$PZ + H^+PZCOO^- \leftrightarrow PZH^+ + PZCOO^- \quad \text{B-13}$$

Table B-1 – Thermodynamic parameters of interest in Independence

Param #	Parameter Location	Parameter Element	Parameter Designation	Parameter Description	Relevant equation
1	Properties>Methods>Parameters>Pure Components> CPAQ0	1	C1	In the heat capacity equation referenced to the infinite dilution in water state for CO3-	C_p=C1+C2*T+C3*T^2+C4/T+C5/T^2+C6/$T^{0.5}$
2	Properties>Methods>Parameters>Pure Components> CPAQ0	2	C2	In the heat capacity equation referenced to the infinite dilution in water state for CO3-	C_p=C1+C2*T+C3*T^2+C4/T+C5/T^2+C6/$T^{0.5}$
3	Properties>Methods>Parameters>Pure Components> CPAQ0	3	C3	In the heat capacity equation referenced to the infinite dilution in water state for CO3-	C_p=C1+C2*T+C3*T^2+C4/T+C5/T^2+C6/$T^{0.5}$

4	Properties>Methods>Parameters>Pure Components>CPAQ0	1	C1	In the heat capacity equation referenced to the infinite dilution in water state for HCO3-	C_p=C1+C2*T+C3*T^2+C4/T+C5/T^2+C6/$T^{0.5}$
5	Properties>Methods>Parameters>Pure Components>CPAQ0	2	C2	In the heat capacity equation referenced to the infinite dilution in water state for HCO3-	C_p=C1+C2*T+C3*T^2+C4/T+C5/T^2+C6/$T^{0.5}$
6	Properties>Methods>Parameters>Pure Components>CPAQ0	3	C3	In the heat capacity equation referenced to the infinite dilution in water state for HCO3-	C_p=C1+C2*T+C3*T^2+C4/T+C5/T^2+C6/$T^{0.5}$
7	Properties>Methods>Parameters>Pure Components>CPAQ0	1	C1	In the heat capacity equation referenced to the infinite dilution in water state for PZCOO-2	C_p=C1+C2*T+C3*T^2+C4/T+C5/T^2+C6/$T^{0.5}$
8	Properties>Methods>Parameters>Pure Components>CPAQ0	2	C2	In the heat capacity equation referenced to the infinite dilution in water state for PZCOO-2	C_p=C1+C2*T+C3*T^2+C4/T+C5/T^2+C6/$T^{0.5}$
9	Properties>Methods>Parameters>Pure Components>CPAQ0	1	C1	In the heat capacity equation referenced to the infinite dilution in water state for PZCOO-	C_p=C1+C2*T+C3*T^2+C4/T+C5/T^2+C6/$T^{0.5}$
10	Properties>Methods>Parameters>Pure Components>CPAQ0	2	C2	In the heat capacity equation referenced to the infinite dilution in water state for PZCOO-	C_p=C1+C2*T+C3*T^2+C4/T+C5/T^2+C6/$T^{0.5}$
11	Properties>Methods>Parameters>Pure Components>CPAQ0	1	C1	In the heat capacity equation referenced to the infinite dilution in water state for PZH+	C_p=C1+C2*T+C3*T^2+C4/T+C5/T^2+C6/$T^{0.5}$
12	Properties>Methods>Parameters>Pure Components>CPAQ0	2	C2	In the heat capacity equation referenced to the infinite dilution in water state for PZH+	C_p=C1+C2*T+C3*T^2+C4/T+C5/T^2+C6/$T^{0.5}$

13	Properties>Methods>Parameters>Pure Components>CPAQ0	1	C1	In the heat capacity equation referenced to the infinite dilution in water state for HPZCOO	C_p=C1+C2*T+C3*T^2+C4/T+C5/T^2+C6/$T^{0.5}$
14	Properties>Methods>Parameters>Pure Components>CPAQ0	2	C2	In the heat capacity equation referenced to the infinite dilution in water state for HPZCOO	C_p=C1+C2*T+C3*T^2+C4/T+C5/T^2+C6/$T^{0.5}$
15	Properties>Methods>Parameters>Pure Components>CPAQ0	1	C1	In the heat capacity equation referenced to the infinite dilution in water state for C5H14-01	C_p=C1+C2*T+C3*T^2+C4/T+C5/T^2+C6/$T^{0.5}$
16	Properties>Methods>Parameters>Pure Components>CPDIEC	1	A_B	In the correlation for the dielectric constant of PZ	ε(T)=A_B+B_B*(1/T-1/C_B)
17	Properties>Methods>Parameters>Pure Components>CPDIEC	2	B_B	In the correlation for the dielectric constant of PZ	ε(T)=A_B+B_B*(1/T-1/C_B)
18	Properties>Methods>Parameters>Pure Components>CPDIEC	3	C_B	This parameter is in the correlation for the dielectric constant of PZ	ε(T)=A_B+B_B*(1/T-1/C_B)
19	Properties>Methods>Parameters>Pure Components>CPIG	1	C_1	In the correlation for Ideal gas heat capacity for HPZCOO	CP_IG(T)=C_1+C_2*T+C_3*T^2+C_4*T^3+C_5*T^4+C_6*T^5
20	Properties>Methods>Parameters>Pure Components>CPIG	2	C_2	In the correlation for Ideal gas heat capacity for HPZCOO	CP_IG(T)=C_1+C_2*T+C_3*T^2+C_4*T^3+C_5*T^4+C_6*T^5
21	Properties>Methods>Parameters>Pure Components>CPIG	9	C_9	In the correlation for Ideal gas heat capacity for HPZCOO for extrapolation below temperatures at C_7	CP_IG(T)=C_9+C_10*T

22	Properties>Methods>Parameters>Pure Components>CPIG	10	C_10	In the correlation for Ideal gas heat capacity for HPZCOO for extrapolation below temperatures at C_7	CP_IG(T)=C_9+C_10 *T^{C_11}
23	Properties>Methods>Parameters>Pure Components>CPIG	11	C_11	In the correlation for Ideal gas heat capacity for HPZCOO for extrapolation below temperatures at C_7	CP_IG(T)=C_9+C_10 *T^{C_11}
24	Properties>Methods>Parameters>Pure Components>CPIG	7	C_7	In the lower temperature limit in the correlation for Ideal gas heat capacity for HPZCOO	N/A
25	Properties>Methods>Parameters>Pure Components>CPIG	1	C_1	In the correlation for Ideal gas heat capacity (probably the Aspen polynomial) for PZ but not used because the DIPPR equation is indicated in THRSWT/7 and parameters for that are assigned in CPIGDP.	CP_IG(T)=C_1+C_2* T+C_3*T^2+C_4* T^3+C_5* T^4+C_6* T^5
26	Properties>Methods>Parameters>Pure Components>CPIG	2	C_2	In the correlation for Ideal gas heat capacity (probably the Aspen polynomial) for PZ but not used because the DIPPR equation is indicated in THRSWT/7 and parameters for that are assigned in CPIGDP.	CP_IG(T)=C_1+C_2* T+C_3*T^2+C_4* T^3+C_5* T^4+C_6* T^5
27	Properties>Methods>Parameters>Pure Components>CPIG	1	C_1	In the correlation for Ideal gas heat capacity (probably the Aspen polynomial) for C5H13-01 but not used because the DIPPR equation is indicated in THRSWT/7 and parameters for that	CP_IG(T)=C_1+C_2* T+C_3*T^2+C_4* T^3+C_5* T^4+C_6* T^5

				are assigned in CPIGDP.	
28	Properties>Methods>Parameters>Pure Components>CPIG	2	C_2	In the correlation for Ideal gas heat capacity (probably the Aspen polynomial) for C5H13-01 but not used because the DIPPR equation is indicated in THRSWT/7 and parameters for that are assigned in CPIGDP.	CP_IG(T)=C_1+C_2*T+C_3*T^2+C_4*T^3+C_5*T^4+C_6*T^5
29	Properties>Methods>Parameters>Pure Components>CPIGDP	1	C_1	In the correlation for Ideal gas heat capacity for C5H13-01 given that THRSWT/7=107 and the parameters came from CPIGDP.	CP_IG(T)=C_1+C_2*((C_3/T)/sinh(C_3/T))^2+C_4*((C_5/T_/cosh(C_5/T))
30	Properties>Methods>Parameters>Pure Components>CPIGDP	2	C_2	In the correlation for Ideal gas heat capacity for C5H13-01 given that THRSWT/7=107 and the parameters came from CPIGDP.	CP_IG(T)=C_1+C_2*((C_3/T)/sinh(C_3/T))^2+C_4*((C_5/T_/cosh(C_5/T))
31	Properties>Methods>Parameters>Pure Components>CPIGDP	3	C_3	In the correlation for Ideal gas heat capacity for C5H13-01 given that THRSWT/7=107 and the parameters came from CPIGDP.	CP_IG(T)=C_1+C_2*((C_3/T)/sinh(C_3/T))^2+C_4*((C_5/T_/cosh(C_5/T))
32	Properties>Methods>Parameters>Pure Components>CPIGDP	4	C_4	In the correlation for Ideal gas heat capacity for C5H13-01 given that THRSWT/7=107 and the parameters came from CPIGDP.	CP_IG(T)=C_1+C_2*((C_3/T)/sinh(C_3/T))^2+C_4*((C_5/T_/cosh(C_5/T))
33	Properties>Methods>Parameters>Pure Components>CPIGDP	5	C_5	In the correlation for Ideal gas heat capacity for C5H13-01 given that THRSWT/7=107	CP_IG(T)=C_1+C_2*((C_3/T)/sinh(C_3/T))^2+C_4*((C_5/T_/cosh(C_5/T))

				and the parameters came from CPIGDP.	
34	Properties>Methods>Parameters>Pure Components>DHVLDP	1	C_1	This parameter uses the DIPPR equation (THRSWT/4=106) for the heat of vaporization of liquid PZ.	ΔH_vap=C_1*(1-T_r)^(C_2+C_3*T+C_4*T^2+C_5*T^3)
35	Properties>Methods>Parameters>Pure Components>DHVLDP	2	C_2	This parameter uses the DIPPR equation (THRSWT/4=106) for the heat of vaporization of liquid PZ.	ΔH_vap=C_1*(1-T_r)^(C_2+C_3*T+C_4*T^2+C_5*T^3)
36	Properties>Methods>Parameters>Pure Components>DHVLDP	3	C_3	This parameter uses the DIPPR equation (THRSWT/4=106) for the heat of vaporization of liquid PZ.	ΔH_vap=C_1*(1-T_r)^(C_2+C_3*T+C_4*T^2+C_5*T^3)
37	Properties>Methods>Parameters>Pure Components>DHVLWT	1	C_1	This parameter uses the Watson equation (THRSWT/4=0) for the heat of vaporization of liquid H2O.	ΔH_vap (T)= ΔH_vap (T1)*((1-T/Tc)/(1_T1/Tc))^(a+b*(1-T/Tc))
38	Properties>Methods>Parameters>Pure Components>DHVLWT	2	C_2	This parameter uses the Watson equation (THRSWT/4=0) for the heat of vaporization of liquid H2O.	ΔH_vap (T)= ΔH_vap (T1)*((1-T/Tc)/(1_T1/Tc))^(a+b*(1-T/Tc))
39	Properties>Methods>Parameters>Pure Components>DHVLWT	3	C_3	This parameter uses the Watson equation (THRSWT/4=0) for the heat of vaporization of liquid H2O.	ΔH_vap (T)= ΔH_vap (T1)*((1-T/Tc)/(1_T1/Tc))^(a+b*(1-T/Tc))
40	Properties>Methods>Parameters>Pure Components>DHVLWT	4	C_4	This parameter uses the Watson equation (THRSWT/4=0) for the heat of vaporization of liquid H2O.	ΔH_vap (T)= ΔH_vap (T1)*((1-T/Tc)/(1_T1/Tc))^(a+b*(1-T/Tc))
41	Properties>Methods>Parameters>Pure	5	C_5	This parameter uses the Watson equation (THRSWT/4=0) for the	ΔH_vap (T)= ΔH_vap (T1)*((1-

	Components> DHVLWT			heat of vaporization of liquid H2O.	T/Tc)/(1_T1/Tc))^(a +b*(1-T/Tc))
42	Properties>Methods>Parameters>Pure Components> DNLDIP	1	A	This parameter uses the DIPPR equation 116 (THRSWT/2=116), typically used for H2O, for the liquid molar density of C5H13-01	kmol/cum=A+B*T^0.35+C*T^(2/3)+D*T+E*T^(4/3)
43	Properties>Methods>Parameters>Pure Components> DNLDIP	2	B	This parameter uses the DIPPR equation 116 (THRSWT/2=116), typically used for H2O, for the liquid molar density of C5H13-01	kmol/cum=A+B*T^0.35+C*T^(2/3)+D*T+E*T^(4/3)
44	Properties>Methods>Parameters>Pure Components> DNLDIP	3	C	This parameter uses the DIPPR equation 116 (THRSWT/2=116), typically used for H2O, for the liquid molar density of C5H13-01	kmol/cum=A+B*T^0.35+C*T^(2/3)+D*T+E*T^(4/3)
45	Properties>Methods>Parameters>Pure Components> DNLDIP	4	D	This parameter uses the DIPPR equation 116 (THRSWT/2=116), typically used for H2O, for the liquid molar density of C5H13-01	kmol/cum=A+B*T^0.35+C*T^(2/3)+D*T+E*T^(4/3)
46	Properties>Methods>Parameters>Pure Components> IONMOB	1	see help	These are coefficients for PZH+ for the Jones-Dole correction to the viscosity of a solution due to the presence of electrolytes.	see Aspen help pages
47	Properties>Methods>Parameters>Pure Components> IONMOB	2	see help	These are coefficients for PZH+ for the Jones-Dole correction to the viscosity of a solution due to the presence of electrolytes.	see Aspen help pages
48	Properties>Methods>Parameters>Pure Components> IONMOB	1	see help	These are coefficients for PZCOO- for the Jones-Dole correction to the viscosity of a solution due to the	see Aspen help pages

				presence of electrolytes.	
49	Properties>Methods>Parameters>Pure Components>IONMOB	2	see help	These are coefficients for PZCOO- for the Jones-Dole correction to the viscosity of a solution due to the presence of electrolytes.	see Aspen help pages
50	Properties>Methods>Parameters>Pure Components>IONMOB	1	see help	These are coefficients for PZCOO-2 for the Jones-Dole correction to the viscosity of a solution due to the presence of electrolytes.	see Aspen help pages
51	Properties>Methods>Parameters>Pure Components>IONMOB	2	see help	These are coefficients for PZCOO-2 for the Jones-Dole correction to the viscosity of a solution due to the presence of electrolytes.	see Aspen help pages
52	Properties>Methods>Parameters>Pure Components>MDH		see help	This is a parameter for the Rackett equation mixing rule for PZ (to determine liquid molar volume). The parameter is VCRKT, which is the critical volume.	see Aspen help pages
53	Properties>Methods>Parameters>Pure Components>MDH		see help	This is a parameter for the Rackett equation mixing rule for PZ (to determine liquid molar volume). The parameter is RKTZRA, which appears to be the compressibility factor.	see Aspen help pages
54	Properties>Methods>Parameters>Pure Components>MDH		see help	This is a parameter for the Rackett equation mixing rule for CO2 (to determine liquid molar volume). The parameter is RKTZRA,	see Aspen help pages

				which appears to be the compressibility factor.	
55	Properties>Methods>Parameters>Pure Components>MDH		see help	This is a parameter for the Rackett equation mixing rule for CO2 (to determine liquid molar volume). The parameter is VCRKT, which is the critical volume.	see Aspen help pages
56	Properties>Methods>Parameters>Pure Components>MDH		see help	This is a parameter for the Rackett equation mixing rule for HPZCOO (to determine liquid molar volume). The parameter is VCRKT, which is the critical volume.	see Aspen help pages
57	Properties>Methods>Parameters>Pure Components>MDH		see help	This is a parameter for the Rackett equation mixing rule for HPZCOO (to determine liquid molar volume). The parameter is RKTZRA, which appears to be the compressibility factor.	see Aspen help pages
58	Properties>Methods>Parameters>Pure Components>MDH		see help	This is a parameter for the Rackett equation mixing rule for C5H13-01 (to determine liquid molar volume). The parameter is VCRKT, which appears to be the compressibility factor.	complicated and ugly, see help page
59	Properties>Methods>Parameters>Pure Components>MDH		see help	This is a parameter for the Rackett equation mixing rule for C5H13-01 (to determine liquid molar volume). The parameter is RKTZRA, which	see Aspen help pages

				appears to be the compressibility factor.	
60	Properties>Methods>Parameters>Pure Components> Review	scalar	scalar	The aqueous gibbs energy of formation for C5H14-01.	scalar
61	Properties>Methods>Parameters>Pure Components> Review	scalar	scalar	The aqueous enthalpy of formation for C5H14-01.	scalar
62	Properties>Methods>Parameters>Pure Components> USRDEF	scalar	scalar	The aqueous gibbs energy of formation for PZCOO-2	scalar
63	Properties>Methods>Parameters>Pure Components> USRDEF	scalar	scalar	The aqueous gibbs energy of formation for PZCOO-	scalar
64	Properties>Methods>Parameters>Pure Components> USRDEF	scalar	scalar	The aqueous gibbs energy of formation for HPZCOO	scalar
65	Properties>Methods>Parameters>Pure Components> USRDEF	scalar	scalar	The aqueous enthalpy of formation for PZCOO-2	scalar
66	Properties>Methods>Parameters>Pure Components> USRDEF	scalar	scalar	The aqueous enthalpy of formation for PZCOO-	scalar
67	Properties>Methods>Parameters>Pure Components> USRDEF	scalar	scalar	The aqueous enthalpy of formation for HPZCOO	scalar
68	Properties>Methods>Parameters>Pure	scalar	scalar	The gibbs energy of formation for HPZCOO	scalar

	Components>USRDEF				
69	Properties>Methods>Parameters>Pure Components>USRDEF	scalar	scalar	The enthalpy of formation for HPZCOO	scalar
70	Properties>Methods>Parameters>Binary Interaction>Henry	1	AIJ	All molecular species were declared as Henry's components (except water, which is the solvent). This is a parameter in the Henry's law correlation for PZ.	H_i,j=AIJ+BIJ/T+CIJ*ln(T)+DIJ*T+EIJ/T^2
71	Properties>Methods>Parameters>Binary Interaction>Henry	2	BIJ	All molecular species were declared as Henry's components (except water, which is the solvent). This is a parameter in the Henry's law correlation for PZ.	H_i,j=AIJ+BIJ/T+CIJ*ln(T)+DIJ*T+EIJ/T^2
72	Properties>Methods>Parameters>Binary Interaction>Henry	3	CIJ	All molecular species were declared as Henry's components (except water, which is the solvent). This is a parameter in the Henry's law correlation for PZ.	H_i,j=AIJ+BIJ/T+CIJ*ln(T)+DIJ*T+EIJ/T^2
73	Properties>Methods>Parameters>Binary Interaction>Henry	4	DIJ	All molecular species were declared as Henry's components (except water, which is the solvent). This is a parameter in the Henry's law correlation for PZ.	H_i,j=AIJ+BIJ/T+CIJ*ln(T)+DIJ*T+EIJ/T^2
74	Properties>Methods>Parameters>Binary Interaction>Henry	1	AIJ	All molecular species were declared as Henry's components (except water, which is the solvent). This is a parameter in the Henry's law	H_i,j=AIJ+BIJ/T+CIJ*ln(T)+DIJ*T+EIJ/T^2

				correlation for C5H13-01.	
75	Properties>Methods>Parameters>Binary Interaction>Henry	2	BIJ	All molecular species were declared as Henry's components (except water, which is the solvent). This is a parameter in the Henry's law correlation for C5H13-01.	H_i,j=AIJ+BIJ/T+CIJ*ln(T)+DIJ*T+EIJ/T^2
76	Properties>Methods>Parameters>Binary Interaction>Henry	3	CIJ	All molecular species were declared as Henry's components (except water, which is the solvent). This is a parameter in the Henry's law correlation for C5H13-01.	H_i,j=AIJ+BIJ/T+CIJ*ln(T)+DIJ*T+EIJ/T^2
77	Properties>Methods>Parameters>Binary Interaction>Henry	4	DIJ	All molecular species were declared as Henry's components (except water, which is the solvent). This is a parameter in the Henry's law correlation for C5H13-01.	H_i,j=AIJ+BIJ/T+CIJ*ln(T)+DIJ*T+EIJ/T^2
78	Properties>Methods>Parameters>Binary Interaction>NRTL-1	1	AJI	This parameter is used for computing tau for the molecule-molecule portion of the NRTL model. Component I is water and J is PZ.	tau_i,j=AIJ+BIJ/T+EIJ*ln(T)+FIJ*T
79	Properties>Methods>Parameters>Binary Interaction>NRTL-1	2	BJI	This parameter is used for computing tau for the molecule-molecule portion of the NRTL model. Component I is water and J is PZ.	tau_i,j=AIJ+BIJ/T+EIJ*ln(T)+FIJ*T

80	Properties>Methods>Parameters>Binary Interaction>NRTL-1	1	AIJ	This parameter is used for computing tau for the molecule-molecule portion of the NRTL model. Component I is HPZCOO and J is CO2.	tau_i,j=AIJ+BIJ/T+EIJ*ln(T)+FIJ*T
81	Properties>Methods>Parameters>Binary Interaction>NRTL-1	2	BIJ	This parameter is used for computing tau for the molecule-molecule portion of the NRTL model. Component I is HPZCOO and J is CO2.	tau_i,j=AIJ+BIJ/T+EIJ*ln(T)+FIJ*T
82	Properties>Methods>Parameters>Binary Interaction>NRTL-1	1	AJI	This parameter is used for computing tau for the molecule-molecule portion of the NRTL model. Component I is CO2 and J is PZ.	tau_i,j=AIJ+BIJ/T+EIJ*ln(T)+FIJ*T
83	Properties>Methods>Parameters>Binary Interaction>NRTL-1	2	BJI	This parameter is used for computing tau for the molecule-molecule portion of the NRTL model. Component I is CO2 and J is PZ.	tau_i,j=AIJ+BIJ/T+EIJ*ln(T)+FIJ*T
84	Properties>Methods>Parameters>Binary Interaction>NRTL-1	1	AJI	This parameter is used for computing tau for the molecule-molecule portion of the NRTL model. Component I is H2O and J is C5H13-01.	tau_i,j=AIJ+BIJ/T+EIJ*ln(T)+FIJ*T
85	Properties>Methods>Parameters>Binary Interaction>NRTL-1	2	BJI	This parameter is used for computing tau for the molecule-molecule portion of the NRTL model. Component I is H2O and J is C5H13-01.	tau_i,j=AIJ+BIJ/T+EIJ*ln(T)+FIJ*T
86	Properties>Methods>Parameters>Binary	1	AIJ	This parameter is used for computing tau for the molecule-molecule portion of the NRTL model.	tau_i,j=AIJ+BIJ/T+EIJ*ln(T)+FIJ*T

	Interaction>NRTL-1			Component I is C5H13-01 and J is CO2.	
87	Properties>Methods>Parameters>Binary Interaction>NRTL-1	2	BIJ	This parameter is used for computing tau for the molecule-molecule portion of the NRTL model. Component I is C5H13-01 and J is CO2.	tau_i,j=AIJ+BIJ/T+EIJ*ln(T)+FIJ*T
88	Properties>Methods>Parameters>Binary Interaction>NRTL-1	1	AJI	This parameter is used for computing tau for the molecule-molecule portion of the NRTL model. Component I is C5H13-01 and J is CO2.	tau_i,j=AIJ+BIJ/T+EIJ*ln(T)+FIJ*T
89	Properties>Methods>Parameters>Binary Interaction>NRTL-1	2	BJI	This parameter is used for computing tau for the molecule-molecule portion of the NRTL model. Component I is C5H13-01 and J is CO2.	tau_i,j=AIJ+BIJ/T+EIJ*ln(T)+FIJ*T
90	Properties>Methods>Parameters>Binary Interaction>NRTL-1	3	CIJ	This parameter is typically computed via a heuristic, and is used to compute alpha, which appears to be symmetrical in this case. Component I is H2O and component J is PZ.	alpha_i,j=CIJ+(T-273.15)*DIJ
91	Properties>Methods>Parameters>Binary Interaction>NRTL-1	3	CIJ	This parameter is typically computed via a heuristic, and is used to compute alpha, which appears to be symmetrical in this case. Component I is HPZCOO and component J is CO2.	alpha_i,j=CIJ+(T-273.15)*DIJ

92	Properties>Methods>Parameters>Binary Interaction>NRTL-1	3	CIJ	This parameter is typically computed via a heuristic, and is used to compute alpha, which appears to be symmetrical in this case. Component I is CO2 and component J is PZ.	alpha_i,j=CIJ+(T-273.15)*DIJ
93	Properties>Methods>Parameters>Binary Interaction>NRTL-1	3	CIJ	This parameter is typically computed via a heuristic, and is used to compute alpha, which appears to be symmetrical in this case. Component I is H2O and component J is C5H13-01.	alpha_i,j=CIJ+(T-273.15)*DIJ
94	Properties>Methods>Parameters>Binary Interaction>NRTL-1	3	CIJ	This parameter is typically computed via a heuristic, and is used to compute alpha, which appears to be symmetrical in this case. Component I is C5H13-01 and component J is CO2.	alpha_i,j=CIJ+(T-273.15)*DIJ
95	Properties>Methods>Parameters>Binary Interaction>NRTL-1	3	CIJ	This parameter is typically computed via a heuristic, and is used to compute alpha, which appears to be symmetrical in this case. Component I is PZ and component J is C5H13-01.	alpha_i,j=CIJ+(T-273.15)*DIJ
96	Properties>Methods>Parameters>Binary Interaction>NRTL-1	3	CIJ	This parameter is typically computed via a heuristic, and is used to compute alpha, which appears to be symmetrical in this case. Component I is C5H13-01 and component J is HPZCOO.	alpha_i,j=CIJ+(T-273.15)*DIJ

97	Properties>Methods>Parameters>Binary Interaction>VLCLK	1	VCA	This parameter is used to calculate the liquid molar volume using the Clarke equation for electrolyte solutions of PZH+ and PZCOO-	See Aspen help pages
98	Properties>Methods>Parameters>Binary Interaction>VLCLK	2	ACA	This parameter is used to calculate the liquid molar volume using the Clarke equation for electrolyte solutions of PZH+ and PZCOO-	See Aspen help pages
99	Properties>Methods>Parameters>Binary Interaction>VLCLK	1	VCA	This parameter is used to calculate the liquid molar volume using the Clarke equation for electrolyte solutions of PZH+ and HCO3-	See Aspen help pages
100	Properties>Methods>Parameters>Binary Interaction>VLCLK	2	ACA	This parameter is used to calculate the liquid molar volume using the Clarke equation for electrolyte solutions of PZH+ and HCO3-	See Aspen help pages
101	Properties>Methods>Parameters>Binary Interaction>VLCLK	1	VCA	This parameter is used to calculate the liquid molar volume using the Clarke equation for electrolyte solutions of PZH+ and PZCOO-2	See Aspen help pages
102	Properties>Methods>Parameters>Binary Interaction>VLCLK	2	ACA	This parameter is used to calculate the liquid molar volume using the Clarke equation for electrolyte solutions of PZH+ and PZCOO-2	See Aspen help pages
103	Properties>Methods>Parameters>Binary	1	VCA	This parameter is used to calculate the liquid molar volume using the Clarke equation for electrolyte	See Aspen help pages

	Interaction>VLCLK			solutions of C5H14-01 and HCO3-	
104	Properties>Methods>Parameters>Binary Interaction>VLCLK	2	ACA	This parameter is used to calculate the liquid molar volume using the Clarke equation for electrolyte solutions of C5H14-01 and HCO3-	See Aspen help pages
105	Properties>Methods>Parameters>Binary Interaction>VLCLK	1	VCA	This parameter is used to calculate the liquid molar volume using the Clarke equation for electrolyte solutions of C5H14-01 and CO3-2	See Aspen help pages
106	Properties>Methods>Parameters>Binary Interaction>VLCLK	2	ACA	This parameter is used to calculate the liquid molar volume using the Clarke equation for electrolyte solutions of C5H14-01 and CO3-2	See Aspen help pages

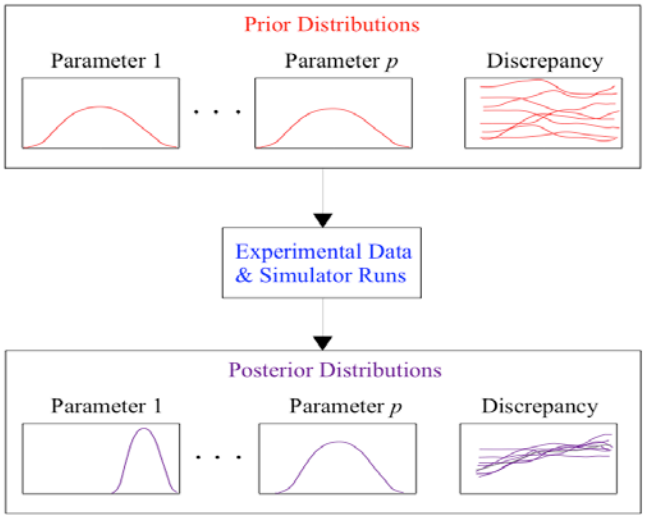

Figure B-1 – A graphical representation of UQ

Table B-2 – Ionic τ values[14]

Location	$\tau_{m,ca}$ or $\tau_{ca,m}$ "a" Values (GMEL-CC)
Properties>Methods>Parameters>Electrolyte Pair>GMEL-CC-1	H2O
	PZH+
	PZCOO-
"	PZH+
	PZCOO-
	H2O
"	PZ
	PZH+
	PZCOO-
"	PZH+
	PZCOO-
	PZ
"	PZH+
	PZCOO-
	HPZCOO
"	PZH+
	HCO3-
	HPZCOO
"	HPZCOO
	PZH+
	HCO3-
"	HPZCOO
	PZH+
	PZCOO-
"	PZH+
	PZCOO-2
	HPZCOO
"	HPZCOO
	PZH+
	PZCOO-2
"	H2O
	PZH+

[14] The parameters in Table B-2 have their greatest impact in the *difference* between each pair of molecule-ion interactions ($\tau_{m,ca}$ and $\tau_{ca,m}$). Therefore, only one parameter is adjusted (highlighted in blue) while the other half of the pairwise interaction is stationary (highlighted in red).

	PZCOO-2
“	PZH+
	PZCOO-2
	H2O
“	PZ
	PZH+
	PZCOO-2
“	PZH+
	PZCOO-2
	PZ
	$\tau_{m,ca}$ or $\tau_{ca,m}$ "b" Values (GMEL-CD)
Properties>Methods>Parameters>Electrolyte Pair>GMEL-CD-1	PZH+
	PZCOO-
	CO2

B.3.3 Uncertainty Quantification

Figure B-2 is a logic diagram of the UQ for the thermodynamic submodels in Independence. The thermodynamic models contain numerous parameters that must be calibrated to be self-consistent with a large amount of data. Because the large number of parameters is difficult to emulate over, the least sensitive and/or partially redundant parameters are fixed, and only a subset of parameters is explored in creating an emulator of the thermodynamic model, calibrating the parameters, and quantifying the uncertainty, as described in Chapter 4. Even with these simplifications, the parameter set is still too large, and the calibration must occur in two stages or tiers, which introduces the substantial complication of propagating the uncertainty correctly from tier 1 to tier 2. In this case, tier one consists of the Henry’s constant model and the piperazine (PZ)/water system without solvated CO_2, which is used to calibrate parameters for the heat capacity, the Henry’s constant, and the activity coefficient for PZ in water. Tier 2 then calibrates energies of formation and activity coefficients for the loaded PZ/water/CO_2 system, using the

equation for the equilibrium constant as obtained from energies of formation and chemical activities to search for a mutually consistent parameter space.

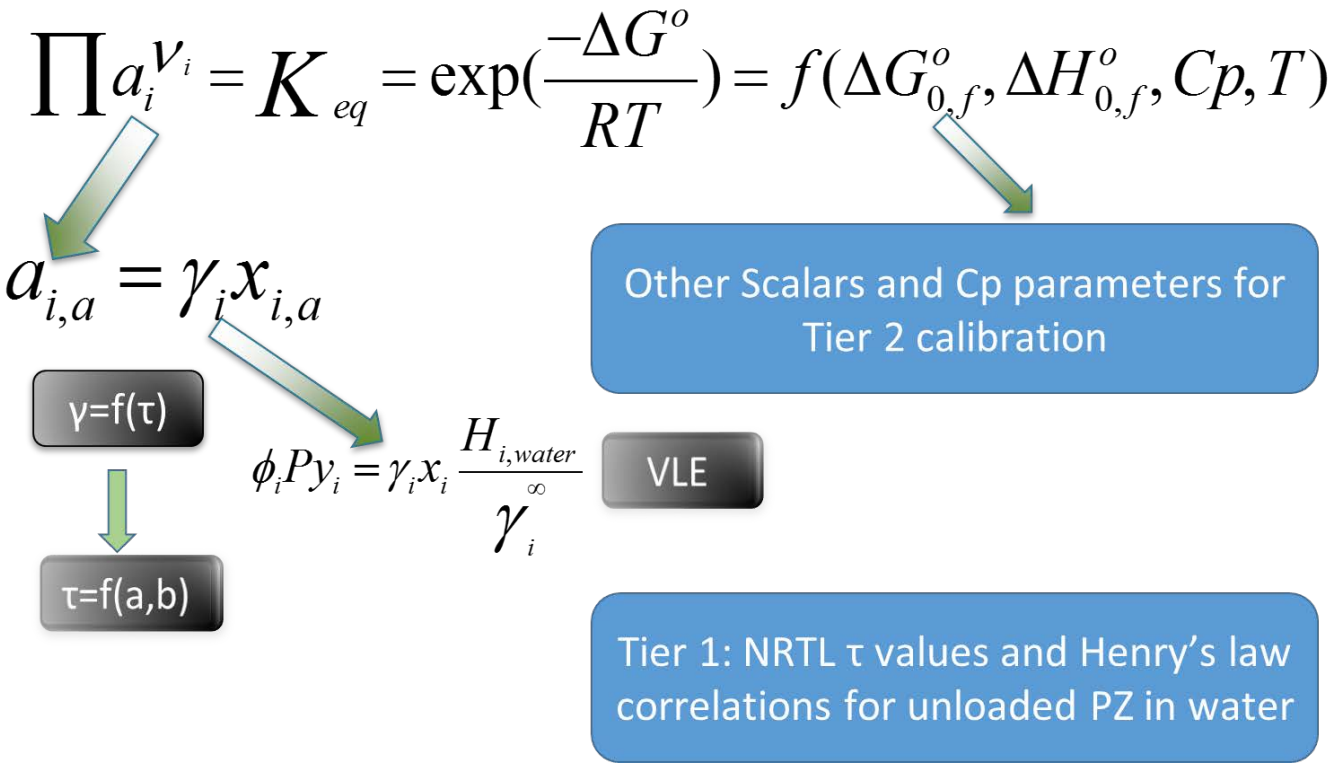

Figure B-2 – Logic diagram of Independence UQ

B.3.4 Results

Tier 1 sample results are shown below, where red lines are the calibrated model prediction at the 95% confidence level, black lines are the calibrated model including discrepancy (also at the 95% confidence level, and black dots are data. Figure B-3 show the calibrated heat capacity model, with excellent model/data agreement. Figure B-4 has relatively poor agreement with large uncertainty, but this is a direct artefact of the data (which has wide scatter). It also recently became apparent that a high temperature data set was excluded from the Henry's constant calibration, which increases uncertainty considerably for a model form that is exponential in temperature. Finally, Figure B-5 shows the univariate (diagonal) and bivariate (off-diagonals)

marginal posterior distributions for the τ and $H_{i,H2O}$ parameters. Note that the τ parameters were well defined by the calibration, and settled on a probability region consistent with past experience (Frailie, 2014). The Henry's constant parameters were not well defined in the univariate marginal, but the bivariate marginal of Henry's constant parameters one and two show that the model is relatively tightly defined when those parameters are conditioned on each other. The third Henry's constant parameter is not refined in any meaningful way either in the univariate or bivariate, which was expected in this case. The empirical model allows for up to five parameters (to span a large temperature range accurately). In this case, the temperature range is narrow, and only two parameters are useful in fitting the data, while the third parameter does not improve the fit, as can be noted from a simple regression of the linearized model.

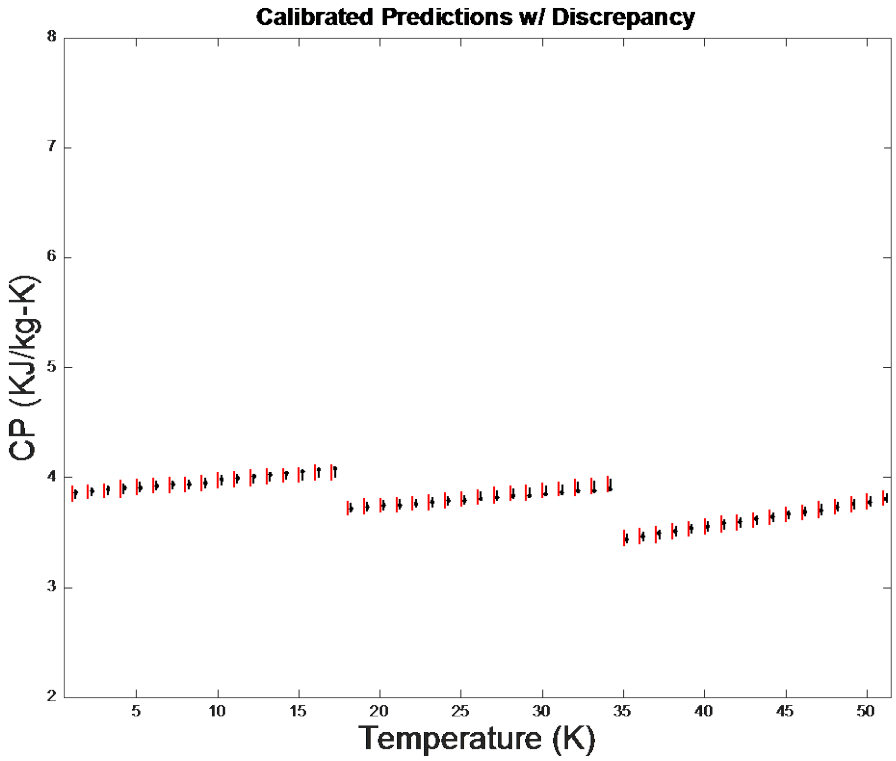

Figure B-3 – Calibrated predictions of the heat capacity, where the black dots are data points, the black lines are predictions including calibrated model discrepancy, and the red lines are the calibrated model without discrepancy. The lines are the result of numerous samples from the parameter posterior distributions.

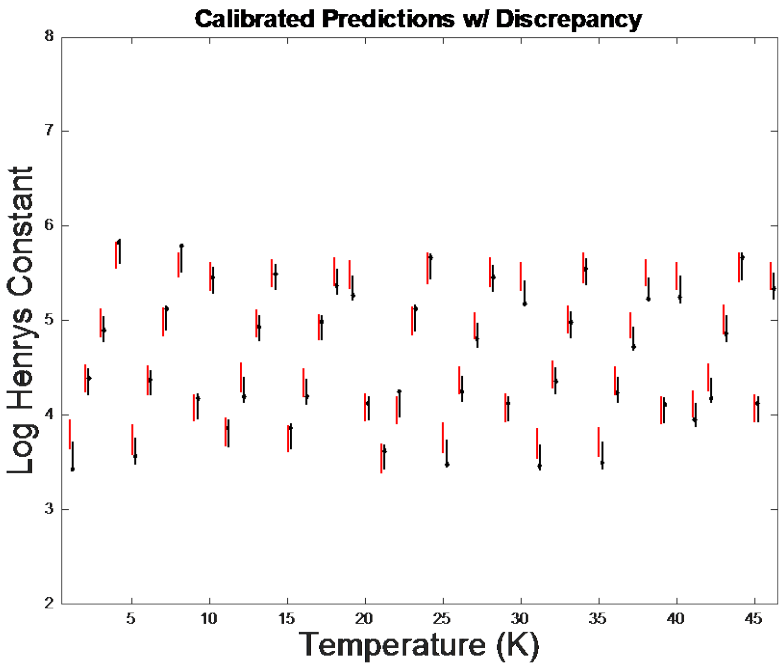

Figure B-4 – Calibrated predictions of the Henry's constant, where the black dots are data points, the black lines are predictions including calibrated model discrepancy, and the red lines are the calibrated model without discrepancy. The lines are the result of numerous samples from the parameter posterior distributions. Piperazine mol fraction is also varied leading to considerable model form error.

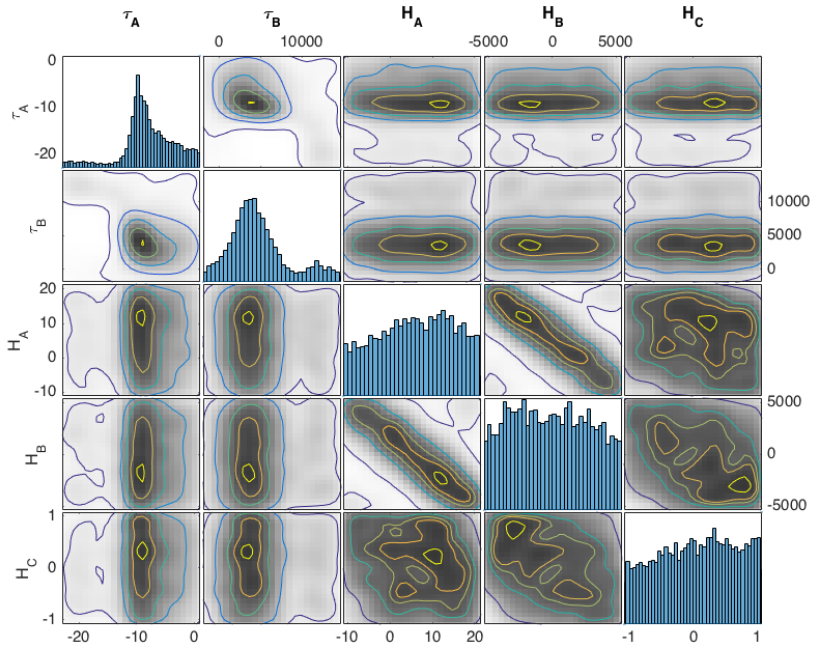

Figure B-5 – Univariate and bivariate posterior marginal PDFs

C. ADDITIONAL CHAPTER SECTIONS

This section includes an eclectic mix of additional chapter sections that added additional insight and detail in their original chapters. There were moved to the appendix for space considerations.

C.1 Chapter 2

C.1.1 Data

This work consisted exclusively of computer modeling as part of the stipulation of the funding. However, all models require critical, rigorous evaluation with data and/or previously validated codes, and relevant data is in short supply for this project. Oxy-fuel combustion has received relatively little attention until recent years, and even now the bulk of experimental data in oxy-coal conditions are not appropriate for the operating regimes of a coal-fired boiler. That said, a search of the literature has turned up several documents that will allow this work to be validated, and provide acceptably accurate parameters. The validation process will also reveal gaps that must be experimentally filled both for optimal, coal-specific accuracy, and to pin down more universal parameters to maximize predictive capabilities.

The relevant data come from several sources including Sandia National Laboratories and various coal researchers around the world, and promising literature sources are listed in Table C-1. The oxy-coal combustion data were originally obtained for a wide variety of purposes, including

gasification studies, CFD of entrained flow reactors, and (in the case of Sandia) to investigate the fundamental details of oxy-fuel combustion.

Table C-1 – Char Oxidation Data

Time (s)	Conversion	Gas % Composition	Temperature Range (K)	Coal Type	Particle d (μm)	Facility Type	Author
Unreported	0.795-0.973	21-35 O_2 Balance CO_2	1100-1500	Sub-anthracite 2 High-volatile bituminous	75-150	Entrained Flow Reactor	(Álvarez et al., 2013)
0.62	0.67-1	5-30 O_2 Balance CO_2 OR 3-21 O_2 Balance N_2	up to 1473 for TGA up to 1673 for DTF	Only proximate and ultimate analysis given (4 coals)	63-90	Drop-Tube Furnace AND Thermogravim-etric Analysis	(Rathnam et al., 2009)
Not Given	0-0.9	21 O_2 Balance CO_2 OR 21 O_2 Balance N_2	673-1173 for TGA 1173-1773 for DTF	Two bituminous coals	74-112	Drop-Tube Furnace AND Thermogravim-etric Analysis	(Naredi and Pisupati, 2011)
Not Given	0.35-0.8	5-30 O_2 Balance CO_2	Up to 2300 K	Black Thunder	106-180 75-106	EFR	(Kim et al., 2014)
Not Given	0.05-1	100 CO_2	1143-1559	Yallourn Taiheiyo Markham Bearpark Cynheidre	Not given	TGA	(Osafune and Marsh, 1987)
Not Given	0-1	.07-100 CO_2 Balance N_2	1313-1573	Indonesian sub-bituminous	53-63	EFR	(Gonzalo-Tirado et al., 2012)
Not Given	Not Given	O_2 12-36 O_2 16 H_2O Balance N_2 or CO_2	~1700	sub-bituminous high-volatile bituminous	75-106	EFR	(Geier et al., 2012)
.04<	Not Given	O_2 12-36 O_2 14 H_2O Balance N_2 or CO_2	~1700	sub-bituminous high-volatile bituminous	75-106	EFR	(Shaddix and Molina, 2009)

C.1.2 Final Note on Model Forms

While the above models appear quite diverse in their derivation and assumptions, it has been observed that they are mutually reconcilable to a high degree over limited ranges (Aris, 1989;

Astarita, 1989; Burnham and Braun, 1999). For example, Senneca et al. used a simple reaction coordinate to capture deactivation rates with relatively good success (Salatino et al., 1999). This simplifies and reduces the computational burden over a more conceptually correct distribution of activation energies and is in accordance with a more complete treatment of complex reactive mixtures as a continuum by Aris.(Aris, 1989) It was also broadly compatible with similar work by Murty et al. (Murty et al., 1969). As a final note, Feng et al. (Feng et al., 2003b) developed a method to investigate the "true" distribution of annealing process activation energies. This method showed that while the other models (distributed activation energy and single activation energy models) may be broadly reconcilable to each other, they lack the flexibility to predict the true deactivation rate of a given coal, especially over broad ranges of conditions. Unfortunately, Feng's method requires heat treatment/reactivity data for a specific coal that are not generally available, so this method cannot be directly applied in most cases. However, the findings from Feng et al. **do** indicate that a more flexible model is needed to reasonably approximate diverse thermal annealing processes over a broad range of coal types and heat treatments. Hurt et al. (Hurt et al., 1998) stated, in creating his annealing model detailed above, "much more work is needed to accurately understand and describe annealing kinetics under all conditions for a wide variety of parent materials." Fortunately, significant research has been completed and documented in the nearly two decades since Hurt's statement, which leads to the model developed in Chapter 6.

C.2 Chapter 4

C.2.1 Final Note on Model Forms

Figure C-1 from a graphical point of view. In Figure C-1 the prior distributions on both **θ** and **IP** are informed by the data (the likelihood function is computed for both internal parameters and model parameters), and a new, posterior parameter space is produced, where parameter values that are likely to explain the data have a high probability density while parameter values that explain the data very poorly are assigned correspondingly low probability densities.

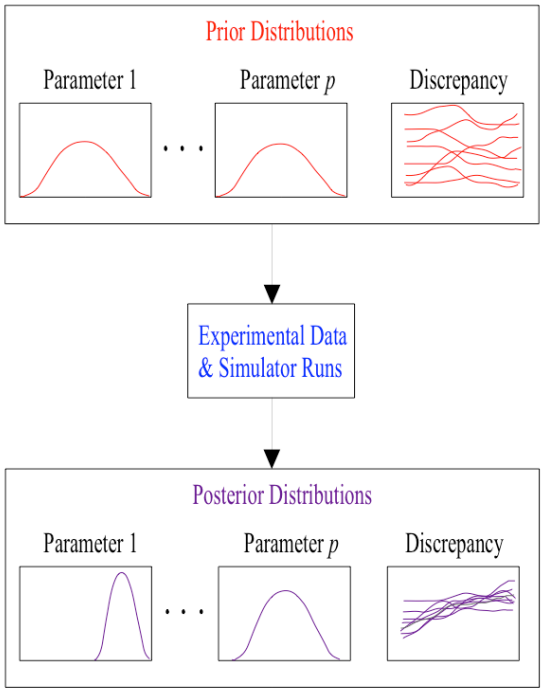

Figure C-1– Graphical representation of model calibration with discrepancy.

The methods outlined in Section 4.4 were applied particularly in Chapter 6 and additional results (for amine-based carbon capture) may be found in found in Appendix B. In general, the layers of models and submodels were unpacked from their "black-box" configuration, emulated by a collection of GPs, and calibrated via Bayesian inference on the parameters used in both the models and the GPs. Because the models are intended to be physically and theoretically sound, and not merely an empirical model that fits the data, the ultimate result of the calibration is not

the only (or even primary) goal. Instead, the discrepancy function offers insight into how the model fails to match reality, and indicates which inputs are most important in reconciling the discrepancy by adjusting the model form to include further physics.

C.3 Chapter 6

Note that there are number of char PC_R and MC_R (predicted and measured relative reactivity values) char values that are greater than 1. This is because the annealing decreases the reactivity by different amounts depend on time temperature profile, heating rate, peak particle temperature and precursor. Thus, even within a single precursor, there is not always an unambiguously most extreme annealing condition to choose as the reference char. However, the modeling results and optimization objective function identically regardless of this idiosyncrasy.

C.3.1 Char Annealing Data for O_2 Reactivity

Table C-2 – Detailed experimental data for char reactivity in O_2[15]

Coal name	PC_R	MC_R	p_0	HR (K/s)	T_p (K)	HTT (s)	Ref HR (K/s)	Ref T_p (K)	Ref HTT (s)
Beulah Zap	3.23	25.7	0.65	1e5	1514	2	1e5	2295	2
Beulah Zap	2.24	22.2	0.65	1e5	1735	2	1e5	2295	2
Beulah Zap	1.68	15.0	0.65	1e5	1925	2	1e5	2295	2
Beulah Zap	1.33	6.70	0.65	1e5	2086	2	1e5	2295	2
Pocahontas	3.69	22.6	0.70	1e5	1606	2	1e5	2388	2
Pocahontas	2.55	6.12	0.70	1e5	1809	2	1e5	2388	2
Pocahontas	2.16	2.68	0.70	1e5	1903	2	1e5	2388	2
Pocahontas	1.73	1.43	0.70	1e5	2032	2	1e5	2388	2
Pocahontas	1.44	1.06	0.70	1e5	2152	2	1e5	2388	2
Pocahontas	1.12	1.00	0.70	1e5	2315	2	1e5	2388	2
Illinois 6	1.56	42.5	0.45	1e5	1585	2	1e5	2155	2
Illinois 6	1.39	31.3	0.45	1e5	1731	2	1e5	2155	2
Illinois 6	1.25	15.5	0.45	1e5	1857	2	1e5	2155	2

[15] PC_R indicates the model prediction of the reactivity ratio between a data point and a reference point (unitless), while MC_R indicates the measured ratio. HR indicates the estimated initial heating rate, and HTT indicates the treatment time.

Coal name	PC_R	MC_R	p_0	HR (K/s)	T_p (K)	HTT (s)	Ref HR (K/s)	Ref T_p (K)	Ref HTT (s)
Beulah Zap	3.23	25.7	0.65	1e5	1514	2	1e5	2295	2
Illinois 6	1.16	6.94	0.45	1e5	1957	2	1e5	2155	2
Illinois 6	1.10	2.68	0.45	1e5	2006	2	1e5	2155	2
South African	1.25	2.08	0.67	16.7	1514	120	16.7	1503	1800
South African	1.22	1.29	0.67	16.7	1465	1800	16.7	1503	1800
South African	1.29	1.61	0.67	16.7	1438	1800	16.7	1503	1800
South African	2.17	6.02	0.67	16.7	1173	1800	16.7	1503	1800
South African	2.86	10.4	0.67	16.7	1173	60	16.7	1503	1800
Cerrejon	0.83	0.75	0.56	1e4	1173	0.51	1e4	973	1
Cerrejon	0.81	0.74	0.56	1e4	1173	0.75	1e4	973	1
Cerrejon	0.80	0.74	0.56	1e4	1173	0.9	1e4	973	1
Cerrejon	0.79	0.73	0.56	1e4	1173	1.12	1e4	973	1
Cerrejon	0.78	0.65	0.56	1e4	1173	1.35	1e4	973	1
Cerrejon	0.77	0.49	0.56	1e4	1173	1.65	1e4	973	1
Cerrejon	0.79	1.15	0.56	1e4	1273	0.17	1e4	973	1
Cerrejon	0.79	0.53	0.56	1e4	1273	0.17	1e4	973	1
Cerrejon	0.81	0.95	0.56	1e4	1273	0.13	1e4	973	1
Cerrejon	0.81	1.01	0.56	1e4	1273	0.13	1e4	973	1
Cerrejon	0.78	0.90	0.56	1e4	1273	0.2	1e4	973	1
Cerrejon	0.78	0.79	0.56	1e4	1273	0.2	1e4	973	1
Cerrejon	0.78	0.73	0.56	1e4	1273	0.23	1e4	973	1
Cerrejon	0.76	0.56	0.56	1e4	1273	0.3	1e4	973	1
Cerrejon	0.75	0.48	0.56	1e4	1273	0.36	1e4	973	1
Cerrejon	0.81	0.48	0.56	1e4	1273	0.12	1e4	973	1
Cerrejon	0.74	0.37	0.56	1e4	1273	0.43	1e4	973	1
Cerrejon	0.74	0.50	0.56	1e4	1273	0.43	1e4	973	1
Cerrejon	0.73	0.33	0.56	1e4	1273	0.54	1e4	973	1
Cerrejon	0.71	0.31	0.56	1e4	1273	0.65	1e4	973	1
Cerrejon	0.70	0.31	0.56	1e4	1273	0.79	1e4	973	1
Cerrejon	0.69	0.30	0.56	1e4	1273	0.96	1e4	973	1
Cerrejon	0.72	1.02	0.56	1e4	1373	0.12	1e4	973	1
Cerrejon	0.70	1.01	0.56	1e4	1373	0.16	1e4	973	1
Cerrejon	0.69	0.98	0.56	1e4	1373	0.19	1e4	973	1
Cerrejon	0.70	0.98	0.56	1e4	1373	0.15	1e4	973	1
Cerrejon	0.72	0.96	0.56	1e4	1373	0.12	1e4	973	1
Cerrejon	0.70	0.95	0.56	1e4	1373	0.16	1e4	973	1
Cerrejon	0.71	0.46	0.56	1e4	1373	0.13	1e4	973	1
Cerrejon	0.68	0.40	0.56	1e4	1373	0.23	1e4	973	1
Cerrejon	0.65	0.33	0.56	1e4	1373	0.4	1e4	973	1
Cerrejon	0.66	0.21	0.56	1e4	1373	0.33	1e4	973	1
Cerrejon	0.64	0.19	0.56	1e4	1373	0.49	1e4	973	1
Cerrejon	0.64	0.18	0.56	1e4	1373	0.59	1e4	973	1

Coal name	PC_R	MC_R	p_0	HR (K/s)	T_p (K)	HTT (s)	Ref HR (K/s)	Ref T_p (K)	Ref HTT (s)
Beulah Zap	3.23	25.7	0.65	1e5	1514	2	1e5	2295	2
Cerrejon	0.63	0.20	0.56	1e4	1373	0.73	1e4	973	1
Cerrejon	0.62	0.16	0.56	1e4	1373	0.89	1e4	973	1
Cerrejon	0.61	0.34	0.56	1e4	1473	0.22	1e4	973	1
Cerrejon	0.60	0.32	0.56	1e4	1473	0.26	1e4	973	1
Cerrejon	0.59	0.20	0.56	1e4	1473	0.31	1e4	973	1
Cerrejon	0.58	0.17	0.56	1e4	1473	0.34	1e4	973	1
Cerrejon	0.57	0.15	0.56	1e4	1473	0.4	1e4	973	1
Cerrejon	0.57	0.14	0.56	1e4	1473	0.46	1e4	973	1
Cerrejon	0.56	0.13	0.56	1e4	1473	0.57	1e4	973	1
Cerrejon	0.55	0.11	0.56	1e4	1473	0.68	1e4	973	1
Cerrejon	0.54	0.11	0.56	1e4	1473	0.84	1e4	973	1
Cerrejon	0.54	0.12	0.56	1e4	1473	1.03	1e4	973	1
Cerrejon	0.53	0.10	0.56	1e4	1473	1.25	1e4	973	1
Cerrejon	0.62	0.39	0.56	1e4	1473	0.17	1e4	973	1
Cerrejon	0.52	0.75	0.56	1e4	1573	0.15	1e4	973	1
Cerrejon	0.51	0.65	0.56	1e4	1573	0.2	1e4	973	1
Cerrejon	0.52	0.62	0.56	1e4	1573	0.15	1e4	973	1
Cerrejon	0.50	0.56	0.56	1e4	1573	0.23	1e4	973	1
Cerrejon	0.50	0.53	0.56	1e4	1573	0.23	1e4	973	1
Cerrejon	0.50	0.29	0.56	1e4	1573	0.28	1e4	973	1
Cerrejon	0.49	0.18	0.56	1e4	1573	0.34	1e4	973	1
Cerrejon	0.48	0.14	0.56	1e4	1573	0.42	1e4	973	1
Cerrejon	0.47	0.11	0.56	1e4	1573	0.51	1e4	973	1
Cerrejon	0.46	0.12	0.56	1e4	1573	0.63	1e4	973	1
Cerrejon	0.45	0.09	0.56	1e4	1573	0.75	1e4	973	1
Cerrejon	0.45	0.09	0.56	1e4	1573	0.92	1e4	973	1
Cerrejon	0.44	0.12	0.56	1e4	1573	1.12	1e4	973	1
Cerrejon	0.42	0.35	0.56	1e4	1748	0.15	1e4	973	1
Cerrejon	0.42	0.31	0.56	1e4	1748	0.14	1e4	973	1
Cerrejon	0.41	0.24	0.56	1e4	1748	0.21	1e4	973	1
Cerrejon	0.41	0.22	0.56	1e4	1748	0.17	1e4	973	1
Cerrejon	0.41	0.16	0.56	1e4	1748	0.22	1e4	973	1
Cerrejon	0.40	0.12	0.56	1e4	1748	0.24	1e4	973	1
Cerrejon	0.40	0.10	0.56	1e4	1748	0.3	1e4	973	1
Cerrejon	0.39	0.10	0.56	1e4	1748	0.37	1e4	973	1
Cerrejon	0.37	0.08	0.56	1e4	1748	0.67	1e4	973	1
Cerrejon	0.36	0.05	0.56	1e4	1748	0.82	1e4	973	1
Cerrejon	0.35	0.04	0.56	1e4	1748	1.01	1e4	973	1
Pocahontas	1.46	1.68	0.75	1e4	2073	0.15	1e4	2073	2
Pocahontas	1.23	1.13	0.75	1e4	2073	0.5	1e4	2073	2
Pocahontas	8.43	2.92	0.75	1e4	1273	0.15	1e4	2073	2

Coal name	PC_R	MC_R	p_0	HR (K/s)	T_p (K)	HTT (s)	Ref HR (K/s)	Ref T_p (K)	Ref HTT (s)
Beulah Zap	3.23	25.7	0.65	1e5	1514	2	1e5	2295	2
Pocahontas	7.27	2.15	0.75	1e4	1273	0.5	1e4	2073	2
Pocahontas	6.18	1.61	0.75	1e4	1273	2	1e4	2073	2
Pocahontas	5.55	1.55	0.75	1e4	1273	5	1e4	2073	2
Pocahontas	3.12	1.80	0.75	1e4	1673	0.15	1e4	2073	2
Pocahontas	2.64	1.41	0.75	1e4	1673	0.5	1e4	2073	2
Pocahontas	2.19	1.39	0.75	1e4	1673	2	1e4	2073	2
Pocahontas	1.93	1.31	0.75	1e4	1673	5	1e4	2073	2
Pocahontas	2.11	2.12	0.75	1e4	1873	0.15	1e4	2073	2
Pocahontas	1.77	1.34	0.75	1e4	1873	0.5	1e4	2073	2
Pocahontas	1.46	1.20	0.75	1e4	1873	2	1e4	2073	2
Pocahontas	1.29	1.09	0.75	1e4	1873	5	1e4	2073	2
Pittsburgh 8	1.22	1.49	0.52	1e4	2073	0.15	1e4	2073	2
Pittsburgh 8	1.12	1.12	0.52	1e4	2073	0.5	1e4	2073	2
Pittsburgh 8	2.89	5.46	0.52	1e4	1273	0.15	1e4	2073	2
Pittsburgh 8	2.67	4.53	0.52	1e4	1273	0.5	1e4	2073	2
Pittsburgh 8	2.44	2.78	0.52	1e4	1273	2	1e4	2073	2
Pittsburgh 8	2.29	2.79	0.52	1e4	1273	5	1e4	2073	2
Pittsburgh 8	1.82	3.08	0.52	1e4	1673	0.15	1e4	2073	2
Pittsburgh 8	1.69	2.33	0.52	1e4	1673	0.5	1e4	2073	2
Pittsburgh 8	1.50	2.08	0.52	1e4	1673	2	1e4	2073	2
Pittsburgh 8	1.42	2.03	0.52	1e4	1673	5	1e4	2073	2
Pittsburgh 8	1.48	2.84	0.52	1e4	1873	0.15	1e4	2073	2
Pittsburgh 8	1.37	2.03	0.52	1e4	1873	0.5	1e4	2073	2
Pittsburgh 8	1.21	1.39	0.52	1e4	1873	2	1e4	2073	2
Pittsburgh 8	1.15	1.30	0.52	1e4	1873	5	1e4	2073	2
Tillmanstone	0.77	0.63	0.77	5	1223	5	5e3	1223	5
Tillmanstone	0.98	0.90	0.77	1e3	1223	5	5e3	1223	5
Pittsburgh 8	1.47	3.34	0.53	1e3	973	2	5e3	1273	2
Pittsburgh 8	1.13	2.17	0.53	1e3	1173	2	5e3	1273	2
Pittsburgh 8	0.99	0.80	0.53	1e3	1273	2	5e3	1273	2
Pittsburgh 8	0.79	0.34	0.53	1e3	1473	2	5e3	1273	2
Pittsburgh 8	0.53	0.14	0.53	1e3	1773	2	5e3	1273	2
Pittsburgh 8	0.83	0.68	0.53	5	1273	2	5e3	1273	2
Pittsburgh 8	0.93	0.77	0.53	50	1273	2	5e3	1273	2
Linby	1.31	2.67	0.54	1e3	973	2	5e3	1273	2
Linby	1.11	1.92	0.54	1e3	1173	2	5e3	1273	2
Linby	0.98	0.97	0.54	1e3	1273	2	5e3	1273	2
Linby	0.77	0.47	0.54	1e3	1473	2	5e3	1273	2
Linby	0.44	0.10	0.54	1e3	1773	2	5e3	1273	2
Linby	0.75	0.50	0.54	2	1273	2	5e3	1273	2
Linby	0.91	0.86	0.54	50	1273	2	5e3	1273	2

Coal name	PC_R	MC_R	p_0	HR (K/s)	T_p (K)	HTT (s)	Ref HR (K/s)	Ref T_p (K)	Ref HTT (s)
Beulah Zap	3.23	25.7	0.65	1e5	1514	2	1e5	2295	2
Illinois 6 (APCS)	2.93	18.4	0.54	1e3	973	2	1e3	1773	2
Illinois 6 (APCS)	2.72	7.06	0.54	1e3	1123	2	1e3	1773	2
Illinois 6 (APCS)	2.23	4.96	0.54	1e3	1273	2	1e3	1773	2
Illinois 6 (SBN)	1.23	3.30	0.44	1e3	973	2	5e3	1273	2
Illinois 6 (SBN)	1.14	1.20	0.44	1e3	1123	2	5e3	1273	2
Illinois 6 (SBN)	0.99	0.95	0.44	1e3	1273	2	5e3	1273	2
Illinois 6 (SBN)	0.83	0.40	0.44	1e3	1473	2	5e3	1273	2
Illinois 6 (SBN)	0.55	0.14	0.44	1e3	1773	2	5e3	1273	2
Illinois 6 (SBN)	0.83	0.26	0.44	2	1273	2	5e3	1273	2
Illinois 6 (SBN)	0.94	0.80	0.44	50	1273	2	5e3	1273	2
South African	9.22	18.72	0.67	15	773	600	16700	2273	2
South African	5.63	11.51	0.67	15	973	1200	16700	2273	2
South African	4.58	6.58	0.67	15	1173	60	16700	2273	2
South African	2.03	4.19	0.67	167	1473	1800	16700	2273	2
South African	1.21	3.32	0.67	167	1673	1800	16700	2273	2
High Volatile Bituminous	1.13	0.83	0.43	0.833	1123	5400	5e4	1673	0.5
High Volatile Bituminous	1.73	1.84	0.43	5e4	1173	0.5	5e4	1673	0.5
High Volatile Bituminous	1.46	1.96	0.43	5e4	1373	0.5	5e4	1673	0.5
Pittsburgh 8	1.66	1.80	0.52	3.3e4	1106	0.49	6.6e4	1627	0.135
Pittsburgh 8	1.34	0.80	0.52	5.4e4	1333	0.28	6.6e4	1627	0.135
Pittsburgh 8	1.71	3.44	0.52	3.5e4	986	0.15	6.6e4	1627	0.135
Pittsburgh 8	1.71	3.77	0.52	3.5e4	986	0.15	6.6e4	1627	0.135
Pittsburgh 8	1.71	3.77	0.52	3.5e4	986	0.15	6.6e4	1627	0.135
Blind Canyon	1.51	8.96	0.46	3.0e4	1097	0.49	6.6e4	1625	0.135
Blind Canyon	1.58	15.0	0.46	2.4e4	1002	0.29	6.6e4	1625	0.135
Blind Canyon	1.20	4.17	0.46	5.3e4	1333	0.49	6.6e4	1625	0.135
Beulah Zap	1.98	0.63	0.58	3.1e4	1027	0.29	7.4e4	1625	0.135
Beulah Zap	1.93	0.53	0.58	3.4e4	1095	0.49	7.4e4	1625	0.135
Beulah Zap	1.41	0.29	0.58	5.9e4	1334	0.49	7.4e4	1625	0.135
Beulah Zap	1.99	0.26	0.58	4.0e4	972	0.15	7.4e4	1625	0.135
Beulah Zap	1.93	0.66	0.58	4.0e4	1095	0.49	7.4e4	1625	0.135

C.3.2 Char Annealing Data of Gasification Reactivity

Table C-3 – Detailed experimental data for char reactivity in CO_2[16]

Coal name	PC_R	MC_R	p_0	HR (K/s)	T_p (K)	HTT (s)	Ref HR (K/s)	Ref T_p (K)	Ref HTT (s)
South African	0.76	0.79	0.69	16.66	1173	1800	16.66	1173	60
South African	0.76	0.83	0.69	16.66	1173	1800	16.66	1173	60
South African	0.76	0.89	0.69	16.66	1173	1800	16.66	1173	60
South African	0.62	0.69	0.69	16.66	1173	18000	16.66	1173	60
South African	0.62	0.79	0.69	16.66	1173	18000	16.66	1173	60
South African	0.62	0.77	0.69	16.66	1173	18000	16.66	1173	60
South African	7.26	3.58	0.69	1.5	1173	60	16667	2273	80
South African	7.26	3.92	0.69	1.5	1173	60	16667	2273	80
South African	7.26	3.31	0.69	1.5	1173	60	16667	2273	80
South African	5.57	2.92	0.69	1.5	1173	1800	16667	2273	80
South African	5.57	3.14	0.69	1.5	1173	1800	16667	2273	80
South African	5.57	2.81	0.69	1.5	1173	1800	16667	2273	80
South African	3.39	1.55	0.69	167	1473	1800	16667	2273	80
South African	3.39	2.05	0.69	167	1473	1800	16667	2273	80
South African	3.39	2.19	0.69	167	1473	1800	16667	2273	80
South African	3.21	1.83	0.69	16667	1873	1	16667	2273	80
South African	3.21	2.47	0.69	16667	1873	1	16667	2273	80
South African	3.21	2.64	0.69	16667	1873	1	16667	2273	80
South African	2.12	2.40	0.69	16667	2273	0.2	16667	2273	80
South African	2.12	2.89	0.69	16667	2273	0.2	16667	2273	80

[16] PC_R indicates the model prediction of the reactivity ratio between a data point and a reference point (unitless), while MC_R indicates the measured ratio. HR indicates the estimated initial heating rate, and HTT indicates the treatment time.

Coal name	PC_R	MC_R	p_0	HR (K/s)	T_p (K)	HTT (s)	Ref HR (K/s)	Ref T_p (K)	Ref HTT (s)
South African	2.12	3.10	0.69	16667	2273	0.2	16667	2273	80
Shenfu	1.73	1.30	0.51	0.1	1223	1200	1e3	1773	1202
Shenfu	1.65	1.20	0.51	0.1	1273	1200	1e3	1773	1202
Shenfu	0.99	0.20	0.51	0.1	1673	1200	1e3	1773	1202
Shenfu	0.99	0.31	0.51	0.1	1673	1200	1e3	1773	1202
Shenfu	1.99	1.90	0.51	1e3	1223	1202	1e3	1773	1202
Shenfu	1.86	0.53	0.51	1e3	1273	1202	1e3	1773	1202
Rhur	2.24	4.32	0.58	16.7	1473	60	16.7	1673	1800
Rhur	2.24	5.36	0.58	16.7	1473	60	16.7	1673	1800
Rhur	2.24	5.50	0.58	16.7	1473	60	16.7	1673	1800
Rhur	1.77	3.11	0.58	16.7	1473	1800	16.7	1673	1800
Rhur	1.77	3.82	0.58	16.7	1473	1800	16.7	1673	1800
Rhur	1.77	4.01	0.58	16.7	1473	1800	16.7	1673	1800
Rhur	1.29	4.32	0.58	16.7	1673	60	16.7	1673	1800
Rhur	1.29	5.36	0.58	16.7	1673	60	16.7	1673	1800
Rhur	1.29	5.50	0.58	16.7	1673	60	16.7	1673	1800
Rhur	2.75	5.73	0.58	5	1173	1800	5	1673	1800
Rhur	2.75	6.61	0.58	5	1173	1800	5	1673	1800
Rhur	2.75	7.05	0.58	5	1173	1800	5	1673	1800
Rhur	1.75	3.41	0.58	5	1473	1800	5	1673	1800
Rhur	1.75	3.92	0.58	5	1473	1800	5	1673	1800
Rhur	1.75	4.55	0.58	5	1473	1800	5	1673	1800
South African	4.58	5.17	0.67	15	1173	60	16700	2273	2
South African	4.58	4.50	0.67	15	1173	60	16700	2273	2
South African	2.03	2.31	0.67	167	1473	1800	16700	2273	2
South African	2.03	2.31	0.67	167	1473	1800	16700	2273	2
South African	2.03	2.09	0.67	167	1473	1800	16700	2273	2
South African	1.21	1.12	0.67	167	1673	1800	16700	2273	2
South African	1.21	0.93	0.67	167	1673	1800	16700	2273	2
South African	1.21	0.95	0.67	167	1673	1800	16700	2273	2
Indian	0.95	0.81	0.60	0.667	1173	300	13.3	1173	300
Indian	0.96	0.95	0.60	1.667	1173	300	13.3	1173	300
Indian	0.99	1.10	0.60	8.33	1173	300	13.3	1173	300
Indian	0.93	0.84	0.60	0.667	1223	300	13.3	1223	300

Coal name	PC_R	MC_R	p_0	HR (K/s)	T_p (K)	HTT (s)	Ref HR (K/s)	Ref T_p (K)	Ref HTT (s)
Indian	0.95	0.89	0.60	1.667	1223	300	13.3	1223	300
Indian	0.99	0.89	0.60	8.33	1223	300	13.3	1223	300
Indian	0.93	0.83	0.60	0.667	1273	300	13.3	1273	300
Indian	0.94	0.88	0.60	1.667	1273	300	13.3	1273	300
Indian	0.99	0.97	0.60	8.33	1273	300	13.3	1273	300
Indian	0.95	0.91	0.60	0.667	1173	300	13.3	1173	300
Indian	0.96	0.95	0.60	1.667	1173	300	13.3	1173	300
Indian	0.99	0.95	0.60	8.33	1173	300	13.3	1173	300
Indian	0.93	0.95	0.60	0.667	1223	300	13.3	1223	300
Indian	0.95	0.98	0.60	1.667	1223	300	13.3	1223	300
Indian	0.99	1.01	0.60	8.33	1223	300	13.3	1223	300
Indian	0.93	0.95	0.60	0.667	1273	300	13.3	1273	300
Indian	0.94	1.05	0.60	1.667	1273	300	13.3	1273	300
Indian	0.99	1.09	0.60	8.33	1273	300	13.3	1273	300
Indian	0.95	1.48	0.60	0.667	1173	300	13.3	1173	300
Indian	0.96	1.16	0.60	1.667	1173	300	13.3	1173	300
Indian	0.99	1.10	0.60	8.33	1173	300	13.3	1173	300
Indian	0.93	1.00	0.60	0.667	1223	300	13.3	1223	300
Indian	0.95	1.07	0.60	1.667	1223	300	13.3	1223	300
Indian	0.99	1.10	0.60	8.33	1223	300	13.3	1223	300
Indian	0.93	1.02	0.60	0.667	1273	300	13.3	1273	300
Indian	0.94	1.06	0.60	1.667	1273	300	13.3	1273	300
Indian	0.99	0.99	0.60	8.33	1273	300	13.3	1273	300
Indian	0.95	0.83	0.60	0.667	1173	300	13.3	1173	300
Indian	0.96	0.79	0.60	1.667	1173	300	13.3	1173	300
Indian	0.99	0.75	0.60	8.33	1173	300	13.3	1173	300
Indian	0.93	0.90	0.60	0.667	1223	300	13.3	1223	300
Indian	0.95	0.97	0.60	1.667	1223	300	13.3	1223	300
Indian	0.99	1.05	0.60	8.33	1223	300	13.3	1223	300
Indian	0.93	0.70	0.60	0.667	1273	300	13.3	1273	300
Indian	0.94	0.91	0.60	1.667	1273	300	13.3	1273	300
Indian	0.99	1.02	0.60	8.33	1273	300	13.3	1273	300

C.3.3 Computational Experimental Design

In designing a computational experiment, the first step was to determine model input and parameter ranges. In Equation 6-8, y is the model output (where the model output is the sum of model predictions, model discrepancy from reality, and observational error). Equation 6-8 has a

vector of model inputs (**x**), and a vector of model parameters (**θ**). In the case of the original annealing model, **x** values were restricted to a time-temperature profile, and **θ** values were limited to the mean and standard deviation of the activation energy distribution and the annealing preexponential value. The range of permissible values for each input and parameter was used to set up a Latin hypercube sampling scheme. The hypercube accepts as inputs the allowed range and probability distribution of each parameter. The range is then divided into a specified number of equiprobable intervals, and one parameter value is chosen at random from each interval. For example, if 10 runs were desirable, the parameter space would be divided into 10 intervals. In the case of a uniform probability distribution, each of the 10 intervals would be of equal "length" in parameter space, while in the case of a normal distribution on the parameter space, the intervals near the mean parameter value would be much "shorter" than the intervals in the tail. Because each interval contributes exactly one parameter value, most of the samples would cluster around the mean, and the low probability sample space would not be well explored. The sampling process is executed for each parameter and input (**θ** and **x**), and the values are then systematically paired to be optimally space filling (McKay et al., 1979). The result is a matrix in which each column "j" contains randomly ordered, unbiased, space-filling samples from the range of parameter (or input) "j", and each row "i" is a set of all necessary input values and model parameters for a single computational experiment. In other words, each row of the matrix constructs a time-temperature profile and designates a value for the mean, variance, and preexponential factor of the annealing activation energy. The number of columns equals the number of parameters plus the number of inputs, and the number of rows is the number of computational experiments to be performed.

C.4 Chapter 7

For lower heating rates, Shurtz et al. (2011) developed a piecewise correlation, briefly described by Table C-4, Figure C-2, and Equation 29. It should be noted that Shurtz et al. (2011) created this low-heating rate (and very laborious) method from limited data. Table C-4 is used to map swelling values from regime 2 (the high heating rate regime) to regime 1 (low heating rate). Regime 1 is modeled as a 4-part piecewise correlation, where the lowest heating rates result in no swelling (implying that all the released volatiles have adequate time to escape the particle, and that the crosslinking is rapid compared to volatile release). The heating rates from regime 2 (column 2 of Table C-4) are used as inputs for Equation 27 for the HHR correlation above, and a swelling ratio is predicted for each heating rate. For example, the first low heating rating swelling ratio is computed by taking the first entry in column two Table C-4 (8.5e3 K/s), computing a value for s_{min}, c_{HR}, and s_{var} from the proximate and ultimate analysis of the coal in question (via the correlations in Table 7-3). This yields some $(d/d_0)_{HHR}$ via Equation 27. Equation 27 is computed for each of the three heating rates in column two of Table C-4, which yields three swelling ratios. Then, the three heating rates given in column 1 of Table C-4 are paired with the three swelling ratios output by Equation 27. The data pairs (a high heating rate swelling ratio and a low heating rate value) may be plotted on a semi-log plot as in Figure C-2. The fourth data point has a swelling ratio of unity and heating rate of 0.01 K/s. The four ordered pairs are adequate to determine a slope and intercept for the three linear equations of the piecewise regime 1 heating rate. The slope and intercept values are then used in Equation 29 to interpolate regime 1 swelling ratios. Any heating rate below 0.01 is assumed to have a swelling ratio of unity.

Table C-4 – Heating Rate Map from Regime 2 to Regime 1

Regime 1 Heating Rate (K/s)	Regime 2 Heating Rate (K/s)
$\dot{T}_{peak} = 8.5 * 10^3$	$\dot{T}_{peak} = 8.5 * 10^3$
$\dot{T}_{mid} = 1000$	$\dot{T}_{mid} = 1.63 * 10^4$
$\dot{T}_{low} = 1$	$\dot{T}_{low} = 3.37 * 10^4$

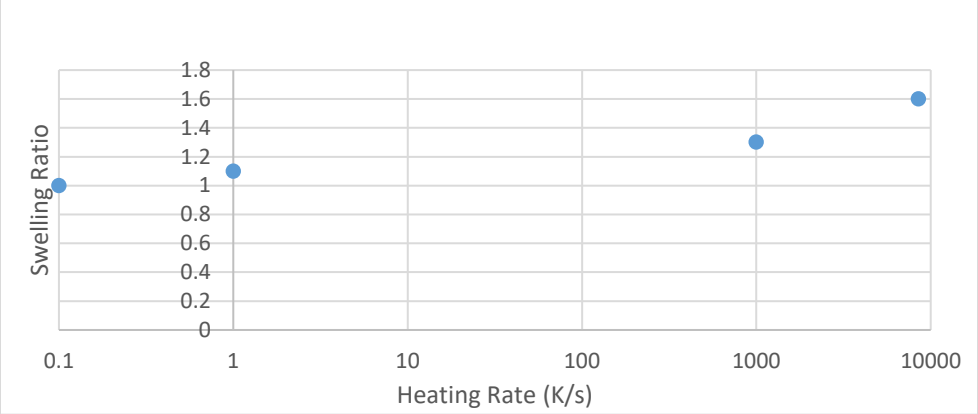

Figure C-2 – Semi-log plot of the low heating rate swelling correlation (swelling ratio values are for illustration only, and do not represent data).

$$\left(\frac{d}{d_0}\right)_{LHR} = m * \log(\dot{T}) + b \qquad \text{C-1}$$

C.4.1 Final Note on Model Forms

While the above models appear quite diverse in their derivation and assumptions, it has been observed that they are mutually reconcilable to a high degree over limited ranges (Aris, 1989; Astarita, 1989; Burnham and Braun, 1999). For example, Senneca et al. used a simple reaction coordinate to capture deactivation rates with relatively good success (Salatino et al., 1999). This simplifies and reduces the computational burden over a more conceptually correct distribution of

activation energies and is in accordance with a more complete treatment of complex reactive mixtures as a continuum by Aris.(Aris, 1989) It was also broadly compatible with similar work by Murty et al. (Murty et al., 1969). As a final note, Feng et al. (Feng et al., 2003b) developed a method to investigate the "true" distribution of annealing process activation energies. This method showed that while the other models (distributed activation energy and single activation energy models) may be broadly reconcilable to each other, they lack the flexibility to predict the true deactivation rate of a given coal, especially over broad ranges of conditions. Unfortunately, Feng's method requires heat treatment/reactivity data for a specific coal that are not generally available, so this method cannot be directly applied in most cases. However, the findings from Feng et al. **do** indicate that a more flexible model is needed to reasonably approximate diverse thermal annealing processes over a broad range of coal types and heat treatments. Hurt et al. (Hurt et al., 1998) stated, in creating his annealing model detailed above, "much more work is needed to accurately understand and describe annealing kinetics under all conditions for a wide variety of parent materials." Fortunately, significant research has been completed and documented in the nearly two decades since Hurt's statement, which leads to the model developed in Chapter 6.

C.5 Chapter 8

C.5.1 CFD Applications

The literature data and the results of fitting the CCK/oxy model to data imply that a CFD simulation should take into account two distributions to accurately capture coal char particles. The first distribution is the diameter distribution of the raw coal particles that form the char. The diameter heavily impacts burnout predictions, and the mean, variance, and distribution form may

propagate that impact on to the CFD simulation. In general, pulverized coal particle diameter distributions follow a Rosin-Rammler distribution, and it is this distribution that should be used in simulating industrial pulverized coal systems. For the experimental literature data used here, the full distribution is expected to be approximately normal after sieving, swelling, and fragmentation, but the optical particle temperature data are likely to be a truncated normal distribution. This is because the small diameter and/or rapidly oxidizable portion of the distribution quickly becomes undetectable due to the small radiative emission from these particles. The exact truncation point in the normal diameter distribution is unknown, and it is not consistent between burner heights, coal type, or O_2 condition. To fully describe the true distribution of a data set, a correlation between particle detectability, temperature, and diameter would be devised. Accurate parameters for such a correlation would assume a char emissivity, require an assumed distribution for the raw coal, and incorporate knowledge of the optical limits of the detecting system. These assumptions, in conjunction with the coal swelling model, would predict the post-devolatilization diameter of a char particle, and the partially-burned diameter at a given height, and appropriate correlation parameters would reconstruct the entire raw coal input diameter distribution.

The second distribution of interest is the change in particle combustion behavior due to maceral character and ash content. For a given particle diameter, the combustion temperatures (from the literature data referenced in this work) vary by approximately ±150 K. If these values are simply used as error bars, the high accuracy of the CCK/oxy model is effectively useless. Instead, this variation should not be treated as error, but as actual variation in any given cohort of particles. The data shown here imply that a normal distribution with a mean of the CCK/oxy temperature

prediction and a variance of approximately 75 K may be appropriate to capture the particle-to-particle variation.

An appropriate CFD application to combine accuracy and computational efficiency is needed. One potential method would be to first determine the initial particle diameter distribution. Given an approximation of that distribution, CCK/oxy can be executed using “n” diameters that cover the distribution in sufficient detail. Bin values separated by 10 microns are likely adequate. For each bin, CCK/oxy should be executed with a gamut of gas temperature and composition profiles, and the output vectors recorded. Finally, the output vectors for a given bin size would be used to train a surrogate function that depends on gas composition, temperature, and the peak temperature in the burnout history of the particle. Such a function would execute very rapidly but potentially capture the majority of the information of the CCK/oxy model. Implementation into a CFD simulation would appropriately weight the available particle diameters and temperature variation within each diameter according to the two distributions described above.

D. CCK/OXY CODES

The entirety of the CCK/oxy code may be found at https://github.com/tmholland86/CCK-oxy. Many of the subroutines were influence by past code that led from CBK through several iterations to the current code. These subroutines were typically written in FORTRAN 77 initially, and translated to MATLAB (and subsequently extended as needed) for greater compatibility within the research group. Details on the evolution of the code is documented to some degree elsewhere (Grant et al., 1989; Fletcher et al., 1992; Hurt et al., 1998; Niksa et al., 2003; Liu and Niksa, 2004; Shurtz, 2011; Shurtz et al., 2011; Shurtz et al., 2012; Shurtz and Fletcher, 2013).

E. ANNEALING CODES

The series of scripts and functions found at https://github.com/tmholland86/CCK-oxy constitute the CCK/oxy Annealing model, and were used to construct and explore the model.